Paleo-Ice Sheet and Deglacial History of the Southwestern Great Slave Lake Area

by

Grant William Hagedorn

A thesis

presented to the University of Waterloo

in fulfillment of the

thesis requirement for the degree of

Masters of Science

in

Earth Sciences

Waterloo, Ontario, Canada, 2022

Author's Declaration

I hereby declare that I am the sole author of this thesis. This is a true copy of the thesis, including any required final revisions, as accepted by my examiners.

I understand that my thesis may be made electronically available to the public.

Abstract

The western Laurentide Ice Sheet (LIS) is known to have experienced complex ice-flow shifts during the last glaciation due to ice divide migration and increasing topographic influence during deglaciation. Several glacial lakes also developed at different elevations during ice margin retreat over the region. However, due to limited field-based studies and surficial mapping, the evolution of the western LIS is still poorly constrained. Improving reconstructions of the western LIS evolution and understanding its net effect on landscapes and surficial sediments can provide important insights into long-term glacial processes, as well as useful knowledge for mineral exploration in glaciated terrains. Furthermore, detailing retreat over this region can help refine continental-scale ice sheet models and help test suggested meltwater drainage pathways to the northwest down the Mackenzie River Valley, which have important implications in paleoclimatology. This research details relative ice-flow chronology and associated till stratigraphy and provides a reconstruction of ice margin retreat and glacial lake positions along a portion of the western LIS situated west of Great Slave Lake, in the Northwest Territories.

Relative ice-flow chronology is established using glacial landforms, outcrop-scale ice-flow indicators, as well as till stratigraphic and provenance analyses. Outcrop-scale indicators show a shift in ice-flow direction from an oldest southwestern (230°) flow, to a western (250°) flow, to a final northwestern (305°) flow. This sequence counters the simple westward flow of other studies and suggests a younger rather than older northwestward ice-flow. Lodged boulders and till clast fabrics from till stratigraphic sections across the study area are broadly consistent with the clockwise ice-flow shift up the stratigraphic column. Indicators of northeast provenance include Canadian Shield (igneous and metamorphic) clasts that are in higher proportions than Mesozoic mudrocks and Paleozoic carbonate rocks that underlie the study area. Major oxides, from till matrix geochemistry, are enriched in metals (SiO_2-Al_2O_3-Fe_2O_3-K_2O-TiO_2-Cr_2O_3) interpreted to indicate a northeast Canadian Shield provenance, however, there is overlap with the geochemical signature of the Mesozoic mudrocks. At least one till unit is associated to the oldest southwest ice-flow phase initially recognized in the striation and landform records based on its compositional signature as well as till fabrics. Younger tills were deposited during the clockwise ice flow shift. These tills are located at surface in lower topographic regions throughout the study area and their composition has an increased carbonate signature from the underlying Paleozoic sedimentary rocks. These tills show some compositional inheritance from the older till unit(s). Within these upper tills is a unit sourced from hyper-saline beds to the northeast. Ultimately, the clockwise rotation of ice flow is preserved in both the erosional (landform and outcrop-scale ice-flow indicators) and depositional (till fabrics and composition) records. The ice-flow chronology shows compelling evidence for major shifts in ice sheet configuration and flow dynamics, as well as related subglacial conditions (e.g. changes in subglacial sediment entrainment) during the last glaciation.

A retreat sequence showing ice margins and pro-glacial lake positions is established using sediment landform assemblages from surficial maps and topographic basins and drainage outlets from the 2m resolution ArcticDEM. Seven optical ages, two from a 223 m a.s.l.beach ridges and five from eolian dunes, and radiocarbon ages from wood and peat were obtained and provide additional chronological constraints within the region. A stepwise pattern of eastward retreat is reconstructed, which shows impounded drainage along the ice margin creating a series of pro-glacial lakes at different elevations along the margin and through time. During this eastward retreat the Snake Creek Moraine was deposited into a shallow pro-glacial lake. The optical age of the beach ridge currently at 223m a.s.l.indicates deposition at 12.0 ± 0.7 ka BP. This is the most limiting age and suggests the previously published ice margin positions used for the region are older as the deposition of the Snake Creek Moraine is estimated at 12.5 cal. ka BP. The eolian optical ages show continual eolian reworking indicating the landscape was exposed after 10.4 ± 0.3 ka BP. The radiocarbon ages of 2.7 – 2.1 cal. ka BP cal. ka BP from wood and peat is much younger and thus not related to deglaciation. The updated ice margin retreat sequence is more detailed than those currently being used currently continental-scale ice sheet models, and also provides new evidence to constrain the evolution of proglacial lakes, which were open to northwestward drainage down the Mackenzie River Valley.

This study provides new insights into the ice-flow and deglacial history of the western LIS, which are constrained by field data and observations. The ice-flow history and till stratigraphy detailed in this research provides new constraints for establishing the locations of past ice divides. Updates to the ice margins and lake limits during deglaciation show complex eastward retreat and geochronology ages indicate the area was deglaciated at an earlier time than previously thought (at least 500 years). Finally, all results from this study provide important new information that should inform mineral

exploration in the area, especially for techniques that utilize surficial sediments to trace, characterize, and locate buried targets of interest in bedrock.

Acknowledgements

I would first like to thank my advisor, Dr. Martin Ross, for all his great advice throughout all aspects of the thesis be it in the field, in edits, or at the Grad House. Additionally, the thesis committee, Dr. John Johnston and Dr. Andrew Stumpf, are thanked for providing thoughtful feedback over the whole course of the thesis.

The Geological Survey of Canada - Geomapping for Energy and Minerals - funded this project 2 Southern Mackenzie Surficial program through a Research Affiliate Program grant and was completed under NWT Scientific Research License No. 16226. Many thanks are given to Roger Paulen and Dr. Rod Smith for their scientific expertise and personal help along the way. Roger, the hospitality and care that you have shown me in the six years of tutelage is nothing less than extraordinary. Rod, your knowledge and conversations have made me an infinitely better Quaternary Scientist… and I forgive you for knocking my beer can tower over. Matt Pyne (GSC) and Steve Day (GSC) are also both thanked for their help in the field and teaching me new techniques that will no doubt be useful in the future. Jamie and Joeli also get shout outs for their help and continued friendship. Robert, we may drive other people crazy but we don’t need ‘em. Fieldwork benefitted from participation and wildlife monitoring provided by: Alan Farcy, James Nadli, and Henry Sabourin (Deh Gáh Got’ie First Nation), Darcy Simba (Ka’a’gee Tu First Nation), Irene Graham and Pat Martel (Kátł’odeeche First Nation), Tom Unka (Denínu Kųę First Nation), and John Delorma (Fort Resolution Métis Nation). Additional assistance was provided by Peter Redvers (Kátł’odeeche First Nation), and Michael Vandell and Bob Head (Fort Providence) who facilitated boat access to sample locations along the upper Mackenzie River.

Many others made my 4 years (I know…) at Waterloo a very enjoyable time. Everyone within the Quaternary crew are thanked (Sam, Tyler, Thomas, Caroline, Rebecca, Robin) especially Ameerah for being a great friend and Jessey for always being there when I needed it. Stacey and Jill are also thanked for being great distractions on both morning and afternoon trips to their office and the many lessons in metamorphic petrology. Jen, Katia, Sara, and John are also all thanked for making my Masters a great experience.

Finally, my friends and family are thanked for all the immeasurable help throughout the Masters. The important friends know who they are, (*insert your name here*). Dad, thanks for teaching me how to think and showing me perspective, I wouldn't have been able to finish without it. Todd, thanks for always reminding that I wasn't finished yet, I wouldn't have been able to finish without that either. Mom, thanks for being my mom, what more is there to say. Lastly, David, the past two and a half years have been amazing … here's to many more up in Sudbury.

Table of Contents

List of Figures

List of Tables

Chapter 1

Introduction

1.1 Research Problem

North American Ice Sheets waxed and waned during the Late Pleistocene (129 to 11.7 cal. ka), before disappearing completely during the mid-Holocene (~6 cal. ka BP; Dyke and Prest, 1987; Dyke, 2004; Stokes et al., 2015; Dalton et al., 2020; Head et al., 2021; Fig. 1.1). The most recent ice sheet, named the Laurentide Ice Sheet (LIS), covered most of central and eastern Canada and had the largest impact on the landscape leaving behind a complex sequence of erosion and deposition (e.g. Gauthier et al., 2019; Rice et al., 2019). Deciphering the erosional and depositional record can give insights into the evolution of the LIS and its proglacial environments. We can address questions about LIS configuration and ice-flow dynamics that shift over time (e.g. Margold et al., 2018), possibly relating shifts to changes in subglacial conditions. In addition, we can constrain the shape and timing of ice margin positions to refine the retreat history of the LIS (e.g. Dyke, 2004; Dalton et al., 2020), and how the retreating ice margin controlled the evolution of proglacial environments (e.g. Lemmen et al., 1994; Evans et al., 2009; Huntley et al., 2017; Utting and Atkinson, 2019). Deciphering ice-flow dynamics and refining ice margins help better understand the long-term behavior of past ice sheets, their response to external and internal forces, and how ice sheets modified the landscape throughout glaciation. Furthermore, creating paleo-ice sheet reconstructions from this increased understanding of the glacial landscape helps understand how current ice sheets may react to climate forcing or help determine the influence of meltwater on ocean circulation patterns (Evans et al. 1999, Calov et al. 2002, Dyke 2004, Stouffer et al. 2006, Stokes et al. 2015, Shepherd et al. 2018).

Processes acting at the ice-bed interface (the subglacial-environment) causing erosion, sediment transport, and deposition are key to the development of ice sheet reconstructions (Trommelen et al., 2012; Margold et al., 2018; Gauthier et al., 2019; Rice et al., 2019). These processes are controlled in large part by the thermal regime at the ice-bed interface. If the interface is below the pressure-melting point, most processes related to basal ice-flow are suppressed; this is referred to as ‘the cold-based thermal regime’. In contrast, if the ice-bed interface is above the pressure-melting point, water may be present and several processes related to basal ice-flow can be activated; this is referred to as the ‘warm-based thermal regime’ (Boulton 1996, Clarke 2005, Menzies et al. 2018). The past thermal regime is an important factor in the subglacial sediment-landform assemblages observed at surface today across glaciated terrains (Benn and Evans 2010, Ely et al. 2016, Menzies et al. 2018). Areas that experienced sustained cold-based conditions may contain relict landforms and sediments that were preserved due to reduced erosion, because ice was frozen to the bed (McMartin and Henderson, 2004; Refsnider and Miller, 2010; Rice, et al., 2019). In contrast, areas that were affected by warm-based conditions may exhibit a variety of more recent subglacial bedforms and sediments that formed as a result of actively flowing basal ice and water (Evans et al. 2009, Stokes et al. 2009, Margold et al. 2015). It is also important to note that subglacial conditions change over time leading to complex glacial records. Changes to ice sheet configuration may lead to a shift in local/regional thermal regime, as well as shifts in ice flow direction, which together can overprint or remold older landforms to varying degrees (Trommelen et al. 2012).

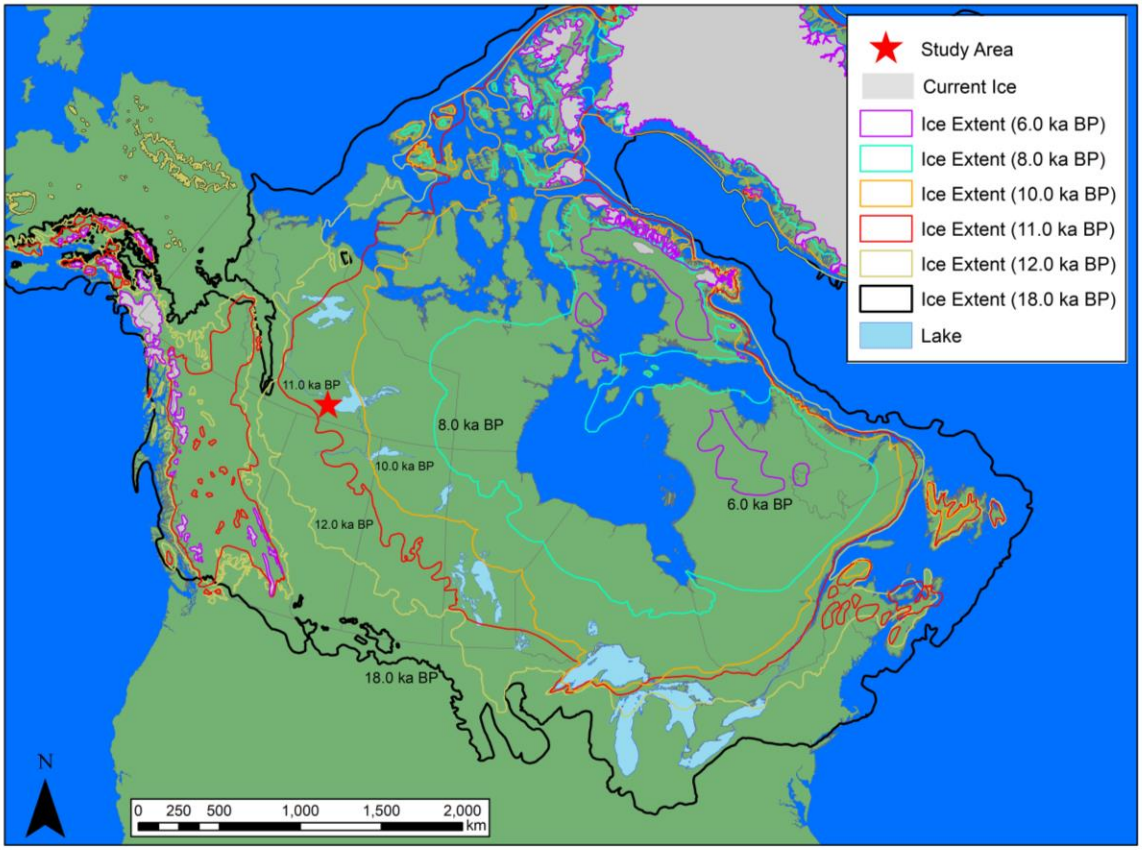

Figure 1.1: Laurentide Ice Sheet extents from the last glacial maximum (18.0 ka BP – Black line) to current ice extents (grey) showing intermediate timesteps (data from Dalton et al., 2020). The relative location of the Keewatin Ice dome is indicated and the red star indicates the general location for this thesis.

During ice sheet retreat, significant modifications to the landscape also occur. Moraines, with a diverse sedimentology, can be deposited along ice margins during ice stillstands and provide a depositional record of former ice margin positions (Brown et al. 2011, Atkinson et al. 2014). Ice sheets also generate significant amounts of meltwater during deglaciation. As the meltwater flows to the ice margin, channels are eroded down into preexisting substrates (e.g., N-channels) or up into ice (e.g., R-channels) and glaciofluvial sediments are deposited (Brennand 2000). Meltwater exiting at the ice margin can be impounded and form glacial lakes due to the recently deglaciated foreland being depressed by the weight of the glacier (glacioisostasy) and ice or moraine blocking natural drainage pathways. Lake processes deposit glaciolacustine sediments and can rework preexisting sediments creating lags and winnowed surfaces. Beach ridges are also created along glacial lake shores and often record a stepwise pattern of relative lake level lowering through glacioisostatic adjustment and incision of outlets (Lemmen et al. 1994, Drzyzga et al. 2012, Utting and Atkinson 2019).

After glacial lake drainage, post-glacial processes affect the landscape. Eolian dunes are deposited as preexisting sediments are exposed to wind and indicate the paleo-wind direction at the time of deposition (Munyikwa et al. 2011). Additionally, thick layers of organic sediment may accumulate over previously deposited sediments, specifically in areas with low topography and poor drainage (Väliranta et al. 2017). Alluvial processes also modify the post-glacial landscapes eroding into the exposed landscape and depositing sediments in a variety of alluvial environments (i.e., river channel, floodplain, fan). Finally, permafrost processes influence the post-glacial environment creating thermokarst lakes through permafrost melt and peat plateaus through frost heave (Sannel and Kuhry 2011).

Reconstructing the above sequence of successive processes, events, and environments is key for LIS and post-glacial reconstructions. Some regions of the LIS have been extensively studied to interpret their glacial history. In contrast, other regions have been subject to much less research leaving important knowledge gaps. One such understudied area is the western margin of the LIS (Dyke 2004, Stokes et al. 2015, Gowan et al. 2016). Along the western margin of the LIS, the region around the southwestern shore of Great Slave Lake is of particular interest (Fig. 1.2) and is hereafter referred to as ‘the study area’. Ice-flow and ice margin positions are poorly constrained with limited surficial mapping in the study area; only large-scale landform interpretation from remotely sensed data (Prest et al. 1968, Dyke and Prest 1987, Fulton 1995, Brown et al. 2011, Margold et al. 2015).

The region also has limited deglacial ages to refine timing of ice retreat and glacial lake formation that are important for reconstructing glacial Lake McConnell (GLM) and its drainage into the Arctic Ocean which has important paleo-climate implications (Tarasov and Peltier 2006, Bednarski 2008, Couch and Eyles 2008, Murton et al. 2010, Tarasov et al. 2012, Munyikwa et al. 2017).

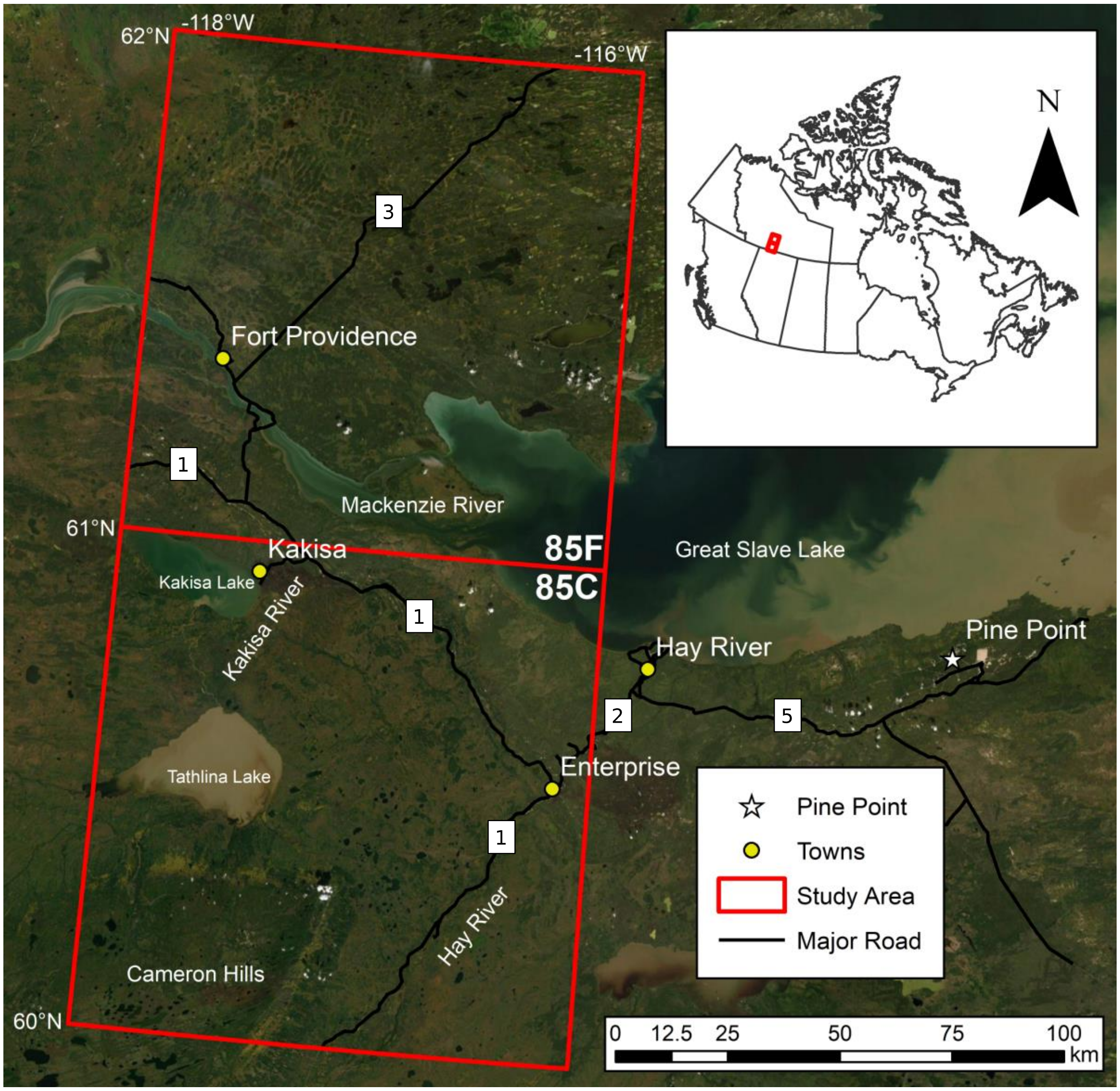

Figure 1.2: Landsat 8 panchromatic image (courtesy of the USGS) of the study area for the thesis (outlined in red). Note NTS sheet numbers are labeled and include NTS 85C and 85F. Towns are shown as yellow dots, with the past producing Pine Point mine indicated. Major highways are included and labeled with associated Mackenzie Highway number. The inset map shows the study area in a Canadian context.

Continental-scale ice sheet reconstructions estimate positions of ice domes and divides which relate to ice-flow directions and subglacial thermal regimes across Canada (Margold et al. 2018). Ice domes and divide locations are difficult to determine because they moved throughout the last glaciation and detailed work is typically needed to decipher the resultant chronology of ice flows and sediments in these regions (Margold et al., 2018; Rice et al., 2019). This thesis will better understand ice sheet behavior and deglaciation over the study area providing evidence for the location and movement of the Plains Ice Divide extending out of the Keewatin Ice Dome (Dyke and Prest 1987, Bednarski 2008, Brown 2012, Gowan et al. 2016, Roy and Peltier 2017, Margold et al. 2018).

Improved understanding of ice-flow directions and glacial sediment provenance also bolster mineral exploration. The coarse fraction of till (> 2.0 mm) originates at the source by two different initial mechanisms: 1) subglacial quarrying of bedrock outcrops by sliding ice (Iverson 1991a, Ugelvig et al. 2016, Hall et al. 2020) and, 2) subglacial entrainment of pre-existing coarse sediment through regelation intrusion and englacial transport (Iverson 1993, Iverson and Souchez 1996) or subglacial deformation (Boulton, 1996; Menzies et al., 2019). The lithology of the coarse fraction of till can thus help establish its general provenance, as well as to determine the relative contribution of local versus distal bedrock sources. This is useful to further constrain ice-flow direction at time of till entrainment and deposition. However, because of the second (re-entrainment) mechanism explained above, pebbles can partly reflect inheritance from older deposits, including older tills. In this case, clast lithology would represent the net effect of more than one sedimentary cycle from different ice flow directions (Trommelen et al. 2013, Hodder et al. 2016). Despite these possible complications, till clast lithologies are useful for provenance analysis and are thus commonly used.

The fine-grained fraction of till via geochemistry is also used as a provenance indicator (Klassen and Thompson 1993, Grunsky 2010, Wang 2018). Observation of the major oxide and trace element geochemistry from the clay size fraction can suggest major bedrock sources that may not be indicated in the coarser fraction due to crushing and comminution of larger clasts. This is the case with weak sediments like shales (Paulen et al., 2007). Furthermore, direct abrasion of clasts contained within the till provide material to the till matrix and can be compared to the observation made in the more coarse fraction of the till (Rice et al. 2013, 2019b, Trommelen et al. 2013). Together, the coarse and fine-grained fractions of till can suggest major bedrock sources indicating ice flow directions.

Tracking ice-entrained material up-ice to a mineralized source can lead to buried mineralized deposits (McClenaghan and Paulen 2018). Ice-flow history is particularly important as sediment and mineral indicator dispersion can record multiple flow trajectories due to re-entrainment processes, resulting in complex net dispersion patterns at the surface (Parent et al. 1996, McClenaghan et al. 2018). The study area has been identified as having high mineral potential for Mississippi-Valley Type deposits (Hannigan 2006a) with indicator minerals already found (Watson, 2011; Day et al., 2018; Paulen et al., 2018, 2019). To adequately follow up these findings, understanding the study areas glacial history is required.

This research also helps others identify areas of permafrost activity, important for its climate change sensitivity (Dredge et al. 1999, Wolfe et al. 2017). Degradation of permafrost terrain can expel greenhouse gases (Schuur et al. 2015) and also provide difficult settings for infrastructure development (Couture et al. 2003). Infrastructure development is further aided through an understanding of the glacial history by delineating different sediments at surface helping determine appropriate locations for construction of roads and buildings (Prowse et al. 2009). The delineation of surficial materials also indicates areas of aggregate resources, a valuable local commodity.

1.2 Previous Regional Deglacial Reconstructions

Large-scale ice sheet reconstructions of the area first began with Craig (1965) who suggests multiple phases of glaciation, as different tills are deposited on top of one another and striations show two ice-flow directions (230° and 310°). The southwest flow is interpreted as later due to its greater impact on the landscape than the northwesterly flow. Craig (1965) also shows an ice-flow map with the southwestward flow splitting when the ice reaches the Cordilleran Ice Sheet. As the reconstruction of the ice margin retreats back to Great Slave Lake (GSL), it is hypothesized that the western arm of GSL would have a funneling effect on the ice sheet, possibly causing the northwesterly flow. Finally, Craig (1965) hypothesized that the ice margin along GSL would be characterized by significant calving and consequently the last phases of retreat would be parallel to GSL eastern boundary.

Craig (1965) named glacial Lake McConnell after R. G. McConnell, the first researcher to identify GLM’s impact on the landscape through strandlines and deltas (McConnell 1890). The maximum extent of GLM was estimated by drawing the uppermost strandlines and extrapolating along elevation contours between the strandlines. This maximum extent is thought to be when the ice margin lay along the edge of the Canadian Shield. An isostatic rebound of about 2 feet (0.6 metre) was estimated by comparing maximum strandline elevations across the lake basin (Fig. 1.3).

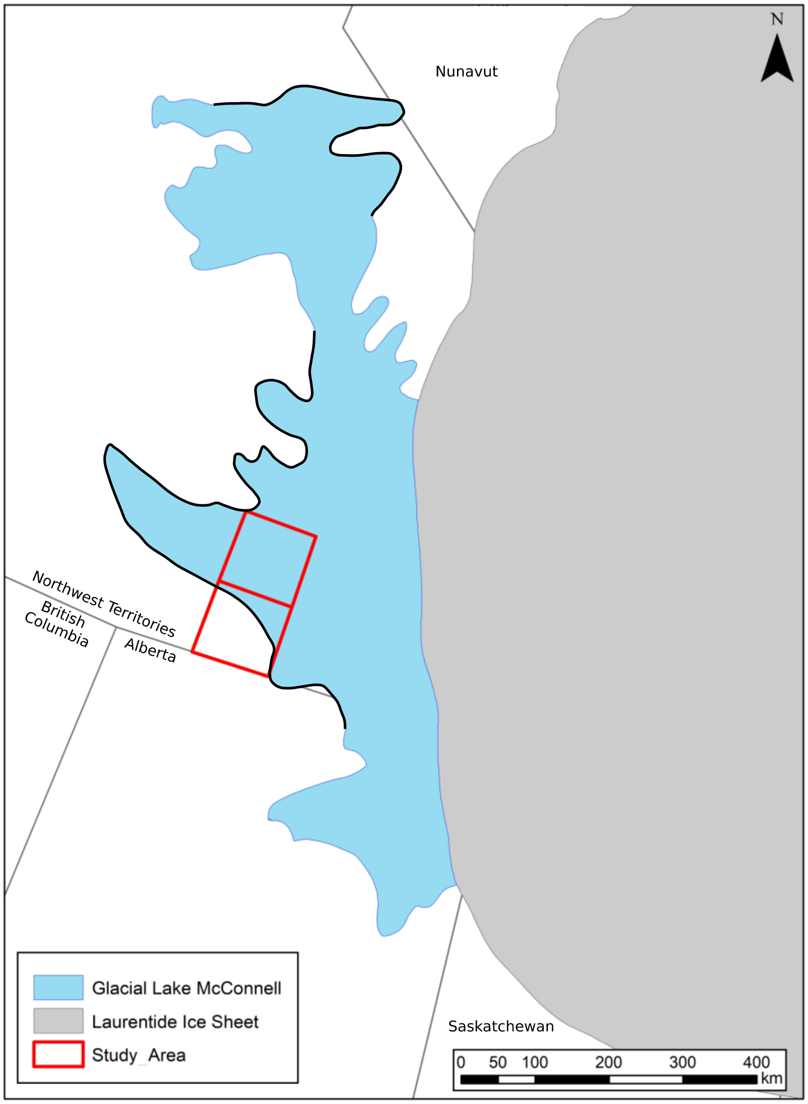

Figure 1.3: The maximum extent of glacial Lake McConnell over the western portion of the LIS. Black lines indicate confident GLM extents along uppermost strandlines. The study area is highlighted in red. The eastern margin of the lake is thought to be in contact with the ice sheet at this lake level (Craig, 1965; Lemmen et al., 1994).

Building on the work of Craig (1965), two studies were released in 1994 advancing the glacial history over the western portion of the LIS. First, Lemmen et al. (1994) studied the proglacial meltwater ponding and drainage along a large portion of the western margin using surficial mapping, landform analysis, and radiocarbon dating. The important time-slices to the evolution of ice and glacial lakes from their reconstruction are presented in Fig. 1.4.

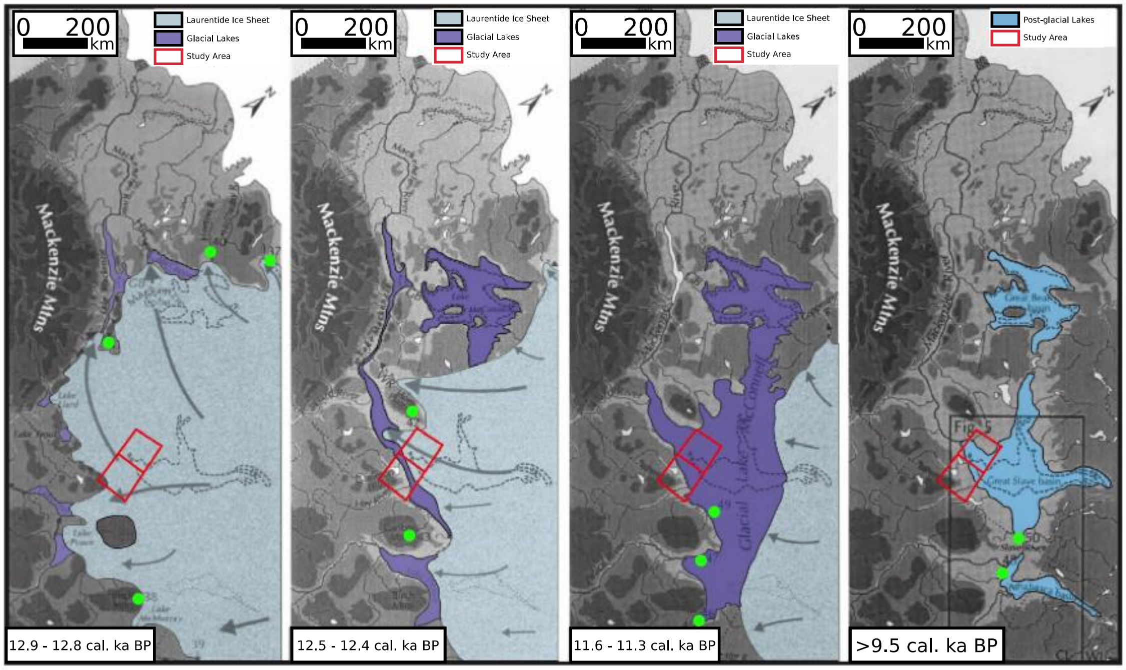

Figure 1.4: LIS flow lines, margins and, glacial lake extents for its western margin at important time steps. The study area for this thesis is outlined in red. Samples used in the reconstruction are highlighted in green (Modified from Lemmen et al., 1994).

In the Lemmen et al. (1994) reconstruction, before 12.9 cal. ka BP the LIS moved broadly southwestward to westward over the study area with topography as a controlling factor. As the ice sheet retreated eastward, ice had a major influence on proglacial meltwater routing because it blocked natural northeast drainage. With continued retreat east, new outlets for meltwater were developed and the landscape isostatically rebounded. At 12.9 to 12.8 cal. ka BP, a lobate ice sheet occurred around topographic highs with smaller ice-damned proglacial lakes against these ice lobes, including glacial Lake Hay in the Hay River valley (Fig. 1.5). They did not identify any major moraines being constructed, the Cameron Hills are ice-free, and all ice is thought to be retreating at this time.

From 12.9 to 12.8 cal. ka BP to 12.5 to 12.4 cal. ka BP the Lemmen et al. (1994) reconstruction shows significant changes to the configuration of the ice sheet and meltwater drainage pathways. These changes were due to a shift from a terrestrial to subaquatic margin along glacial Lake Mackenzie and glacial Lake Peace prior to GLM (Fig. 1.5). The Snake Creek Moraine was shown to have been deposited subaquosly along the ice margin as glacial Lake McConnell formed over this time period. At 12.5-12.4 cal. ka BP the three basins that will eventually coalese into GLM (Great Bear, Great Slave, Athabasca) are still separated by ice.

At 11.6-11.3 cal. ka BP the ice sheet deposited the Cree Lake Moraine to the south, but the northern margin location around Great Bear Lake is uncertain. Furthermore the Lemmen et al. (1994) reconstruction suggests that ice retreated from the Snake Creek Moraine quickly due to an absence of glaciofluvial or ice-contact deposits and the presence of many iceberg scours. The quick recession is further supported by the Great Slave Lake basin that deepens to the east, which would increase calving along the ice margin in contact with GLM (estimated at 600 to 800 km in length). Lemmen et al. (1994) call this the Mackenzie phase of GLM when GLM was at its largest extent connecting the Great Bear, Great Slave and Athabasca lake basins. During the Mackenzie phase, GLM had a maximum elevation of approximately 290 m a.s.l.and used the Mackenzie river as the main outlet (Fig. 1.4). There was no evidence presented for an outburst flood linking GLM to glacial Lake Agassiz to the southeast (Lemmen et al., 1994).

Lemmen et al. (1994) final time step, < 9.5 cal. ka BP, shows full deglaciation of the study area; although they suggest this happened around 10.2 cal. ka BP from radiocarbon ages from fossil wood from both the Slave Delta and the Peace Delta. GLM meltwater input from the ice-sheet diminished and through glacioisostatic uplift and incision of outlets GLM drainage into the Arctic Ocean. All three basins were separated by approximately 9.1 ka BP at 214 m a.s.l.and continual retreat of GSL levels to the modern day extent occurred.

The second reconstruction of the western margin of the LIS was published by Smith (1994). He aimed to improve Craig (1965) reconstruction by creating a deglacial chronology of GLM, identifying different outlets of GLM over this chronology, discussing the major deltas associated with GLM, and reviewing influences of lake area and depth. The Smith (1994) reconstruction is similar to that of Lemmen et al. (1994), but has comparable lake levels approximately 800 years older and invokes an outburst flood linking glacial Lake Agassiz to glacial Lake McConnell.

Smith (1994) defined three phases of GLM based on outlets. The first is the Hare Indian Phase from 11.8-11.5 cal. ka BP where GLM was located solely in the northwest portion of the Great Bear Lake basin using the Hare Indian River as an outlet. With further ice retreat, from 11.5-11.0 cal. ka BP the Great Bear Phase of GLM occurred and occupied most of the Great Bear Lake basin using the Great Bear River as the primary outlet. The final phase of GLM, the Mackenzie Phase, was the longest (11–8.3 cal. ka BP) and largest containing all three (Great Bear, Great Slave, Athabasca) lakes basins at 10.5 cal. ka BP. Glacioisostatic uplift and outlet incision was responsible for the drainage of the Mackenzie phase down the Mackenzie River.

Smith (1994) also describes the deltas deposited into GLM. This includes the Liard delta dated at 11.5 cal. ka BP sourced from meltwater of the Mackenzie Ice Lobe, the Peace Delta dated at 10.8 - 8.8 cal. ka BP and the largest of the three, and the Athabasca delta dated at 10.8-8.8 cal. ka BP thought to record the outburst flood from glacial Lake Agassiz at 9.9 cal. ka BP. These glacial Lake Agassiz waters were directed northwest down the Clearwater River valley, and north down the Athabasca River valley, and flowed into GLM. At this time GLM's outlet was down the Mackenzie River where significant outlet incision at the Liard Moraine is observed. An attempt was made to estimate the flow volume and speed of the outburst flood using the amount of incision that occurred at the Liard Moraine outlet. Smith (1994) further uses the Peace and Athabasca delta shapes and shoreline development to suggest that the lake underwent steady slow drainage until 8.8 cal. ka BP. At 8.8 cal. ka BP, the drainage rate shifted as a result of outlet incision of the Mackenzie River becoming the primary method for drainage. After 7.1 cal. ka BP, glacioisostatic rebound was responsible for the drainage rates of GLM and then proto-GSL.

The most commonly referenced large-scale ice margin reconstruction is that of Dyke (2004) which built upon previous work (Dyke and Prest 1987) to create a new map of deglaciation across central and northern Canada. Using a compiled radiocarbon database and updated mapping throughout Canada a more precise (500 year time step) deglaciation reconstruction was created. Dyke (2004) reconstructed ice margins within the study area mirror the older reconstructions over the southwestern shore of GSL showing deglaciation between 11 – 10 ka BP (Fig. 1.1). The similarity to older reconstructions is a result of limited new data from the work done in 1994. The work of Dyke (2004) has recently been updated by Dalton et al. (2020), and through similar methods describes the LIS retreat across Canada. The data presented by Dalton et al. (2020) will be used in this thesis.

Gowan et al. (2016) also used published ages to create an updated recontruction for the western magin of the LIS but with a focus on ice thickness. They incorporated a variety of data sets including glacial isostatic adjustment observations (relative sea rise indicators, permanent GPS uplift records, present day lake level change, postglacial tilt of glacial lake level indicators) and used simple ice physics to match the observed glacial isostatic adjustment. Their model suggests an ice dome east of GSL with an ice thickness of 3500 m from 20 – 17 cal. ka BP (the Plains Ice Divide). Ice thinned quickly from 17 - 14 cal. ka BP and then slowed until 11 cal. ka BP when the ice dome east of GSL starts to move into Nunavut. In this model the study area was deglaciated by 12.5 cal. ka BP when the ice margin crosscut the Great Slave Lake basin. Gowan et al. (2016) show the ice sheet was thinner than previously thought and that the western margin of the LIS could be the source for Meltwater Pulse 1A, an influx in glacial meltwater observed in the marine isotopic record.

The highlighted studies demonstrate the broad state of knowledge over the surrounding regions and the study area. Uncertainties with regards to the glacial history within the study area are still present and often raised throughout these studies; the largest issue being limited field constraints (i.e., bedrock erosive indicators, landform analysis, dated material). With this background information, site-specific geoscience data will be presented to further detail the glacial and deglacial history of the region.

1.3 Previous Local Work

Previously researched areas surround the thesis study area. Both the Geological Survey of Canada (GSC) and the Alberta Geological Survey (AGS) have mapped the surficial geology of the surrounding area (Fig. 1.3). These maps date back from 1970 by researchers to the southeast (Bayrock, 1970) to as recent as 2019 using remote predictive mapping to the northwest (Geological Survey of Canada, 2019). These remote predictive mapping campaigns are indicated on Fig. 1.5 and are considered a first pass at determining surficial materials over the landscape. Geologically, these maps span a variety of different environments and use different unit labels dependent on the year the mapping took place and which Survey conducted the work. Even with these mapping differences, the surrounding surficial maps provide a basic geologic background for what was observed in the study area.

Further geoscience research in the surrounding area include those of Bednarski (2008) to the west, Sharpe et al. (2017) to the east, site-specific GSC research projects at Pine Point to the east (Oviatt et al. 2013b, 2013a, 2014, 2015, Rice et al. 2013, McClenaghan et al. 2018), a large GSC/AGS project to the south (McCurdy et al. 2007, Paulen et al. 2007, 2011), additional work on eolian dunes in northern Alberta (Wolfe et al., 2004, 2007; Munyikwa et al., 2011, 2017) and, a GSC project to the north (Wolfe et al. 2017, 2018, O’Niell et al. 2019).

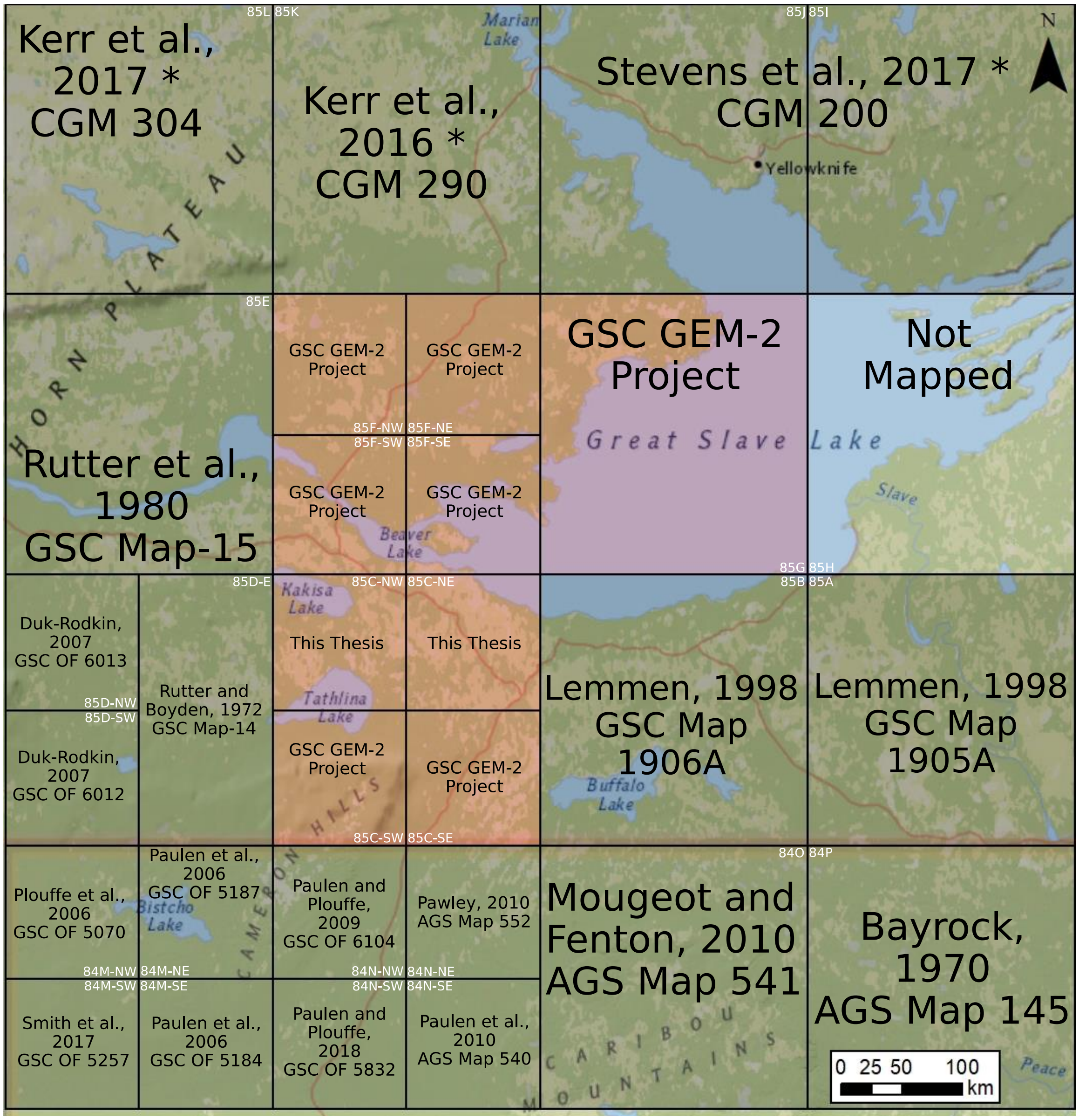

Figure 1.5: Surficial geology maps in the surrounding area. Areas shaded in red are included in the larger Geological Survey of Canada Geomapping for Energy and Minerals - 2 Project of which this thesis is a part. Greyed areas are completed maps with map number and reference given. References with a * indicate maps created using remote predictive methods.

To the west, Bednarski (2008) reconstructed the LIS over northeastern British Columbia. Ice margin positions were estimated and the evolution of glacial lakes in the area using glacial landform associations, detailed surficial mapping, and various other remote sensing datasets. The reconstruction shows regional southwestward flow from the Keewatin Ice Divide to the Cordillera where ice deflected north and south when converging with the Cordilleran Ice Sheet (CIS). As the LIS retreated eastward, an open corridor between the LIS and the CIS routed drainage to the north with occasional glacial lake formation. Glacial lake formation was influenced by the LIS blocking natural drainage pathways to the northeast. Ice thickness was identified as an important control on advance and retreat with ice lobes in lowlands between topographic highs. The retreat rate of the LIS from northeastern BC was rapid, but moraines and minor readvances did occur. Based on limited age constraints, Bednarski (2008) show that the majority of the landscape was ice free by 11 cal. ka BP. After 11 cal. ka BP, glacial Lake Mackenzie and GLM were major inputs for northward meltwater drainage.

Sharpe et al. (2017) studied glacial dispersal and ice flow history of the east arm of Great Slave Lake. They determined uniform westward flow from bedrock ice-flow indicators and sediment landforms (i.e. striations, s-forms, drumlins, eskers) as well as clast and mineral dispersal (i.e. buff coloured sandstone, carbonates, kimberlite indicator minerals). Westward flow is presented as part of the Great Slave Lake flow tract extending from the Keewatin Ice Divide to the western shore of GSL. They claim that complex ice flow histories are likely isolated over Canada and not present in mid- to distal- ranges from an ice divide suggesting that use of only striation measurement can be misleading and that striations need to be constrained with compositional transport indicators.

Closer to the east, studies were completed to decipher the ice flow history at Pine Point (Fig. 1.2). Results led to a reconstruction that differs markedly from Sharpe et al. (2017), with compelling evidence indicating major shifts in ice flow direction occurred in the area during the last glaciation. Bedrock erosive features were used to decipher ice flows and observed stratigraphy was correlated those ice flows through till macro and micro fabrics. The sequence of flows presented includes a youngest southwest (230°), an intermediate northwest (possibly north-northwest) (300-330°) and a final southwestern flow (250°) (Rice et al., 2013; Fig. 1.6). This history aligns with landforms observed in the region, having the latest southwest phase crosscutting intermediate northwest trending landforms (Oviatt et al., 2014; Rice et al., 2019; Fig. 1.6).

The till stratigraphy at Pine Point is split into four units (Fig. 1.6). Unit A is a very dark greyish-brown till, has a silty sand matrix, and 13% clast content with multiple well rounded quartzite pebbles. Unit A is suspected to have in-filled karst features in the region with steep plunges from a clast fabric. Unit B is a pale brown till, has a sandy-silt matrix and contains 13% clasts. Unit B was found to have higher concentrations of sphalerite grains, likely sourced from local Mississippi-Valley Type hosting bedrock strata. Unit C is a light olive brown till, with a sandy silt matrix, 13% clasts, many of which are polished and faceted. Unit C is the thickest and contains less sphalerite, pyrite, and kyanite than Unit B. Unit D is the uppermost till unit and is brown, sandy-silt matrix, 17% clasts and is compositionally similar to Unit C. GLM sediments and organics cap the stratigraphic section. Further research at another Pine Point pit indicated similar flow directions from striations and surficial dispersion of elements associated with the bedrock mineralization (Oviatt et al. 2015, McClenaghan et al. 2018). Most recently, these three ice flow directions were further corroborated with a till micromorphology study (Rice et al. 2019).

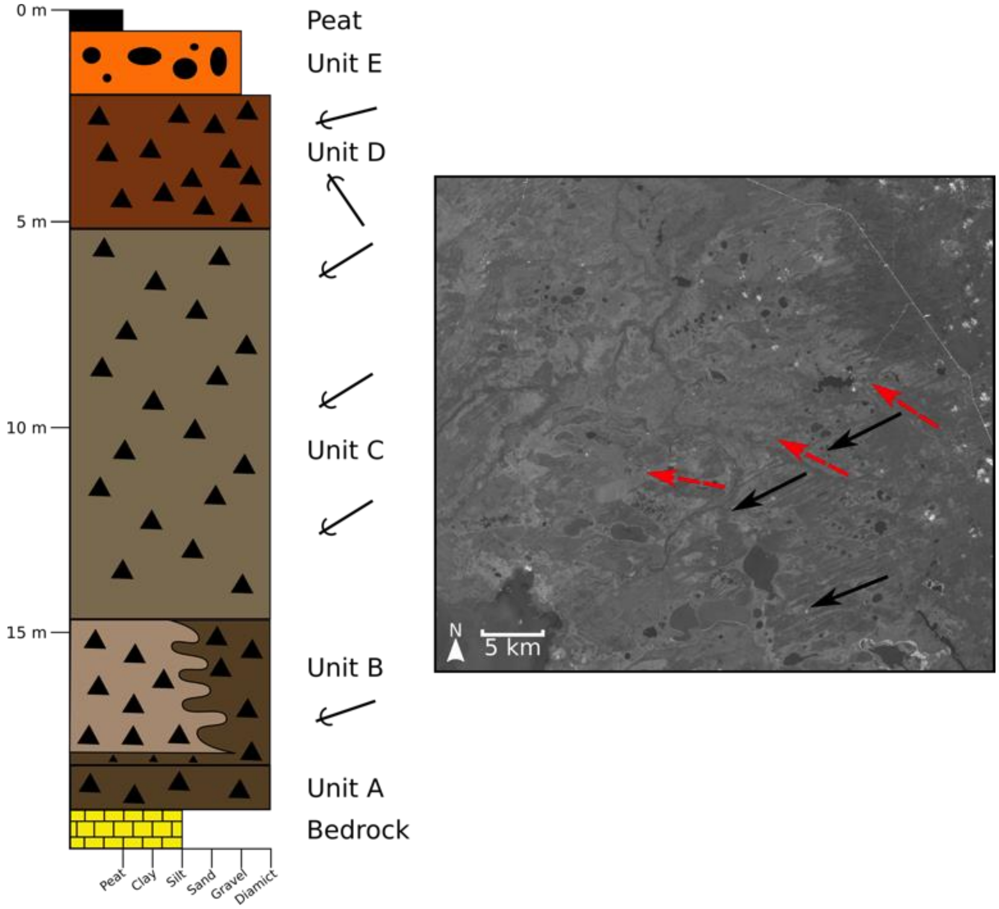

Figure 1.6: Simplified stratigraphic log and landform record synthesized from Rice et al., 2013 and Rice et al., 2019 work at Pine Point. The stratigraphic column shows the four till units (Unit A-D) and interpreted ice-flow direction from clast fabrics. Stratigraphy shows a rotation in ice flow from southwest (bottom of Unit C) to northwest (bottom of Unit D) then again southwest (top of Unit D). The landform record shows large landforms from the intermediate northwestward flow (red dashed arrows, 300°) crosscut by smaller southwest oriented flutes (black arrows, 250°).

To the south in Alberta, work to find possible mineralization was completed by a joint GSC and AGS project (Plouffe et al. 2006, 2008). With a significant mapping focus (Fig. 1.5), this research interpreted ice flow throughout Alberta and slightly north into southern Northwest Territories (Paulen et al., 2007, 2011; Fig. 1.7). Ice lobes were controlled by topography during both advance and retreat phases, and thus diverged around uplands like the Cameron Hills, similar to that suggested by Bednarski (2008; Fig. 1.7). At the LGM, ice was thicker than these uplands and flowed southwest across the landscape deflecting north and south at the LIS - CIS convergence (Paulen et al., 2007; Bednarksi, 2008).

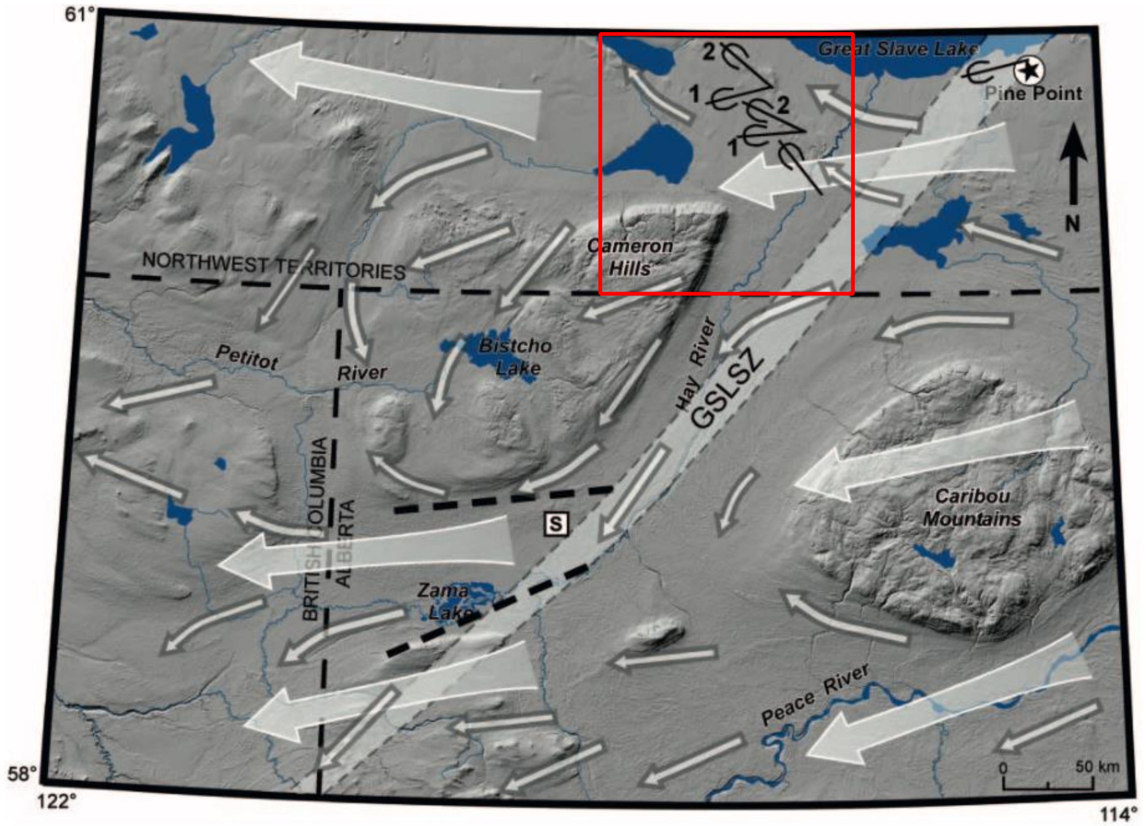

Figure 1.7: Summary of Late Pleistocene regional ice-flow patterns for northwestern Alberta and southwestern Northwest Territories depicted on SRTM generated hillshade model; the southern portion of the study area for this thesis is shown in red. The large arrows indicate ice flow during the LGM and are broadly west to southwest with ice overtop of the regional uplands. Small arrows indicate younger deglacial lobate ice-flow trajectories that are often channeled between regional uplands. Striation measurements are shown; numbers refer to the relative age of ice flow (1 = oldest) (from Paulen et al. 2007).

Optical ages from eolian dunes to the south were compiled by Munyikwa et al. (2017) to futher understand LIS retreat in Alberta. They collected and analyzed new samples samples and incorporated previously published ages (Wolfe et al. 2004, 2007, Munyikwa et al. 2011) to create a chronology of the LIS margin, contrasting it to other ice sheet reconstructions. Results indicate that ice sheet retreat began prior to 15.7 cal. ka BP, and most of central Alberta was open to aeolian activity by 15.0 cal. ka BP. Continued retreat moved the ice margin from northeastern Alberta around 12 cal. ka BP and the whole province was deglaciated by 10.4 cal. ka BP. They further add that optical dating seems to systematically provide earlier ages of deglaciation than comparable radiocarbon ages (Fig. 1.8). The early deglacial timing has implications for meltwater routing into the Arctic Ocean, as a northward drainage pathway would be ice-free.

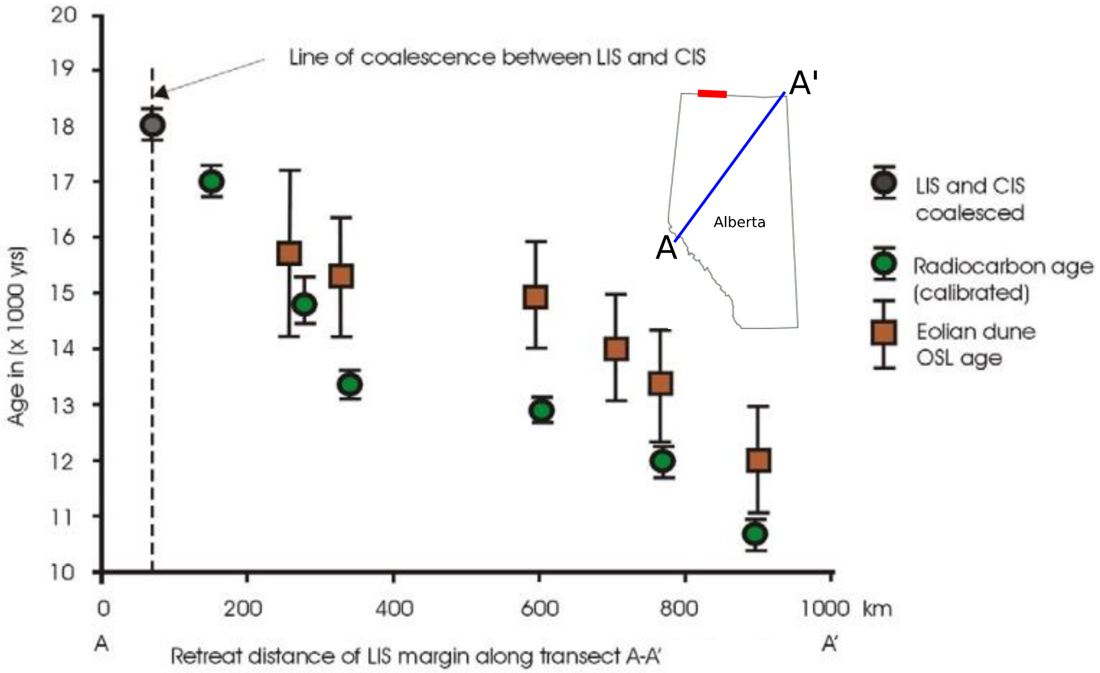

Figure 1.8: Comparison between radiocarbon and optical retreat chronologies of the LIS margin along a 1000 km transect trending SW-NE in central and northern Alberta (A-A'). The border to the thesis study area is highlighted in red. The calibrated radiocarbon ages are consistently younger than optical dates (modified from Munyikwa et al., 2017).

Ages were also obtained to the north by O'Neill et al. (2019) around the shore of GSL. Their aim was to understand how the landscape developed since LIS retreat and GLM inundation. Using surficial mapping and optical ages their reconstruction shows that before 9.5 cal. ka GLM extent reached between 290-300 m a.s.l. By 9.5 cal. ka GLM levels had dropped to 216 m a.s.l. During GLM inundation the landscape underwent significant modification through winnowing of previously deposited sediments and development of beach ridges. Their oldest optical age is 7130 ± 530 (SAW12-22) from littoral sand providing a minimum age for GLM at 170 m a.s.l. O'Neill et al. (2019) show that with continual GLM retreat sediments were exposed for eolian dune formation and the accumulation of organics.

1.4 Geologic Setting

1.4.1 Project Locality

The study area is located ~ 80 km west of the town of Hay River and ~250 km southwest of Yellowknife and encompasses the southwestern shore of Great Slave Lake, specifically National Topographic Series (NTS) sheets 85C (Tathlina Lake) and 85F (Falaise Lake; Fig. 1.2). Towns within the study area include Enterprise, Kakisa and Fort Providence, which are connected via Mackenzie Highways 1, 2, and 3. Significant water features include the west arm of GSL, Kakisa and Tathlina Lakes, the upper reaches of the Mackenzie River, and a portion of the Hay River.

A combination of bedrock characteristics (i.e., lithology), glacial history, and glacial lake events affected the physiography of the region. Topography ranges from 45 to 946 m a.s.l.with an average elevation of 320 m a.s.l.(Fig. 1.9). Overall the region shows little topographic variation; significant relief is observed on the slopes of the Cameron Hills in the southwest corner of the study area, a bedrock escarpment following Mackenzie Highway 1 crosscutting southeast-northwest over the study area, bedrock uplands south of Kakisa Lake, and in river channels (Fig. 1.9). Low permeability sediments and the regionally flat terrain leads to significant ponding of water and a weak drainage pattern expressed as large expanses of spruce bog and fen containing peat with low lying vegetation and mosses (Lemmen 1990). Raised areas above organics are characterized by dense mixed forest containing jack pine, large aspen, and white spruce trees. The study area lies in the discontinuous permafrost zone causing sediments and organics to be locally frozen (Heginbottom et al. 1995). Thermokarst lakes and peat plateaus are also found on the landscape and are dynamically shifting due to climate change (Burn and Smith 1990).

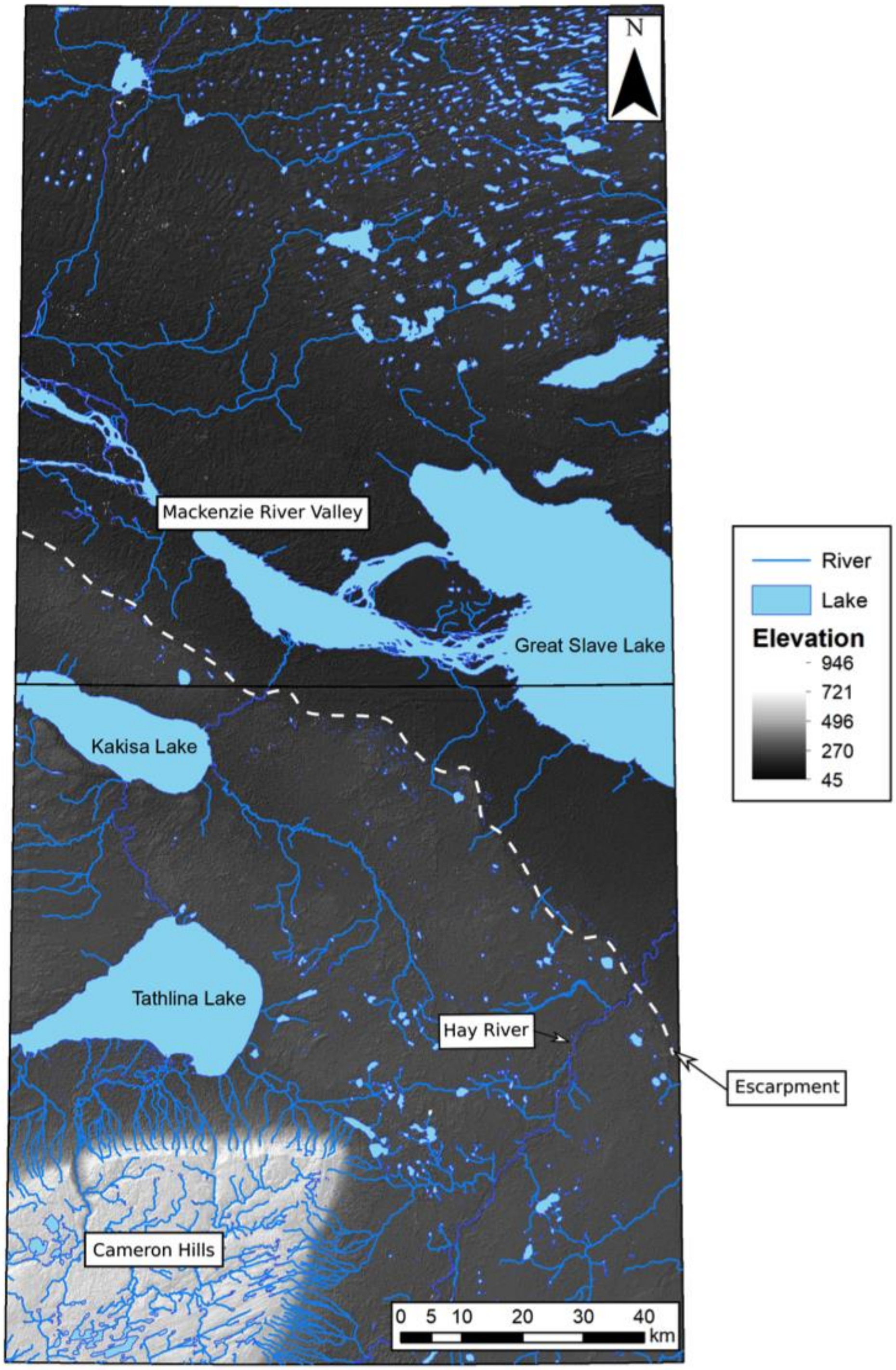

Figure 1.9: Digital Elevation Model from the 2 m resolution ArcticDEM over the study area (Porter et al. 2018)**. The bedrock escarpment can be seen as one topographic step south of GSL along with the highest elevations atop the Cameron hills in the southwest corner.**

1.4.2 Bedrock Geology

Bedrock geology is important for the glacial history because it can provide insight into former ice-flow directions by tracing clast provenance. Provenance studies have been widespread across Canada using traceable bedrock lithologies and broad bedrock geology clasts percentages in the till to help decipher ice flow direction (e.g., Hicock, 1987; Klassen and Thompson, 1993; Trommelen et al., 2013; Hodder et al., 2016; Rice, 2020). Furthermore, as a glacier overrides sedimentary rocks significant amount of silt and clays is produced as sedimentary strata have low competency. In contrast, a larger sand component is created over crystalline bedrock due to the increased hardness of the minerals (Dreimanis and Vagners 1974). Subglacial grain size differences lead to different subglacial conditions (i.e., pore water pressure) that cause shifts in ice sheet configuration. Some trends between the two type of bedrock strata beneath ice sheets include: faster flow over sedimentary bedrock (Boulton 1996), a changed margin retreat rate at the Canadian Shield boundary (Dyke 2004, Margold et al. 2018), and an increased number of eskers on the Canadian Shield (Brennand 2000).

Archean and Proterozoic crystalline basement rocks outcrop 150 km north east of the study area (Fig. 1.10). The Great Slave Lake Shear Zone trends north-east/south-west through these basement rocks an represents the boundary between the Archean Slave Microcraton and the Churchill Province formed via a Proterozoic orogenesis (Hoffman 1987, Majorowicz and Hannigan 2006).

Above the crystalline basement, Western Canada Sedimentary Basin (WCSB) rocks were deposited. The lower part of the WCSB in the study area is a thick carbonate sequence (350 – 600 m) and dips 1.9 m / km west, deposited during the Paleozoic (Rhodes et al. 1984). Parts of the carbonate sequence, referred to as the Presqu'ile Barrier (Keg River, Sulfur Point, Watt Mountain Formations), show significant evidence of dolomitization and kartstification (Rhodes et al., 1984; Hannigan, 2006a; Okulitch, 2006; Fig. 1.10). Kartstification created extensive cavities that allowed mineralizing fluids to migrate from beneath the Cordilleran orogeny along the GSLSZ and precipitate in the open spaces, locally dolomitizing the host rock. The world class Pine Point Mississippi-valley Type lead-zinc deposit is hosted in these karst and replacement features with mainly galena and sphalerite mineralization (Hannigan 2006b).

Finally, flat-lying Mesozoic shales, siltstones, and sandstones of the upper WCSB are located in the southwestern portion of the study area (Okulitch, 2006; Fig. 1.10). Isolated outliers of

Mesozoic sedimentary bedrock could possibly be preserved elsewhere where erosion did not completely removed them. Erodible sedimentary bedrock at surface was exposed to extensive preglacial weathering processes and glaciation that created much of the unconsolidated sediment observed today.

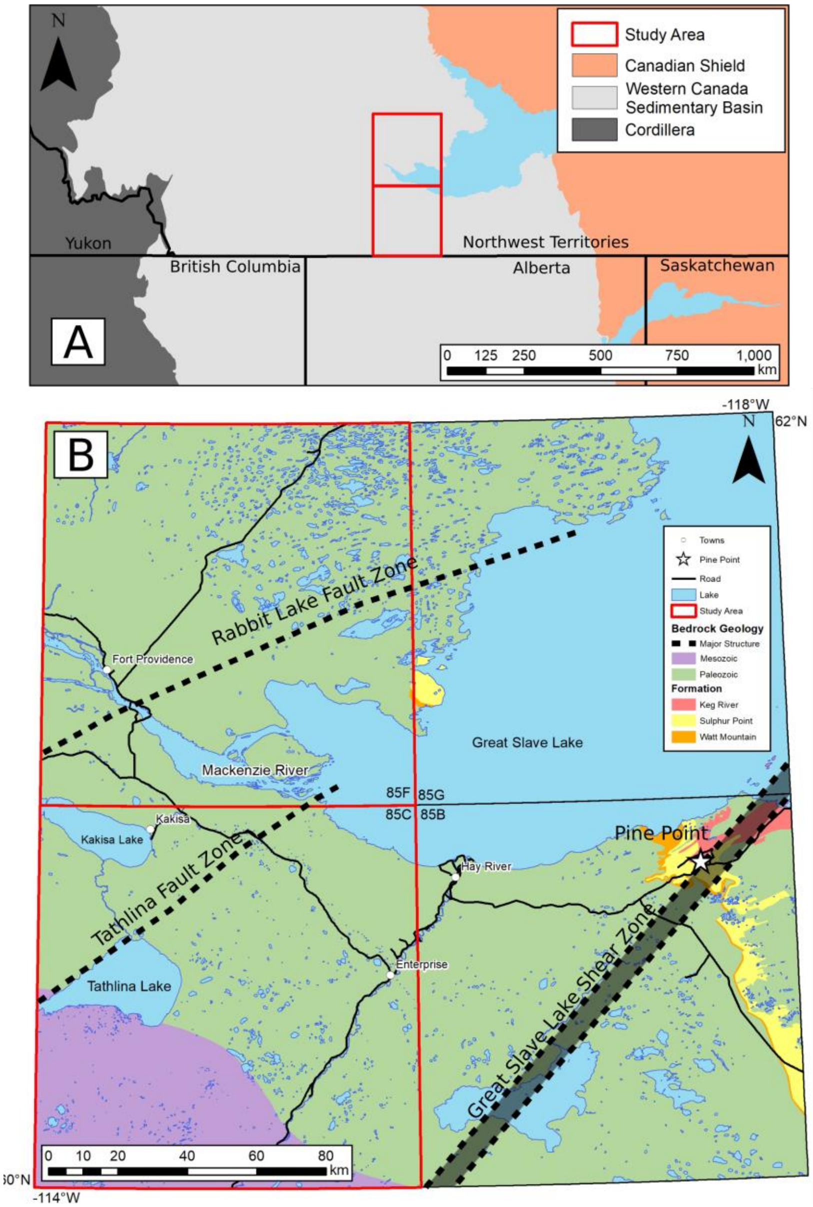

Figure 1.10: A) The study area in a broad context to surrounding bedrock domains; The Canadian Shield is at surface 150 km to the east and the Cordilleran is at surface 500 km to the west. B) Bedrock Geology of the study area. Pine Point Mississippi-Valley Type formations are highlighted and the Pine Point mine is indicated by a star (Okulitch 2006)**. Major basement structures are dashed lines and are labeled. These structures are thought to be pathways for mineralizing fluids (Rhodes et al. 1984, Hannigan 2006a).**

1.4.3 Surficial Geology

Thick unconsolidated sediments cover bedrock within the region. Subglacial till comprises the most of this cover with maximum thicknesses greater than 25 m (Lemmen, 1990; Smith and Lesk-Winfield, 2010; Smith et al., 2020). A variety of till units are observed in the area, differentiated based on colour, grain size, clast lithologies, and consolidation (Craig, 1965; Lemmen, 1990; Rice et al., 2013). These till units have also been shown to have been deposited by different ice-flow events with directions measured through clast fabrics and till micromorphology at Pine Point (Rice et al., 2013; Menzies et al., 2019; Rice et al., 2019). Till exposed at surface has locally been reworked through erosion (washing and winnowing) leaving a cap of reworked sediments.

Glaciofluvial sediments are sparse over the study area, with meltwater corridors being mainly erosive and limited esker deposition. Where glaciofluvial deposits are found, their composition is mainly boulders and cobbles (Craig 1965). The limited esker formation was impacted by substrates in the study area and if deposited were likely reworked by GLM (Craig 1965, Brennand 2000).

Glaciolacustrine sediments are also found at surface in the study area. They consist mostly of coarse and sublittoral facies including sorted sand and gravel, cobble lags over winnowed tills, and boulder and cobble beach ridges. Thicknesses of glaciolacustine sediments vary, but where present tend to be less than 2 m (Lemmen 1990). Prominent beach ridges associated with glaciolacustrine nearshore environments are observed and show a stepwise pattern back to GSL.

Holocene, eolian and alluvial sediments along with organics deposits are the youngest sediments at surface in the region. Eolian dunes are composed of sorted fine sands, originally derived from glaciolacustine and glaciofluvial deposits (Craig 1965, Lemmen 1990, Oviatt et al. 2014). Both parabolic and transverse dunes are found and indicate a easterly and westerly paleo-wind directions (Wolfe et al. 2007, Oviatt et al. 2014, Munyikwa et al. 2017). The dunes are now vegetated and thus mostly inactive, although some blowouts occur. Alluvial sediments are found associated with the Hay River, which has incised into bedrock restricting its floodplain. The Kakisa River also has alluvial deposition but is not topographically constrained allowing its channel to migrate more freely.

Organic deposits, bog and fen, cover a significant portion of the study area. Peat has formed in stagnant areas of water where organics build up. As the organic layer becomes thicker, fens shifts to sphagnum dominated bogs, although both are present within the study area (Bauer et al. 2003, Väliranta et al. 2017). Organic thicknesses estimated from seismic shothole drillers' logs (n-210;

Smith and Lesk-Winfield, 2010) average 2.76 m, which could be slightly overestimated because peat less than one-metre thick was often not recorded.

1.5 Thesis Objectives

This research objective was to resolve several poorly constrained aspects of the study area's glacial history. Firstly, an updated ice-flow chronology is needed to compare and integrate with those of the surrounding regions. Surrounding studies show complex ice-flow directions, and yet a gap remains over the study area (Section 1.2; Fig. 1.5). Confirming ice-flow directions in the region can help continental-scale reconstructions more accurately define ice movement over the study area and the location of ice-domes and divides.

Furthermore, detailed work at Pine Point has shown thick succession of till of differing composition and depositional ice-flow directions (Rice et al., 2013; McClenaghan et al., 2018; Rice et al., 2019). It is unknown if stratigraphy and sediment provenance is similar in the study area. Till stratigraphy and composition are important aspects for mineral exploration and can help further explain ice-flow chronology.

Finally, there is still uncertainty about the ice margin positions along the western LIS margin. This is due to a lack of chronological control and limited field research in the remote Canadian north (Dyke 2004, Stokes et al. 2015, Gowan et al. 2016). These gaps are important for climate modeling, due to glacial Lake McConnell and its northern drainage into the Arctic Ocean.

The knowledge gaps and outstanding issues described are the main rationale and motivation behind the Geological Survey of Canada (GSC) Geo-Mapping for Energy and Mineral 2 (GEM-2) Program for which this thesis research is part (Paulen et al. 2017, 2019a). This M.Sc. research addresses specific issues and questions about the glacial history southwest of Great Slave Lake. Specifically the objectives are:

1) Improve ice-flow chronology and establish their relative age relationships based on outcrop scale ice-flow indicators and glacial landforms;
2) Establish relationships between glacial stratigraphy, glacial sediment characteristics (e.g. fabric, composition), and ice-flow phases as determined by erosional and landform indicators;
3) Update ice margin positions and further constrain local retreat history and glacial lake extents.

1.6 Methodology Overview

To address the thesis objectives a combination of remote, field, and laboratory methods were used (Fig. 1.11). The overall strategy was to develop a holistic interpretation of ice-flow chronology, glacial sediment stratigraphy and composition, as well as deglaciation events. In this section, basic concepts and methods are summarized.

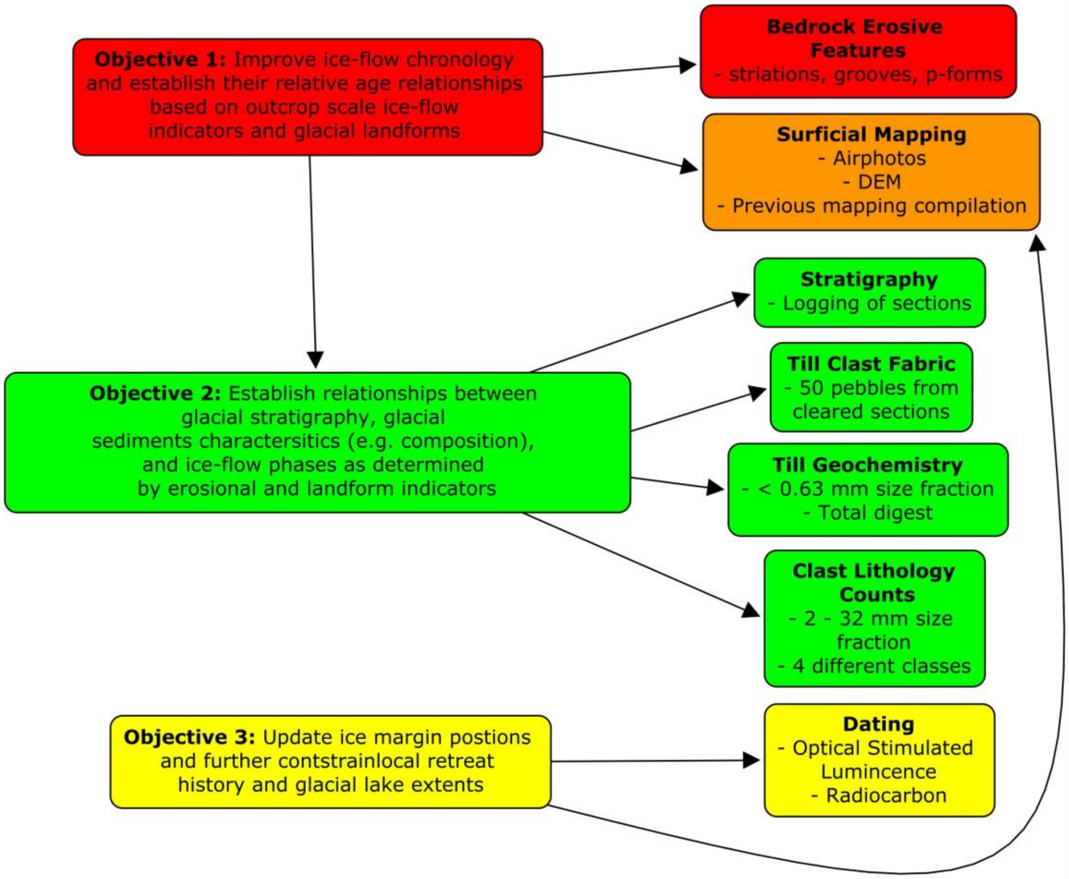

Figure 1.11 Methodology overview flowchart for techniques used in the thesis.

1.6.1 Glacial Landsystems

Objectives described above require detailed maps of surficial geology including surficial sediment compositions, interpretation of depositional environments, and landforms. Mapping and interpreting these characteristics are essential for understanding ice sheet dynamics, for linking the surficial record with the near-surface stratigraphy, refining and updating ice margin positions, and determining glacial lake extents. Surficial mapping of two map sheets (Fig. 1.5) was completed specifically for this purpose, while other surrounding maps (other GEM 2 maps in production and legacy maps) were also used to put these aspects in a broader context. The two maps for this thesis were made using 1:60 000 scale stereo pair air photos with linework being drawn directly on the air photos and then digitized at the GSC. Mapping was aided significantly by other remote sensing data, specifically the 2m resolution ArcticDEM (Porter et al. 2018) and Landsat-8 imagery (courtesy of the United States Geological Survey). These remote sensed datasets allowed for observation of the land surface where it may have been obscured by vegetation and accentuated features on the landscape via a hillshade. Surficial units were ground-truthed throughout the two field seasons (2017, 2018) with 169 stations visited to improve accuracy of mapped polygons (Fig. 1.12). The surficial maps were created at 1:100 000 scale and are published (Hagedorn et al., 2021a, Hagedorn et al., 2021b) along with several other surrounding maps (Smith et al., 2021) as part of the GSC's GEM-2 Program (see Fig. 1.5).

1.6.2 Establishing Ice-flow Phases from Surface Records

Bedrock can be abraded and polished by debris protruding from the basal ice leaving indicators of ice flow direction such as linear striations and grooves (Iverson 1991b, Rea et al. 2000, McMartin and Paulen 2009). However, due to extensive sediment cover and the soft nature of the exposed bedrock, observation and preservation of bedrock erosive features at surface is limited in the study area. Nonetheless, a total of 66 measurements of outcrop-scale ice flow erosional features were collected during fieldwork at 43 different sites (Fig. 1.12). Ice flow direction was determined by measuring the azimuths of the striae and grooves after analyzing the shape of the outcrop to determine the abraded (up-ice) side and plucked (down-ice) side (Rea et al., 2000). It is also possible at certain sites to determine the relative chronology of indicators of contrasting trends based on established techniques (e.g., McMartin and Paulen, 2009). This is possible when 1) striations and grooves are crosscutting each other at a certain oblique angle on the same surface, but the erosional characteristics allow to determine which set formed first; 2) ice flow indicators occur on different surfaces at different elevation on an outcrop allowing relative chronology to be established based on the concept of lee side preservation. The relative chronology established from outcrop-scale indicator analysis was then compared with the subglacial streamlined landforms identified through mapping (see section 1.6.1) to integrate all observed multi-scale ice-flow indicators for the final interpretation and reconstruction of regional ice flow phases.

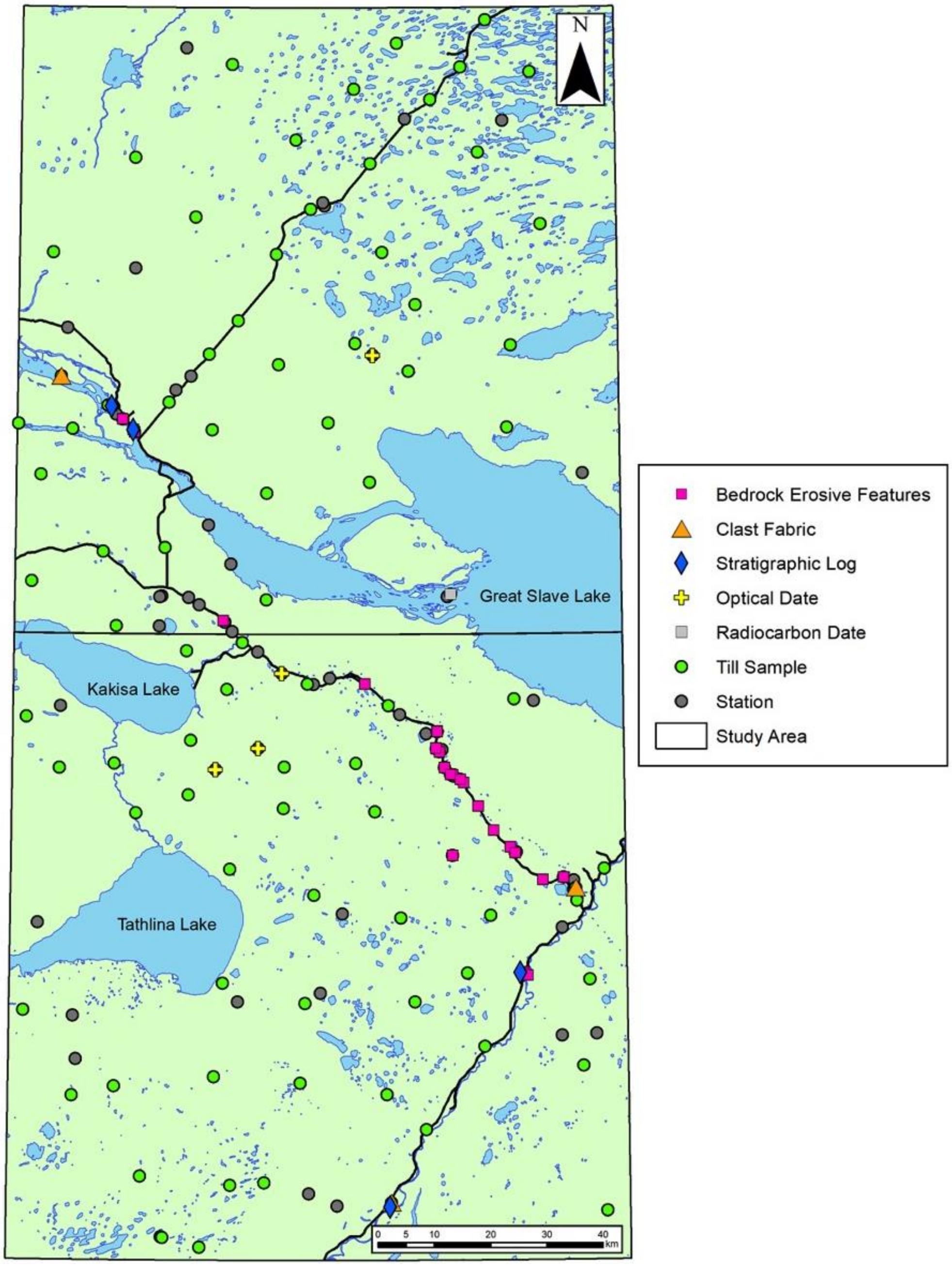

Figure 1.12: Station locations throughout the study area (n=169). A station is any location where a field observation was recorded. Note some locations had several types of samples taken. For example, a location can be both a location for a stratigraphic log and also have a till sample collected. Striations along the Mackenzie River are from boulder top striations.

1.6.3 Establishing Till Stratigraphy and Provenance of Till Units

1.6.3.1 Stratigraphic Logging

Stratigraphic logging provides information on the temporal changes in ice sheet erosional and depositional conditions (Menzies et al. 2018). Vertical exposures in the study area are focused to the Mackenzie River but also were found in borrow pits and quarries throughout the study area (n=3; Fig. 1.12). At sites where stratigraphy was exposed, description of major units and their sedimentological characteristics (grain size, sorting, colour, compaction) were recorded along with the thicknesses of the units (Evans and Benn, 2004). Samples and clast fabrics were taken from each different till unit observed when possible. These sections were also extensively photographed.

1.6.3.2 Determining ice flow from till clast fabrics

Elongated clasts in subglacial traction tills tend to align parallel to the main direction of shear with a slight up-ice dip, and can thus provide useful insights into ice flow direction during till entrainment and deposition (Benn 2004). To measure the direction of shear, clast long axis dip trend and plunge were recorded for six pits at four different sites in the study area. For each pit, a minimum of 50 clasts were recorded with minimum 2:1 a-axis (longest) to b-axis (perpendicular to a-axis) ratio. Normalized eigenvalues (S_1, S_2, S_3) and the related eigenvectors (V_1, V_2, V_3) were calculated from the three by three matrix of the sums of cross products of the direction cosines from the trend and plunge direction measurements (Mark 1973). For till fabrics, the eigenvectors and eigenvalues provide information about the principal orientations of clasts and the overall strength of the spatial alignment (strength of the fabric), respectively. Several computer programs allow rapid calculation of these parameters, in addition to plotting data on a choice of diagram including rose diagrams and equal-area stereonets. The latter are particularly useful to interpret the overall shape of the fabric. For this thesis, the OSXstereonet was used (Allmendinger et al., 2013; Cardozo and Allmendinger, 2013).

It is important to note that not all till fabrics are useful indicators of ice-flow direction. Some fabrics are too isotropic to determine, with sufficient confidence, an ice flow direction. It appears that most researchers use an S_1 value of 0.54 as minimum threshold to infer ice-flow direction from till fabric data; this is thus what was used in this thesis as well (Hicock et al. 1996, Paulen and McClenaghan 2014, Hodder et al. 2016).

1.6.3.3 Till Sampling Strategy

Till samples (n= 97; Fig. 1.12) were taken to detail the composition of the till at surface or throughout stratigraphic sections with two contrasting tills. Sample spacing was approximately 10-12 km apart as an attempt to measure the regional composition of the till. Sampling was aided by road and helicopter access, but due to the dense brush and boggy terrain sampling at regular distance intervals was not possible. Surface pits were hand dug (average sample depth of approximately 0.8 m) to obtain unoxidized C-horizon till following procedures outlined in McClenaghan et al. (2013) and quality control guidelines outlined in Plouffe et al. (2013). A five gallon pail was filled with till for heavy mineral identification and clast lithology counts and a 3 – 5 kg bag of till was collected for matrix geochemistry and other analyses. Heavy minerals were not used in this thesis but were extracted for other studies as part of the larger GSC GEM 2 project. Care was taken to minimize contamination at and between sites and caution used to prevent outside sediments and vegetation from entering the sample. Between sites, shovels and other equipment were thoroughly cleaned.

1.6.3.4 Till Provenance from Clast Lithology Counts

The heavy mineral bulk till samples were sent to Overburden Drilling Management in Ottawa and processed to obtain the coarse fraction of the till used for clast lithology counts. The bulk till samples were disaggregated and underwent a 2.0 mm wet sieve. The <2.0 mm size fraction was used for heavy mineral identification. The >2.0 mm size fraction was wet sieved again at 5.6 mm, with the 2.0 – 5.6 mm fraction stored and the >5.6 mm fraction washed with oxalic acid to remove staining (Plakholm et al. 2020). The acid-washed clasts were split into four equal volumes and one split (n ~300) was classified into four broad categories with fifteen subcategories (Table 1). The categories were based on the local bedrock geology and bedrock lithologies in the surrounding area that could possibly be found in the study area (Fig. 1.11). Pebble counts using the same classification scheme have been published and can thus be compared (Plakholm et al. 2020). Pebble count percentages are then used to infer the relative proportion of different bedrock sources incorporated within a till sample.

Table 1.1: Pebble count classification scheme based on provenance domains in the region.

Canadian Shield (Igneous and Metamorphic)	Paleozoic Sedimentary Rocks	Cordilleran	Mesozoic Sedimentary Rocks	Other
Felsic Intrusive	Limestone/ Dolostone	Quartzite	Sandstone	Vein Quartz
Mafic Intrusive	Sandstone	Chert	Black Shale	
Metavolcanic	Siltstone/ Mudstone/ Shale		Coal	
Metasedimentary			Ironstone (Siderite)	
Arkosic Quartzite				

1.6.3.5 Till Provenance from Till Matrix Geochemistry

Similar to clast lithology, till matrix (< 0.063 mm) composition can provide useful insights into till provenance (McClenaghan et al. 2013b). Part of a till matrix is generated by abrasion and comminution rather than quarrying, reducing mineral grains to their terminal sizes (Dreimanis and Vagners 1974). However, it is important to note that frictional stress during transport can reduce the grain size of large clasts originally produced by quarrying or re-entrainment (Boulton 1978, 1982, Clarke 2005). Till matrix is thus a more complex blend of bedrock sources including components derived from abrasion, comminution of larger clasts of various origin, as well as re-entrainment of pre-existing fine sediment. In addition, it is prone to post-glacial geochemical changes due to weathering and soil forming processes, although this is less effective in carbonate tills (McClenaghan et al. 2018). Interpretation of till matrix must thus be carried out with caution. Nonetheless, it is often useful for provenance analysis because the first-cycle of abrasion on bedrock sources tend to dominate over the others.

A portion of the geochemistry sample was sent to Bureau Veritas laboratories. Digestions and analyses were completed on a 30 g sample of the < 0.63 mm material. Each sample underwent a lithium borate fusion followed by inductively coupled plasma emission spectrometry and mass spectrometry was also applied for total till matrix geochemistry assessment, which are the main results used in this thesis. In addition, a modified aqua regia digestion (1:1:1 HNO_3 : HCl : H_2O) for ultratrace element determination by inductively coupled plasma mass spectrometry was completed but not used in this thesis. Eleven silica blanks, six field duplicate samples and ten standards were inserted within the geochemistry samples sent for analysis; a ratio of 1:20. Five different standard materials and two different types of blanks were included. Quality control and quality assurance statistics were completed using standard methods ensuring the validity of geochemical interpretations (Piercey, 2014; Appendix D).

Geochemical results presented in this thesis are for till provenance purposes only and relies on elemental composition differences between bedrock lithologies. This is discussed further in Chapter 2. Detailed work on the mineral exploration application of this data set is being completed by other researchers as part of the GSC project (Paulen et al. 2018) and will not be further discussed in this thesis.

1.6.4 Constraining the Local Timing of Deglaciation

As explained in section 1.2 and 1.3, the study area lacked age constraints related to ice retreat. Different strategies exist to constrain deglaciation in an area. Techniques that provide timing of deposition in proglacial environments proximal to the ice margin, such as radiocarbon and luminescence dating, have been used extensively to provide minimum ages of deglaciation. As a result, radiocarbon-based chronologies have been developed over the last several decades and are currently still the only ice sheet scale dataset available (Dyke 2004, Dalton et al. 2020). However, other techniques, such as in situ cosmogenic nuclides dating, have been used locally and regionally and have provided excellent age constraints for deglaciation (Balco et al., 2009; Margold et al., 2019; Kelley et al., 2020). Future ice sheet chronologies will most likely integrate datasets from several methods. In this thesis, due to the nature of the surficial materials available and composition of the bedrock, optical dating of eolian and beach sands in addition to radiocarbon dating of organic macrofossils was applied to constrain the timing of deglaciation and glacial lake history within the study area.

Seven optical age samples were collected over the two field seasons (Fig. 1.13). Only one raised sandy beach ridge was identified in the study area; all others observed consisted of coarser cobble-gravel material. For that one beach ridge the optical age samples were collected by clearing the vertical face into what was identified as horizontally bedded sand, interpreted as upper plane beds deposited on the beach foreshore. The sediment facies was identified and the depositional environment was interpreted prior to sampling. For eolian dune sampling, massive fine sand was sampled at depth in a dug pit from the crest of the dune. At all sites a 30 cm long, 5 cm diameter black ABS tube was hammered horizontally into well-sorted sand, within the freshly excavated area averaging 1.5 m deep. When full of sand, the tube was excavated and both ends capped to prevent light exposure.

The samples were sent to the University of Fraser Valley where optical ages were determined using the methods of Neudorf et al. (2015) and Wolfe et al. (2018). K-feldspar grains were mounted and analyzed using a TL/OSL DA-20 reader with a calibrated 90Sr/90Y β source that delivered ~5–6 Gy/min of β particles (Bøtter-Jensen et al. 2010). A single-aliquot regenerative dose (SAR) approach was used to determine the equivalent dose rate for the samples. Fading rates were also obtained for the samples and used for correction (Huntley and Lamothe 2001). Ages were calculated using a Central Age Method (CAM) on the weighted mean equivalent dose values and the environmental dose rate (Galbraith et al. 1999). Further Details can be found in Appendix H.

One basal peat sample was collected at a site where a thick deposit of peat directly overlay till, and was exposed due to undercutting of the riverbank and sediment topple. The sample's organic macrofossil content and species composition was assessed at PALEOTEC Services in Ottawa. Suitable fragments of organic material were selected for AMS radiocarbon dating at the Andre E. Lalonde AMS Laboratory in Ottawa. Further details can be found in Appendix I.

Ages obtained for this thesis were incorporated into a GIS with ages of the surrounding research for interpretation (Hagedorn et al., 2022). All the optical ages were used to create a cumulative probability density function in OxCal (Bronk Ramsey 2009, 2020) to help determine the timing of events and account for uncertainty within the study area.

1.7 Thesis Structure

This thesis contains four parts: An introduction chapter (Ch. 1), two chapters designed as two part publishable manuscript (Ch. 2 and 3) and a conclusion chapter (Ch. 4). The thesis research was undertaken as part of a joint project with GSC and the University of Waterloo with Roger Paulen (GSC Ottawa) and Dr. Rod Smith (GSC Calgary) and supervision by Dr. Martin Ross. Several other M.Sc. projects comprise the overarching GSC GEM2 project including those undertaken by Robert King (Memorial University) and Jamie Sapera (Brock University).

The introduction provides the scientific rationale for the thesis, a summary of the geological settings, as well as the main research objectives, and an overview of the research methods. The rationale is explained by identifying knowledge gaps and issues through a synthesis of the geoscience literature for the surrounding region and over the study area.

Chapter two is co-authored by Roger Paulen, Rod Smith and Martin Ross and outlines the LIS ice flow history over the study area relating it to the stratigraphy observed. I am the lead author and conducted the bulk of the work. Some samples were taken without myself present, including two till fabrics along the Mackenzie River completed by Roger Paulen. Bedrock erosive features and landforms are used to create the ice-flow history over the landscape. This ice-flow history is then correlated to the stratigraphy observed using clast fabrics and boulder top striations and further supported by till compositional data (clast lithology counts and matrix geochemistry).

Chapter three outlines the deglaciation of the study area and is coauthored by Rod Smith, Roger Paulen, and Martin Ross. The surficial geology maps are used to help define the retreating ice margin over the study area using sediment landform associations. Optical and radiocarbon ages are presented and integrated into surrounding ages from previous research to help outline deglaciation and glacial lake levels. The reconstruction presented for the study area is then compared and contrasted to the currently proposed glacial history.

Chapter four includes a discussion of the major findings of my research. It provides an integrated analysis of the research and outlines the major contributions of the work and implication of the research to a variety of fields. Future work is also suggested. Appendices are attached containing references to GSC publications completed during the partnership and data used in the thesis.

Chapter 2 – Ice-flow History and Till Stratigraphy in the Southwestern Great Slave Lake Area; implications for the regional configuration of the Laurentide Ice Sheet

2.1 Introduction

Studies of past and present glaciers have demonstrated that, at the ice-sheet scale, ice flows radially from inner regions of thicker ice (ice domes or ice divide/dispersal centers) toward regions of thinner ice (ice margins) at variable velocities, mostly through a series of discrete ice streams (e.g. Rignot et al. 2011; Rignot and Mouginot 2012; Clark et al. 2012; Stroeven et al. 2014; Margold et al. 2015). The Laurentide Ice Sheet (LIS), the largest ice sheet in North America during the late Pleistocene (e.g. Dyke et al. 2003; Dalton et al. 2020), had an additional characteristic that may not apply to all ice sheets; its ice domes and divides migrated over time across considerable distances (e.g. McMartin and Henderson 2004; Veillette et al. 1999; Clark et al. 2000; Rice et al. 2019). Furthermore, during deglaciation ice flow becomes increasingly controlled by topography due to ice sheet thinning (e.g. Stroeven et al. 2014). This temporal shift in glacial dynamics and ice sheet topography can lead to important regional and local changes in ice-flow phases and in turn the characteristics of subglacial sediment produced during those different phases. Many glaciated regions of Canada thus show evidence for multiple crosscutting ice-flow phases in the form of a complex erosional and depositional record (Prest et al., 1968; Dyke and Prest, 1987; Boulton and Clark 1990; Veillette et al. 1999; Clark et al. 2000; Stumpf et al., 2000; Dyke, 2004; Trommelen et al., 2012; Hodder et al. 2016; Margold et al., 2018; Rice et al., 2019; Gauthier et al. 2020). Deciphering the erosional and depositional record helps understand the long-term evolution of past ice sheets, important to understanding ice sheet behavior.

The LIS history has remained poorly constrained in several regions. One such region is around southwestern Great Slave Lake where ice flow history and stratigraphy are still generalized and incomplete. The region was influenced by the Keewatin Ice Dome to the east (Fig. 2.1), but the location and timing of the Plains Ice Divide (Fig. 2.1), which split ice flow southwest through Alberta and northwest through to the Yukon, is uncertain (Dyke and Prest 1987, Bednarski 2008, Brown 2012, Gowan et al. 2016, Roy and Peltier 2017, Margold et al. 2018). The Laurentide-Cordilleran Ice Sheet convergence is also thought to have influenced ice flow into the Great Slave Lake region adding further complexity (Paulen et al. 2007, Bednarski 2008). Topographic uplands funneled ice flow to lowlands between them creating the Great Slave Lake and Hay River Ice Streams, but these effects in relation to ice-flow chronology are still speculative (Paulen et al. 2011, Brown 2012, Margold et al. 2018). Additionally, surrounding areas have been characterized by regional and site specific ice-flow reconstructions showing varying degrees of ice-flow complexity and contrasting ice-flow chronologies (Bednarski, 2008; Paulen et al., 2011; Brown, 2012; Rice et al., 2013; Oviatt et al., 2015; Sharpe et al., 2017; Paulen et al., 2019a) that have yet to be put into a consistent regional reconstruction. Therefore, deciphering the ice flow chronology for the southwestern Great Slave Lake region will help address uncertainties in ice sheet evolution, filling an important knowledge gap in our understanding of the LIS.

The objective of this chapter is to reconstruct the glacial dynamics of southwestern Great Slave Lake area by documenting and interpreting outcrop-scale ice flow erosional indicators and subglacial landforms, as well as till clast fabrics and till composition (for provenance analysis) in the southwestern Great Slave Lake Area. Based on these observations and previous studies, we discuss the potential controlling factors and regional implications of identified ice-flow phases.

2.2 Regional Setting

The study area is located in southern Northwest Territories and includes the towns of Fort Providence, Kakisa and Enterprise with Hay River 15 km to the east. Highways connect the communities. Major water features include Kakisa and Tathlina lakes, the Hay and Kakisa rivers, the upper reaches of the Mackenzie River and a portion of southwestern Great Slave Lake (Fig. 2.1A).

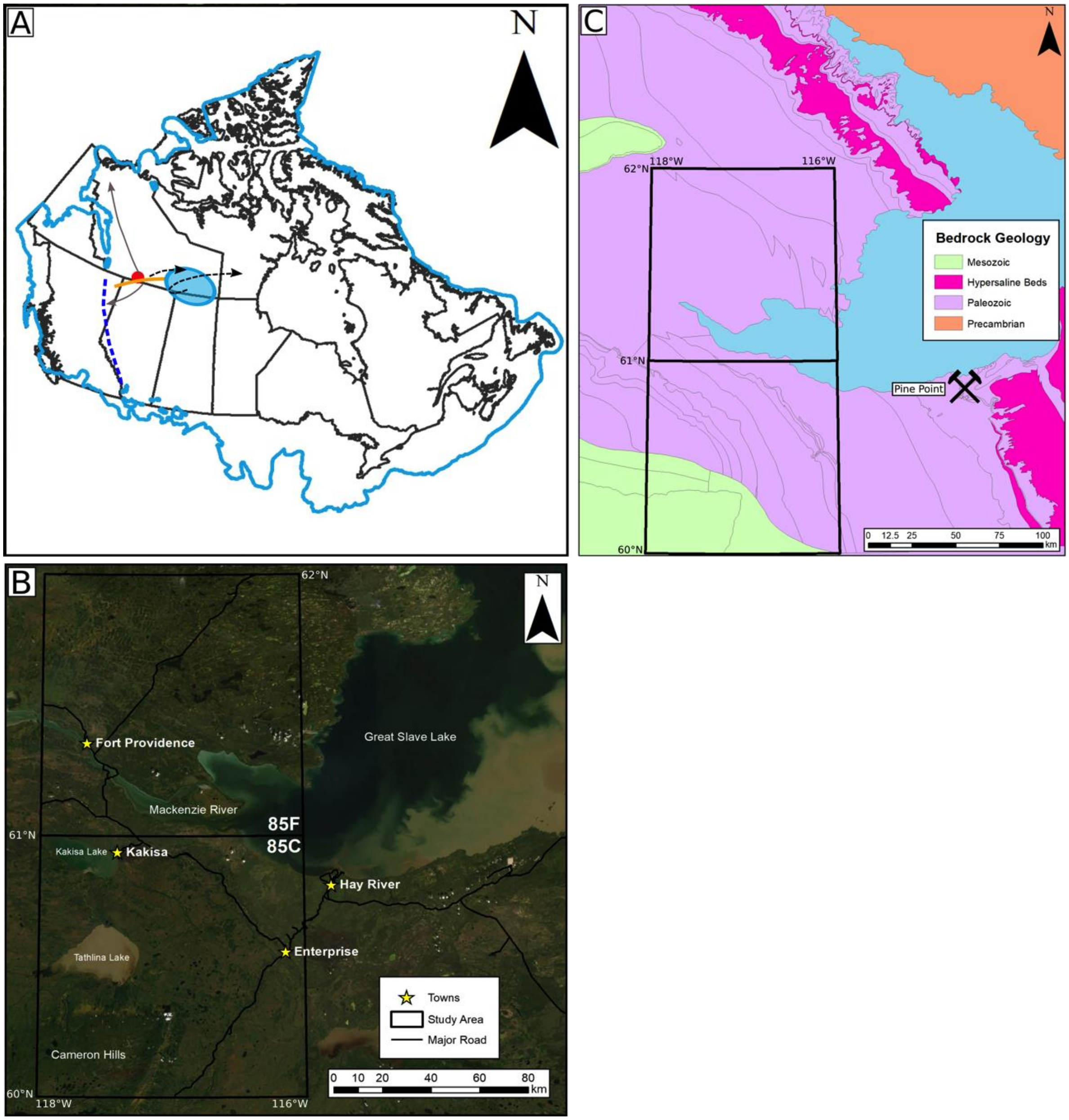

Figure 2.1 A) The maximum extent of the LIS in a Canadian context. The study area is indicated by a red dot, the Keewatin Ice Dome is shown along with the location of the Plains Ice Divide (Blue dome and orange line respectively). Migration of these features throughout glaciation is shown, as dashed arrows while the resulting ice flow are grey arrows. The blue dashed line indicates the approximate location of the LIS-CIS convergence (locations estimated from Dyke and Prest, 1988 and Margold et al., 2018). B) Location of the study area, main geographic features, and related map sheets (NTS 85C and F) with a GeoEye satellite image as background. C) Bedrock geology of the study area and surrounding regions (Okulitch 2006). Contacts between different formations within the WCSB Paleozoic (mainly carbonates) and Mesozoic (mainly shales) are shown and hypersaline beds of the Paleozoic strata are highlighted due to their compositional difference. The mine symbol indicates the Pine Point mining district.

2.2.1 Bedrock Geology

The region is underlain by Precambrian (Archean and Proterozoic) crystalline basement rocks, which outcrop at surface to the east (Fig. 2.1B). The Western Canadian Sedimentary Basin (WCSB), a thick (350 – 600 m) gently dipping (1.9 m/km west) carbonate sequence, is atop the basement rocks and was deposited during the Phanerozoic (Rhodes et al., 1984; Okulitch, 2006). The bedrock surface in the study area consists mostly of Paleozoic carbonate strata from the WCSB and vary in composition due to depositional environment, most notably are hypersaline beds east of the study area (Rhodes et al., 1984; Okulitch, 2006; Fig. 2.1B). Differential erosion of the WCSB strata created escarpments and bedrock uplands. Paleo-karst features occur locally within dolomitized WCSB carbonates and served as conduits for mineralizing fluids, which created the world class Pine Point Mississippi Valley Type Deposit (Hannigan, 2006). Finally, low dip angle WCSB Mesozoic shales, siltstones, and sandstone occur in the southwest portion of the study area although other non-eroded caps of Mesozoic sediments are preserved elsewhere (Okulitch, 2006; Fig. 2.1B). Weak sedimentary strata were easily eroded by subglacial processes, which supplied large sediment volumes to the subglacial environment, and controls the topography observed in the area today.

Average compositions for the main bedrock domains were obtained through global averages and used to compare to the till geochemistry results. These broad domains include, limestone/dolostone, shales, and Canadian Shield lithologies. The compositions are presented in Table 2.1.

Table 2.1: Average whole rock geochemistry of different lithologies presented in Parker and Fleischer, 1967.

Element	Limestone (Paleozoic Lithologies)	Igneous (Canadian Shield Lithologies)				Shale (Mesozoic Lithologies)
		Granite	Felsic Granite	Intermediate	Basalt	
SiO_2	2.4	33.05	32.3	26	23	7.3
Al_2O_3	0.42	7.7	7.7	8.85	7.8	8
Fe_20_3	0.38	2.19	2.7	8.56	8.65	4.72
MgO	4.70	0.545	0.56	2.18	4.6	1.5
CaO	30.23	1.515	1.58	4.05	7.6	2.21
Na_2O	0.4	2.71	2.77	3	1.8	0.96
K2O	0.27	3.36	3.34	2.3	0.83	2.66
MnO	0.11	0.0515	0.06	0.12	0.15	0.085
Cr_2O_3	0.0001	0.0013	0.0025	0.005	0.017	0.0099

2.2.2 Physiography

Regionally, the area is low-relief with topographic features related to bedrock geology. Relief features include bedrock knobs south of Kakisa Lake and the prominent bedrock escarpment south of Great Slave Lake. The Cameron Hills has the highest elevation at 946 m a.s.l. with the average elevation of 320 m a.s.l.and the lowest elevation of 45 m a.s.l. (Fig 2.2). The flat relief and sediment compositions have created large expanses of organics due to weak drainage. These organics are typically less than 2 m thick and manifest as spruce bogs and fens with low lying vegetation and mosses. Areas with slightly higher elevation are characterized by better drained substrates allowing dense mix forest of jack pine, aspen, and white spruce to grow (Lemmen 1990). The study area lies within the discontinuous permafrost zone, causing sediments and organics to be locally frozen along with the presence of thermokarst lakes and peat plateaus (Heginbottom et al. 1995).

2.2.3 Surficial Geology and Stratigraphy

Bedrock outcrops are at surface mainly on uplands and around the escarpment but is otherwise largely covered by glacial sediments. Glaciolacustrine sediments are common in lower lying areas and consist of coarse shoreline and sublittoral facies including sorted sand and gravel, cobble lags, winnowed tills and cobble beach ridges (Lemmen 1990). Glaciolacustrine sediments vary in thickness but are typically < 0.5 m. More recent sediment remobilization includes eolian deposition by winds, alluvial deposition associated with major rivers, and organic accumulation due to weak drainage over the landscape (Hagedorn et al., 2021a; Hagedorn et al., 2021b). These sediments compose landforms that include sub-parallel beach ridges, iceberg scours, and eolian dunes.

Total sediment thicknesses range from 1 to > 25m (Smith and Lesk-Winfield, 2010) with till found at surface over and having thicknesses of > 20m (at Pine Point). Till veneers (< 2 m) are associated with bedrock highs and the thickest tills are found below the escarpment. Glacial landforms including streamlined ridges and moraine are predominantly composed of till. Previous research defined several till units in the region, differentiated based on colour, grain size, pebble lithology, and other sedimentological characteristics (Craig, 1965; Lemmen, 1990).

The first observation of different tills at surface in the region was that of Craig (1965) who noted large variations in grain size distribution across 25 till samples. They suggest that till composition varied with landform sampled, rather than the underlying bedrock. Specifically, Craig

(1965) observed a silty to clayey grey brown till and a stoney yellow-brown till although no further detail into the composition or location of the tills is presented.

Further work by Lemmen (1990) suggested that the till compositional differences were related to changes in the underlying bedrock. Although they do not specifically define different till units; their observations of the tills include a slightly stony to stony till, a calcareous silt to silty clay matrix till, total carbonate content of all tills ranging from 12% to 81%, and the presence of shield clasts in all tills. A more detailed till study was completed at Pine Point (Rice et al. 2013), east of the study area. Four stacked till sheets were documented at Pine Point and correlated to ice flow phases. One till unit was directly related to the underlying bedrock (e.g., containing relatively high proportions of galena and sphalerite from the local MVT deposits) but other units contained more distal traveled clasts.

2.2.4 Quaternary History

During the LGM, ice is thought to have flowed across the study area either to the southwest (e.g. Paulen et al., 2007; Bednarski, 2008; Paulen et al., 2019) or to the northwest (e.g. Dyke and Prest, 1987; Brown, 2012; Gowan et al., 2016; Margold et al., 2018). This depends on the position and timing of formation of the Plains Ice Divide, which separated ice flow going south into Alberta from ice flow going north and northwest into the Mackenzie Trough ice stream (Fig. 2A; Fisher et al., 1985; Dyke and Prest, 1987; Lemmen et al., 1994; Paulen et al., 2007; Bednarski, 2008; Brown, 2012; Gowan et al., 2016; Roy and Peltier, 2017; Margold et al., 2018). After separation of the Laurentide and Cordilleran ice sheets, ice flowed southwestward to westward towards the western LIS margin (Bednarski 2008, Sharpe et al. 2017).

As the ice sheet continued to retreat and thin it became more topographically controlled, with the uplands eventually becoming ice-free. During this late stage phase of ice, a lobe flowed northwestwardly down the Mackenzie River Valley between the Cameron Hills and the Horn Plateau to the north (Lemmen et al., 1994; Paulen et al., 2007; Bednarski, 2008; Refer to Fig. 1.5). The current estimate of ice margin retreat in the study area is between 12.9-12.8 cal. ka BP, based on two radiocarbon ages from organic lake sediment and moss (Lemmen et al. 1994, Dyke 2004, Dalton et al. 2020). During deglaciation of the study area, glacial lakes formed along the ice margin due to glacioisostatic depressed basins and ice-lobes blocking natural northeast drainage, the largest of these being glacial Lake McConnell (GLM; Lemmen et al. 1994, Smith 1994, Bednarski 2008, Couch and

Eyles 2008, Utting and Atkinson 2019). GLM then drained via isostatic adjustment and incision of outlets.

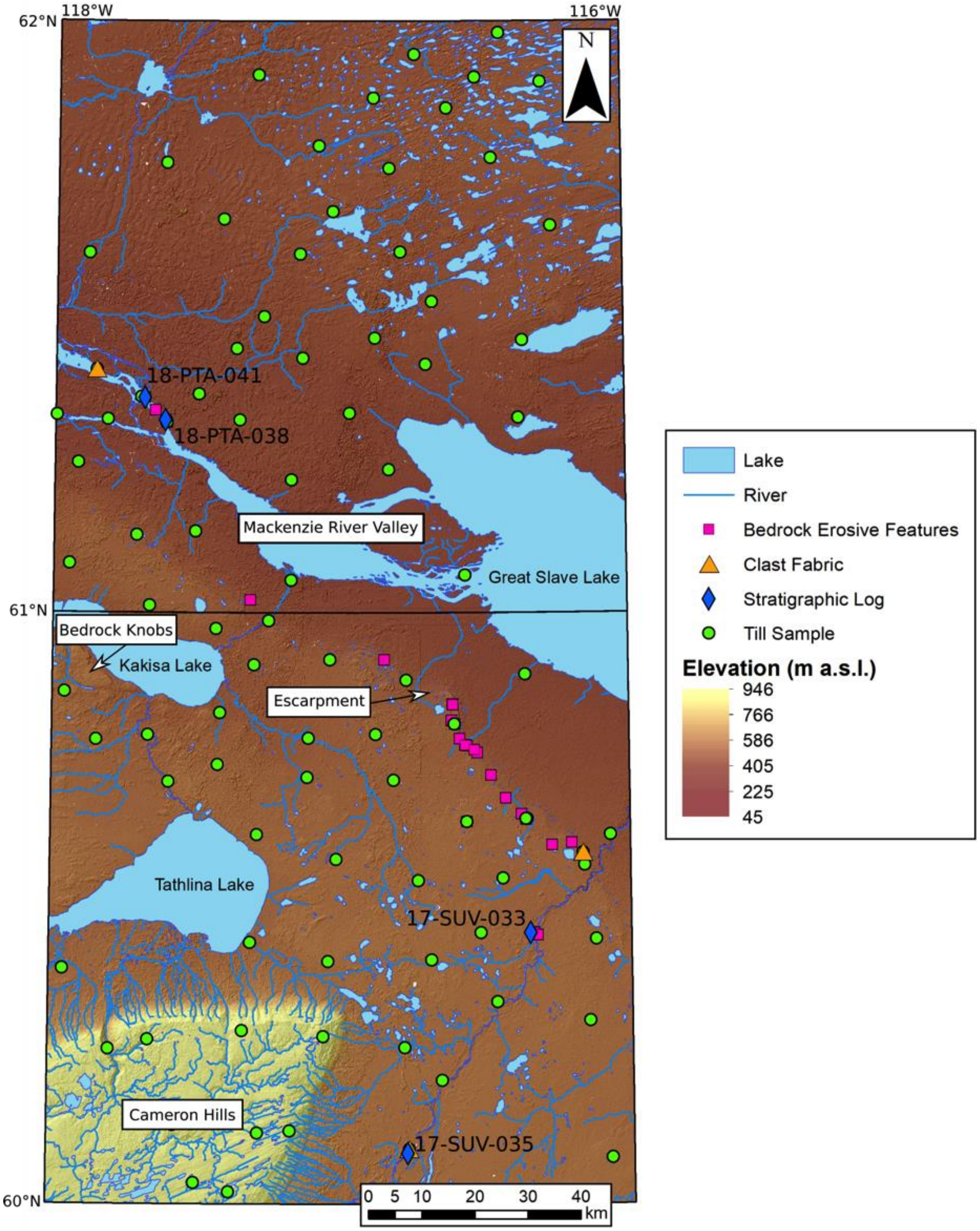

Figure 2.2: Digital Elevation Model from the 2m resolution ArcticDEM over the study area (Porter et al. 2018)**. Important topographic features in the study area are labeled. Locations of sites used in the research are indicated and stratigraphic locations have the station number labeled.**

2.3 Methods

2.3.1 Ice-Flow Indicators

2.3.1.1 Outcrop-scale Ice-Flow Indicators

Outcrop-scale ice flow indicators are commonly used to decipher ice flow phases in areas of discontinuous drift cover, especially on the Canadian Shield (e.g. Boulton et al., 1985; Iverson, 1991; Parent et al. 1995; Batterson and Liverman, 2001; McMartin and Paulen, 2009). However, preservation of these features on sedimentary rocks is typically lower due to weathering. Nonetheless, 66 measurements were taken from 43 bedrock surfaces in the study area (Fig. 2.2). Quarries and borrow pits were targeted as exposed bedrock was more easily accessible. At other locations, particularly along the bedrock escarpment, thin sediment cover over bedrock was carefully removed to not damage the bedrock surface and cleaned with water. Sediment-covered areas had an increased preservation potential due to protection from surface weathering processes. Most bedrock erosive features were recorded from this bedrock escarpment area.

Striations, grooves and p-forms were observed, measured, and photographed. At multiple locations these features crosscut one another allowing establishment of a relative age relationship (Parent et al., 1995; Veillette et al., 1999; Paulen et al., 2013). Unidirectional trend of linear bedrock erosive features was determined using criteria like depth change of the feature, form of the feature (i.e. nailhead), and sculpting of the outcrop via polished and plucked surfaces (Rea et al. 2000, McMartin and Paulen 2009, Benn and Evans 2010, Menzies et al. 2018). In some cases, however, it was not possible to establish ice flow direction and measurements are thus reported as bidirectional. The frequency and distribution of each ice flow direction provided insight into the relative strength and coverage of an ice flow phase. All measurements were compiled into a GIS to facilitate visualization and spatial analysis and interpretation. The sites shown in this chapter are the important sites for the interpretation (i.e. multiple flow sets) but all sites were used to determine ice flow groupings and age. The complete list of outcrop-scaled ice flow indicator measurements can be found in Appendix B.

2.3.1.2 Subglacial Landforms

Detailed surficial mapping was completed to identify subglacial streamlined landforms as indicators of ice flow direction. Elongated subglacial landforms, such as drumlins and crag-and-tails, were mapped as linear features along their crest using 1:60 000 stereo pair aerial photographs, aided by the 2 m resolution ArcticDEM (Evans 2012, Chandler et al. 2018, Porter et al. 2018). The stoss-lee relationship of subglacial landforms allowed for the determination of ice flow direction, but some landforms had symmetrical or complex shapes and were thus mapped as bidirectional (Evans et al., 1999; Menzies et al., 2018). In the study area, landforms rarely crosscut one-another to give relative age relationships between flows (Clark, 1993; McClenaghan et al., 2018; Rice et al., 2019). Previous large-scale landform compilations from remotely sensed data were also integrated into a database with the mapped landforms of this research (Prest et al. 1968, Fulton 1995, Brown et al. 2011, Margold et al. 2015). The complete database of landforms mapped and compiled from the older compilations was used to determine ice flow directions over the study area.

Furthermore, the spatial extent, location, and dimensions of landforms also provided useful information for interpreting the coverage and relative strength of the different ice flow phases. Once combined, the landform and outcrop-scale ice flow data were used to create an ice flow chronology and to interpret glacial dynamics evolution over the study area.

2.3.1.3 Till Clast Fabrics

Clasts in subglacial till (Evans et al. 2006) tend to align parallel to the main direction of shear (Hicock et al., 1996; Benn, 2004; Paulen and McClenaghan, 2015), which often correspond to ice flow direction. Therefore, the overall orientation of clasts in a till can provide useful information about ice flow direction at time of till deposition. When clast fabrics are completed on different till units at the same stratigraphic site, shifts in ice-flow direction can be discerned and a relative age of ice-flow phases can be established and compared to the relative chronology based on the landform an outcrop-scale features (Paulen et al. 2007, Rice et al. 2013, Hodder et al. 2016, McClenaghan et al. 2018).

A total of six fabrics were completed; three from a single site (18-PTA-041), with the remaining three fabrics completed at three different sites (Fig. 2.2). For fabric measurements, a till surface was cleaned both vertically and horizontally to reduce bias in the selection of measured clasts. A total of 50 clasts with a minimum 2:1 a-axis (longest) to b-axis (perpendicular to a-axis) ratio were excavated and an aluminum knitting needle emplaced parallel to the a-axis. This knitting needle represented the clast trend and plunge which were recorded and used for analysis (Benn 2004).

For each fabric, the trend and plunge of the a-axis were plotted on a lower hemisphere stereonet using the “Stereonet” software (Allmendinger et al., 2013; Cardozo, and Allmendinger, 2013). Normalized eigenvalues (S_1, S_2, S_3) and eigenvectors (V_1, V_2, V_3) were also calculated. Here we used $S_1 > 0.54$ as a threshold for inferring ice flow direction at time of till deposition (Benediktsson et al. 2016). The shape of the fabric and the eigenvalues together help determine whether a fabric is useful for ice flow direction determination. Furthermore, the fabric modality was classified (Hicock et al. 1996). These classifications are somewhat subjective but when used with the eigenvalues they give a better measure of whether a fabric can be used in interpretation of ice-flow. Fabrics with girdle-like, spread bi-modal and bimodal clusters classification that plot in the lower fields of the girdle cluster isotropic ternary diagram are thought to be fit for ice flow direction determination (Hicock et al., 1996; Paulen and McClenaghan, 2015). For suitable clast fabrics the ice flow direction was determined from V_1. Weaker fabrics are still useful for other purposes of this research but were not used to constrain ice flow direction.

2.3.1.4 Lodged Boulders

Lodged elongated boulders and their striated upper surfaces are also useful for constraining ice flow direction within till stratigraphy (Hicock and Dreimanis 1989). Care was taken in the selection of boulders. To determine that ice flowed by sliding atop an elongated and lodged (immobile) boulder, the boulder A-B plane surface has to be relatively flat and leveled, and the flat upper surface must be polished with multiple parallel striations aligned with the a-axis of the boulder. Ideally, the boulders shape also shows a well-developed stoss-lee form. These characteristics are important as boulders can be remobilized and abraded during transport within the subglacial environment, overprinting pre-existing striations. The majority of these measurements were obtained from a discontinuous boulder lag separating two till units along the Mackenzie River with some measurements from isolated boulders lodged within a single till unit.

2.3.2 Till Stratigraphy

Stratigraphic information can help understand temporal changes in ice sheet erosive/depositional conditions over time through superposition of different units (Piotrowski et al. 2004, Menzies et al. 2018). Stratigraphic exposures in the study area were concentrated along the Mackenzie River with rare vertical exposures of sediments found in borrow pits and quarries (Fig. 2.2). At stratigraphic sections description of major units and their sedimentological characteristics such as grain size, sorting, colour, compaction and thickness was recorded (Evans and Benn 2004). Sites were documented photographically and digital stratigraphic logs produced. Stratigraphic sites include 18-PTA-041, 18-PTA-038, 17-SUV-035, and 17-SUV-033 (Fig. 2.2). The first two sites are in close proximity to one another and along the Mackenzie River, the latter two are located in the southern portion of the study area at a borrow pit and quarry, respectively. Clast fabrics were completed at stratigraphic sites where possible and till samples were collected from different till units observed at stratigraphic sites.

2.3.3 Till Composition/Provenance

A total of 97 till samples were collected throughout the study area for analysis (Fig. 2.2). Most of these samples were collected at dug surface pits along with targeted samples at till sections where stratigraphy was apparent. Sampling sites were limited due to extensive bog and fen creating a spacing of samples ~ 10 km apart from one another.

At surface sites, samples were collected in the unoxidized C-horizon and care was taken to minimize contamination from sediments and soil above the C-horizon (Spirito et al. 2011, McClenaghan et al. 2013a). A 3 – 5 kg sample bag of till was filled for matrix geochemistry and a 5-gallon pail was filled for heavy mineral identification and clast separation for provenance analysis. Between sites shovels and other equipment were thoroughly cleaned. Quality assurance and quality control guidelines were followed including blanks, field duplicates and reference material at a ratio of about 1:20 (Plouffe et al., 2013). No issues with the data were found (See Appendix D for QA/QC details).

2.3.3.1 Till Matrix Geochemistry

The 3-5 kg bag of till was sent to the GSC Sediment Laboratory where it was processed including sieving of the samples to produce a <0.63 um fraction (Girard et al. 2004). This < 0.63 um fraction was then sent to Bureau Veritas for till matrix geochemical assessment. A full suite of elements was analyzed on a 30 g sample of the <0.63 um material using two digests; a modified aqua regia digestion (1:1:1 HNO_3:HCl:H_2O) using inductively coupled plasma mass spectrometry for ultra-trace element determination and lithium borate fusion using inductively coupled plasma emission spectrometry and mass spectrometry for total till matrix geochemistry.

The major oxides from the total digest were used for provenance analysis (SiO_2, Al_2O_3, Fe_2O_3, MgO, CaO, Na_2O, K_2O, TiO_2, P_2O_5, MnO, Cr_2O_3). The total digest is better suited for provenance analysis because it fully breaks down the till matrix components ensuring that even the most resistant minerals are dissolved. This is important for tills in the region, as weaker digestions do not dissolve many minerals of Canadian Shield provenance.

A principal component analysis (PCA) was applied using the major oxides. PCA has been used to understand compositional data, such as till matrix composition, because it reduces the dimensionality of a multivariate dataset, which helps understand and interpret till compositional variability (Grünfeld, 2007; Grunsky 2010; Refsnider and Miller, 2013; McMartin et al., 2016). The purpose of the PCA is to help extract meaningful information from till geochemical dataset by analyzing its compositional variability. The maximum number of variables is, however, limited by the dimensionality (degree of freedom) of the dataset. In addition, not all variables may be of interest due to low variance or if results are close to or below detection limit. Based on the number of samples and variance of the different variables, ten major oxides were selected for the PCA: SiO_2, Al_2O_3, Fe_2O_3, MgO, CaO, Na_2O, K_2O, TiO_2, MnO, and Cr_2O_3. P_2O_5 was the only major oxide not included in this analysis, mainly due to a low variance and limited use as a provenance indicator in the region. In addition, because compositional data is usually parts of a whole reported as parts per unit (in this case weight percent), the variables (e.g. major oxides) sum to a constant. This type of compositional data is referred to as closed data. Before applying PCA on this type of data it is important to transform the data to address this problem of closure (Grunsky 2010). Here, a centered log-ratio (clr) transformation (Aitchison 1986) was applied to the selected subcomposition. The data is then normalized to unit variance to minimize the number of possible solutions.

The PCA then takes the above clr-transformed and normalized data and reduce it to fewer components (principal components) that explain most of the data variability. It creates a new set of dimensions, which is a linear combination of the original variables. Eigenvalues and eigenvectors are obtained from the covariance matrix of the subset and the data points are projected onto the eigenvectors with the largest eigenvalues. Data preparation was completed in Excel and then brought into IoGAS where the CLR transformation and standardization were applied. The PCA was also carried out in IoGAS.

The first principal component of the PCA explains the greatest variability within the dataset. The subsequent principle components explain further variation in the dataset. Geological interpretation of these principle components is done by looking at results in the form of PC scores and elemental loadings in tables and biplots such as PC1 vs. PC2 and relating these to geological and geochemical processes (Grunsky 2010).

K-means clustering is another method to understand structure within a data set (Grunsky 2010, Wang 2018). It aims to group samples with similar compositions together, which in a till geochemistry context would suggest similar provenances. Specifically, the clustering method group samples to minimize the distance of that point to the closest clusters centroid. To determine these centroids, K-mean clustering assigns a random number of centroids that must be lower than the number of total samples within the dataset. Then every sample is assigned to the closest centroid. Finally, k-means are calculated based on the distance between the points within each cluster. The last two steps are repeated until the squared distance is minimized for each data point; this is when the best centroids to explain the data clustering are found. A scree plot is used to determine how many clusters are needed to explain a significant portion of the squared error. This is usually assigned at the first major inflection point on the scree plot line. For this dataset it was determined to be four clusters (Fig. 2.3). K-means clustering was completed on the clr data in IoGAS.

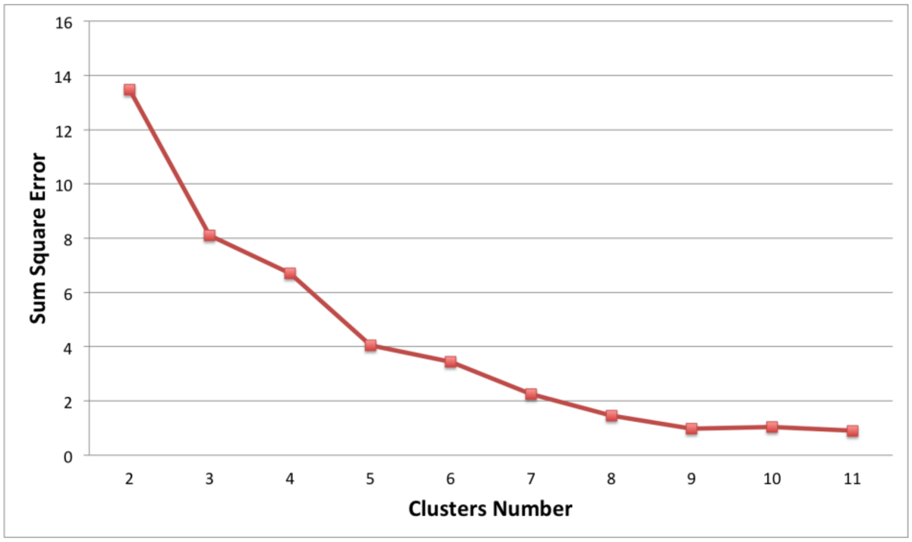

Figure 2.3: Scree plot of the Sum Square Error for the data against the number of k clusters. The first inflection point can be observed at K=4 meaning four clusters was best suited to explain the data.

The geochemistry data was also subjectively split into different classes in an attempt to explain trends geographically and geologically. The first classification was geographic based on topographic features and landforms across different regions of the study area; which was a suggested control on till composition by Craig (1965). The four geographic classes were: 1. Within 5 km of the escarpment, 2. The middle areas between other classes, characterized as flat and lower-lying, 3. The northern portion of the study area, characterized by southwest trending landforms with the classification ending at the southernmost extent of these landforms and, 4. The Cameron Hills, the largest topographic feature in the study area and characterized by southwest trending landforms. The geographic classes also relate to interpreted subglacial conditions. Classes 3 and 4 contain streamlined features indicative of fast ice flow, and thus possibly more distal till provenance, while the escarpment would act as a potential source of local material due to plucking of jointed rocks by ice (Krabbendam and Glasser, 2011; Menzies et al., 2018; Rice et al., 2019). The differences within Class 1 to 3 and 4 could result in differing till compositions at surface due to these subglacial conditions. The remaining portion of the study area was not characterized by any subglacial landforms and was thus classified together.

Underlying bedrock was also used to classify the till samples because local bedrock is another potentially important source or the overlying till composition; this was the suggested control on till composition by Lemmen et al. (1994). Four bedrock geology classes were used and include: 1. Mesozoic Sediments. 2. Paleozoic formations of primarily limestone. 3. Paleozoic formations split between limestone and shale. 4. Paleozoic formations of primarily shale. These bedrock classes were divided based on sedimentological differences between formations as, due to the large number of different formations within the WCSB, including each formation would not succinctly show trends in the geochemical data (Okulitch, 2006).

2.3.3.2 Clast Lithology Counts

The 5-gallon pails collected were sent to Overburden Drilling Management in Ottawa for heavy mineral identification along with clast separation. These clasts were sieved and acid washed to clean them for classification. The 2 - 32 mm clast (pebble) fraction of the samples were coned and quartered to get a representative portion of the total fraction and then classified (*n*~300). The classification scheme had four broad categories representative of the surrounding bedrock geology that would be indicative of provenance and are the same as previously published work. They include

Canadian Shield, Paleozoic sedimentary rocks (mainly carbonates), Mesozoic sedimentary rocks (mainly shales), and Cordilleran clasts (Plakholm et al., 2020). These four classes were split into 15 subclasses to further differentiate within the four categories (Fig. 2.4; Table 2.1). Clast lithology count percentages were used for broad provenance analysis of the tills indicating ice flow directions responsible for deposition (Trommelen et al., 2013).

Different types of clasts are present at different sieving fractions due to competency within the subglacial environment. The most extreme case of this would be jointed and brittle rocks, like laminated shales, not being present at all within the clast size fraction of the till (Plouffe et al., 2006; Paulen et al., 2007; Paulen, 2009). A bias within specific size fractions towards clasts of certain provenance is possible as a result and thus extra care must be taken in the interpretation of clast lithology counts in this study.

2.4 Results

2.4.1 Ice-Flow Indicators

2.4.1.1 Outcrop-scale Ice-Flow Indicators

Outcrop-scale ice flow indicators show ice flow directions ranging from southwest (230°) to northwest (305°; Fig. 2.5). At most sites, only the southwest ice-flow direction is preserved. However, at 11 sites, cross cutting relationships of striations and grooves allowed relative ice-flow chronology to be determined (Fig. 2.5A). Notably, the most southwestward flow is the oldest at all the sites with evidence of multiple ice flow directions.

Most bedrock erosive features found in this study occur along the escarpment because bedrock is well exposed there and a resistant limestone cap provides a more competent surface for preservation of abraded surfaces. As a result, the ice flow indicator data has a limited spatial extent and certain, more topographically controlled ice flows may not have overtopped the escarpment and therefore are not recorded.

Figure 2.4: Sample photos of the different lithology classes used in the clast counts from till samples. Canadian Shield: A) Felsic Intrusive, B) Mafic Intrusive, C) Metasedimentary, D) Metavolcanic, E) Quartzite. Paleozoic sedimentary rocks: F) Limestone/Dolostone, G) Sandstone, H) Shale. Mesozoic sedimentary rocks: I) Coal, J) Sandstone, K) Ironstone, L) Shale. Cordilleran: M) Quartzite, N) Chert.

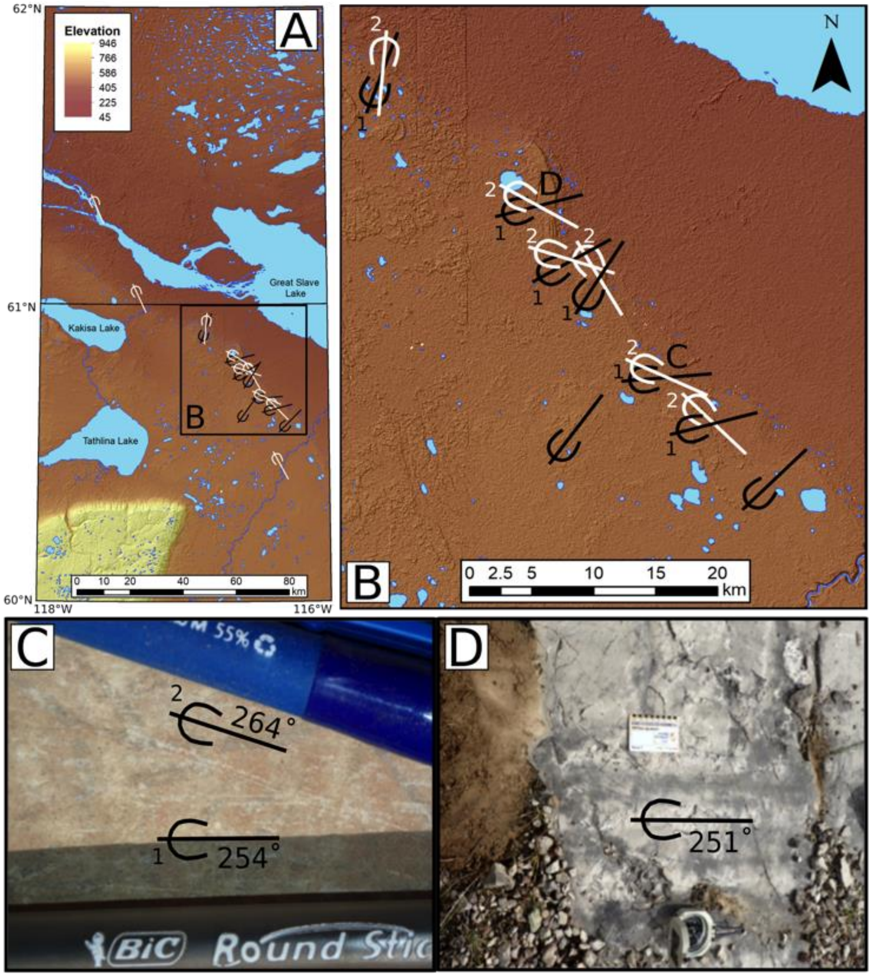

Figure 2.5: A) Outcrop-scale ice flow indicators throughout the study area on the 2m resolution ArcticDEM (Porter et al., 2018). B) Inset map showing more details and the relative age relationships (1 = oldest). Measurements indicate ice flows to the southwest (250°), the west (280°) and northwest (305°). C) Evidence of cross-cutting striae indicating a shift from 254° to 264°; D) Pair of grooves oriented 251°.

2.4.1.2 Landforms

The landform record over the study area shows streamlined features in a variety of westward directions ranging from southwest (230°) to northwest (305°; Fig. 2.6). The compilation of mapped landforms includes mega-scale glacial lineations (MSGL), drumlins streamlined bedrock, and other minor sculpted terrain features (Prest et al. 1968, Brown et al. 2011). These landforms show limited evidence of crosscutting within the study area, but crosscutting relations were observed to the east with a southwest flow overprinting a westward flow (Oviatt and Paulen 2013, Rice et al. 2013, McClenaghan et al. 2018).

Southwest (230°) trending landforms were observed in the northern portions of NTS 85F, between the escarpment and Great Slave Lake, on the Cameron Hills, and on the bedrock knobs south of Kakisa Lake (Fig. 2.7A). The southwest landforms in northern NTS 85F span a large area (Fig. 2.6A and B). Landforms in northern NTS 85F terminate at a series of moraines and do not extend down to the Mackenzie River (Brown et al., 2011). Landforms atop the Cameron Hills have been previously identified as part of the Great Slave Lake Ice Stream (Margold et al. 2015, 2018). Southwest trending landforms between the escarpment and GSL are associated with thrust blocks and do not extend above the escarpment. They show slight variation in orientation to the previously mentioned southwestward flows and are typically shorter than other landforms in the area (Hagedorn et al., 2021b). Below Kakisa Lake, sculpted bedrock features indicate a southwest flow direction on the up-ice side of bedrock knobs with faint crosscutting by a northwest flow direction (Hagedorn et al., 2021a).

Westward (280°) landforms are observed along the western border of the study area (Brown et al., 2011; Fig. 2.7A). Two small westward bedrock features are also observed on the knobs below Kakisa Lake and show similar characteristics to the southwest sculpted bedrock features described above (Hagedorn et al, 2021a). Although westward flows are limited at surface in the study area, westward landforms are more prevalent west of the study area (Bednarski 2008, Brown et al. 2011).

Northwest (305°) landforms were found on the flat low-lying area between the escarpment and the Cameron Hills (Fig. 2.6A). These northwest landforms are subdued on the landscape, likely reworked by GLM, and are found in isolated patches with the largest cluster south of Enterprise (Brown et al., 2011). Younger northwestward-sculpted bedrock features crosscut younger southwestward features on bedrock knobs below Kakisa Lake. Northwest - southeast trending flutes are observed in the northern Cameron Hills and are interpreted as indicating southeast ice-flow direction based on morphology and association with other landforms (Smith et al., 2021). This southeast flow set is local (Fig. 2.6A) and likely related to late-stage ice overtop the Cameron Hills flowing down into the Cameron River Valley.

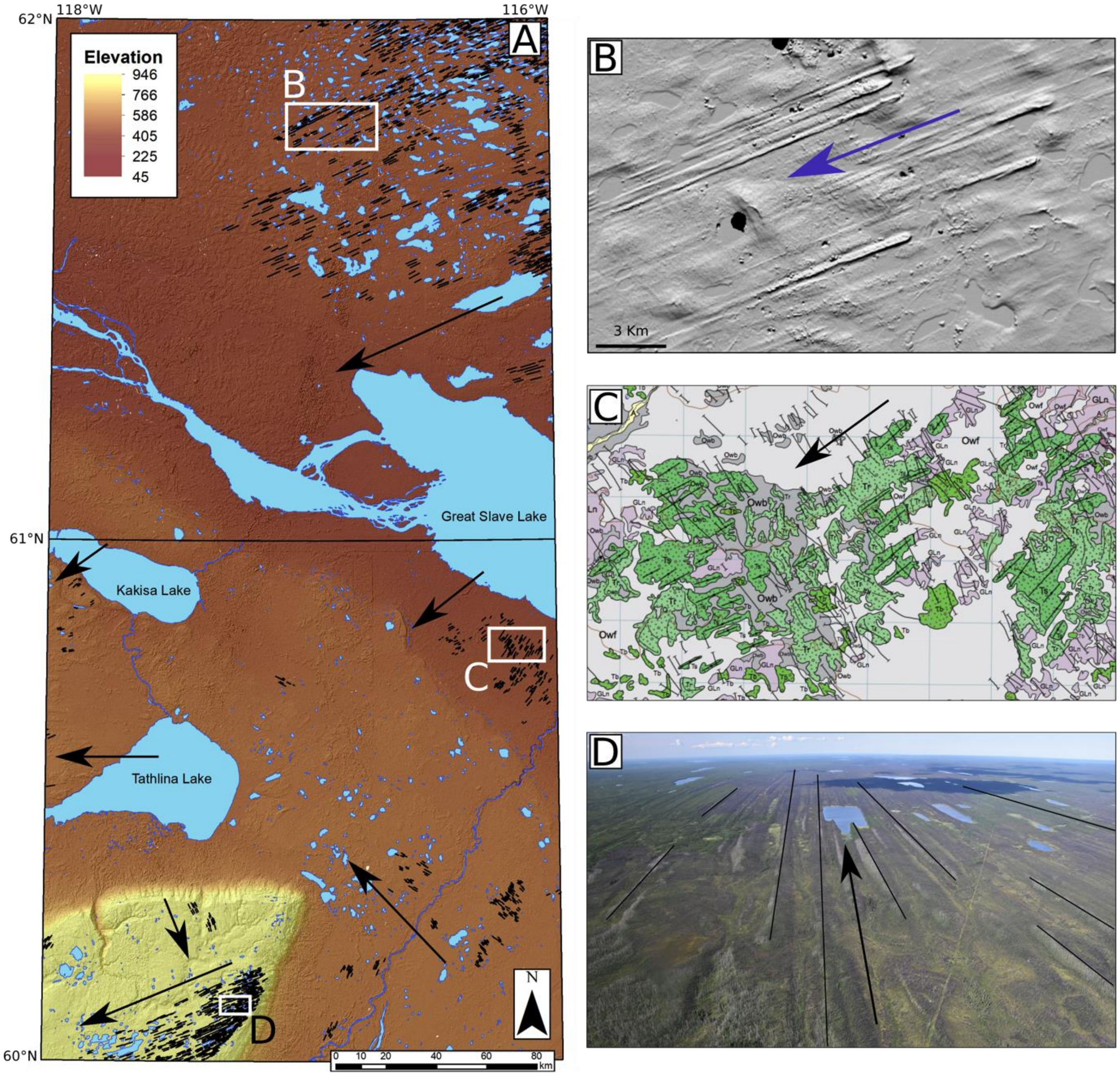

Figure 2.6: A) Landforms in the study area. Background image is 2m resolution ArcticDEM (Porter et al., 2018). Large arrows represent ice-flow directions for the landforms in the surrounding area including B) the southwest (230°) streamlined ridges in the north of the study area, C) between the escarpment and Great Slave Lake and D) on the Cameron Hills. Southwestward flow indicators also occur on the bedrock knobs south of Kakisa Lake. Westward (280°) flow indicators are observed just within the study area west of Tathlina Lake. Northwest (305°) flow indicators occur between the Cameron Hills and the escarpment.

2.4.2 Till stratigraphy and sedimentology

Stratigraphic sections along the Mackenzie River (Fig. 2.2) show two till sheets with a clear stratigraphic contact, distinguishable in the field by their color and degree of compaction or consolidation. The lower till is grey brown with a loamy matrix. It contains 10% clasts and has well-developed fissility. The upper till at the Mackenzie River sections is brown-beige with red brown mottles and has a clayey-silt matrix with 15% clasts. A massive clast-supported gravel cap is found at surface and consists of mainly local limestone lithologies (Fig. 2.8, 2.9). This unit is interpreted to be fluvial in origin.

The two tills are separated by a sheared contact locally defined by discontinuous deformed and well-sorted, massive, coarse sand lenses. A discontinuous boulder pavement also occurs along the contact. Parallel striations on the top surfaces of lodged boulders together with the stoss-lee form indicate a westward (~280°) ice-flow direction (Fig. 2.7, 2.8).

The lowest fabric at section 18-PTA-041 reveals a weak clast fabric (S_1=0.46) and was classified as polymodal girdle (Fig 2.8). This fabric also plots with low isotropy and elongation (Fig. 2.9). The fabric does suggest a possible southwestern ice flow, but it remains uncertain due to the classification and weak S_1. Another fabric was completed at site 18-PTA-035, which is located about 10 km to the west of 18-PTA-041. Only one till was observed at this other site, but it has similar sedimentological characteristics as the lower till of 18-PTA-041. The strong fabric (S_1=0.71) from that till is classified as spread bi-modal, and plots with low isotropy and high elongation (Fig. 2.7, 2.9). The fabric indicates a southwest ice flow direction.

The middle fabric at 18-PTA-041 was completed just above the contact between the two tills. The strength of the fabric is moderate (S_1=0.59), and it is classified as spread bi-modal with low isotropy and intermediate elongation (Fig 2.7, 2.9). The ice flow direction responsible for depositing this fabric is uncertain, but could indicate southwestward ice flow. The uppermost fabric is somewhat stronger (S_1=0.61), shows a clear spread bi-modality, and has a low isotropy and high elongation suggesting ice flow towards the northwest (Fig. 2.7, 2.9).

Another stratigraphic site, where two tills are observed, is located in southern NTS 85C (Site 17-SUV-035; Fig. 2.2). The lower till at this location is light grey, gravelly with <5% sub-rounded to sub-angular clasts of a variety of lithologies, and has a high fissility (Fig. 2.10, 2.11). It is continuous over the exposed area with an observable thickness of 2.5 m, although it pinches out to the north. The clast fabric in the lower till unit is relatively strong (S_1 = 0.65), is classified as spread bi-modal, and has low isotropy and high elongation (Fig. 2.9, 2.10). This clast fabric indicates ice flow towards the southwest. The upper till unit at this location is a dark grey brown clayey-silt till with abundant small platy shale clasts and gravel. 17-SUV-035 is capped by an approximately 0.4 m thick silty sand layer that was observed at several other sites in the flat lying areas of the study area (Fig. 2.10, 2.11).

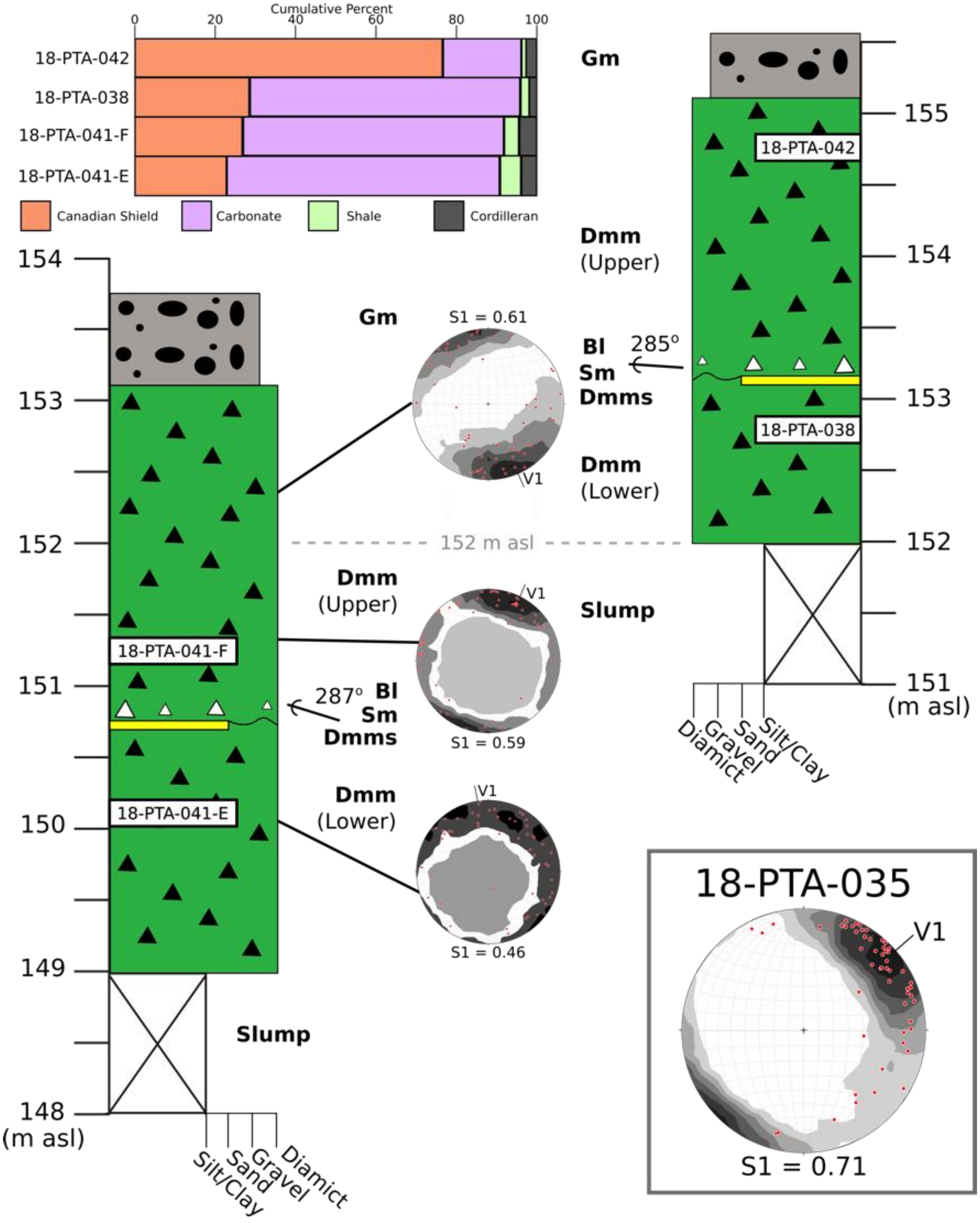

Figure 2.7: Stratigraphic logs from two sections along the Mackenzie River. See Fig. 2.2 for locations. Till samples were collected where sample numbers are labeled and clast lithology counts indicated, see below for geochemistry. Two tills are observed, separated by a sheared contact, and a discontinuous well sorted, massive, coarse sand lens. A discontinuous boulder pavement also defines the contact at the bottom of the upper till unit and records a westward (280°) direction from boulder top striations. The lower till is grey brown, with a loamy matrix, 10% clasts and well developed fissility. Although the lower grey till is characterized by a weak clast fabric at 18-PTA-041 a strong southwest clast fabrics was observed from this till unit 10km to the west (18-PTA-035), and just above the till contact. The upper till unit is brown-beige with red brown mottles and has a clayey-silt matrix with 15% clasts. A clast fabric at the top of this till records a northwest ice-flow direction. A massive clast-supported gravel cap of fluvial origin is found at surface and mainly consists of locally-derived limestone.

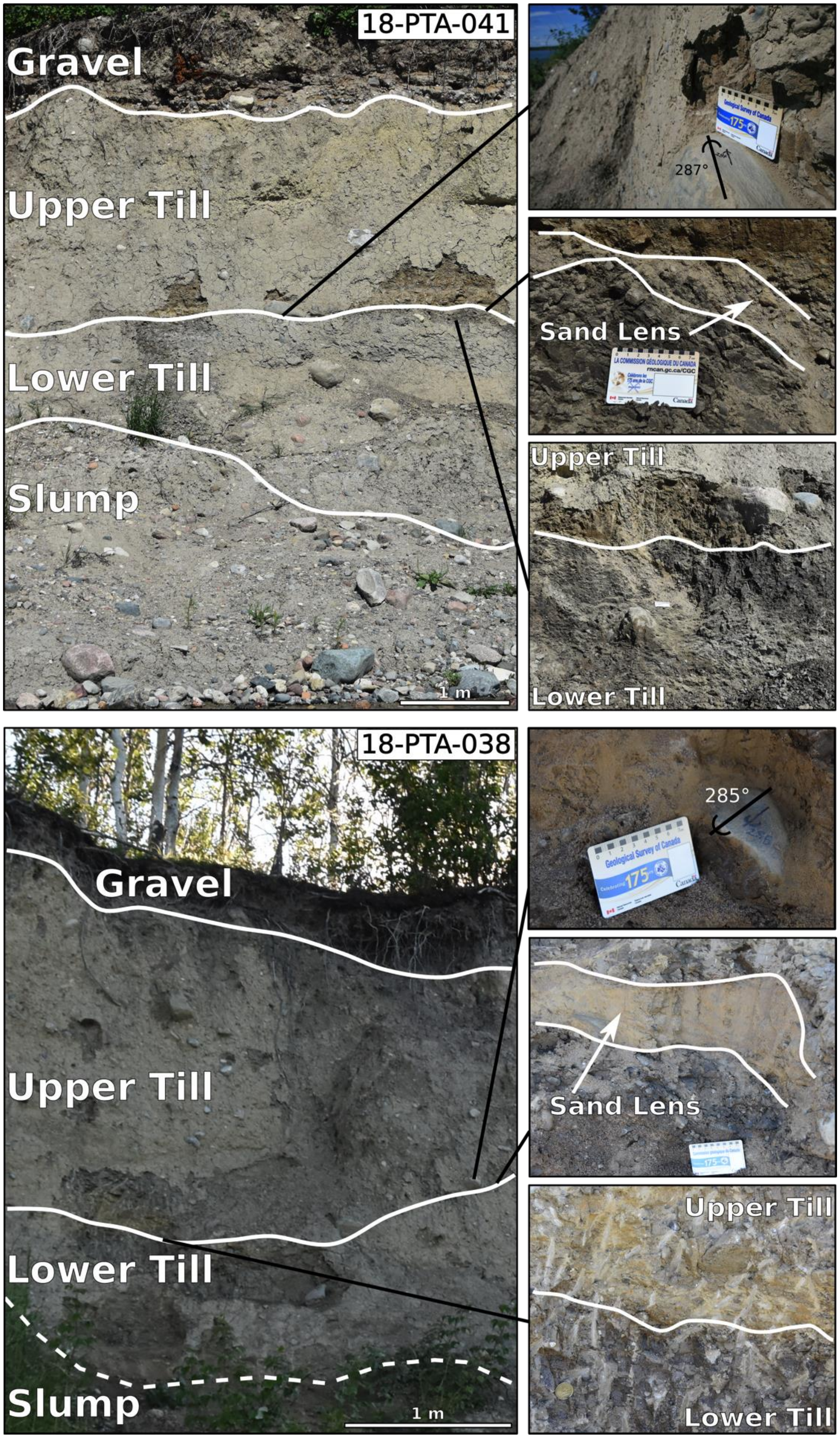

Figure 2.8: Photos associated with stratigraphy at 18-PTA-041 and 18-PTA038.

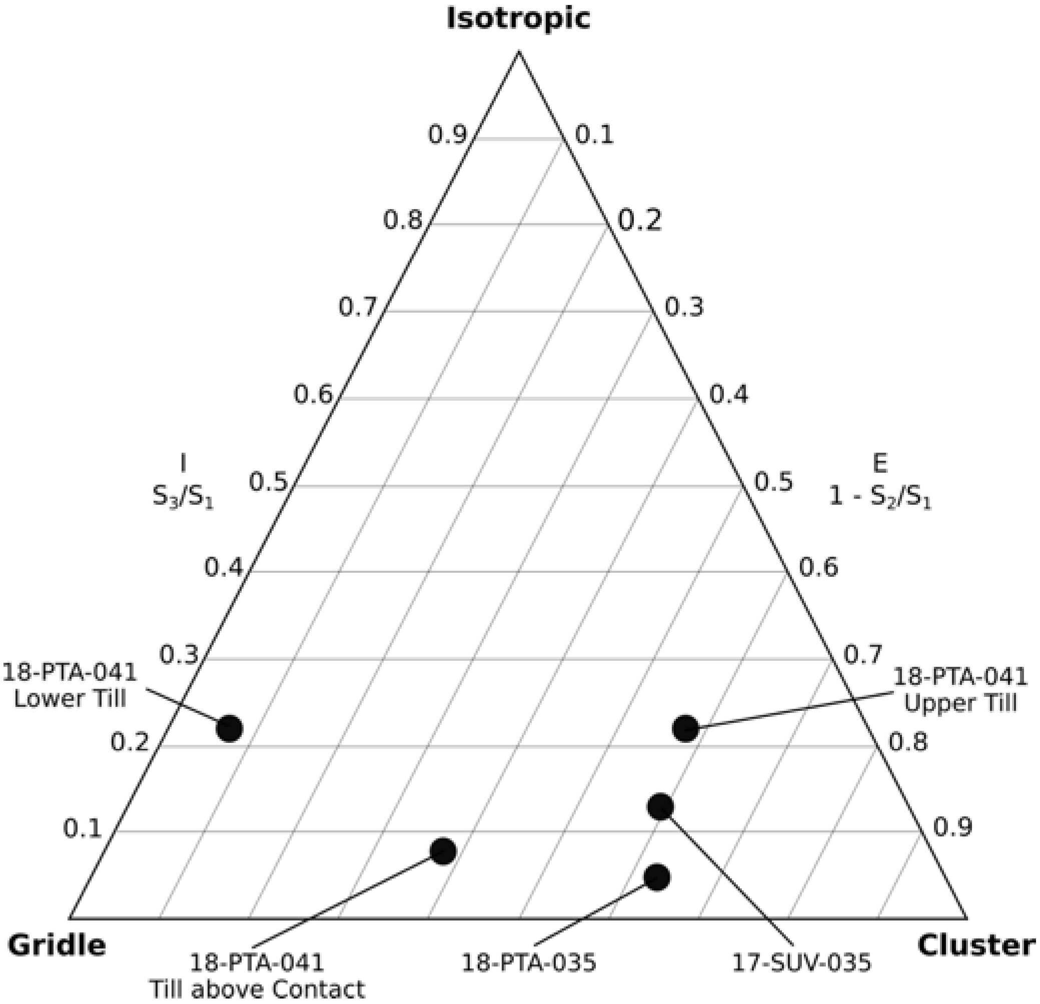

Figure 2.9: Clast fabrics plotted on a isotropy – elongation ternary diagram after Hicock et al., 1996. Most samples plot towards cluster with high elongation and low isotropy, except the ones from 18-PTA-041 section.

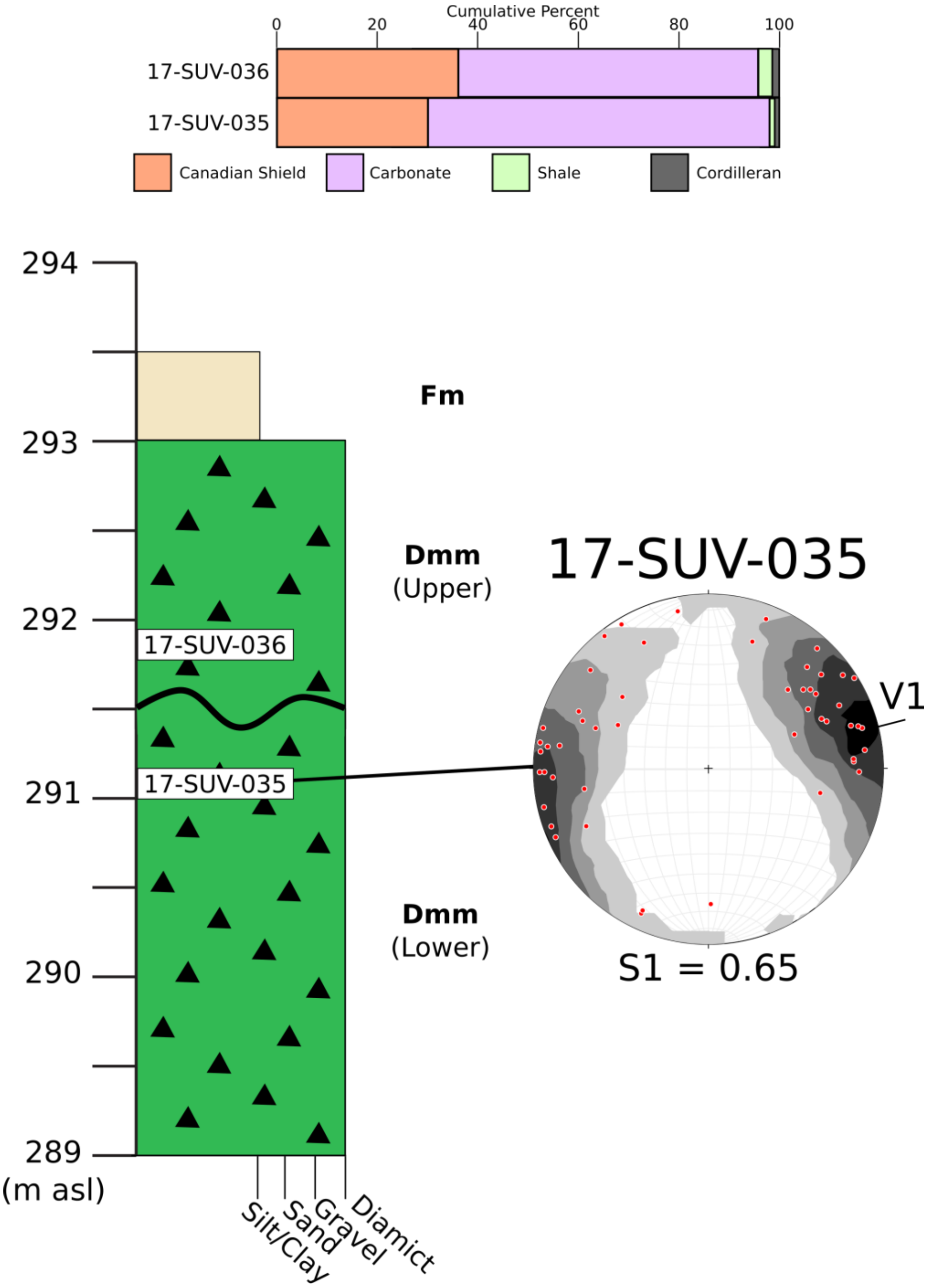

Figure 2.10: Stratigraphic log from a borrow pit in the south of the study area (Fig. 2.2 for location). Till samples were collected where samples numbers are labeled and clast lithology counts indicated, see below for geochemistry. The lower till is characterized by a light grey color and a gravelly texture with <5% sub-rounded to sub-angular clasts, has a high fissility, A clast fabric on this lower till unit gave a southwestward ice flow direction. The upper till unit is a dark grey brown clayey-silt till with ~2% limestone and shield clasts, although the till contains abundant small platy shale clasts and gravel. No boulder lag was found at this site but the contact between till units is undulating. Silty sand caps this site approximately 0.4 m in thickness.

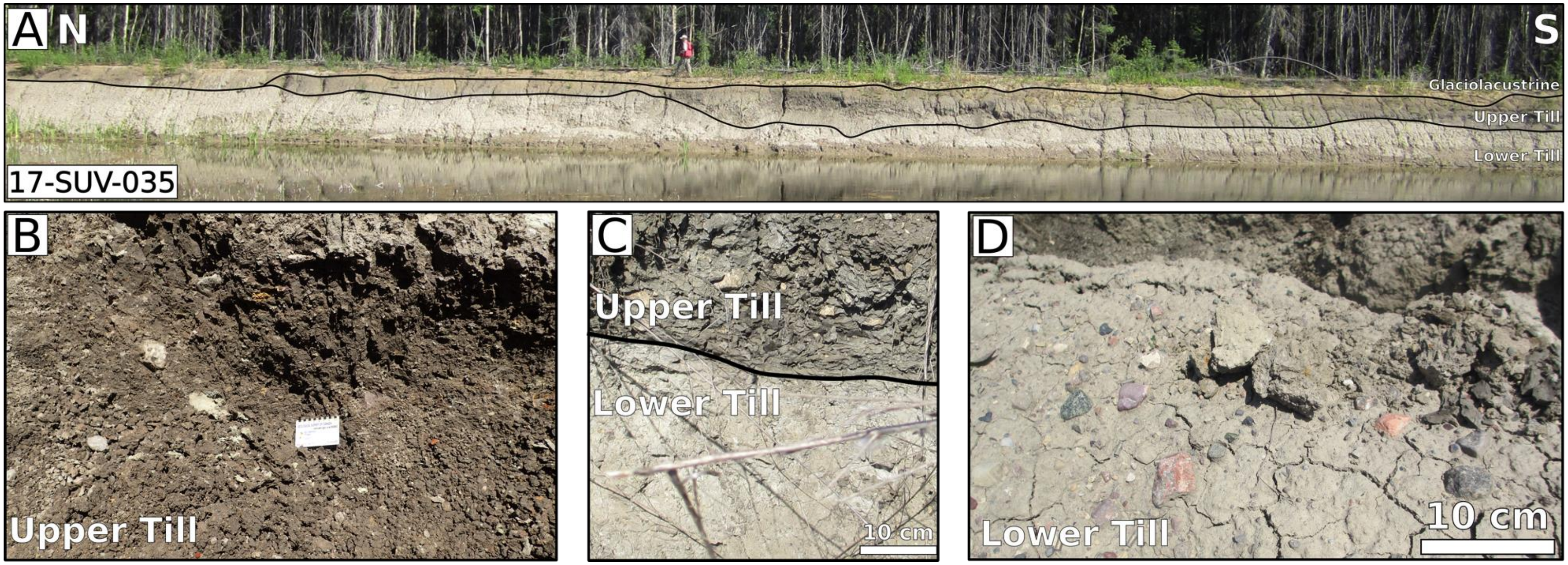

Figure 2.11: A) Lateral extent of till units at the 17-SUV-035 site (see Fig. 2.2 for location). An (B) upper till, (C) till contact, and (D) lower till were observed at the site. The tills are continuous across the borrow pit. The lower till is about 2.5m in thickness, whereas the upper till unit is discontinuous over the site. Its maximum thickness reaches 2m and is pinching out to the north.

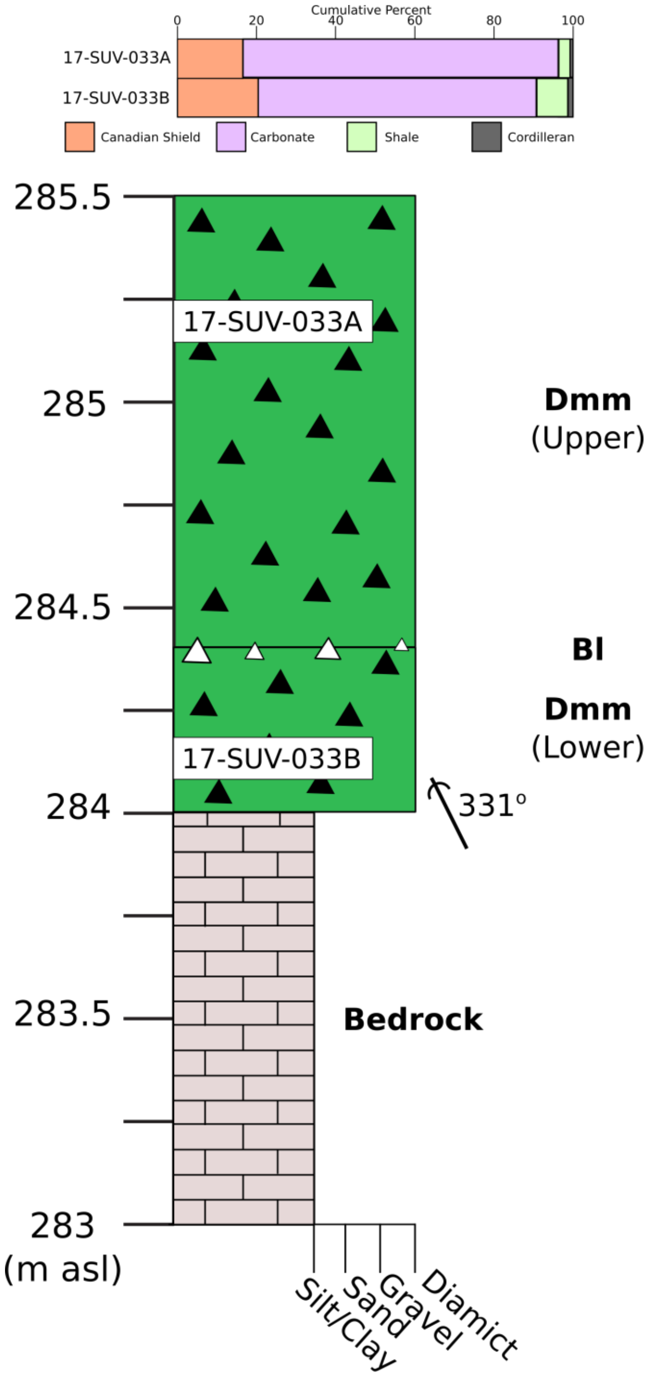

Figure 2.12: Stratigraphic log of a section exposed at a bedrock quarry (17-SUV-033); see Fig. 2.2 for locations. Till samples are labeled and clast lithology counts indicated; see below for till matrix geochemistry. The lower till was a dark gray brown with a silty-sand matrix and 10% clasts containing mixed lithologies. This lower till unit was only 0.2 – 0.35 m thick, lay directly on bedrock, and was difficult to trace across the whole section. Striation measurements from the bedrock surface gave a flow direction of 331°. The upper till unit is ~ 1.2 m thick lighter grey brown diamicton with a silty-clay matrix, and it contains about 10% clasts of almost all angular limestone. A discontinuous boulder lag separates the till units

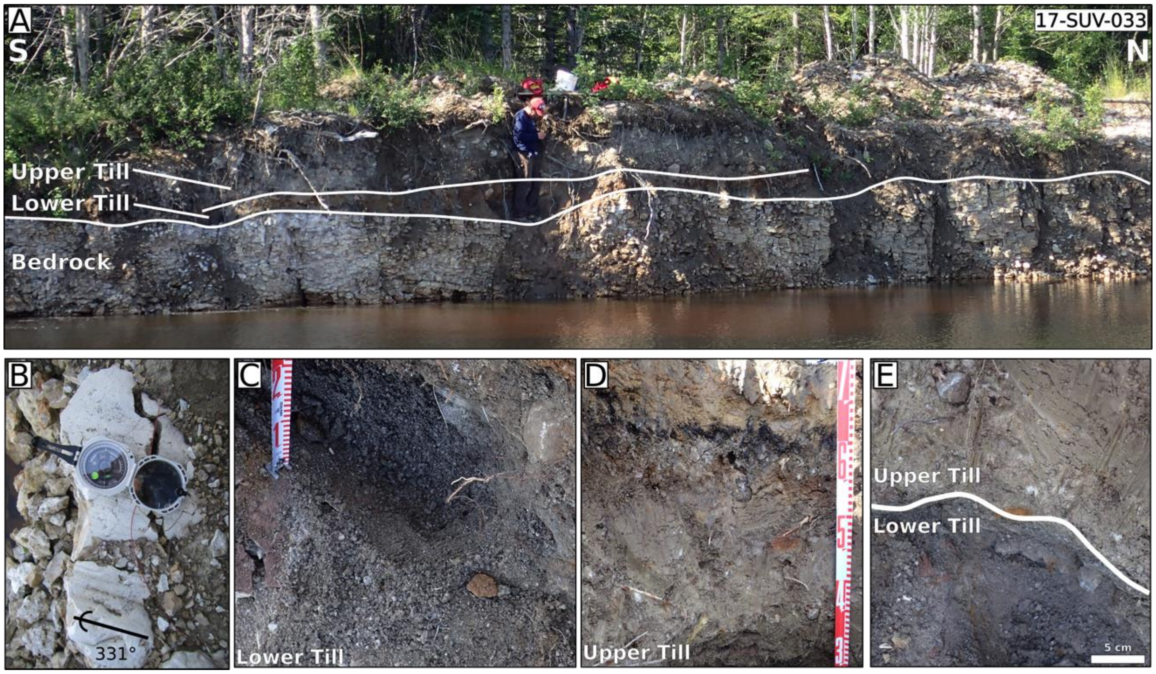

Figure 2.13: A) Overview of the lateral extent of till sheets at site 17-SUV-033, and (B) details of striations, (C, D) till facies, and (E) stratigraphic contact.

The last stratigraphic site also has two tills (17-SUV-033; Fig. 2.12, 2.13). At 17-SUV-033 the lower till is dark gray brown with a silty-sand matrix. This lower till unit is only 0.2 – 0.35 m thick and is lying directly on bedrock. Striation measurements on bedrock exposed at this quarry indicate a northwest (331°) ice flow direction. The upper till unit has a lighter grey brown color, a silty-clay matrix, and contains abundant angular limestone clasts. The upper till is about 1.2 m thick. The contact between the two tills is marked by a discontinuous boulder pavement (Fig. 2.12, 2.13). This site is along the side of a quarry and due to terrain and till thicknesses, it was not possible to obtain boulder top striations or a clast fabric.

2.4.3 Till Composition

2.4.3.1 Till Geochemistry

The PCA indicates that about 95% of the geochemical variability within the data is contained in the first five principal components (Table 2.2). PC1 vs. PC2 was used to display the data as these components explain a large amount of variation within the data (~78%). Furthermore, visual plot comparison of PC1 vs. PC3 against PC1 vs. PC2 did not reveal any important differences and no other PC show any important geological processes. Therefore, only the PC1 vs. PC2 biplot is presented and interpreted herein (Fig. 2.14). Samples with negative PC1 scores have higher MgO and CaO content, whereas SiO2, Al_2O_3, TiO_2 and Cr_2O_3 form a geochemical assemblage with positive PC1 scores. Fe_2O_3 and K_2O are in the positive PC1 space, but also appear to influence PC2. More clearly, PC2 separates Na_2O (negative) against MnO (positive). A summary of the loading values for the major oxides is given in Figure 2.15.

The elemental associations are further supported by the correlation matrix (Table 2.2). Strong positive relationships are observed between groups formed by CaO-MgO, and by SiO_2-Al_2O_3-Fe_2O_3-TiO_2-Cr_2O_3; which is the PC1 component. These two groups have strong negative correlations to one another. In the PC2 component, Na_2O has weak correlations to other elements, with the strongest being -0.42 and -0.50 to CaO and MnO, respectively (Table 2).

The first classification scheme, k-means clusters, is shown on the PC biplots (Figure 2.15A), as well as spatially (Figure 2.17A). The clusters have a group with high CaO, MgO and MnO and low Na_2O (Cluster 1, red), a cluster in the center of the PCA with a mix of all major oxides (Cluster 2, blue), a cluster with higher CaO and MgO and high Na_2O (Cluster 3, green), and a cluster with low CaO and MgO, high SiO_2, Al_2O_3, Fe_2O_3, K_2O, TiO_2, and Cr_2O_3 and moderate Na_2O (Cluster 4, orange).

Table 2.2: Percent and cumulative percent of the Principle Components (PC).

	Percent	Cumulative Percent
PC1	60.08	60.08
PC2	18.21	78.29
PC3	7.832	86.13
PC4	5.627	91.75
PC5	3.201	94.95
PC6	2.567	97.52
PC7	1.28	98.8
PC8	0.9682	99.77
PC9	0.2313	100
PC10	1.58E-19	100

The geographic classification scheme shows a similar trend to that of the k-means clusters (Fig. 2.14C, 2.16B). The escarpment class is similar to that of Cluster 1, the middle class is similar to Cluster 2, the northern class is similar to Cluster 3, and the Cameron Hills class is similar to Cluster 4 (cf. Fig. 2.14A). Divergence between the classification schemes exists as some samples of the Middle class plot with Cluster 4 field typically associated with the Cameron Hills.

The final classification scheme, underlying bedrock geology, is also shown (Fig. 2.14E, 2.16C). The underlying bedrock classification on the PCA shows the Mesozoic class (green) plots similarly to Cluster 4 (cf. Fig. 2.14A), but the Paleozoic classes (purples) do not show any obvious trends other than broadly plotting together within the Cluster 1, 2 and 3 areas.

Additionally, plotting of the stratigraphic samples on the PCA shows a trend between samples collected at the same site (Fig. 2.14F). For three of the four stratigraphic sites, the lower till has a more positive PC1, whereas the upper till plots in the negative PC1 space. This indicates enrichment in CaO and MgO moving up the stratigraphic column. The one outlier to this trend is the section at 18-PTA-042 where the trend reverses and the tills become more positive in the PC1 space moving up the stratigraphy.

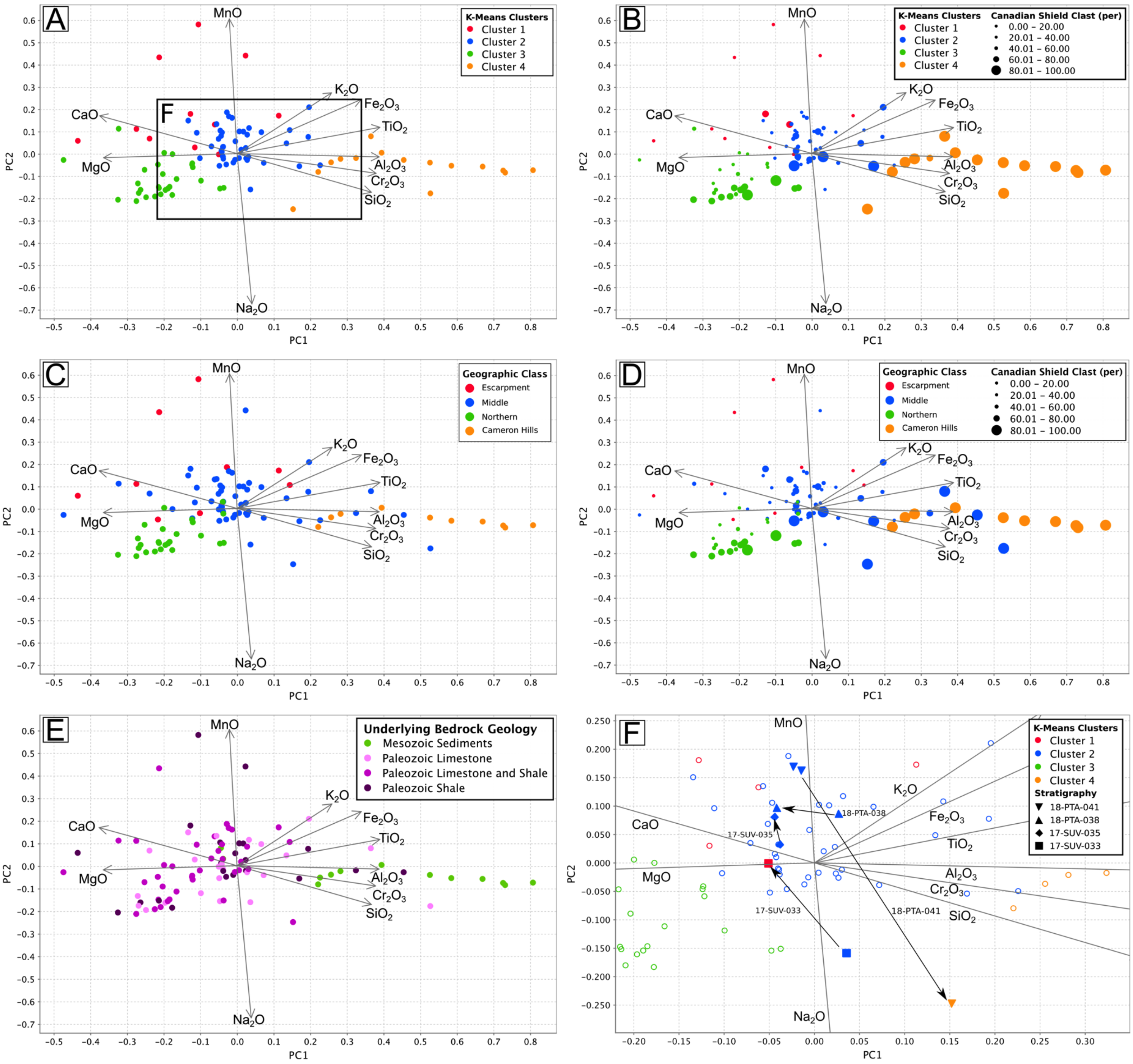

Figure 2.14: PCA Plots with A) K-means clusters, B) K-means clusters with Canadian Shield clast percentage, C) Geographic classes, D) Geographic Classes with Canadian Shield clast percentage, E) Underlying bedrock classes, F) inset from A showing stratigraphic section samples. Arrows point from lower till sample to upper till sample.

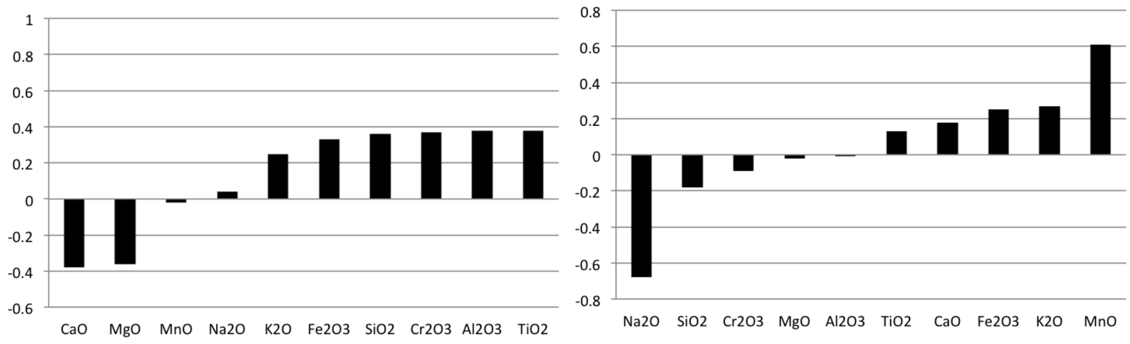

Figure 2.15: PC loading scores for major oxides included in the PCA. PC1 has strong negative scores for CaO and MgO and strong positive scores for SiO_2, Al_2O_3, Fe_2O_3, TiO_2, and Cr_2O_3. PC2 has a strong negative score for Na_2O and a strong positive score for MnO. All other elements within PC2 show moderate to weak loadings.

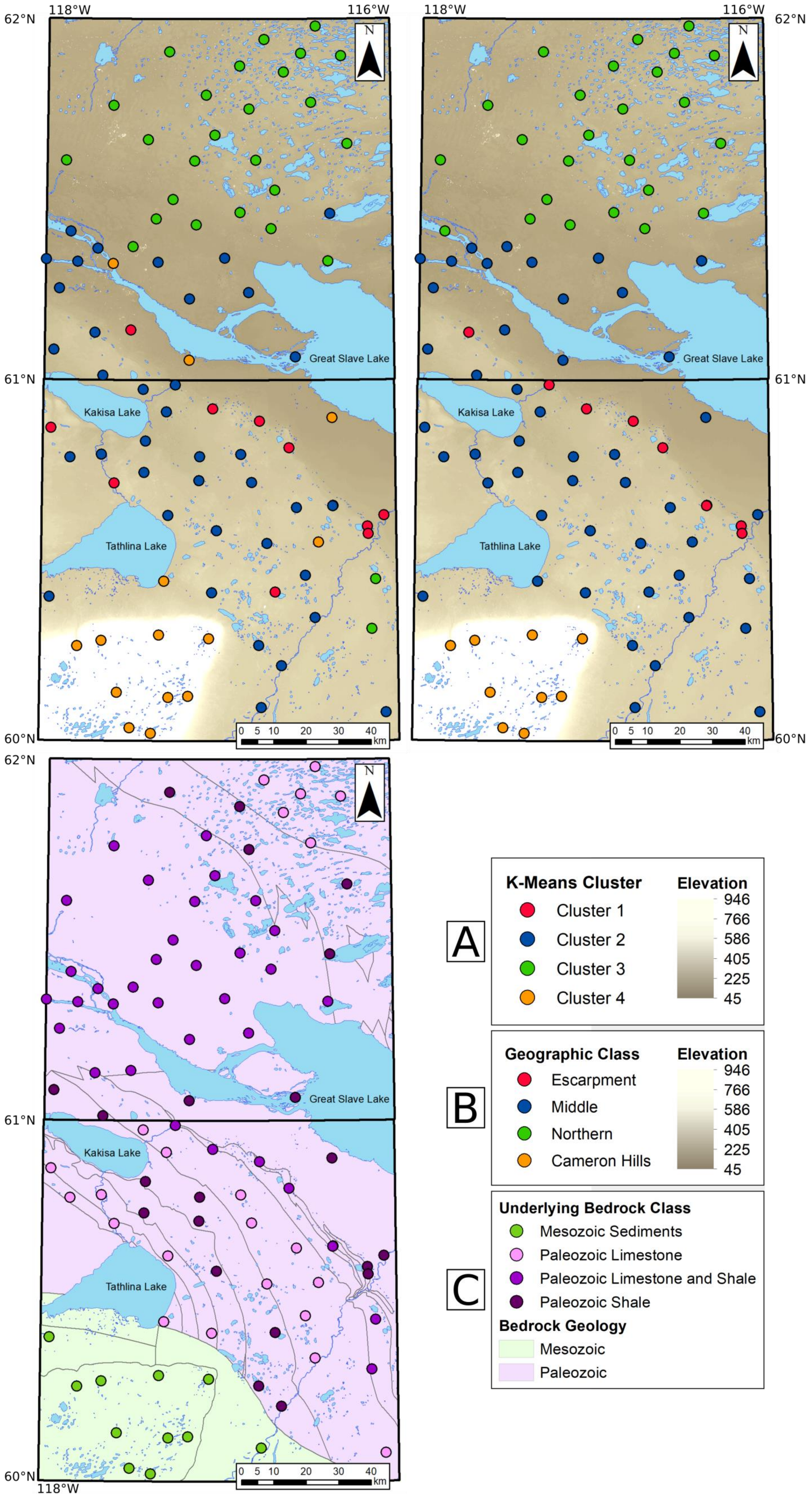

Figure 2.16: Classification Schemes. A) K-means clusters with DEM background. Cluster 1 is red, Cluster 2 is blue, Cluster 3 is green and cluster 4 is orange. B) Geographic classes applied to the till samples through the study area. Background image is the 2m resolution Arctic DEM (Porter et al., 2018). The classification scheme includes samples collected along the bedrock escarpment (red), the middle flat low lying areas (blue), the northern areas with southwest trending landforms (green) and the Cameron Hills upland region with southwest trending landforms (orange). C) Bedrock geology classes applied to the till samples throughout the study area. Background image is a simplified bedrock geology based on age of deposition; boundaries between formations can still be observed (Okultich, 2006). Classes include the Mesozoic sediments (green), Paleozoic formation of primarily limestone (light purple), Paleozoic formations of split limestone and shale (purple) and Paleozoic formation of primarily shale (dark purple). The Paleozoic was split into three classes including all the formations and did not succinctly show trends within the data.

Table 2.3: Correlation matrix of major oxides included within the PCA.

Correlation	SiO_2	Al_2O_3	Fe_2O_3	MgO	CaO	Na_2O	K_2O	TiO_2	MnO	Cr_2O_3
SiO_2	1	0.7561	0.6471	-0.7739	-0.8297	0.2394	0.3382	0.8831	-0.214	0.7508
Al_2O_3	0.7561	1	0.6753	-0.789	-0.8266	0.07267	0.691	0.8524	-0.1387	0.8561
Fe_2O_3	0.6471	0.6753	1	-0.6828	-0.7192	-0.1643	0.4661	0.8014	0.2602	0.691
MgO	-0.7739	-0.789	-0.6828	1	0.6975	-0.07161	-0.4344	-0.8059	-0.03038	-0.8158
CaO	-0.8297	-0.8266	-0.7192	0.6975	1	-0.4198	-0.5	-0.7763	0.07663	-0.8168
Na_2O	0.2394	0.07267	-0.1643	-0.07161	-0.4198	1	-0.2577	-0.1244	-0.4985	0.1609
K_2O	0.3382	0.691	0.4661	-0.4344	-0.5	-0.2577	1	0.5602	0.1021	0.511
TiO_2	0.8831	0.8524	0.8014	-0.8059	-0.7763	-0.1244	0.5602	1	0.02673	0.7904
MnO	-0.214	-0.1387	0.2602	-0.03038	0.07663	-0.4985	0.1021	0.02673	1	-0.1663
Cr_2O_3	0.7508	0.8561	0.691	-0.8158	-0.8168	0.1609	0.511	0.7904	-0.1663	1

2.4.3.2 Till Clast Lithology Counts

Clast lithology counts show different composition between tills spatially and stratigraphically. Generally, three compositional groups were observed within the data set. One group is characterized by a large (> 70%) Canadian Shield component and a low carbonate (Paleozoic) content. These tills are typically the lower tills at stratigraphic sites, but some are surface samples from the Cameron Hills and the lowland regions. It is important to note that samples within this group, especially atop the Cameron Hills, could have a high Mesozoic shale component that was lost during the processing of the till samples due to the shale's weak an friable nature (Paulen et al. 2007). These small clasts are observed in thin sections from the top of the Cameron Hills (Paulen, 2021 Pers. Comms.)

Another group observable within the clast lithology data include samples with ~ 70% carbonate (Paleozoic) and 30% Canadian Shield material. These samples have less than 5 % shale (Mesozoic) and Cordilleran clasts. Samples within this group are typically from surficial till samples throughout the lower lying regions of the study area. This till clast composition is the most common in the dataset.

Finally, a group with almost exclusively (> 80%) local angular carbonate (Paleozoic) clasts is also identified. This group includes samples in close proximity to the escarpment. This is the smallest till clast composition in the dataset.

2.4.3.3 Data integration – Pebble lithology vs. till matrix geochemistry

Here the pebble lithology counts and till matrix geochemistry are combined. There is a clear relationship between clast lithological composition and Cluster 1 and Cluster 4 of the till matrix geochemistry. Cluster 1 (CaO-MgO-MnO) has a low proportion of Canadian Shield clasts and a high proportion of carbonate (Paleozoic) clasts (Fig. 2.17). Cluster 4 (SiO_2-Al_2O_3-Fe_2O_3-K_2O-TiO_2-Cr_2O_3) shows the opposite relationship; high Canadian Shield and low Carbonate (Paleozoic) rocks, but with input from the underlying Mesozoic shale bedrock influencing the till matrix composition. Clusters 2 and 3 have similar proportions of both Canadian Shield and carbonate (Paleozoic) clasts, with a higher carbonate percentage (~70 %). Shale (Mesozoic) and Cordilleran lithologies are typically less than 5% and no clear trends are identified within the dataset (See Appendix E for full clast lithology counts).

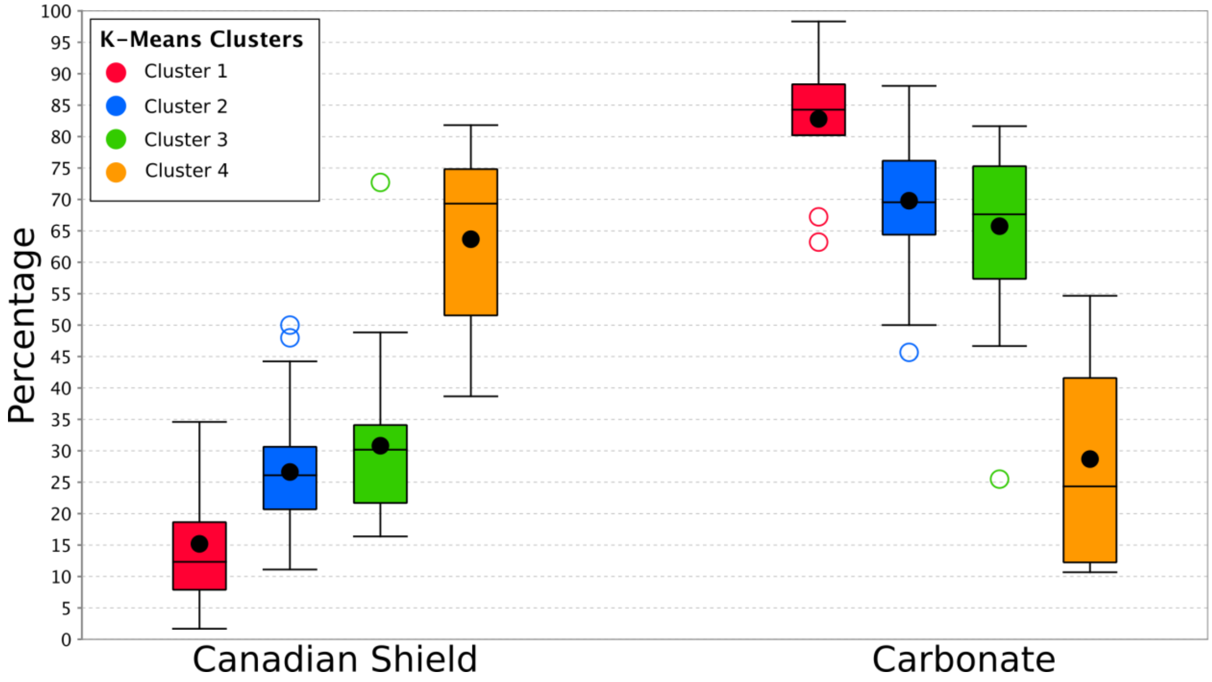

Figure 2.17: Box plots of the Canadian Shield and carbonate (Paleozoic) clast percentages based on Clusters.

Plotting the Canadian Shield clast percentage on the PCA allows further exploration into the potential relationship with till matrix geochemistry (Fig. 2.14B, 2.14D). Samples that plot more negative in PC1 have lower Canadian Shield percentages. When the geographic classification scheme is used the escarpment has the lowest percentages of Canadian Shield clasts (again plotting most negative in PC1 space) and the Cameron Hills have the highest percentages (similar to the box plots of the Clusters). The relationship with the 'Middle' and 'Northern' groups is more complex. A few surficial samples belonging to the 'Middle' and 'Northern' classifications have high Canadian Shield clast content, similar to the Cameron Hills classification. Interestingly, most of the samples from the 'Middle' group with a high Canadian Shield content plot in the same PC1-PC2 space as the Cameron Hills samples, and together form Cluster 4 group of samples.

Furthermore, CaO/Al_2O_3 ratio has been used as a proxy for determining the contribution of carbonate versus calcic feldspar in the till matrix (e.g. Ross et al., 2011). Here, the CaO/Al_2O_3 is used in a similar way and compared against the proportion of Canadian Shield clasts (Fig. 2.18). There is an inverse relationship between the CaO/Al_2O_3 ratio and Canadian Shield clast content indicating less

CaO from carbonate sources for Cluster 4 to a more carbonate source for CaO that is depleted in Al (Cluster 1).

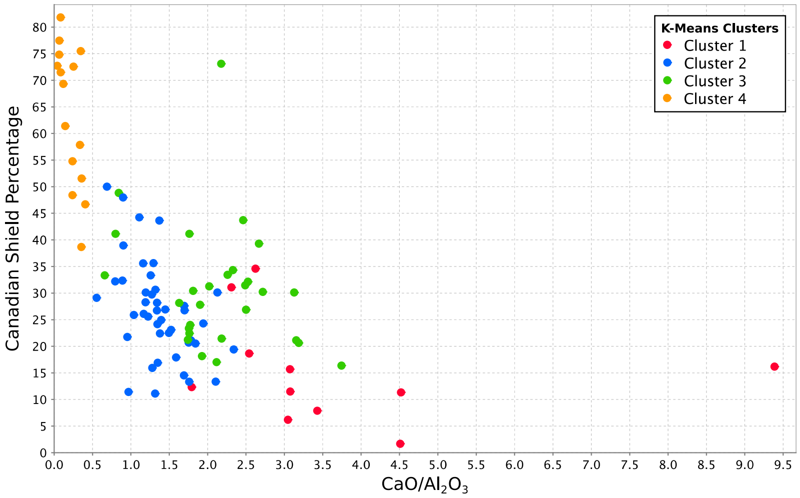

Figure 2.18: CaO/Al_2O_3 ratio versus Canadian Shield clast percentage. As the CaO/Al_2O_3 ratio increases the Canadian Shield clast percentage decreases.

2.5 Discussion – Paleo-ice flow reconstruction

2.5.1 Southwestward (230°) Ice Flow Phase

The southwestward ice-flow phase is the oldest preserved in the study area as evidenced by the oldest striations found on the escarpment, commonly crosscut by features of the younger westward and northwestward flows (Fig. 2.6). Additionally, southwest striations are often found with no crosscutting on bedrock surfaces covered by till. Similarly protected striated outcrops have been used to constrain older ice flow phases in other sectors of the LIS (McClenaghan et al., 2018; Rice et al., 2019; Gauthier et al. 2020).

The stratigraphic record also provides supporting evidence that the southwestward flow is the oldest preserved in the study area. The fabrics completed on the lowermost tills at 18-PTA-035 and 17-SUV-035 both indicate a southwestward flow (Fig. 2.8, 2.11). Note that bedrock does not outcrop at these locations, which means that it is uncertain whether the lower till is the one directly overlying bedrock. Nonetheless, the combination of oldest southwestward ice flow indicators and lowermost observed till with southwest-trending fabrics suggest a correlation to the same southwest ice flow phase.

The southwest-trending subglacial lineations atop the Cameron Hills form a flow set that is herein correlated to that same oldest southwest flow phase. This flow set is on a surface that is approximately 450 meters above the surrounding terrain and the landforms within it are straight parallel (Fig. 2.7) suggesting limited (if any) topographic influence. A relatively thick ice sheet is thus required to produce such a flow set. Outside of the Cameron Hills flow set, southwest-trending glacial lineations on isolated bedrock knobs southwest of Kakisa Lake and in the northern extent of the study area (Fig. 2.7) are also correlated to this oldest southwestward flow phase.

Indicators of southwestward flow are also found in the region surrounding the study area. Striations along an escarpment west of the study area indicate an oldest southwest flow (Paulen et al. , 2019) and landforms surrounding Trout Lake, also to the west of the study area, have a southwest direction (Bednarski 2008). There is thus extensive evidence for a regional southwest ice flow phase that preceded all the other observed ice flows.

Regionally, reconstructions of the western LIS indicate an old southwestward flow related to a time when the LIS - CIS coalesced and split LIS flow along the convergence southwest and northwest with the direction related to the Plains Ice Divide (Bednarski, 2008). The most recent estimates indicate that separation between the ice sheets occurred around 14.9 cal. ka BP (Dalton et al., 2020; Norris et al., 2021). The flow set on top of the Cameron Hills (Ice Stream #145) was tentatively placed at about 13.9 cal. ka BP by Margold et al. (2018), but the timing of this flow set remains poorly constrained. The fragmented nature and the elevation of the flowset, and the lack of topographic influence on the MSGLs suggest that the paleo-ice stream that formed the Cameron Hills flowset could be older than previously suggested due to the requirement for thick ice.

Till characteristics and composition also indicate subglacial sediment entrainment towards the southwest. Firstly, fabrics from the lowermost tills observed are consistent with sediment transport towards the southwest. Secondly, the composition of the lowermost till is consistent with an increased quantity of northeast provenance associated to the Canadian Shield. Clast lithology counts from the lower tills at stratigraphic sites show clear evidence for distal provenance. Furthermore, the lower tills have a relatively low CaO and MgO content from local carbonates, and a higher content in the distal Canadian Shield pathfinders including SiO_2, Al_2O_3, Fe_2O_3, TiO_2, and Cr_2O_3 (Parker and Fleischer, 1967; Cameron, 1969; Qing and Mountjoy, 1994; McLennan, 2001; Normandeau et al., 2015; Fig 2.15). The lower till is thus confidently attributed to a southwestward ice flow direction, which dispersed material over a large distance down-ice.

The surficial till on the Cameron Hills is similar in composition to a few locations in the lower lying areas (Fig. 2.15). For instance, surface till samples collected within the southwestward MSGL's atop the Cameron Hills have a high Canadian Shield content similar to the lower till. However, these samples also have a Mesozoic shale component that is not accounted for within the clast count data. The mudrock geochemical signature is also difficult to distinguish from a shield signature because the two have a relatively similar, or largely overlapping major oxides' composition (Parker and Fleischer, 1967). Nonetheless, what is most striking about this till is the low Paleozoic carbonate content, which represents a large proportion of the bedrock in the dispersal area to the northeast. This means it was a till with a high initial Canadian Shield composition (distal provenance) that only started incorporating rock detritus southwest of the Canadian Shield domain when it encountered the mudrocks of the Cameron Hills. This till is therefore correlated to the lower till, which is the till with a distal provenance signature, and both are interpreted to have been produced by a strong southwestward flow, i.e. a paleo-ice stream. On the basis of the above evidence, and together with relative age relationships, it is proposed that the lower till and the surficial till associated with southwest-trending MSGLS with a similar geochemical signature and Canadian Shield clast content belong to the same till sheet, which was deposited during a strong, ice streaming southwest ice flow phase.

There is also clear stratigraphic evidence that the lower till intersects the surface in some places, which reinforces the idea that some flowsets on the landscape are relict surfaces associated to that till. The best example of this is found at 17-SUV-035 (Fig. 2.12). The upper till is discontinuous and pinches out to the north where the lower till is found closest to surface. The spatial patchwork of different tills at surface conforms to the current understanding of the subglacial environment with different levels of erosion and deposition due to shifting subglacial conditions both spatially and temporally (Piotrowski et al. 2004, Gauthier et al. 2019, Menzies et al. 2019).

2.5.2 Westward Ice Flow (280°)

As the ice margin retreated eastward and thinned it became more topographically controlled (Bednarski 2008, Paulen et al. 2011). The Mackenzie River Valley is an extensive topographic feature west of the study area that channeled ice to the west-northwest as the ice margin entered the valley

(Craig 1965, Lemmen et al. 1994, Bednarski 2008, Dalton et al. 2020). Other topographic features like upland regions also had an influence on ice flow directions of the retreating ice sheet. The Horn Plateau, Cameron Hills, and Caribou Mountains split and focused ice down the lowland areas between them.

In the study area, evidence for westward ice flow was found along the escarpment (i.e. striations) and boulder-top striations from stratigraphic sites along the Mackenzie River. Outcrop-scale indicators of westward flow from the escarpment all postdate evidence for southwestward flow, but predate indicators of northwestward flow (Fig. 2.6). The boulder top striations from stratigraphic sites along the Mackenzie River also show evidence of westward ice flow at the contact between the two till units (Fig. 2.8). This westward ice flow phase is thus an intermediate ice flow phase that followed the southwest phase and preceded the younger phases.

Evidence for westward flow from the landform record is limited in the study area. Westward-trending glacial lineations occur along the western border of the study area, close to Tathlina Lake, and continue into the lowlands to the west (Fulton 1995, Bednarski 2008, Brown et al. 2011). More pronounced westward landforms are found to the west below Mackenzie Highway 1 and are associated with westward striations observed on a bedrock escarpment (Bednarski, 2008; Paulen et al. 2019).

Westward landforms are more isolated and smaller than landforms created by the older southwestward flow. Additionally, this westward flow did not obliterate records of the oldest southwest flow. Due to its limited influence on the landscape and stratigraphic record this westward flow was weaker and shorter-lived. Finally, this flow possibly did not affect the whole study area as ice had become thin enough to form ice lobes in the valleys, leaving higher terrain, like the Cameron Hills ice free (Bednarski 2008, Paulen et al. 2011, Dalton et al. 2020).

The till composition data shows the effect of re-entrainment and mixing of tills during the westward phase. The ‘mixed’ upper till is represented by the middle grouping of clast composition (70% carbonate from the Paleozoic strata and 30% Canadian Shield clasts). Similarly for the till geochemistry, Cluster 2 is a typical hybrid till from a compositional point of view; it is between the till compositional end-members (Fig. 2.15A). This trend is also observed in the CaO/Al_2O_3 ratio (Fig 2.18).

The stratigraphic sections support the mixing and incorporation of the lower till material into the upper. A sheared contact is found at many sites where lower and upper tills are in contact indicating that the lower till was at least partly eroded and re-entrained by younger flows. This situation led to incorporation of lower till material into at least the lower portion of the upper till (Boulton, 1996; Menzies et al., 2019; Fig. 2.11, 2.12), something referred to as compositional inheritance (e.g. Stea and Finck, 2001; Trommelen et al., 2013). The compositional similarities within the clast counts at stratigraphic sites are evidence of this inheritance (Fig. 2.8 and 2.11). The geochemical data between till samples at the stratigraphic sites also supports the transition in till composition. The upper till samples have a more negative PC1 than the lower till indicating a shifting till composition to more local Ca and Mg sources (Fig. 2.15F).

The apparent reduction in Canadian Shield material is twofold for the upper till. Firstly, the possible Mesozoic shale source areas are limited to northeast of the Cameron Hills and therefore not diluting the upper tills. Secondly, to the east, the distance to the Canadian Shield boundary is approximately 250 km, compared to 80 km to the northeast (Fig. 2.1B). Therefore, during the streaming ice of the southwestward flow, transport distance for Canadian Shield clasts was shorter than during the westward flow allowing more distance for incorporation of Paleozoic carbonate material.

The separation of Clusters 2 and 3 is due to their different Na_2O content and is related to this westward flow (Fig. 2.15A). The source of the Na_2O for Cluster 3 is the hypersaline beds of the WCSB (Fig. 2.1A). These beds are located all along the east of the study area, but due to the strike and dip of the beds, they are closest to the study area in the northeast. As the ice became more channelized down the Mackenzie River Valley during the westward ice flow phase, it transported material from these beds into the study area’s northern portion. The lack of a Na signature over the rest of the study area is due to the properties of hypersaline minerals like halite, which quickly disaggregate and/or dissolve over a short glacial transport distance; in other words, they do not travel far within the subglacial environment (Dreimanis and Vagners 1974, Shilts 1984, Menzies et al. 2018). Interestingly, two samples on the eastern margin of NTW 85C plot within Cluster 3, and would be the closest samples to these hypersaline units to the east in the southern part of the study area (Fig. 2.17A).

Another possible explanation for the increased Na in Cluster 3 is from Canadian Shield minerals, like plagioclase feldspars. This explanation is not supported by the data. Specifically, Cluster 3 is depleted in elements associated with a Canadian Shield source like SiO_2, Al_2O_3, Fe_2O_3, TiO_2, and $Cr_2O_{3,\ \text{which}}$ are enriched in the Cluster 4 assemblage. In addition, the CaO/Al_2O_3 ratio suggests mainly a local source for the Ca (Fig 2.15A; 2.19). Clast lithology counts between Cluster 2 and 3 are almost identical further supporting limited Canadian Shield contribution to the Na concentration in those till samples (Fig. 2.18). There is thus compelling evidence for the hypersaline WCSB beds to be the main source of Na in the Cluster 3 till.

2.5.3 Northwestward Ice Flow (305°)

As the ice margin retreated further east the channeling effects of the Mackenzie River Valley became more pronounced. The channeling continued to rotate the flow further clockwise to the northwest, which was the final ice flow phase for much of the study area (Lemmen et al. 1994). This was a discrete flow of relatively thin ice with limited erosion and sediment transport, especially outside the Mackenzie River Valley. However, within the study area, there is clear evidence of this phase in the outcrop-scale erosional features, and in the landform and sedimentary record.

Outcrop-scale ice-flow features indicating northwest flow are the youngest found along the escarpment (Fig. 2.6). The landform record for the northwest flow is limited to isolated patches in the center of the study area (Fulton 1995, Brown et al. 2011). These landforms are smaller, often subdued and discontinuous as a result from being inundated by GLM (Fig. 2.7). The northwestward flow’s effect on the landscape was likely limited, again, owing to the limited capacity of a thin lobe to erode and entrain sediment. The lobe also had a small spatial extent at a time when the margin was closer if not within the study area.

One clast fabric from just below the upper till top contact at 18-PTA-041 (Fig. 2.8) indicates a clear direction of shear towards the northwest. Another till fabric completed near the lower contact, with lodged boulders indicating ice flow towards 287°, is weakly indicative of southwest ice flow. However, this lower fabric shape shows considerable spread, which makes ice flow interpretation uncertain; the fabric should thus not be used for that purpose. The more reliable data, the striated boulder at the lower contact and the upper strong fabric together record a simpler and more gradual shift in ice flow as the Mackenzie River Basin began channeling more ice.

The northwest ice flow rotation did not have a major influence on till provenance. The mixing continued as described above, and contributed to the final composition of the upper till (Clusters 2 and 3). Overall, Clusters 2 and 3 were deposited as the ice flow shifted from westward (the boulder top striations at the contact between the two tills) to northwest (clast fabric from the top of the till unit). Note that ice flow in the north of the study area that is flowing into the Mackenzie River valley was not as much to the northwest as elsewhere due to the funneling affect. Finally, it is possible that most of the upper till was deposited during the westward phase and only later; its top portion was sheared by the northwest ice flow. More detailed fabric work and provenance fingerprinting would be required to verify this.

The geochemical data also indicates that an isolated high local content till was deposited (Cluster 1) during the final stages of deglaciation. This cluster is characterized by high CaO and MgO and low SiO_2, Al_2O_3, Fe_2O_3, TiO_2, and Cr_2O_3, and the related till has a high proportion of Paleozoic carbonate clasts (Fig. 2.15A, 2.18). These samples are located in close proximity to the bedrock escarpment, where plucking would have been enhanced (Boulton 1996, Krabbendam and Glasser 2011, Pedersen et al. 2014). Thin ice is less erosive, but could still lead to plucking where jointed and irregular bedrock outcrops, especially under fluctuating effective pressures (Hallet 1996; Iverson et al. 1995). The interpretation of this Cluster 1 till is that final ice flow phases were weaker, but locally produced a till with a high Paleozoic carbonate content.

2.5.4 Late Southwestward Surge

Evidence for a final southwest surge out of the GSL basin is also present between the escarpment and Great Slave Lake as a series of streamlined landforms that end in thrust ridges (Hagedorn et al., 2021B). This landform association has been linked to surges in other locations (Evans and Rea 1999, Evans et al. 1999, 2008, 2009) and the Great Slave Lake bathymetry lends itself to surging as the western arm is shallow and steadily deepens to the east leaving large portions of the ice margin with a thicker calving front in the proglacial lakes. The thicker calving front can lead to instabilities and consequently surging (Bentley et al. 1979, Favier et al. 2014, Quiquet et al. 2021)

No striation evidence of this final southwestward surge was found as it likely did not overtop and deflected around the escarpment, or if it did, was weak and did not leave a trace. To the east a final southwest flow direction was found at Pine Point, where northwest landforms are cross-cut by this later southwest flow. This flow would be expected all around the LIS western margin flowing out of Great Slave Lake calving into GLM (Oviatt and Paulen, 2013; Rice et al., 2013; Rice et al., 2019; their Figure 2).

This late southwest surge is could possibly emplace the upper till at 18-PTA-042, which has higher Canadian Shield content (Fig. 2.8). It is important to note that this final phase only affected low-lying portions of the study area and evidence of this final southwest phase is lacking above or on the escarpment, which means that this final till was only emplaced locally and discontinuously. Several samples collected within the lowest regions close to Great Slave Lake do plot within Cluster 4 further supporting the possible presence of a Canadian Shield rich till associated with a late-stage southwest surge (Fig. 2.17A). Alternatively, these Canadian Shield rich till could indicate occurrence of the lower till at surface, which would indicate that the till below at these sites is older than the southwestward flow observed in this research.

2.6 Implications

2.6.1 Ice Flow History and regional ice sheet configuration

The study presented here documents a clear record of ice sheet dynamics involving a clockwise shift of ice flow over time. The oldest phase recognized in the area involves an ice stream that created MSGLs and carried material from the Canadians Shield (>80 km) to the southwest across the study area (Fig. 2.19A). The ice sheet had to be relatively thick (e.g. 2-3 km), as ice flow was not deflected by any topographic features. This ice flow phase is not captured in most LIS reconstructions and models, which mainly show ice sheet configurations conducive to westward or northwestward ice flow in the study area (e.g. Fisher et al. 1985; Gowan et al. 2016). This has important implications for the position and timing of the Plains Ice Divide, as well as the evolution of the Mackenzie Through and Bear Lake ice streams' catchments (Margold et al. 2018). Clearly, a different ice sheet configuration and dynamics is required for a southwest-trending ice streaming phase to occur in the study area. Specifically, the Plains Ice Divide could not be located south of Great Slave Lake with the Mackenzie Through ice stream catchment extending into the area - a typical configuration shown on several LIS reconstructions at times of thick ice (e.g. LGM; Fig. 2.20). It is also important to note that evidence documented elsewhere in the broader region (Prest et al. 1968), as well as north of Great Slave Lake, in the Lac de Gras area show evidence for an old southwest-trending ice flow phase across the region (e.g. Ward et al. 1996; Kelley et al. 2020). The age of this regional southwest

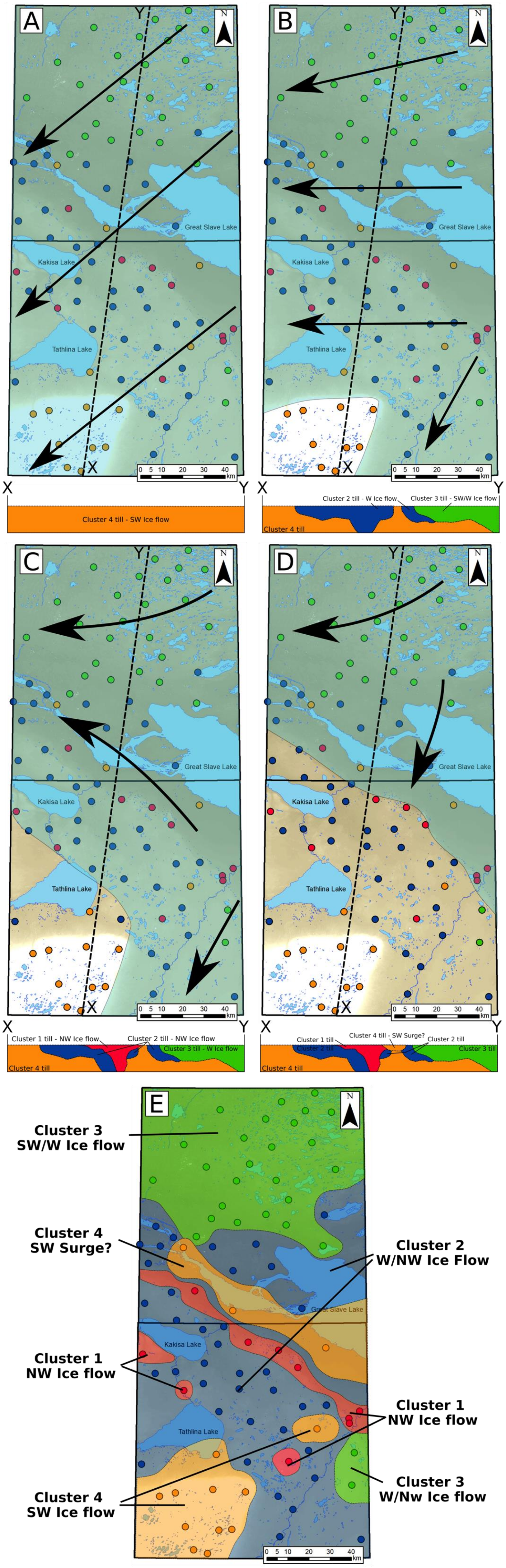

Figure 2.19 Summary of ice-flows and till stratigraphy in the study area. Note that ice margins shown above are described in more detail in Chapter 3. Cross sections are not to scale. A) Oldest southwest ice flow moved across the study area. This flow was strong and occurred under a thick ice sheet, creating SW trending MSGL atop the Cameron Hills. During this SW flow, the lower Cluster 4 till unit was deposited. This till has an increased Canadian Shield/Mesozoic component. B) As the ice sheet thins it begins to rotate to more westward flows down the Mackenzie River Valley. Cluster 2 and 3 tills are deposited and incorporating more local carbonate material. The undulating contact with Cluster 4 till suggests material from Cluster 4 is incorporated being completely remove in some areas. The contact between Cluster 2 and 3 tills is unknown. C) Northwest ice flow occurs due to funneling of the Mackenzie River Valley as the ice sheet continued to thin. During the NW flow, Clusters 2 and 3 are still being deposited (note Cluster 3 is more westward due to its location relative to the Mackenzie River Valley). In close proximity to escarpments, Cluster 1 till is deposited consisting of almost only local angular limestone material. D) A final SW surge occurs out of the Great Slave Lake Basin due to the increased calving front into a proglacial lake. This surge could deposit the Cluster 4 till observed at surface in some of the lower lying areas. E) Estimated till compositions at surface throughout the map area as a result of the ice flow history. Note the discontinuous nature of till units at surface.

ice flow phase is unknown, but no evidence has yet been found constraining it to a previous glaciation. Whatever the case may be, the southwest ice flow phase preceded the LIS configuration with the Plains Ice Divide south of the area and the Mackenzie Trough Ice Stream as shown in most LIS reconstructions.

The southwestward flow phase was followed by a period of ice sheet thinning and an increasing influence of topography on ice flow patterns. The net effect of this change was a gradual clockwise shift of ice flow to the west and northwest as the ice sheet became more lobate, specifically down the Mackenzie River Valley (Fig 2.19B, C). These west and northwestward flows have a less prominent landform record in the study area and are associated with increased incorporation of local bedrock material into the till. Evidence and interpretation presented by Bednarski (2008) to the east and Paulen et al. (2011) to the south are both consistent with this reconstruction. They show broad clockwise shifts in ice flow that are related to deglaciation and topography across the region.

Several researchers have recognized a northwest ice flow phase in the area, and placed its onset during and after the LGM, which put the Plains Ice Divide to the south of Great Slave Lake at that time (Brown, 2012; Margold et al., 2018). The northwest trending landforms observed in the study area have been used to support this hypothesis. Most ice sheet models have also reproduced this configuration, showing thickest ice south of Great Slave Lake over the Plains Ice Divide (Fisher et al. 1985; Gowan et al. 2016; Roy and Peltier, 2017).

In this study, the evidence for a NW ice flow phase postdates the southwest ice flow phase. The only possible evidence of an old NW ice flow in the area would be the NW-trending striations at the base of a till sequence (Fig. 2.13). Our current interpretation is that the surficial carbonate-rich till at that location is related to the northwest or late-stage southwest readvance/surge (Fig. 2.19). The location of the site is consistent with the reconstructed extent of that local late-stage flow. It is possible that the NW striations overlain by two till sheets represent uniquely preserved evidence for an old northwest ice flow phase that preceded the old southwest ice flow phase described above.

Due to regional implications of the ice flow reconstruction presented herein, it is important to consider the other ice flow shifts documented in surrounding regions. Studies north of Great Slave Lake, in the Lac de Gras area 400 km to the NE, show compelling evidence for an old southwest-trending ice flow phase across the region followed by a clockwise shift of ice flow (e.g. Ward et al.

1996; Kelley et al. 2020) similar to what is described here in this study. In contrast, Sharpe et al. (2017) did not report any evidence of ice flow shift through time for the area encompassing the eastern arm of Great Slave Lake. Their reconstruction thus involves a coeval radiating ice flow pattern across the eastern arm of Great Slave Lake that would have produced most, or all the preserved surficial record. Here, we argue that this reconstruction is not compatible with the regional evidence of ice flow shifts through time, and therefore does not reflect the evolution of the LIS recorded in the surrounding regions, including this study area.

At Pine Point, the lowest till unit found within karst depressions in the bedrock was not observed in the study area, although most till exposures in the study area do not extend down to bedrock. The ice flow record also shows some differences compared to the one documented in this study. At Pine Point, the oldest ice flow phase is westward (290°), based on striations found underneath thick till (Rice et al., 2013; McClenaghan et al., 2018; Rice et al., 2019; Fig 1.7). Interestingly, this old westward flow was followed by a northwest ice flow phase, which preceded the regional southwest ice flow. It appears that the record at Pine Point relates to a longer history of glaciation than in the study area. However, the thick (~20 m) stratigraphic sequence at Pine Point does not include any non-glacial layers, which suggest it may have been deposited completely during the last glaciation. The oldest westward flow at Pine Point could relate to an advance of an earlier glaciation event that never reached the study area. Alternatively possible oldest westward striations within the study area could have been obliterated by ice advances that did not affect Pine Point, as it was never deglaciated during that time. A possible location for the extent of this interstadial ice margin that retreated from the study area but not so far as Pine Point would be the Hay River Valley. Oldest westward flows are observed up to this point, but do not cross it (Paulen, et al., 2019). When the ice-sheet began to advance again leading up to the LGM the trends between the study area and Pine Point begin to correlate although ice flow directions are slightly different due to proximity to the Mackenzie River Valley.

Overall, the western margin of the LIS was highly dynamic in the region with major shifts in ice flow direction, most likely due to changes in ice surface topography and configuration, such as the migration of the Plains Ice Divide and ice thinning and increasing topographic influences channeling ice into lobes.

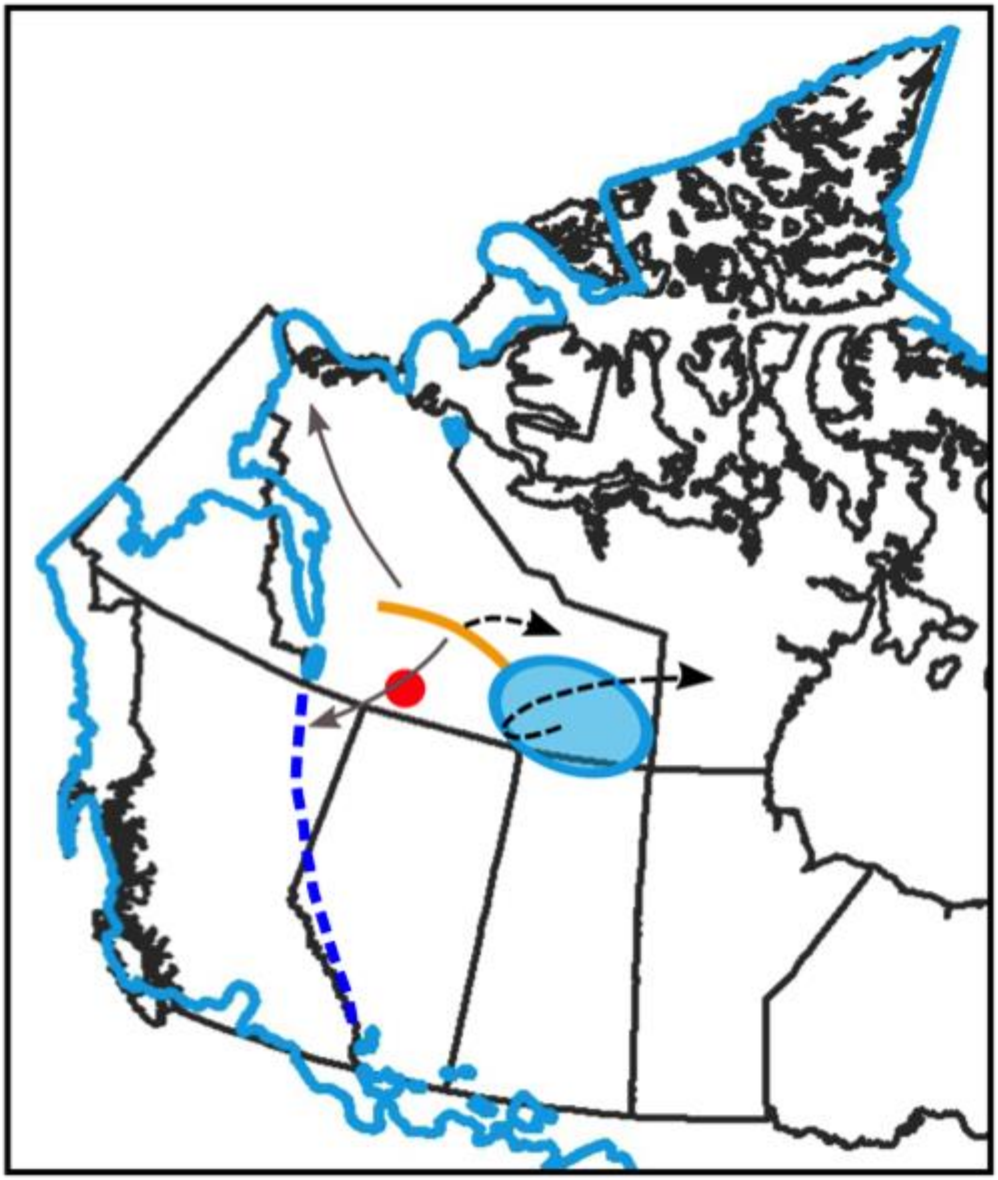

Figure 2.20: Proposed reconfiguration of the western sector of the LIS. The location and movement of the Keewatin Ice Dome is the same, but the Plain Ice Divide (Orange) has moved north of the study area, and the subsequent ice flow is to the southwest while northwest flow still feed the Mackenzie River. The Plains Ice Divide moves with the Keewatin to the east and becomes smaller, leading to the thinner westward and northwestward ice flows observed in this study.

2.6.2 Till Stratigraphy, compositional patterns and mineral exploration

Till stratigraphy and geochemistry are linked to different provenance due to shifts in ice flow direction. This research shows that lower tills were deposited by southwestward flows with Canadian Shield and Mesozoic Shale components (Cluster 4; Cameron Hills) and the geochemical signature shifts with the westward to northwestward flows to more local Paleozoic carbonate provenance in the lower lying area (Clusters 3, 2, 1; Northern, Middle, Escarpment; Fig 2.19). This is contrary to what might be expected, as typically provenance indicators in till tend to decrease with down-ice distance from their bedrock contact (Dreimanis and Vagners 1974, Shilts 1984, Lemmen et al. 1994, Trommelen et al. 2013, McMartin et al. 2016, Menzies et al. 2018). The apparent Canadian Shield dispersal inversion documented in this study is thought to be due to the clast dilution of the Mesozoic shale and different tills occurring at surface in different places in the study area. A classic continuous down-ice dispersal fan assumes a single surficial till sheet (Shilts 1984, Boulton 1996, McClenaghan and Paulen 2018). Here, we have shown clear evidence that the surficial till is not the same everywhere across the study area; simple dispersal patterns therefore cannot be used to fully explain till composition at surface (Fig 2.19E). There is a till in the study area, which mainly occurs as the 'lower till' and outcrops in only a few places, most notably on top of the Cameron Hills. The lower till appears to have an increased Canadian Shield content everywhere it was found, but smaller Mesozoic material are also abundant, such as on the Cameron Hills. This contrasts with the other tills at surface in the region further to the east (Clusters 1, 2, 3) which appear to have less input from the Canadian Shield.

It is interesting to note the difference between Canadian Shield clast proportions between the lower till and the other tills located at similar distances down-ice the southern shield/sedimentary platform boundary. Normally, when ice flows from hard igneous rocks onto softer sedimentary rocks, the uptake of sedimentary rocks in the dispersal area rapidly dilutes shield clasts from up-ice (e.g. Clark, 1987; Strobel and Faure, 1987). Here, the proportion of Canadian Shield clasts was maintained to above 40% in all lower till samples at distance up to 80 km down-ice the Canadian Shield boundary. It is however important to note that for the specific case of the Cameron Hills, the proportion of 'Canadian Shield' clasts remains high in the till because of the weak and friable nature of the underlying Mesozoic shale. Nonetheless, clasts of Paleozoic carbonates remain low in that till as well.

The composition of the younger tills can be explained by the changing configuration of the ice-sheet during deglaciation (Fig. 2.19B, C, D). During that time, subglacial conditions changed, local erosion increased and along with mixing from the lower till unit, new compositionally distinct till units were produced. It has been suggested (e.g. Iverson, 1991, 1993) that during deglaciation, thinner ice tends to favor the formation of subglacial cavities. Normal effective stress varies more across the bed, and intense pressure fluctuations along a linked-cavity drainage system leads to large pressure gradients, which encourage quarrying (Iverson 1991a, 1993, Cohen et al. 2006). Therefore, the theory would indeed predict the change in till composition, as documented here, and linked to thinning ice during deglaciation. It may be counterintuitive to link thinner ice to enhanced local bedrock erosion, but the highly jointed sedimentary rocks would be quite sensitive to effective pressure fluctuations and large volumes of locally-derived till could have been produced during deglaciation despite thinner ice. Finally, the composition of the younger tills clearly indicates the lower till, and any other possibly pre-existing units, were discontinuous in the area allowing direct erosion of local bedrock in many places.

The observation of different till units at surface has implications for mineral exploration in the region (Fig. 2.19E). The area has been identified as highly prospective for Mississippi-Valley type deposits (Hannigan, 2006; Paulen et al., 2018; Paulen et al., 2019) and can be covered by thick till stratigraphy (Rice et al., 2013; Rod Smith, Pers. Comm). As such, understanding ice flow and till unit provenance are important for applying drift prospecting to finding mineral deposits under sediment cover (McClenaghan and Paulen 2018).

This research indicates that care is needed when applying drift prospecting to this terrain. Four distinct compositional groups (clusters) are recognized. As mentioned above, a surficial till sampling program in the area would probably sample till from different units with contrasting dominant provenance. For example, if a sample atop the Cameron Hills has a high concentration of pathfinder elements, its source could be anywhere northeast into the Canadian Shield. Complexity exists when sampling off the Cameron Hills as well as some samples in different geographic classes have the same composition as the Cameron Hills samples. Therefore, fragmented discontinuous dispersal trains could be found at the surface similar to what has been documented elsewhere in similar settings on prairie sedimentary rocks (e.g. Ross et al. 2009). The till stratigraphy and provenance in the region has complex implications for drift prospecting and thus caution and meticulous analysis are needed for meaningful interpretation of result.

2.7 Conclusion

At least four LIS ice-flow phases are preserved on the landscape of southwestern Great Slave in the form of outcrop-scale erosional features and subglacial streamlined landforms, as well as in the observed till stratigraphic record. The ice flows indicate an oldest southwestward (230°) flow, followed by a clockwise shift to westward (280°) flow and, then northwestward (305°) flow. These shifts in ice-flow were related to an eastward retreat of the ice margin and increasing topographic influence due to thinning ice. The final southwest flow was recorded in only a small portion of the study area and represents a late stage surge out of the Great Slave Lake basin.

The southwest ice-flow phase produced the lower till at stratigraphic sites and till atop of the Cameron Hills. This till has an increased Canadian Shield content compared to other tills. On the Cameron Hills, it could be partly due to the break up of the more locally derived Mesozoic mudrocks, which would be underrepresented in the coarse clast fraction. Nonetheless, this till has a low Paleozoic carbonate content everywhere it was found. It was likely deposited during an ice-stream event as is indicated by the MSGL's atop the Cameron Hills. Regionally, this phase is correlated to other documented old SW-trending ice flow phases such as near Lac de Gras north of the study area. This older, regionally extensive southwest ice flow phase requires a different ice sheet configuration than the one commonly shown for LGM and deglaciation with the Plains Ice Divide to the south of Great Slave Lake and with Mackenzie Through and Bear Lake ice streams' catchments extending into the study area. For this flow phase, the main ice divide influencing the area had to instead be located to the northeast of Great Slave Lake (i.e., Keewatin). Ice streaming was to the southwest, which means it either preceded the Mackenzie Trough ice stream, or the latter did not extend as far into the LIS at that time. It is interesting to note that there is a widespread record, although fragmented, of long SW-trending ice streaming across the prairies to the south (e.g. Ross et al. 2009; O'Cofaigh et al. 2010), which shows that the Plains Ice Divide was not necessarily a long-standing feature of the LIS during the last glaciation and, perhaps developed only after the LGM. The older NW ice flow phase documented at Pine Point (Rice et al. 2013, McClenaghan et al. 2018) is not confidently recognized in this study.

Later, during deglaciation, thinning ice most likely promoted the development of subglacial cavities, which along with normal effective pressure fluctuations would have encouraged quarrying of the local sedimentary rocks. This shift in subglacial conditions, along with changing ice flow direction, would together explain the incorporation of more local sedimentary detritus in the younger upper till.

Altogether the ice sheet’s evolution depicted here shows a complex ice-flow history, which produced multiple compositionally distinct till units resulting from either more than one glaciation and/or ice divide migration and shifting ice stream dynamics due to thinning ice and the development of competing ice streams. Further work into understanding the pattern of ice margins retreat and when these changes occurred is presented in the next thesis chapter.

Chapter 3

Ice Margin Retreat and Glacial Lake History of the Southwestern Great Slave Lake Area

3.1 Introduction

The Laurentide Ice Sheet (LIS) reached its maximum extent at approximately 21 cal. ka BP, at which point the ice sheet covered the majority of Canada (Dyke 2004, Dalton et al. 2020). After 21 cal. ka BP, the LIS margins retreated across the Canadian landscape which caused shifts in ice flow directions due to changing arrangement of the ice domes/divides, increasing subglacial topographic influence, and increased lobation of the ice margin (McMartin and Henderson, 2004; Hodder et al., 2016; Margold et al., 2018; Rice et al., 2019; Chapter 2 of this thesis). Ice margin retreat occurred at different rates across the LIS depending on margin type (terrestrial vs. aquatic), subglacial thermal regime (warm-based vs. cold-based), local topography, and other geologic factors (Lemmen et al. 1994, Dyke 2004, Boulton and Hagdorn 2006, Stokes and Tarasov 2010, Carrivick and Tweed 2013, Ullman et al. 2015, Gowan et al. 2016, Margold et al. 2018, Dalton et al. 2020). As a result, it is often difficult to trace ice margin positions, determine the timing of deglaciation, outline glacial lake extents, and track glacial lake drainage routes across the LIS.

Ice margin positions, timing of deglaciation, glacial lake extents and glacial lake drainage routes are all integral components of LIS modeling. LIS models are used to understand the ice sheet's impact on past global climate, and the influence of the global climate cycles on the extent of the LIS (Calov et al. 2002, Balco and Rovey II 2010, Shakun and Carlson 2010, Stokes and Tarasov 2010, Tarasov et al. 2012, Stokes et al. 2015). Furthermore, the pattern of deglaciation of the LIS can be used as an analogue for modern ice sheets that are melting, allowing insights into possible meltwater discharge and climatic changes (Evans et al. 1999, 2009, Rignot et al. 2011, Shepherd et al. 2018). It is therefore important that ice margin positions, timing of deglaciation, glacial lake extents and glacial lake drainage routes used in LIS models be as accurate as possible.

A detailed understanding of deglaciation is lacking across certain regions of the LIS; one such region is the western sector of the LIS (Dyke 2004, Tarasov et al. 2012, Stokes et al. 2015, Gowan et al. 2016, Dalton et al. 2020). The western sector of the LIS has sparse chronological constraints creating loosely constrained ice margin positions (Dalton et al., 2020). The extent of glacial lakes is also poorly constrained over the western sector of the LIS due to limited mapping and field work in the region (Craig 1965, Lemmen et al. 1994, Smith 1994, Dyke 2004, Dalton et al. 2020). Consequently, uncertainties exist in the location and timings of glacial lakes over the western sector of the LIS, specifically around the southwestern shore of Great Slave Lake (GSL). This study aims to detail deglaciation over the southwestern GSL area using detailed surficial mapping and new field data (Fig. 3.1).

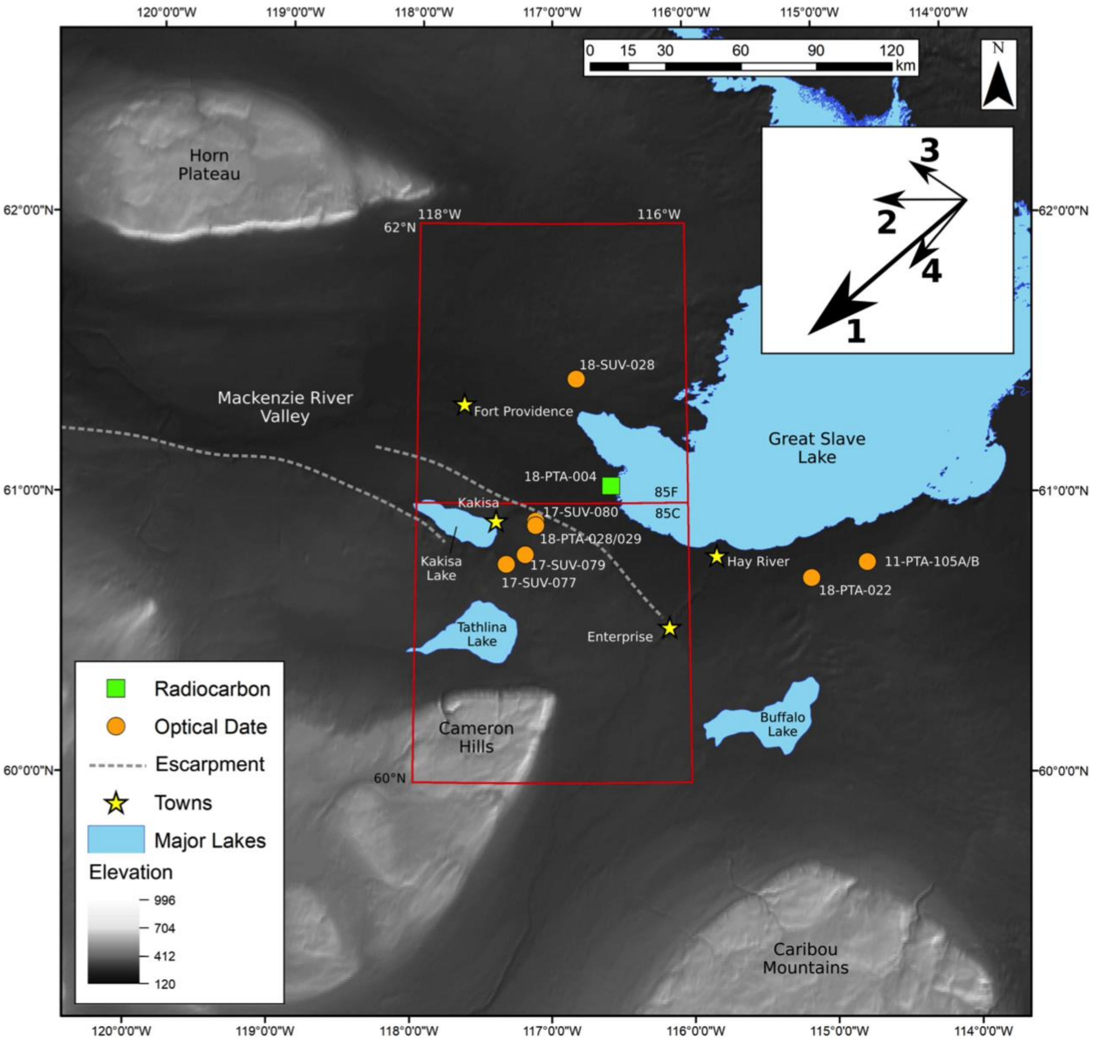

Figure 3.1: Digital Elevation model over the study area from the Global Multi-resolution Terrain Elevation Data (GMTED2010, courtesy of the USGS). Dashed lines indicate two escarpments. Upland regions include the Horn Plateau, the Cameron Hills, and the Caribou Mountains. Ice flow phases and associated direction are summarized in the top right of the figure (1 = oldest phase); see Chapter 2 of this thesis for details on ice flow history. Only the northern and southwestern quarters of NTS 85C have completed maps (Hagedorn et al., 2021a, Hagedorn et al., 2021b, Smith et al., 2021, Paulen et al., 2021). New field data includes the radiocarbon and optical ages, specifically 18-PTA-028/029 where a beach ridge was dated.

Understanding the deglaciation of the western LIS is important for multiple reasons. Glacial Lake McConnell (GLM), the second largest proglacial lake of the LIS is located along the western LIS margin (McConnell 1890, Craig 1965, Lemmen et al. 1994, Smith 1994). GLM represents a large quantity of meltwater that was eventually drained, due to ice margin retreat, northwestward down the Mackenzie River into the Arctic Ocean. Glacial Lake Agassiz is thought to have drained through GLM into the Arctic Ocean via the Clearwater Spillway (Fisher and Smith 1994, Smith 1994, Tarasov and Peltier 2006, Bednarski 2008, Couch and Eyles 2008, Murton et al. 2010, Tarasov et al. 2012, Munyikwa et al. 2017, Norris et al. 2019). However, GLM's northwestward drainage has not yet been precisely constrained (e.g., Tarasov and Peltier 2006) but is thought to have contributed to a major influx of glacial meltwater at the onset of the Younger Dryas (YD, ~12.9 cal. ka BP); an event observed in various proxy records which is thought to have caused a weakening of the Atlantic Overturning Circulation (AMOC), which in turn influenced global climate (Broecker et al. 1989, Tarasov and Peltier 2005, Condron and Winsor 2012, Gowan et al. 2016). Understanding the arrangement and sequence of ice margins and glacial lakes along the western margin of the LIS will help address when and where northwestward drainage from GLM could have occurred and determine whether it corresponds to the timing of the meltwater event at the onset of the YD.

3.2 Background

3.2.1 Physiography

The physiography of the study area is related to the underlying bedrock geology (Refer to Fig. 1.10). The area is relatively flat due to the Phanerozoic sediments that cover the majority of the region (Fig. 3.1). Topographic features in the study area are typically due to differential erosion within sedimentary beds (i.e., bedrock escarpment south of GSL, Cameron Hills). The Hay and Kakisa rivers have also incised into bedrock, creating narrow topographical depressions. The Mackenzie River Valley lies in the western portion of the study area and is a large feature with gently sloping sides oriented northwest – southeast (Fig. 3.1). The regionally low relief terrain in combination with the underlying impermeable substrates has made the study area favorable for organic deposits to accumulate.

3.2.2 Ice Flow

Four separate ice-flow phases are recorded in the study area (Paulen et al., 2007; Bednarski, 2008; Rice et al., 2013; Oviatt et al., 2015; Rice et al., 2019; Paulen et al., 2019; Chapter 2 of this thesis). The oldest flow (1) was to the southwest (250°) followed by a clockwise shift (2) to the west (280°), and then (3) northwest (300°; Fig. 3.1). The ice-flow phases were impacted by topography during deglaciation, primarily by the funneling of ice down the Mackenzie River Valley. A final late ice readvance (4) southwest (250°) out of the Great Slave Lake Basin occurred, but it only influenced the study area below the eastern escarpment.

3.2.3 Deglacial History and Glacial Lake McConnell

Deglaciation is thought to have first occurred along the western margin of the study area around 13.0 cal. ka BP (Lemmen et al., 1994; Dyke, 2004; Bednarski, 2008; Dalton et al., 2020; Fig 3.2). As the ice retreated, it impounded drainage along the ice margin due to a northeastward draining landscape. The evolution of glacial lakes along the western LIS margin was therefore a complex sequence of meltwater impoundment and drainage as basins filled and new outlets were exposed due to ice retreat. Some of these early lakes include glacial Lake Mackenzie in the Mackenzie River valley, glacial Lake Hay in the Hay River valley and glacial Lake Peace in the Peace River valley (Mathews 1980, Lemmen et al. 1994, Couch and Eyles 2008, Huntley et al. 2017, Utting and Atkinson 2019). As ice retreated further eastward larger lake basins were exposed (Great Bear, Great Slave and Athabasca Lake basins), which eventually coalesced into GLM.

Richard G. McConnell first discovered evidence of GLM during an expedition to the Canadian Northwest (McConnell, 1890). McConnell observed well-developed sub-parallel raised beach ridges and raised deltas on the landscape, which he used to hypothesize that a larger body of water once covered the area. Since McConnell's initial observations, further research has been completed on GLM to understand its extent and evolution through time (Craig, 1965; Lemmen et al., 1994; Smith, 1994).

The initial stage of GLM was the Hare Indian Phase and occurred when only small portions of the western study area were deglaciated (Lemmen et al. 1994, Smith 1994). During the Hare Indian phase GLM was small and only existed in the northwest portion of the Great Bear Lake basin using the Hare Indian River as the outlet flowing northeast (Refer to Fig. 1.5). This phase of GLM was estimated to have occurred around 13.0-12.8 cal. ka BP by Lemmen et al. (1994) or 13.7 – 13.3 cal.

ka BP by Smith (1994). The range of values between the two reconstructions was due to the selection of radiocarbon dates used in the reconstruction and then the extrapolation of the selected radiocarbon ages to limit ice margin location at a regional extent. The ~ 800 cal. ka BP age difference between Lemmen et al., (1994) and Smith (1994) is consistent throughout their reconstructions but they have similar lake extents and evolutions for GLM.

As the ice sheet continued to retreat through the study area, a significant portion to the north became ice-free and allowed the Great Bear Lake Basin to be filled with glacial meltwater (Refer to Fig. 1.5). This marks the second phase of GLM, the Great Bear Phase, which began at 12.5 – 12.4 cal. ka BP according to Lemmen et al., (1994) or 13.3 – 12.8 cal. ka BP according to Smith (1994). This second phase of GLM used the Great Bear River as the primary outlet flowing northwest. During this phase of GLM, the southern parts of the study area that were deglaciated were likely covered by a proglacial lake, possibly the southern most extents of glacial Lake Mackenzie (Lemmen et al. 1994, Smith 1994, Couch and Eyles 2008).

During the Great Bear phase of GLM, the Snake Creek Moraine was deposited (Lemmen et al. 1994, Bednarski 2008). This moraine is approximately 120 km long and runs sub-parallel to the southwestern shore of Great Slave Lake along the eastern bedrock escarpment. Lemmen et al. (1994) appear to be the first to have identified this moraine and suggest that it was deposited mostly subaqueously due to ice-flow shifts in response to the deglaciation of the Great Bear Lake Basin. Furthermore, Lemmen et al. (1994) suggest that ice retreat from the Snake Creek Moraine was rapid toward the Paleozoic - Canadian Shield boundary to the east. They use the lack of ice contact and glaciofluvial sediments east of the Moraine and a significant amount of iceberg scours as evidence for this fast ice retreat. The eastward deepening bathymetry of the Great Slave Lake Basin also supported the fast retreat as topography decreases making the ice margin unstable.

During and after the rapid retreat of the ice margin from the Snake Creek Moraine, the Mackenzie Phase of GLM occurred which encompassed the Great Bear, Great Slave, and Athabasca lake basins (Refer to Fig. 1.4). The Mackenzie phase was the longest and largest in the evolution of GLM and lasted from 11.6 - 9.5 cal. ka BP (Lemmen et al. 1994), or 12.6 - 9.3 cal. ka BP (Smith 1994). During the Mackenzie phase of GLM the maximum water level is thought to be around 300 m above sea level (the uppermost strandline elevation) not accounting for Glacioisostatic Adjustment

(GIA). The lake had an extensive contact with the ice margin to the east (600 to 800 km) and used the Mackenzie River to the west as the main outlet.

The Mackenzie phase also differs between Lemmen et al. (1994) and Smith (1994). The Smith (1994) reconstruction invokes a large drainage event from glacial Lake Agassiz northwest into GLM at 11.3-11.2 cal. ka BP. This event was routed down the Clearwater River valley to the Athabasca River valley and then into GLM. Smith (1994) suggests that the incision into the Liard Moraine, which was acting as a limit to drainage down the Mackenzie River during the Mackenzie phase of GLM, is a result of this meltwater influx. In contrast, Lemmen et al. (1994) state that there is no evidence for a significant drainage event connecting glacial Lake Agassiz to GLM. Nonetheless, the two authors agree that drainage of GLM after ~ 9.4 cal. ka BP occurred through mainly glacioisostatic adjustment and incision of outlets down the Mackenzie River to present lake extents.

3.2.4 Surficial Geology

Landforms and sediments in the study area record the deglacial history of the landscape. Glaciofluvial drainage is recorded by meltwater corridors that indicate outlets for proglacial lakes (Craig, 1965; Lemmen, 1990; Hagedorn et al., 2021a, Hagedorn et al., 2021b, Smith et al., 2021). These meltwater corridors appear to be mostly erosional into underlying sediments and bedrock although glaciofluvial sediments were locally deposited within and around these corridors. These glaciofluvial sediments are typically thin, discontinuous and composed of sand and gravel.

The glaciolacustrine record on the landscape is more extensive. There are raised beach deposits associated with several different proglacial lakes, or lake phases, and are typically composed of local limestone cobbles with a sandy matrix (Craig 1965, Lemmen 1990, Lemmen et al. 1994). The most widespread glaciolacustrine sediments are nearshore deposits and are typically less than 1 m thick and consist of pebbly sand and silt. Older sediments, mostly till, that were inundated by a glacial lake were locally winnowed by wave action creating discontinuous boulder lags on the sediment layers upper surfaces up to 0.5 m thick.

After deglaciation, eolian processes remobilized previously deposited glaciofluvial and glaciolacustrine sand into dune fields with transverse and parabolic morphologies suggesting both eastward and westward wind directions (see Appendix G). These dunes are typically greater than 2 m in amplitude and are composed of well-sorted massive medium to fine sand. Some dunes show blowouts, but the majority are stabilized today due to vegetation. Similar dunes have been dated south and north of the study area using optical dating methods on eolian sands (Wolfe et al., 2004, 2007; Munyikwa et al., 2011, 2017; O'Neill et al., 2019; Fig. 3.2).

3.2.5 Ice Margin Retreat and Lake Phases Chronology

Radiocarbon and optical ages are sparse in the region surrounding the study area. The Lemmen et al. (1994) and Smith (1994) reconstructions were created using two radiocarbon ages from organic lake sediments and moss and two additional radiocarbon ages on fossil wood from the Slave Delta (Great Slave Lake) and the Peace Delta (Lake Athabasca). The fossil wood ages were specifically used to determine the timing and extent of glacial Lake McConnell in the reconstructions (Lemmen et al., 1994; Smith, 1994; Refer to Fig. 1.5; Fig. 3.2). These ages are used as limiters for the reconstructions, but have difficult interpretation due to their stratigraphic context and the transport history.

Additional radiocarbon ages have been obtained since 1994 and used in the continental scale reconstructions (i.e. Dyke, 2004; Dalton et al., 2020), yet limited changes to the margin were made in the study area (Table 3.1; Fig 3.2). Recently, radiocarbon dating was completed by O'Neill et al. (2019) on charcoal and peat along the shore of Great Slave Lake to the north of the study area. The O'Neill et al. (2019) ages were targeted to date the recession of Great Slave Lake, and are consequently the youngest (Table 3.1).

Optical dating methods were also used by O'Neill et al. (2019) to the north in conjunction with radiocarbon ages. They sampled a variety of sand deposits (littoral, eolian, and wedge) with the goal of constraining glacial lake level phases over the region. The variety of deposits show a range in ages, depending on the elevation of the sand deposit consistent with the lowering of water levels and the depositional environments (Table 3.2; Fig. 3.2).

To the south, several optical ages were obtained from eolian dunes and littoral sands from the High Level, Wood Buffalo and Sandy Lake Sand Hills dune fields (Wolfe et al., 2004, 2007; Oviatt and Paulen, 2013, Munyikwa et al., 2011, 2017; Table 3.1; Fig 3.2). Together these ages show that for northern Alberta, optical ages are systematically younger than radiocarbon ages in the area (Munyikwa et al., 2017; Refer to Fig. 1.8). It is suggested that the younger age of deglaciation presented in the optical ages could be a common trend in areas currently constrained by only radiocarbon ages, like the study area of this thesis.

Overall, a sparse radiocarbon record was used to create a deglacial sequence in the study area (Lemmen et al., 1994; Smith, 1994). These margins are still being used in continental scale ice sheet reconstructions (Dyke, 2004; Dalton et al., 2020). Newer methods of dating (i.e. optical ages) suggest that the radiocarbon chronology is perhaps too old, and have yet to be systematically integrated within a new reconstruction of the western LIS (Brown 2012, Munyikwa et al. 2017, Kelley et al. 2020, Stoker et al. 2020). There is thus a need to add new age constraints to update deglacial ice margin positions along the western LIS.

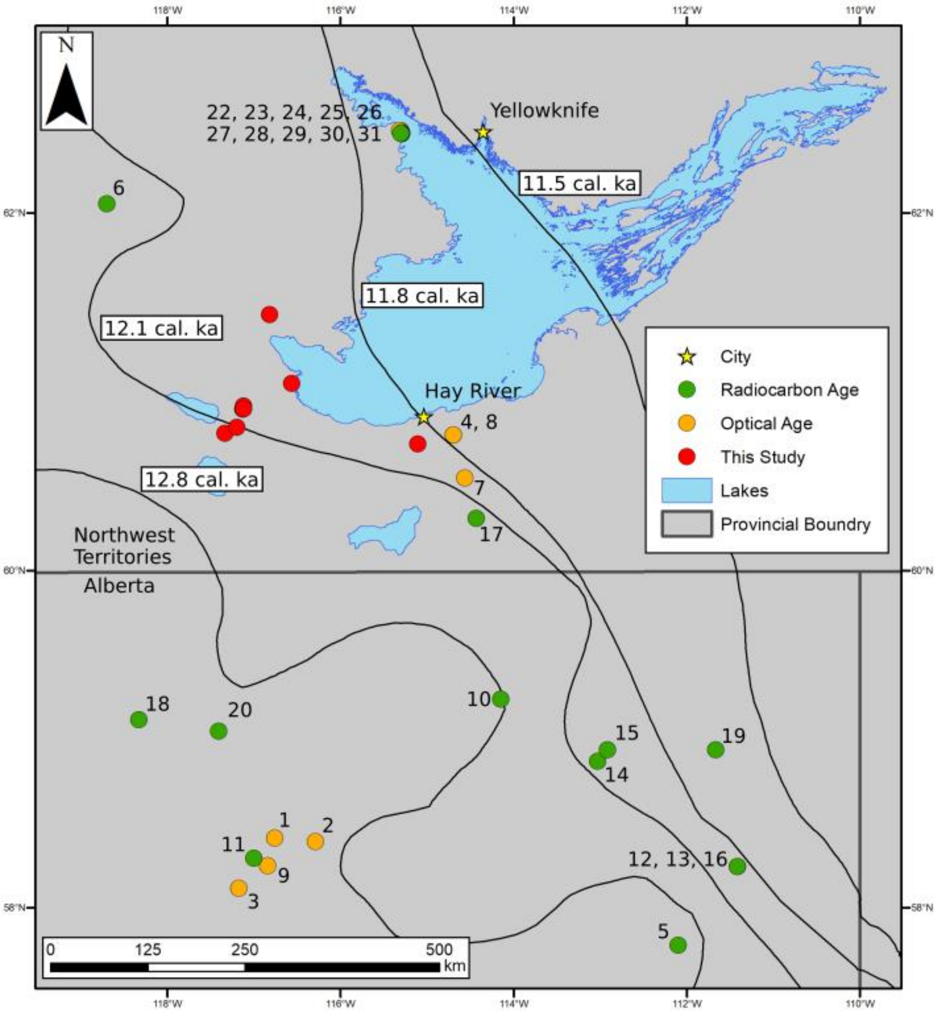

Figure 3.2: Ice margins and age locations for the region surrounding the study area. The ice margins are from Dalton et al. (2020). Radiocarbon (green) and Optical (Orange) ages are shown and listed in Table 3.1 and 3.2 respectively, with corresponding number for reference. Samples within this thesis are highlighted in red.

Table 3.1: Existing (published) radiocarbon ages for samples from the regional study area. Radiocarbon ages were calibrated using the IntCal20 curve at 2-sigma uncertainty. See Section 3.3.2.1 for details. Number relates to labels on Fig. 3.2 and * indicate those included in Dyke's (2004) compilation and ice sheet model reconstruction.

Number	Sample ID	Material	Radiocarbon Age (^{14}C BP)	Age (cal. ka BP)	Reference
5 *	Beta-8287	Gyttia	10740 ± 150	11.83 – 11.10	Vance, 1986
6 *	GSC-3524	Lake Sediment	10500 ± 100	12.72 – 12.04	MacDonald et al, 1987
10 *	GSC-3313	Lake Sediment	10200 ± 245	12.67 – 11.23	MacDonald et al., 1987
11 *	AECV-439C	Bone	10080 ± 150	12.44 – 11.21	Beaudoin, 1988
12 *	GSC-3402	Wood	9910 ± 90	11.73 – 11.19	Smith and Fisher, 1993
13 *	GSC-4302	Wood	9910 ± 190	12.06 – 10.74	Rhine and Derald, 1988
14 *	WAT-2661	Wood	9850 ± 40	12.62 – 10.33	Smith, 1994
15 *	WAT-2662	Wood	9830 ± 40	12.61 – 10.28	Smith, 1994
16 *	AECV-1183C	Wood	9710 ± 130	11.40 – 10.66	Smith and Fisher, 1993
17 *	GSC-5343	Lake Sediment	9260 ± 70	10.64 – 10.25	Lemmen et al., 1994
18 *	AECV-983C	Peat	9170 ± 170	10.79 – 9.78	Zoltai, 1993
19 *	GSC-5884	Picea	8720 ± 80	10.12 – 9.54	Bednarski, 1999
20	AECV-1425C	Peat	8400 ± 100	9.54 – 9.13	Vitt et al., 2005
24	UOC-2619	Peat	3850 ± 3700	3.86 – 3.70	O'Neill et al., 2019
24	UOC-0932	Charcoal	2070 ± 25	2.12 – 1.94	O'Neill et al., 2019
29	UOC-0933	Charcoal	1277 ± 1065	1.28 – 1.06	O'Neill et al., 2019
31	UOC-0931	Charcoal	264 ± 23	264 - 27	O'Neill et al., 2019

Table 3.2: Existing (published) OSL ages for samples from the regional study area. Number relates to labels on Fig. 3.2.

Number	Sample ID	Material	Age (BP)	Reference
1	SAW05-01	Eolian	13400 ± 1200	Wolfe et al., 2007
2	SAW05-02	Eolian	11700 ± 1000	Wolfe et al., 2007
3	SAW05-04	Eolian	11000 ± 1000	Wolfe et al., 2007
4	11-PTA-105A	Eolian	11100 ± 1100	Oviatt and Paulen, 2013
7	SFU-O-159	Eolian	10500 ± 500	Wolfe et al., 2004
8	11-PTA-105B	Eolian	10500 ± 900	Oviatt and Paulen, 2013
9	SAW05-03	Eolian	10300 ± 900	Wolfe et al., 2007
21	SAW12-22	Littoral	7130 ± 530	O'Neill et al., 2019
22	SAW12-01	Eolian	5940 ± 670	O'Neill et al., 2019
23	SAW12-03	Littoral	5060 ± 560	O'Neill et al., 2019
25	SAW12-20	Eolian	2700 ± 390	O'Neill et al., 2019
26	SAW12-21	Wedge	2630 ± 200	O'Neill et al., 2019
28	SAW12-23	Wedge	1660 ± 180	O'Neill et al., 2019
30	SAW12-02	Littoral	972 ± 82	O'Neill et al., 2019

3.3 Methods

3.3.1 Mapping

Two 1:100 000 maps of surficial geology (NTS 85C NW and NE) including surficial sediment texture, interpretation of depositional environments, and landforms were created as part of this thesis (Hagedorn et al., 2021a, Hagedorn et al., 2021b; Appendix A). These maps were used to describe basal ice sheet characteristics and refine former ice margins, meltwater drainage pathways and glacial lake extents as the LIS retreated eastward through the study area. Additional adjacent map sheets are also being completed as part of the larger GSC GEM2 project, with the NTS 85C SW being complete at the time of this research (Smith et al., 2021). The surficial maps are being published along with several other surrounding maps as part of the GSC's GEM-2 Program (Paulen et al., 2017;

Paulen et al., 2019; Hagedorn et al., 2021a, 2021b, Paulen and Smith, in prep; Smith et al., 2021; Refer to Fig. 1.5).

Maps were made using 1:60 000 scale stereo pair air photos with surficial geology interpretation drawn directly on the air photos and then digitized at the GSC. The digitization process retained the details of the original line work but cover a 1:100 000 extent. Air photos were obtained from the National Air Photo Library in Ottawa. Most of these photos were taken in the 1970's and large changes to the landscape are not expected.

Surficial mapping was aided by other remote sensing data and confirmed with fieldwork. The 2 m resolution ArcticDEM (Porter et al. 2018) and Landsat-8 imagery (courtesy of the United States Geological Survey) provided more recent remote sensing data across the study area. These high-resolution datasets showed elevation and vegetative differences that were not discernable in the legacy air photos. The accuracy of the mapping was further increased via ground truthing throughout the two field seasons (2017, 2018) at 169 stations. Many of the ground truthed locations were targeted to specifically determine unknown features observed in the air photos prior to the field season. At these locations the co-ordinates, elevation, vegetation and surficial material were recorded.

The mapping process defined surficial unit polygons, which represented the major sediment type at surface with an interpretation of its depositional environment or genesis. Delineation between surficial materials was based on a variety of characteristics such as vegetation, elevation, surface roughness, reflectance and surrounding mapped polygons. For example, taller trees on an elevated surface often characterize regions of till while low-lying areas of smaller brushes characterize regions of organics. The categories for the different sediments and environments were defined by the GSC's Surficial Data Model and include, Bedrock, Till (Subglacial), Glaciofluvial, Glaciolacustrine, Alluvial, Colluvial, Eolian, and Organics (Deblonde et al. 2012). These broad environments were then split into specific descriptors like veneer, blanket, undifferentiated, and hummocky, etc. Some of these polygons were identified as washed or contained Thermokarst; these features had an overlay placed on the polygon.

A variety of glacial landforms were also mapped in conjunction with the sediments at surface. For the majority of these landforms a line was drawn along the crest or depression of the feature. A mapped polygon unit often defined the extent of many of these linear features. For example, a moraine ridge had a line symbol drawn along the moraine ridge crest, but the spatial extent of the moraine would be defined by the Till Moraine (Tm) polygon in which the line symbol was contained. Of specific interest for the ice margin reconstructions presented in this thesis include moraines (in particular the Snake Creek Moraine), raised beach ridges, iceberg scours, and eolian dune crests, although a large number of other landforms were observed (Hagedorn et al., 2021a, 2021b).

3.3.2 Elevation Data

Elevation of shorelines represent modern elevations from the digital elevation model and are reported in meters above sea level. In this region, glacial lakes extended mostly parallel to the ice margin and previous uplift reconstructions have an consistent uplift rate across the area of about 5 mm yr^{-} (Sella et al. 2007, Wu et al. 2010, Peltier et al. 2016, Li et al. 2020). Therefore, shoreline features for a single lake lying at a similar elevation were correlated to the same lake phase. However, glacioisotatic adjustment becomes an important factor between lakes that formed at different times (Lemmen et al. 1994, Tarasov et al. 2012, Gowan et al. 2016, Roy and Peltier 2017). Specifically, glacial lake features are today at a higher elevation than when they formed, but the surface extending from older lake shorelines to younger lake shorelines is also tilted. Therefore, elevations of paleolakes are relative and the surface linking them through space and time is also tilted (Fisher and Smith 1994, Lemmen et al. 1994, Drzyzga et al. 2012, Hickin et al. 2015).

3.3.3 Dating Methods

Different dating techniques used to constrain ice margin chronologies (radiocarbon dating, optical dating and cosmogenic dating) require different materials and thereby date different events and environments. Selection of a dating technique in an area is based on availability and type of datable material, ease of sampling, and analytical cost. Cosmogenic nuclide dating was not completed for this study due in part to the paucity of large quartz-bearing erratics, which are best for dating moraines and other deglacial features (Ivy-Ochs and Kober 2008, Balco et al. 2009, Kelley et al. 2020). Local bedrock consists of carbonate rocks, which limit the applicability of the technique on exposed bedrock surfaces as fewer isotopes can be used. This method will thus not be discussed further.

3.3.3.1 Radiocarbon Dating

A radiocarbon age indicates how long ago a living organism stopped absorbing and/or exchanging carbon dioxide with its surrounding CO_2 reservoir. Today, most radiocarbon analyses are done using an Accelerator Mass Spectrometer (AMS), which measures the $^{14}C/^{12}C$ or the $^{14}C/^{13}C$ ratio of the sample and compares it to a standard (Jull 2007). It is assumed that upon death, the ratio was in equilibrium with the contemporaneous reservoir (Jull et al., 2013). However, fractionation between the heavier isotopes (^{14}C and ^{13}C) and ^{12}C occurs between reservoirs. For instance, terrestrial plants have a lower $^{13}C/^{12}C$ ratio compared to the contemporaneous atmosphere in which they grew. Furthermore, the $^{14}C/^{12}C$ fractionation is twice that of $^{13}C/^{12}C$. Changes in the global $^{14}C/^{12}C$ ratio also occur because global mean ^{14}C production rate in the upper atmosphere is affected by temporal variations in the geomagnetic field (van der Plicht 2007). To address these complications, standardization and calibration procedures must be applied to laboratory measurements. Specifically, radiocarbon ages are first reported by laboratories in ^{14}C years (Mook and van der Plicht, 1999), and are then normalized to account for isotopic fractionation between reservoirs. These ages are referred to as ‘conventional’ ^{14}C ages, which must then be calibrated to account for past variations in ^{14}C production (Remier and Remier, 2007). This allows conversions of radiocarbon ages to calendar years, which is critical for comparison to ages from other methods, such as optical dating methods. Conversions of radiocarbon ages make use of standardized, and frequently updated calibration curves, the most recent version of which is IntCal20 (Reimer et al., 2020). The age conversion suggests a range of calendar years based on the intersection of the time period on the calibration curve (Bronk Ramsey 2008, 2009). OxCal v4.4 was used for this thesis to convert radiocarbon ages to calendar years using the IntCal20 curve (Bronk Ramsey, 2020). Ages were rounded to the nearest 10 years at the end and presented at a 95% confidence limit (2-sigma; Millard, 2014). This method of conversion was used on all radiocarbon ages presented in the thesis to allow for comparison to optical ages.

Radiocarbon dating can be used on a wide range of organics but the specific organic material sampled impacts the corrections applied and, sometimes, the interpretation (Bronk Ramsey 2008, Jull et al. 2013). For example, when radiocarbon ages are used to constrain ice margin retreat, the ages are considered minimum ages, but the time lag between a peat age and ice margin retreat may be even greater than that based on a mollusk from a glaciomarine deposit. This is because it takes more time for peat to accumulate in cold environments after deglaciation than for mollusks to colonize a water basin in contact with the retreating ice margin. Additional error and uncertainty may exist also with radiocarbon ages from older sampling and laboratory methods. A critical analysis of each age is thus important.

One radiocarbon sample was collected in the study area from basal peat near the upper reaches of the Mackenzie River (Fig. 3.1). At this site, a thick deposit of peat directly overlay till, and was exposed due to undercutting of the riverbank and sediment topple (Fig. 3.3). The peat at the till contact was carefully excavated and put into a sample bag and sealed. This peat was then sent to PALEOTEC Services in Ottawa for assessment of the samples organic macrofossil content and species composition. Suitable fragments of organic material were selected for AMS radiocarbon dating at the Andre E. Lalonde AMS Laboratory in Ottawa.

Upon arrival to the laboratory sample pretreatment and processing procedures were completed following methods outlined in Crann et al. (2017) and Murseli et al. (2019) with information about equipment used as outlined in St-Jean et al. (2017). The radiocarbon analyses were performed on a 3MV tandem accelerator mass spectrometer and measured ^{12,13,14} C^{+3} ions at 2.5 MV terminal voltage. The samples were both background corrected and corrected for fractionation using AMS measured $^{13}C/^{12}C$. The fraction of modern carbon ($F^{14}C$) was calculated as the ratio of the corrected sample $^{14}C/^{12}C$ to the standard $^{14}C/^{12}C$ in the same data block (Remier et al. 2013). The actual radiocarbon ages were reported in ^{14}C yrs. BP and were calculated using the equation -8033ln($F^{14}C$) (Stuiver and Polach 1977). Error with the ages is reported as 1σ and is based on the counting statistics and $^{14}C/^{12}C$ and $^{13}C/^{12}C$ variation between the different data blocks. Full information pertaining to these dates is available in Appendix I.

Radiocarbon ages from three different size fractions (bulk, 0.17 – 4 mm and >4 mm) of peat and wood were obtained. The ages were then calibrated as described above and combined using a probability density function tool in OxCal. This tool adds the probabilities of the age ranges for each sample together to suggest the most likely age due to overlap within the individual samples age ranges.

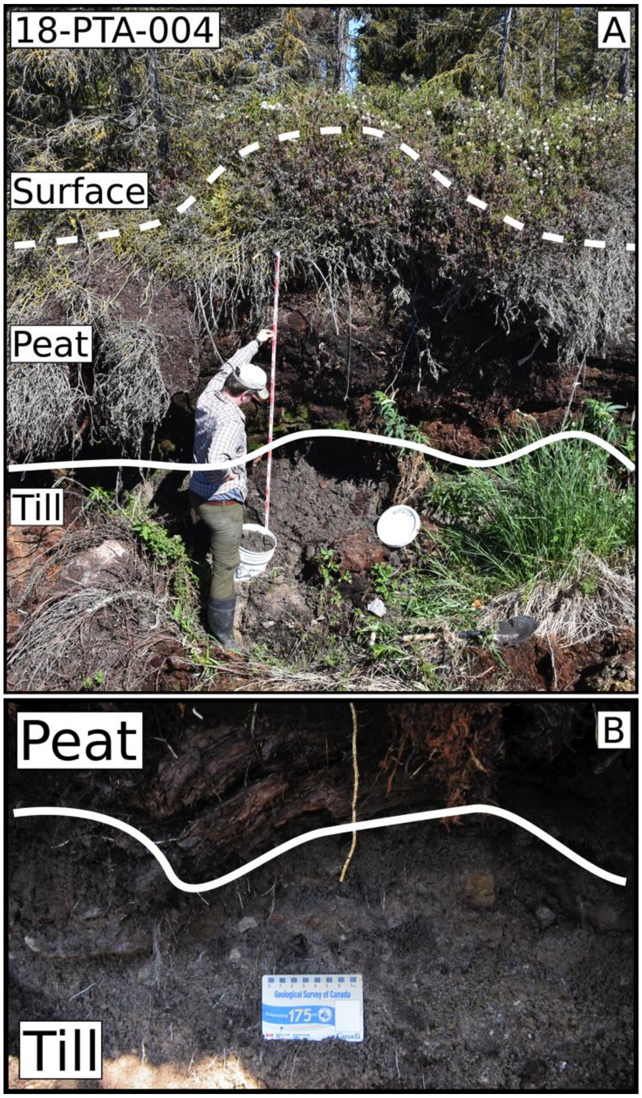

Figure 3.3: A) Stratigraphy at site 18-PTA-004 where the radiocarbon sample was collected for this thesis (See Fig 3.1 for location). B) Sample location of basal peat and wood that was in contact with till.

3.3.3.2 Optical Dating

Optical dating was also used to constrain timing of ice retreat in this study. This method determines the amount of time since sand grains were last exposed to sunlight, which normally corresponds to when grains were last transported by a sedimentary process (Lian and Roberts 2006). Radioactivity in rocks and sediment lead to some ionization within crystals and mineral grains. Electrons released by the ionization can be trapped within defects of the crystal lattice (Huntley and Lamothe 2001). The environmental radiation dose rate is assumed to be constant within and around minerals in a rock or sediment. As such, the electron trapping process from the environmental radiation dose is considered to occur at a constant rate over the whole burial time. When these minerals are eroded and transported by sedimentary processes, they generally become exposed to sunlight. Some electron traps are sensitive to sunlight and will effectively lose all their trapped electrons during sedimentary transport. Once deposited, the sand grains will again start accumulating electrons in their light-sensitive traps (Lian and Roberts 2006, Bøtter-Jensen et al. 2010, Neudorf et al. 2015). In the laboratory, electrons can be released from light-sensitive traps, and in the process, emit light whose intensity is proportional to the number of released electrons. Assuming complete resetting of the traps prior to deposition, and good estimates of the local environmental radiation dose, these measurements can give the age of the sand deposit, or more precisely when the measured sand grains were last buried by a few centimeters of additional sediment, which is sufficient to block exposure to sunlight (Huntley and Lamothe 2001).

The interpretation of the sedimentary environment is critical at every step from sampling to interpretation of optical ages. First, certain sedimentary processes provide better exposure to sunlight during sediment transport than others. Secondly, the age of certain deposits may provide more accurate age estimate for specific events than others. For instance, a beach ridge represents a specific lake level, whereas eolian sand dunes represent an ice and glacial lake free landscape. Additionally, the sample depth within a sand deposit can influence the age returned, with the deeper deposited sand being older than sand closer to the surface (Munyikwa et al. 2011). Ideally, sand from the very bottom down from the crest of the dune would be sampled to constraint the age of the beginning of that environment, but it is not always possible to access that part of a deposit.

Optical dating methods yield ages in calendar years before present (BP). They typically do not need any calibration. However, the accuracy of the age may depend on several factors, including the validity of the main assumptions (e.g. constant local radiation dose rate).

Seven optical samples were collected throughout the 2017 and 2018 field seasons (Fig. 3.1); two were collected from a GLM beach ridge at 223 m a.s.l.(Fig. 3.4) and five were collected from eolian dunes spread throughout the study area (Fig. 3.5). For the beach ridge, sand samples were collected by clearing the vertical face into what was identified as horizontally bedded sand (Fig. 3.4B and 3.4C), interpreted as upper plane beds deposited on the beach foreshore. The sediment facies was identified and the depositional environment interpreted prior to sampling. It is important to note that this location represents a unique beach ridge where sand was observed as most beaches in the region consist of open-framework, clast-supported limestone cobble and pebble-gravel. For sampling of the eolian dunes, massive fine sand was sampled at depth in a pit dug down from the crest of the dune. The crest was targeted as sediments down from the crest of the dune are likely the oldest, providing better limits on the time of land exposure and eolian sand deposition; sands from the periphery of the dune are more likely to be deposited later or remobilized (Wolfe et al. 2004) These pits were usually dug to deeper than 1.5 m to get below any influence from organics and roots. For both depositional environments, once suitable sand was found, a vertical face of freshly cleared sand was created. A 30 cm long, 5 cm diameter black plastic tube was hammered horizontally into this vertical section until the tube was completely filled with sand (See Appendix G for details). A 1-litre bag of sand from the sampling depth was also collected for investigations of particle size, moisture and lithic content. Once full, it was excavated and both ends capped to prevent light exposure before transport to University of the Fraser Valley (UFV) for processing and analysis.

At UFV, the outer portions of the tube were removed in a dark room. A portion of the sand was separated to determine concentrations of ^{40}K, Th, U, and Rb using neutron activation analysis. The 180-250 um sand-sized fraction was then acid treated to remove carbonates and organic materials, after which quartz and K-feldspars were concentrated using heavy liquid separation. The fading rates from the separated K-feldspar grains were used because sample 17-SUV-077 had analytical issues with its “weak” fast component quartz. After treating the K-feldspar grains to remove aging issues caused by the grains outer rim, they were mounted for analysis using a Risø TL/OSL DA-20 reader with a calibrated 90Sr/90Y β source that delivered ~5–6 Gy/min of β particles (Bøtter-Jensen et al., 2010). Analysis was completed at 50°C with the grains being stimulated by infrared light

In order to determine the age of a sample, the equivalent dose (D_e) using a single-aliquot regenerative dose (SAR) approach was used with ~100 grains aliquots. The D_e values were validated through a dose recovery experiment whereby grains were bleached in direct sunlight then had a ~20 Gy laboratory dose applied to record the given dose rate. The measured/given dose ratio was 1.01 ± 0.1, validating the SAR method. Furthermore, fading ratios were obtained from 12 aliquots of each sample from an infrared stimulated luminescence signal. The fading rate for correction was obtained from the Huntley and Lamothe (2001) model. To further ensure usability of the ages, over dispersion values were calculated and all values were less than 18%, suggesting that the grains were sufficiently exposed to sunlight and reset before subsequent burial, except for sample 18-PTA-028. For the latter, an over dispersion of 37% was observed and an age was calculated using the Minimum Age Model (MAM). The difference between the MAM and the Center Age Model (CAM) was insignificant, allowing the use of the CAM for all samples. Ages were calculated using a CAM on the weighted mean equivalent dose values and the environmental dose rate (Galbraith and Laslett, 1993; Galbraith et al., 1999). Similar to the radiocarbon ages, the optical ages were combined in OxCal to create a probability density function (see Sect. 3.3.2.1). A probability density function was completed on the beach ridge samples (n=2) and also the five eolian dune samples separately as they two types of locations represent different depositional processes.

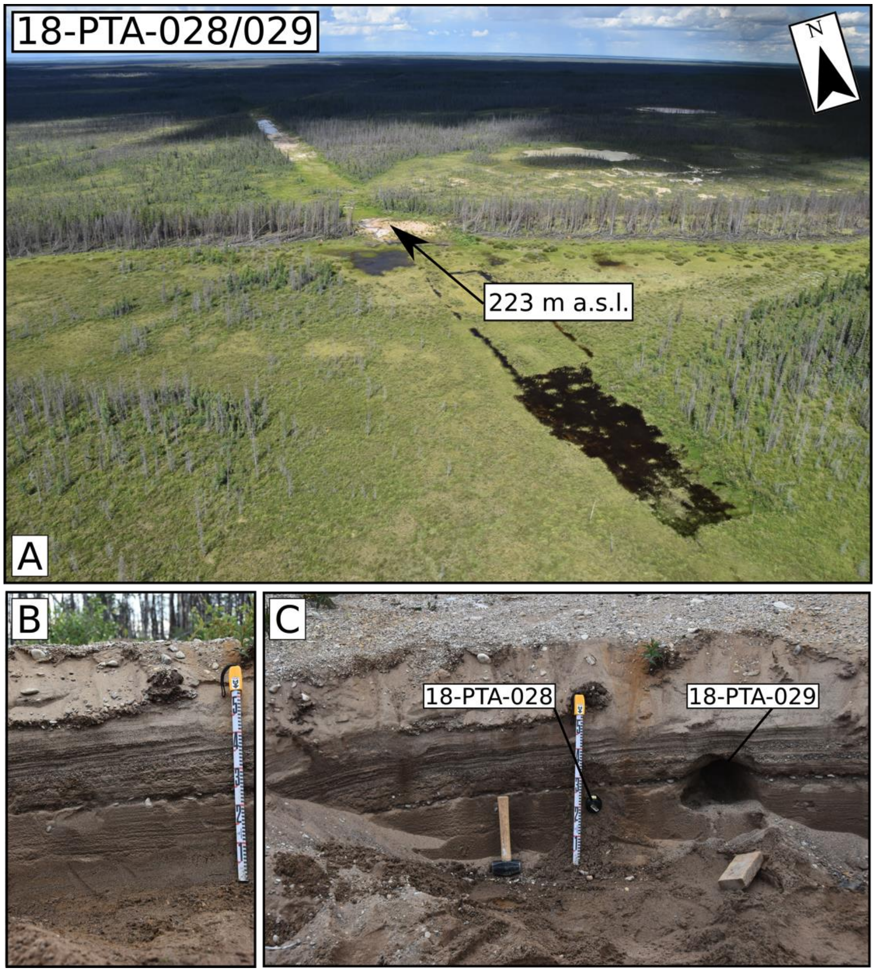

Figure 3.4: A) Image from helicopter showing the beach ridge at 223 m a.s.l.where 18-PTA-028 and 18-PTA-029 were taken. B and C show the stratigraphy of the beach ridge with upper-plane beds dipping the north. Care was taken at this site to remove the surface sand that may have been exposed to sunlight to not skew the optical ages returned.

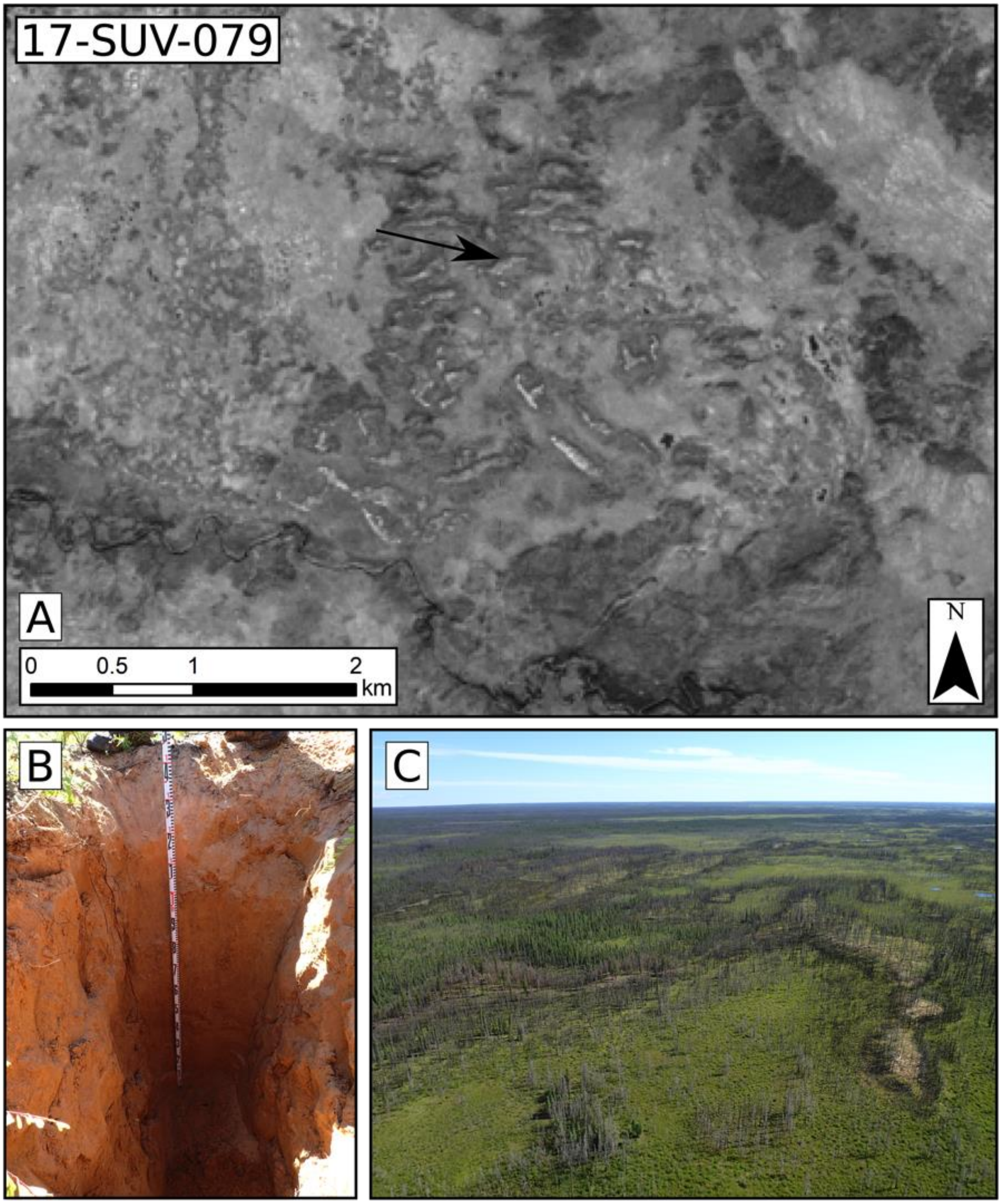

Figure 3.5: A) Landsat 8 Band 8 image of the dune field where 17-SUV-079 was taken (See Fig. 3.1 for location). B) Pit dug to sample sand within dune. C) Areal photo of the dune.

3.4 Results

3.4.1 Surficial Geology

3.4.1.1 Till (T)

Till at surface was common in the study area. Till veneers occurred along escarpments and atop bedrock knobs, whereas till blanket occurred elsewhere, reaching up to 25m in thickness east of the escarpment (Smith and Lesk-Winfield, 2010; Fig 3.6A). Landforms on the till sheet included hummocky topography along the northeastern shore of Tathlina lake and streamlined ridges (e.g. drumlins) in the center of the study area and below the escarpment (Fig 3.6 B; C). Drumlins below the escarpment appear subdued (<5m in amplitude) and terminate at transverse to ice flow thrust blocks also composed of till, mapped as till ridges (< 5 m thick). Streamlined till was also found atop the Cameron Hills as mega-scale glacial lineations (Fig. 3.6D). For interpretation of how the streamlined till features integrate into the ice flow reconstruction of the region refer to Chapter 2 of this thesis.

A series of prominent ridges form a larger recessional moraine complex, the Snake Creek Moraine, along (both above and below) the eastern escarpment (Lemmen et al., 1994; Bednarksi, 2008). These moraine ridges are individually discontinuous, sub-parallel, about 4 m high, and composed of washed till at surface due to extensive reworking by GLM, commonly observed as a winnowing of sediments on their surface or as superimposed beach ridges. The ridges locally have small lakes and fen in the low-lying areas between them. Together the ridges form a complex up to 1.5 km wide that stretches for 120 km trending northwest-southeast.

The composition of the till found throughout the study area is explained in detail in Chapter 2. Four compositionally different tills have been identified in the region ranging from a ‘distal’ higher Canadian Shield content end member to a ‘local’ Paleozoic carbonate end member. Till in the study area is winnowed in many places, which is characterized by a thin (<0.5m) and discontinuous layer of openwork cobble boulder lag at the surface of the till. This facies helps determine where glaciofluvial and/or glaciolacustrine winnowing processes have occurred.

3.4.1.2 Glaciofluvial (GF)

Glaciofluvial sediments are limited in the study area. Of particular interest for ice margin reconstructions are meltwater systems that formed under the ice sheet, at the ice sheet margin, and at outlets from ice-dammed proglacial lakes. Four meltwater systems were observed in the study area. A system to the east of Tathlina Lake, a system just south of Kakisa Lake between bedrock highs, a system along the upper reaches of the Kakisa river at the outlet from Tathlina lake, and a system west of the Snake Creek Moraine.

The northern portion of the meltwater systems east of Tathlina Lake consists of two large well-defined major meltwater corridors with ice-contact glaciofluvial sediments on their eastern flanks (Fig 3.6C). These ice-contact sediments are poorly-sorted sand and gravel with minor diamicton and are < 2m thick. A major meltwater corridor and esker ridge defines the southern portion of this system that extends to the northern tip of the Cameron Hills. All channels within this meltwater system have fans on their western ends indicating westward flow into Tathlina Lake.

The meltwater system south of Kakisa Lake is a deeply incised channel (~ 25 m) with limited glaciofluvial sediment (Fig 3.6E). It has well-defined lateral margins and indicates meltwater drained to the northwest off the western escarpment. There does not appear to be any fan or delta associated with this meltwater corridor, although it is located at the westernmost extent of the study area.

The meltwater system that surrounds the Kakisa River at the outlet of Tathlina Lake has a series of meltwater channels with glaciofluvial contact and hummocky sediments to the northeast (Fig. 3.6F). These hummocks and ice-contact sediments consist of poorly-sorted sand and gravel with minor diamicton. The channels of this meltwater system are short, thin and anastomosing, often with glaciofluvial plain sediments surrounding or contained within the channels. These plain sediments are low relief, < 2m thick, composed of gravel, sand and minor silt, moderately sorted and massive to crudely stratified. The meltwater within these channels flowed to the north evidenced by a fan at their northern extent between Kakisa and Tathlina lakes. The northward drainage was in the same direction as the modern Kakisa River, but the extent of the glaciofluvial system is well outside the modern floodplain.

The final meltwater system is the largest. It consists of subaerial meltwater channels west of the Snake Creek Moraine. The subaerial meltwater channels are small and represent a braided river system that flowed to the northwest terminating as a fan deposit. Glaciofluvial plain sediments were deposited within the channels and are surrounded by washed till to the north and south. Along the eastern extent of this meltwater complex is a large deposit of glaciofluvial ice-contact sediments which have been also locally reworked by glaciolacustrine processes (Fig. 3.6G). Additionally, a larger meltwater channel flowed to the northeast and overprinted the smaller meltwater channels (Fig. 3.6G).

Other glaciofluvial sediments of note include small glaciofluvial fans found west of breaks between moraine ridges (Fig 3.6A). These fans are sometime connected to esker systems on the moraine's eastern (up-ice) side. These esker and subaqueous fan systems are typically small and often reworked by glaciolacustrine action.

3.4.1.3 Glaciolacustrine

Glaciolacustrine sediments were deposited in proglacial lake basins limited to the northeastern sector of the study area and surrounding Tathlina Lake. Glaciolacustrine sediments are typically < 2 m thick and massive to poorly stratified. Littoral sediments are composed of sand and silt often deposited in-between beach ridges. These beach ridges were composed of cobble-gravel to sand and have a relief of ~ 2 m. Beach ridges can be traced for 100s of meters to kilometers across the landscape and are subparallel. A delta was also found at the terminus of the Cameron River north of the Cameron Hills indicating meltwater flowed into a proglacial lake (Fig. 3.6H).

Iceberg scours are associated with the glaciolacustrine sediments and two groupings are observed. One grouping occurs on the northern flank of the Cameron Hills (Fig 3.6H). These iceberg scours trend northwest – southeast to northeast - southwest and are short and sparse. The second grouping of iceberg scours is more prevalent on the landscape and occur extensively below the escarpment (Fig. 3.6B). These scours trend northwest southeast and are longer than others in the study area. They often end on upland regions of till, but some crosscut the streamlined and ridged till.

3.4.1.4 Post-Glacial Sediments

A variety of other sediments were found at surface whose origin is related to postglacial processes. Eolian (E) dunes were observed in several patches throughout the study area, often in proximity to glaciofluvial or glaciolacustrine sediments. Dunes indicate eastward and westward wind directions based on parabolic and transverse morphologies. These dunes are typically > 2 m thick and composed of fine to medium well sorted sand (see Fig. 3.5 and Appendix G for details).

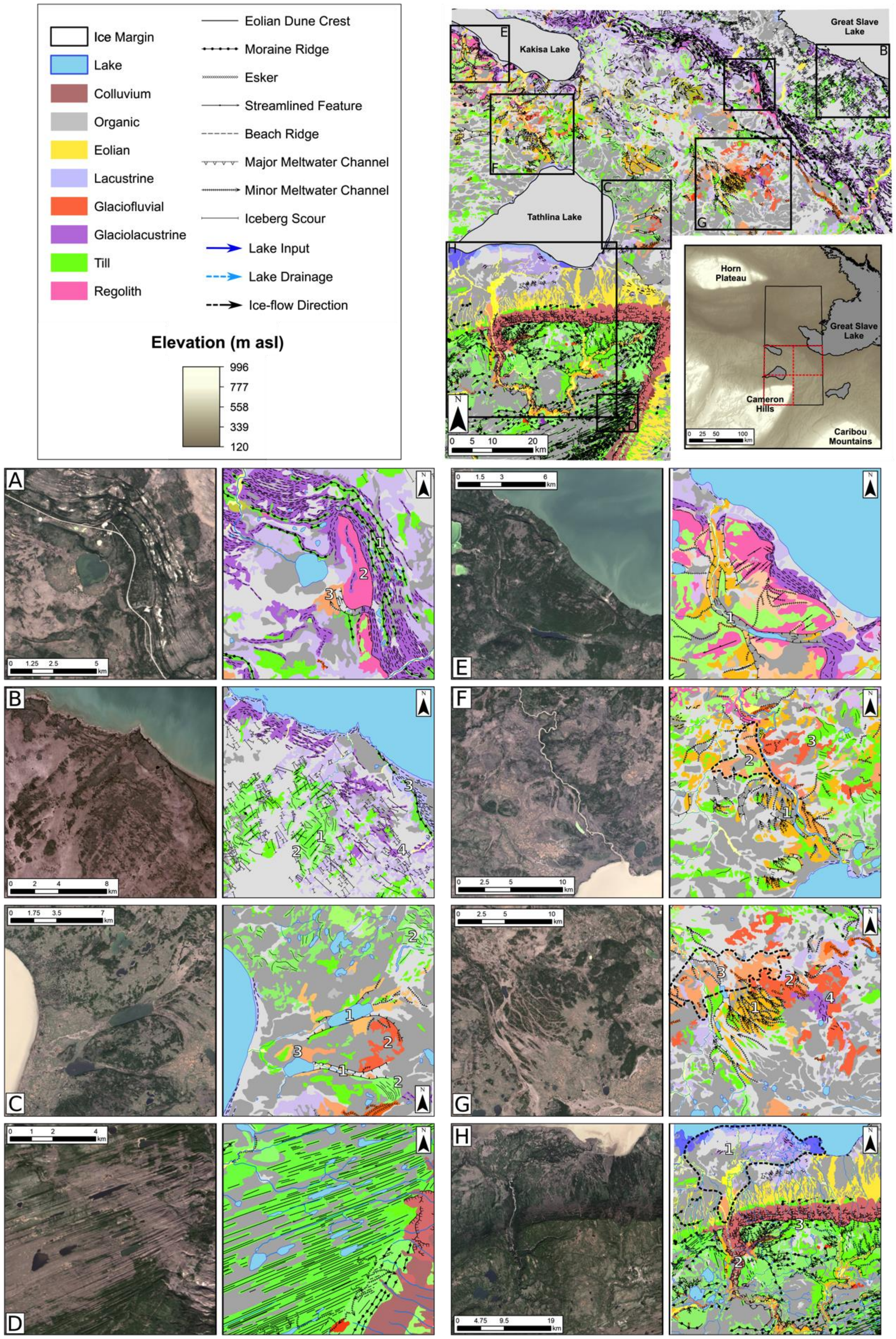

Figure 3.6: Examples of sediment-landform assemblages in the study area. The left images are Landsat8 pan-sharpened true-colour images, whereas the figures on the right correspond to the associated mapped surficial geology. See larger map for locations of panels A) Snake Creek Moraine ridges (1) along bedrock escarpment (2) with meltwater channel and fan breaking through moraine (3). B) Streamlined landforms (1) and thrust blocks (2) below the bedrock escarpment. A moraine ridge (3) is observed close to the shore of Great Slave Lake and iceberg scours (4) cover the landscape. C) Meltwater channel system east of Tathlina Lake. The meltwater channels (1) have till ridges and glaciofluvial contact sediments to their eastern boundary (2) and a fan at the western outlet (3). D) Mega-scale glacial lineations atop the Cameron Hills. E) Deeply incised (25 m) meltwater channel (1) system south of Kakisa Lake. F) Meltwater channel (1) system at the outlet of Tathlina Lake. A fan (2, outlined) is observed at the northern end of the meltwater channels. Till ridges and ice-contact glaciofluvial sediments (3) also occur in this area. G) Meltwater channel system east of the Snake Creek Moraine. Meltwater channels terminate (1, 2) at a glaciofluvial fan (3, outlined). Ice-contact glaciofluvial sediments are also locally winnowed and reworked into beach ridges (4). H) Glaciolacustine delta (1, outlined) at the outlet of the Cameron River. Also observed is the deep incision of the Cameron River (2) and the moraine ridges on the northern flank of the Cameron Hills (3).

Other post-glacial sediments include alluvial (A) sediments found along modern rivers and within small alluvial fans as streams crossed the eastern escarpment. Colluvial (C) sediments are found along the flanks of the Cameron Hills, along some slopes of bedrock highs, and at the banks of bedrock incised river channels. Lacustrine (L) sediments were also deposited from Holocene lakes in the region as their water levels decreased due to isostatic adjustment. These lacustrine sediments were differentiated from glaciolacustrine sediments based on inferred time of deposition, with lacustrine sediments being quite limited and surrounding present lake basins. Finally, organics (O) cover large expanses of the study area in the form of bogs and fens. These bogs and fens are locally frozen as indicated by thermokarst terrain.

3.4.2 Geochronology

3.4.2.1 Optical ages

Optical dating results are listed in Table 3.3. The PDF of the two ages from the beach ridge shows a peak at 12 ± 0.7 ka BP (Fig 3.7, blue). The seven eolian dune ages show two peaks on a PDF (Fig. 3.7, orange). The first peak is higher and at 10.4 ± 0.3 ka BP derived from five of the seven eolian optical ages (17-SUV077, 17-SUV-079, 17-SUV-080, 11-PTA-105A, 11-PTA-105B). The second peak is at 8.2 ± 0.4 ka BP, which is formed by two younger ages (18-PTA-022, 18-PTA-028). The two clusters of ages do have a slight overlap, thereby causing the two-peaked eolian PDF.

3.4.2.2 Radiocarbon ages

Six radiocarbon ages were obtained from the one organic sample collected at 18-PTA-004. Results are listed in Table 3.4. Five of the six ages suggest a similar onset for organic formation; bulk peat being the lone sample. The five similar ages gave a highest probability overlap at 2.35 cal. ka BP but the total PDF ranges from 2.7 – 2.1 cal. ka BP (Fig. 3.8). The bulk peat sample yielded an older age range from 3.2 to 3.0 cal. ka BP and did not overlap with any of the other five radiocarbon ages (Fig. 3.8).

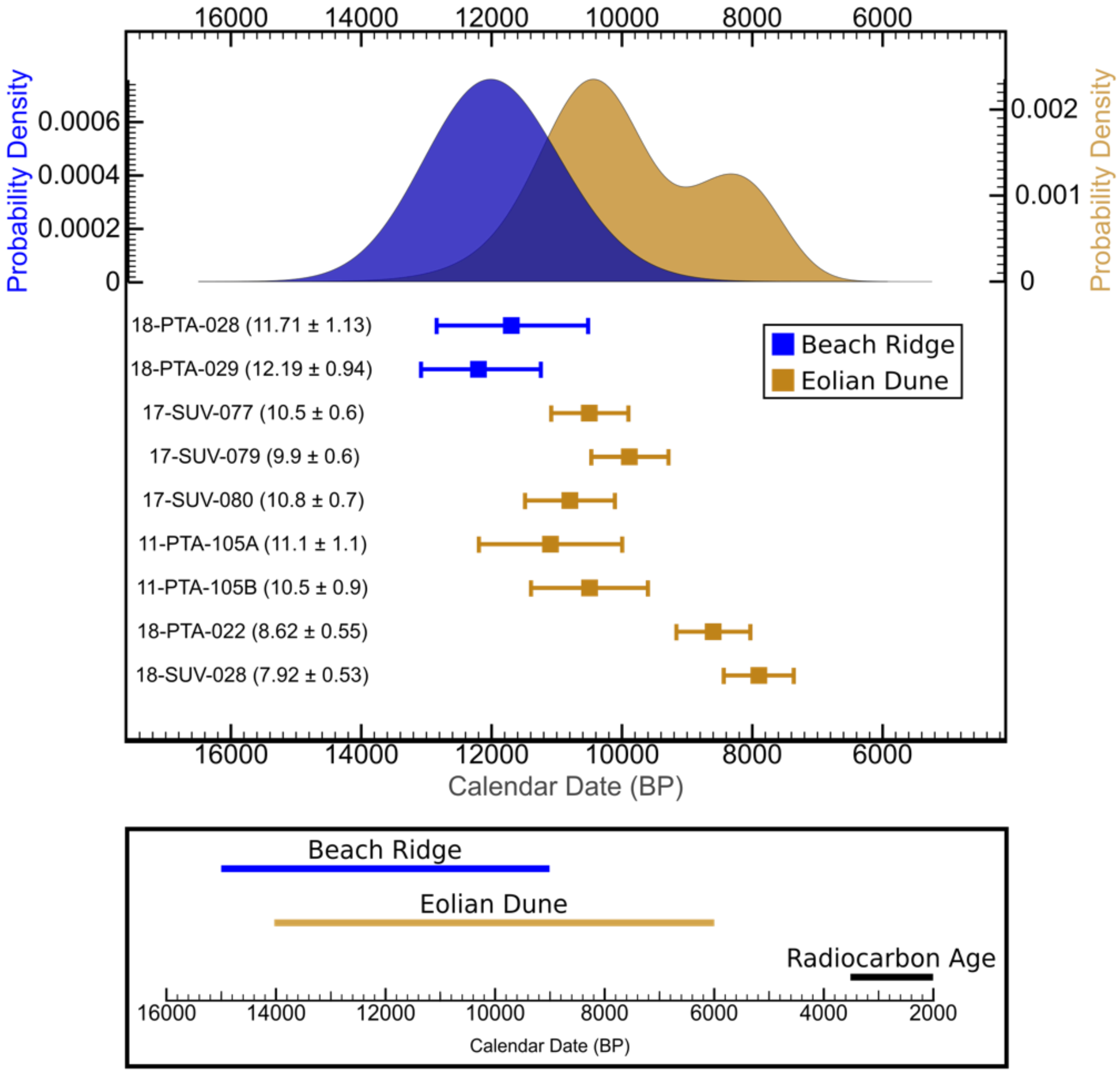

Figure 3.7: Age probability curves for optical results from the beach ridge (blue) and the eolian dunes (orange). Refer to Figure 3.1 for locations. Individual corrected CAM ages with 1 sigma error are plotted below the curves and are reported in ka beside their sample ID. Beach ridge ages form a peak at 12 ± 0.7 and eolian samples show two peaks at 10.4 ± 0.3 and 8.2 ± 0.4 ka BP. Lower chart indicates the full range from different environments and methods (radiocarbon explained below).

Table 3.3: Optical dating results. Further information on the samples and results (e.g., D_e, Fading rates) is included in Appendix H.

Station	Latitude	Longitude	Sample Media	Elevation (m a.s.l.)	Sample Depth (m)	Corrected Age (BP)
17-SUV-077	60.7829	117.3367	Eolian Dune	253	1.35	10500 ± 900
17-SUV-079	60.8173	117.1974	Eolian Dune	244	1.4	9900 ± 600
17-SUV-080	60.9371	117.1212	Eolian Dune	231	1.4	10800 ± 700
18-PTA-028	60.9216	117.1287	Beach Ridge	223	0.7	11710 ± 1130
18-PTA-029	60.9216	117.1287	Beach Ridge	223	0.65	12190 ± 940
18-PTA-022	60.7220	115.1062	Eolian Dune	221	1.6	8620 ± 550
18-SUV-028	61.4451	116.8202	Eolian Dune	199	1.45	7920 ± 530

Note: All ages presented are calculated using CAM (described above). For 18-PTA-028 the over dispersion was higher (37%) and equivalent dose and age was found using the MAM with an insignificant difference.

Table 3.4: Radiocarbon ages from 18-PTA-004. Further details are included within Appendix I.

Sample	Latitude	Longitude	Material	Sample Depth (m)	Age (^{14}C years)	Age (cal. ka BP)
18-PTA-004	61.0628	116.5655	Peat (bulk)	3.5	2917 ± 26	3.16-2.96
18-PTA-004	61.0628	116.5655	Peat (1.70 – 4 mm)	3.5	2247 ± 30	2.34 – 2.15
18-PTA-004	61.0628	116.5655	Peat (> 4 mm)	3.5	2351 ± 29	2.47 – 2.33
18-PTA-004	61.0628	116.5655	Wood (bulk)	3.5	2451 ± 22	2.70 – 2.36
18-PTA-004	61.0628	116.5655	Wood (1.70 – 4 mm)	3.5	2373 ± 26	2.49 – 2.34
18-PTA-004	61.0628	116.5655	Wood (> 4 mm)	3.5	2421 ± 25	2.70 – 2.35

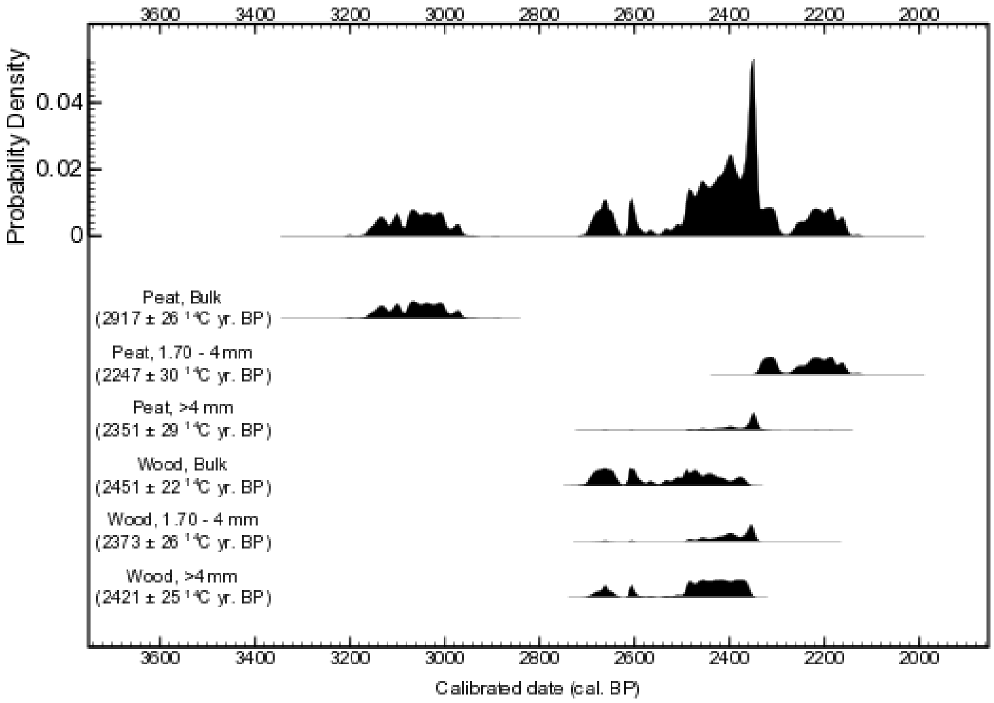

Figure 3.8: Probability Density Functions (PDF) of the radiocarbon ages from peat and wood samples collected at 18-PTA-004. The different ages are from different size fractions used for analysis. Functions for each graph show the converted age to cal. ka BP with the ^{14}C age shown beside the sample label to the left. These values are also displayed in Table 3.4. The composite PDF at the top of the figure show a highest likelihood of organic deposition at a 2.35 cal. ka BP. Note the peat bulk PDF plots outside of the main age distribution with a 3.2 to 3.0 cal. ka BP age range at 2-sigma error.

3.5 Ice Margin Reconstruction

A sequence of ice margin positions and proglacial lakes are reconstructed based on observations from surficial sediments, landforms, and topography from the 2m resolution ArcticDEM. A detailed description of the observations used for each margin is given in Table 3.5. Ice margins highlight important periods during the deglaciation of the study area, but only limiting ages were obtained as part of this thesis to constrain their timing. As such, the margins presented here are broadly correlated to the other reconstructions in Section 3.6.1 to provide approximate time estimates, but issues within these chronologies exist (Munyikwa et al. 2017, Kelley et al. 2020, Stoker et al. 2020). Each ice margins is discussed in detail below.

Table 3.5: Summary table of criteria used to delineate each ice margin.

	Sedimentology	Landforms	Topography
Margin 1	- Till moraine on the northern flanks of the Cameron Hills - Thick glaciofluvial sands and cobbles sequence atop the Cameron Hills - Glaciolacustrine nearshore, ridge and delta sediments north of the Cameron Hills	- Moraine ridges along the Northern flanks of the Cameron Hills - Deeply incised meltwater channels atop the Cameron Hills - Delta at former inputs levels from Cameron River and Kakisa River - Beach ridges along the northern and southern extents of the basin including on the delta - Ice berg scours on the delta from the Cameron River	- Ice margin along the flanks of Cameron Hills - Ice margin follows decreasing topography down the Mackenzie River - Glaciolacustrine delta at 275 a.s.l.at input from Kakisa River - Glaciolacustrine delta at 290 m a.s.l.at input from Cameron River - Beach ridge at 275 – 290 m a.s.l. - Lake topographically impounded against the ice sheet to its east
Margin 2	- Glaciofluvial contact and ridged till to the east of meltwater channels - Glaciofluvial fans at west end of meltwater channels - Limited glaciolacustine nearshore and ridge deposition	- Meltwater channels east of Tathlina Lake - Deeply incised meltwater channel south of Kakisa Lake - Till ridges to the east of meltwater channel - Beach ridges at southern extent of Tathlina lake	- Ice margin follows western escarpment (280 m) west down the Mackenzie River Valley and turns northward at end of escarpment - Ice margin follows 280 m contour to arc down Hay River Valley - Opening of outlet south of Kakisa lake at 265 m a.s.l.defines lake level

Table 3.5 continued.

	Sedimentology	**Landforms**	**Topography**
Margin 3	- Glaciofluvial contact and hummock sediments along the Kakisa River - Ridged till to the east of the glaciofluvial sediments - Glaciofluvial terrace and plain sediments along meltwater channel complex at outlet of Tathlina Lake - Glaciofluvial fan sediments at northern terminus of meltwater channels	- Ridges in glaciofluvial contact glaciofluvial hummock and till along the Kakisa River - Meltwater channel complex at outlet of Tathlina lake - Deeply incised meltwater channel south of Kakisa Lake	- Ice margin at or below the crest of the western escarpment and follows this feature down the Mackenzie River Valley - Similar level of ice retreat across the margin - Outlet south of Kakisa Lake is in use to 245 m a.s.l.

Table 3.5 continued.

	Sedimentology	Landforms	Topography
Margin 4	- Glaciofluvial contact sediments just west of Snake Creek Moraine - Glaciofluvial ridge sediments feeding fan deposit - Glaciofluvial fan attached to meltwater channels - Glaciolacustrine nearshore and ridge sediments below 240 m a.s.l. - Winnowing of surficial sediments below 240 m a.s.l.	- Minor meltwater channels crosscut by Major meltwater channel just west of Snake Creek Moraine - Beach ridges along 240 m a.s.l.specifically around bedrock knobs south of Kakisa Lake - Lack of ice burg scours	- Ice blocking lowest outlet to feed major meltwater channel released by lake in Hay River Valley from Hay Lobe - Ice margin follows 260 m contour down the Mackenzie River Valley between the two escarpments - Ice Margin constrained by Ice Margin 3 blocking drainage of proglacial lake and Snake Creek Moraine of Margin 5 - Outlet through western end of Kakisa Lake - Water level at approximately 240 m a.s.l. - shallow proglacial lake

Table 3.5 continued.

	Sedimentology	**Landforms**	**Topography**
Margin 5	- Till moraine sediments of the Snake Creek Moraine - Subaquatic glaciofluvial fans at outlets of eskers and meltwater channels through the Snake Creek Moraine - Glaciolacustine nearshore and ridge sediments west of Snake Creek Moraine - Winnowing of sediments, specifically the glaciofluvial contact sediments of Margin 4	- Snake Creek Moraine ridges - Meltwater channels and esker ridges breaking thought Snake Creek Moraine - Hummocks (often filled with lakes) between moraine ridges - Beach ridges west of Snake Creek Moraine	- Ice margin along eastern escarpment down into the Mackenzie River Valley (follows Snake Creek Moraine) - Lake levels and depth similar to Margin 4 - Outlet of lake still west though Kakisa Lake
Margin 6	- Streamlined and ridged till below the escarpment - Till moraine close to the shore of Great Slave Lake - Glaciolacustrine nearshore and ridge sediments below eastern escarpment - Winnowing of Snake Creek Moraine and sediments below the eastern escarpment	- Glacial lineations with thrust blocks - Small moraine ridge close to shore of Great Slave Lake - Abundant ice burg scours below the eastern escarpment - Continuous sub-parallel beach ridges	- Ice margin follows 160 m a.s.l.contour defined by small moraine in study area and down into the Mackenzie River Valley - Water level at 240 m a.s.l.but deeper basin due to elevation different between areas above and below eastern escarpment - Outlet down the Mackenzie River Valley, similar to modern day
Water Level 223 m	- Glaciolacustine nearshore and ridge sediments (cobble and sand) - Reworking and modification of Snake Creek Moraine	- Continuous sub parallel beach ridges	- 223 m a.s.l.beach ridge in the study area - Glacial Lake McConnell outlet down the Mackenzie River, draining due to isostatic rebound and incision of outlet

Table 3.5 continued.

	Sedimentology	Landforms	Topography
Water Level 200 m	- Glaciolacustrine nearhshore and ridge sediments - Eolian sands remobilized from previously deposited glaciolacustrine and glaciofluvial material	- Continuous sub-parallel beach ridges - Transvers and parabolic eolian dunes indicating a westward paleo-wind direction	- 200 m a.s.l.beach ridge in the study area - Optical age of dune related to elevation due to exposure to eolian processes as water level retreated - Glacial Lake McConnell outlet down the Mackenzie River, continuing to drain due to isostatic rebound and incision of outlet

3.5.1 Margin 1

Ice Margin 1 is the oldest in the study area and is recorded primarily by moraines on top of the Cameron Hills (Smith et al., 2021a; Fig 3.6H; 3.9). These moraines indicate the ice sheet was sufficiently thick behind the margin to create a moraine at ~500 meters above surrounding terrain. Deep meltwater channel incisions atop the Cameron Hills also provide evidence for relatively large volumes of meltwater supplied by the ice sheet. The incision and path of the meltwater shows that northward drainage of the Cameron River channel was blocked until ice moved northeastward, causing southwestward drainage (Smith et al., 2021a). With subsequent retreat the opening of drainage to the north created a large delta. This delta was deposited in an embayment within the ice margin and into a glacial lake that stretched along the northern margin of the Cameron Hills (Fig 3.9).

The ice sheet extended overtop the western escarpment and down the Mackenzie River valley forming the Mackenzie Lobe (Lemmen et al. 1994, Dyke 2004, Bednarski 2008, Dalton et al. 2020). Ice margin 1 is also considered coeval to lobes of ice that extended out of the GSL region north of the Horn Plateau and south down the Hay River valley (Fig. 3.9; inset map). The reconstructed margin also surrounded the Caribou Mountains and extended down the Peace River valley to the southeast (Mathews, 1980; Lemmen et al., 1994; Paulen et al., 2007; Brown, 2012; Utting and Atkinson, 2019; Fig. 3.9; inset map). These correlations are explained in more detail within Section 3.6.1.

The southwestward and westward ice flows described in Chapter 2 preceded Margin 1. At the time of Margin 1, ice flow was topographically controlled, especially by upland regions, escarpments, and valleys (Mathews 1980, Lemmen et al. 1994, Paulen et al. 2007, Bednarski 2008, Margold et al. 2018) as indicated on Fig. 3.9 (inset map) and as described in Chapter 2 of this thesis.

There was one proglacial lake in the study area at the time of Margin 1 (Fig. 3.9). It was a 90 km long lake transverse to the ice margin that filled a basin north of the Cameron Hills. This lake had a surface reaching a maximum elevation of 290 m a.s.l.in close proximity to the ice margin, evidenced by beach ridges along the Cameron Hills, glaciolacustrine nearshore sediments, and the delta formed from northward meltwater drainage along the Cameron River (Fig. 3.9). The western extent of the lake had a maximum limit at 275 m a.s.l.and was defined by shoreline and the delta at the outlet of the Kakisa River west of the study area (Rutter and Boyden, 1972). The two uppermost shorelines can be traced around the southern and northwester portions of the lake. The morphologies observed in remotely-sensed data of the proposed raised delta show a deranged drainage network indicative of fluvial progradation onto a delta due to lake lowering. This proglacial lake also facilitated the creation of small and short iceberg scours on the northern flank of the Cameron Hills.

No outlet for the proglacial lake north of the Cameron Hills was identified in this research. The lake was topographically constrained to the north, south, and west, and was blocked by the ice sheet to the east. One possibility is that this lake was short-lived in a closed basin until the ice margin retreated further to the east and exposed a natural outlet (i.e. at Margin 2). Alternatively, the lake perhaps was draining subglacially to the northeast through Tathlina Lake (Fig. 3.9). However, this would require the potentiometric surface in the ice to be lower than the lake level, which is unlikely. In addition, no evidence for subglacial drainage was found to support this scenario, but it could either not be preserved or hidden under current day Tathlina Lake.

The proglacial lake was oriented transverse to the ice margin meaning its shorelines were impacted by differential glacioisostatic adjustment. A transect through the lake shows that the highest continuous beach ridge shows this adjustment (275 vs. 290 m; Fig 3.10 Transect A – A’). This gives a rate of about 0.25 m per km that is similar to regional rates suggested by other researchers (Lemmen et al., 1994; Gowan et al., 2016). Beach ridges are at similar elevations across the narrow lake as this orientation is approximately parallel to the ice margin retreat and therefore isobases (Fig. 3.10 Transect B - B’).

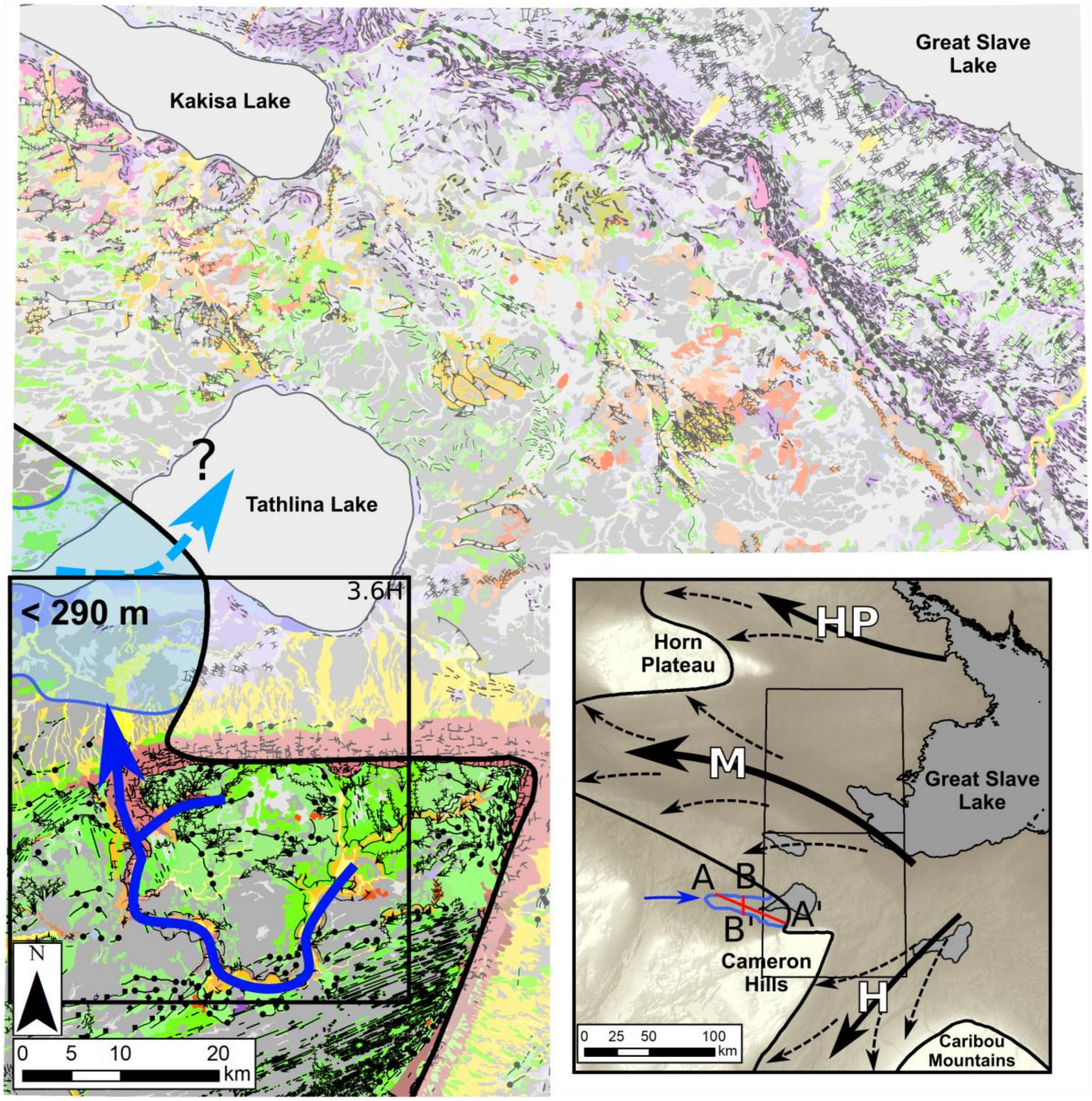

Figure 3.9: Margin 1 reconstruction. Legend same as Fig. 3.6, locations of relevant sediment landform associations from Fig. 3.6 indicated. Key features – Ice around the Cameron Hills above escarpments, Ice lobes down river valleys (M=Mackenzie lobe; H=Hay lobe; HP=North of Horn Plateau lobe), glacial lake north of the Cameron Hills at 290 m a.s.l., inputs from the Cameron River creating large delta, drainage unclear either subglacial or no drainage at all.

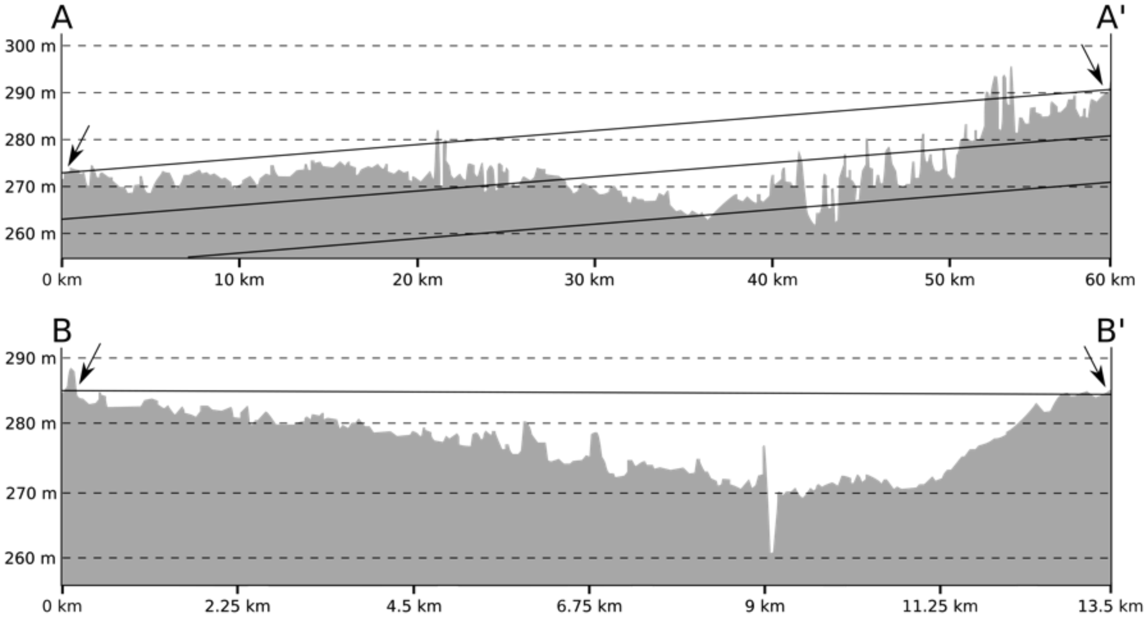

Figure 3.10: Elevation transects of the lake north of the Cameron Hills. Refer to Figure 3.9 above for locations. The A to A' transect links the uppermost beach ridge (indicated with arrows) that is traceable along the lake, transverse to the ice margin. The solid lines represent the isobase connecting the two shorelines, a change in lake level of approximately 15 m over 60 km or a rate of 0.25 m/km (275 m at A to 290 m at A'). The transect across the lake shows similar elevations for the uppermost strandlines (indicated by arrows) at 285 m. Notice the line connecting the beach ridges is virtually parallel to present elevations.

3.5.2 Margin 2

Following Margin 1, the ice margin retreated by ~ 30 km north of the Cameron Hills to the western escarpment and extended around the southern slopes of the Cameron Hills along the 280 m contour (Fig. 3.11). The southern lateral margin of the Mackenzie lobe followed the western escarpment before turning northward at the end of the escarpment. All the lobes in the area experienced further retreat up their respective valleys including the Mackenzie, the Hay, the Peace lobes, and the lobe north of Horn Plateau. The Hay River lobe retreated more than the others in the study area, perhaps because of the lower topography, size and thickness of the lobe and possible differences in subglacial conditions.

Ice flow towards Margin 2 remained similar in organization and direction as during Margin 1. There was northwestward ice flow into the Mackenzie and Horn Plateau lobes, although the erosive power was perhaps weakened at that stage due to a thinning ice sheet. To the south of the study area there was still southwestward flow into the Hay lobe (Bentley et al. 1979, Stokes et al. 2015, Margold et al. 2018).

As the ice margin retreated off the Cameron Hills, meltwater locally ponded and produced small lakes between the northern and northeastern slopes of the Hills and the ice sheet

(Fig. 3.6 H). The main change to the meltwater system, from Margin 1 to Margin 2, was the opening of a new drainage outlet located just south of Kakisa Lake (Fig. 3.6E). The outlet is at 265 m a.s.l., which controlled the lake level shown on Figure 3.11. This lake was located over the Tathlina Lake basin and extended northward along the ice margin to the outlet.

Glaciolacustrine deposition appears to have been limited in the proglacial lake during Margin 2, which is mainly defined by shorelines along its southern extent, and small deltas on its eastern margin. Most of the eastern side of the lake was in contact with the ice sheet, except a small area on the southeastern side (Fig. 3.6C; 3.11). There, a series of short meltwater channels connected to small deltas to indicate westward subaerial meltwater flow from the ice margin into a proglacial lake (Fig. 3.6C; 3.11). Ice-contact glaciofluvial sediments at the upstream end of the meltwater channels (Fig. 3.6C; 3.11) provide additional constraints to the position of Margin 2 at that time. The apparent systems tract of ice-contact sediment, meltwater channels, and deltas suggest a contemporaneous sediment-landsystem.

The lack of glaciolacustrine deposition in the northern portion of the lake could indicate the lake was short-lived although due to GIA uncertainties with absolute lake levels exist. The outlet south of Kakisa Lake was incised deeply (25 m) and there is also little glaciofluvial deposition in that area (Fig 3.6E), which suggests sustained erosion and rapid drainage. Additionally, inputs into the lake were waning; the Cameron River was no longer being fed by meltwater and glaciofluvial features on the ice-contact and ice-proximal side of the lake are small. This drainage outlet south of Kakisa Lake was flowing northwest out of the map area (Fig. 3.11).

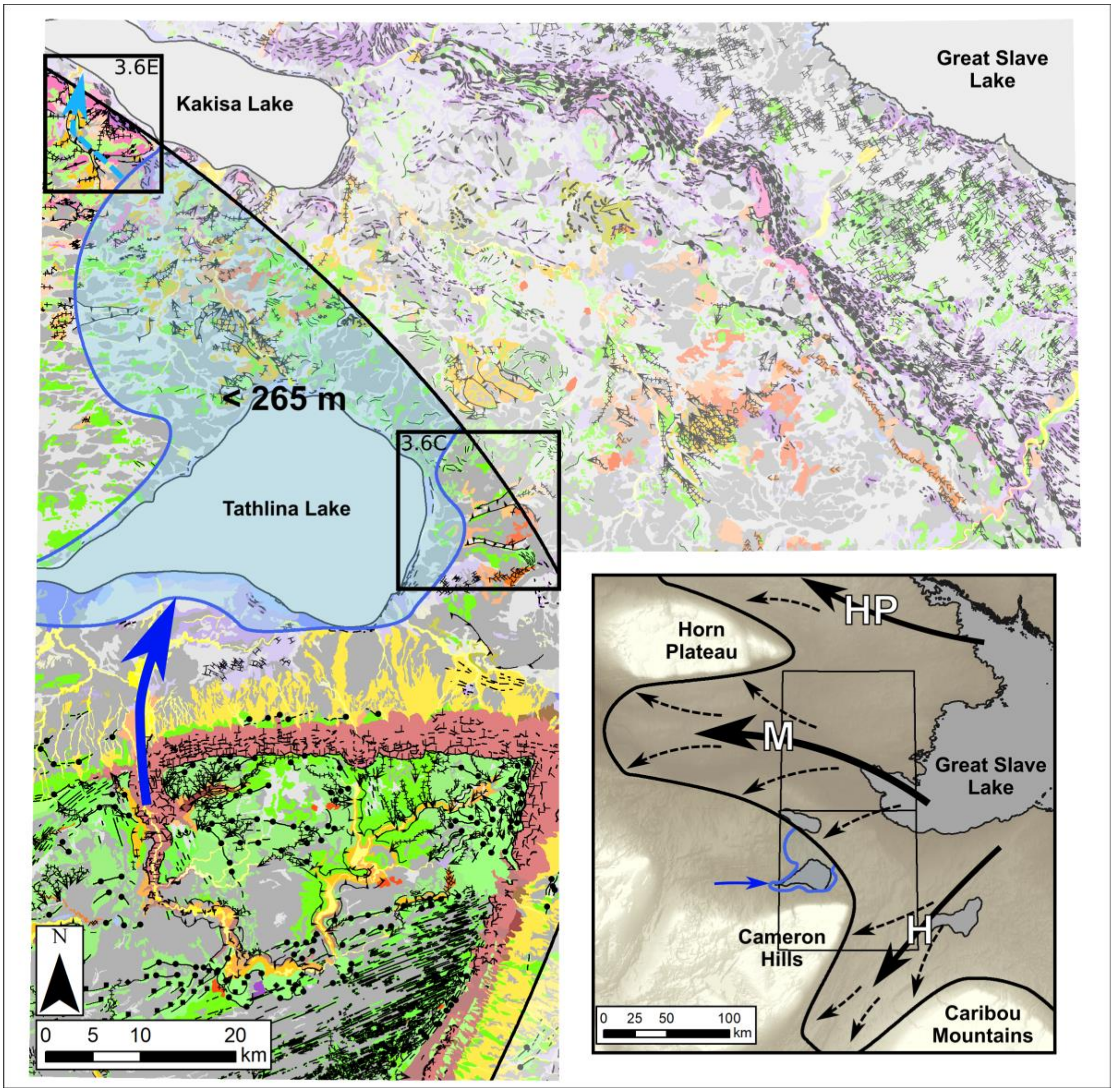

Figure 3.11: Margin 2 extents. Legend same as Fig. 3.6, locations of relevant sediment landform associations from Fig. 3.6 indicated. Key features – Ice margin along western escarpment arcing south to the Hay Lobe and north to the Mackenzie Lobe, Ice retreat eastward in all lobes, glacial lake at 265 m a.s.l., opening of drainage outlet south of Kakisa River.

3.5.3 Margin 3

Ice margin retreat was minimal between Margin 2 and 3 with lowering of the proglacial lake level as the main change between the two (Fig. 3.12). The Mackenzie Lobe continued to thin and retreat up the Mackenzie valley with the lateral ice margin position now just below the western escarpment. A similar magnitude of thinning and retreat occurred along the southern flanks of the Cameron Hills.

Ice flows at the time of Margin 3 were similar to those during Margins 1 and 2, but with presumably further reduction in their erosive power due to ice thinning. Northwestward flow down the Mackenzie River Valley rotated to more westward flow as the lobe's terminus moved up the valley.

Between Margins 2 and 3, minor ice-contact glaciofluvial sediments were deposited along the Kakisa River indicating the presence of an ice margin in this area (Fig. 3.6F). These ice-contact sediments form a ridge that is responsible for the rectilinear drainage observed in the path of the present day Kakisa River. More ice-contact glaciofluvial sediments also occur east of Kakisa River, which further constrain the ice margin position. In addition, small till-cored ridges (possibly crevasse squeeze ridges) sub-parallel to the interpreted ice margin near the glaciofluvial sediments suggest an ice proximal environment in this area.

The outlet south of Kakisa Lake was still in use, although this lake level (245 m a.s.l.) is the lowest to use this outlet (Fig. 3.6E). The outlet from Margin 2 was lowered by erosion to 245 m a.s.l. At 245 m a.s.l., Tathlina Lake was reduced to its approximate modern extent and a small proglacial lake developed north of Tathlina Lake in contact with the ice margin. Again, all elevations are present day and do not account for GIA.

The outlet of Tathlina Lake to the north and down the Kakisa River contains abundant glaciofluvial deposits along with a myriad of northward draining meltwater channels (Fig 3.6F). These likely formed during a time when Tathlina Lake water levels were falling and the outlet was finding an efficient drainage route northward. A small delta associated to the 245 m a.s.l.lake level further supports the interpretation of a lake at this elevation and that these channels lead from Tathlina Lake into the proglacial lake to the north. The northern proglacial lake is further defined by minor shorelines and glaciolacustrine sediments around the bedrock outcrop that controls the drainage pathway (Fig. 3.6E).

The drained northwest out of the study area and through a chasm between the escarpment (western bank) and the lateral ice margin of the Mackenzie Lobe (eastern bank). Meltwater traveled along the southern Mackenzie lobe margin and eventually reached glacial Lake Mackenzie. The lateral drainage along the ice is supported by heavily channelized sediments observed along the escarpment further west although this is outside the mapped area of this thesis.

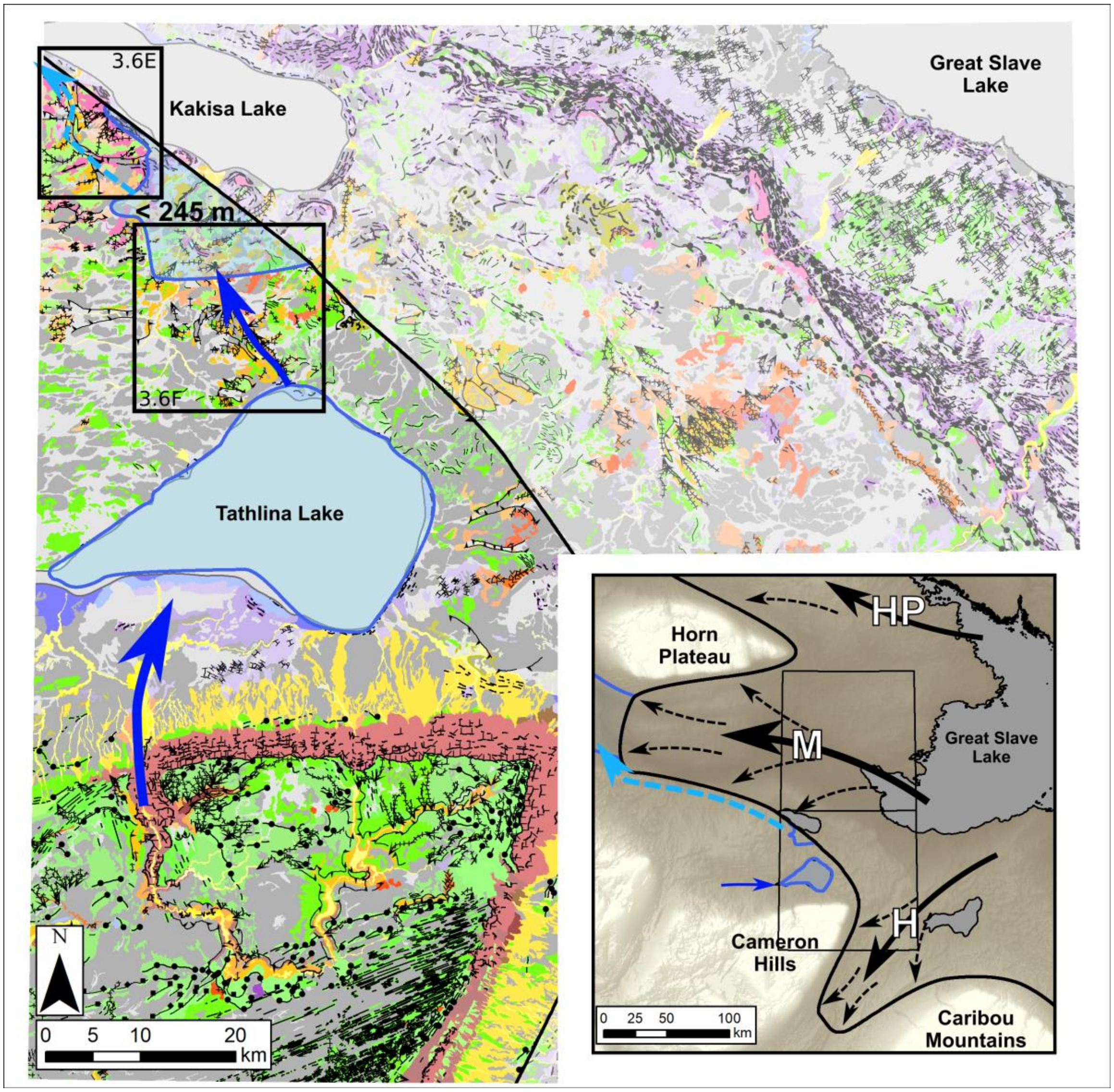

Figure 3.12: Margin 3 extents. Legend same as Fig. 3.6, locations of relevant sediment landform associations from Fig. 3.6 indicated. Key features – Ice margin similar to Margin 2 some retreat in the lobes, small glacial lake at 245 m a.s.l., proglacial lake input from Tathlina Lake through Kakisa river, drainage through outlet south of Kakisa Lake and along the ice margin.

3.5.4 Margin 4

The next ice margin lay between the two escarpments in the study area (Fig. 3.13). The reconstructed margin is not well constrained with surficial geology in the north of the study area but follows the present day 260 m a.s.l.contour defining the southern lateral margin of the Mackenzie lobe. In the south of the study area the last portion of the Hay lobe existed for a short time (hash marked area on Fig. 3.13). Extensive evidence of the margin occurs in this area mainly as meltwater channels and ice-contact to proximal glaciofluvial sediments. All ice lobes retreated further up their respective valleys including the Mackenzie lobe, the lobe north of the Horn Plateau, and the Peace lobe (Mathews 1980, Utting and Atkinson 2019). The differing rates of retreat between lobes is due to the amount of ice catchment within the systems, with the Mackenzie river basin being the largest, and the dynamics of the system like the topographic gradient and margin type (aquatic vs. terrestrial) and subglacial conditions (Bentley et al. 1979, Marshall et al. 1996, Layberry and Bamber 2001, Dove et al. 2017, Margold et al. 2018).

Ice-flow directions remain similar to during previous Margins, although southwestward flow stopped with the final retreat of the Hay lobe into the larger ice sheet. Ice flows during Margin 4 were likely weaker in erosive power due to the thinning of the ice sheet.

The level of the ice-contact lake during Margin 4 was lowered to 240 m a.s.l.as defined by the highest set of beach ridges within the northern part of the map area. These beach ridges are relatively well developed and are associated with glaciolacustrine nearshore deposits and winnowed sediments. The lake during Margin 4 extended between the bedrock highs south of Kakisa Lake and contained the then ice-free portions of the Kakisa Lake basin (Fig. 3.13). To the west, the lake extended between the western escarpment and the ice sheet connecting to glacial Lake Mackenzie (Lemmen et al. 1994, Couch and Eyles 2008, Huntley et al. 2017). Overall, the 240 m a.s.l.lake was likely shallow (although GIA would have made the lake deeper than the present day elevations suggest) and narrow in the study area, indicated by the low regional gradient in the area and the lack of iceberg scours.

The proglacial lake was fed by inputs from the south. The large meltwater complex on the north side of the then small Hay lobe represents an ice marginal braided river system transitioning downstream to a fan delta at the 240 m a.s.l.water level (Fig 3.6G). These channels were likely fed by subglacial meltwater. When the Hay lobe retreated further eastward it eventually opened a drainage outlet for water dammed along its southern margin in the Hay River valley. This drainage was routed northeast along the Hay lobes northern lateral extent following the regional topographic gradient and crosscut the braided system with the large meltwater corridor.

Due to ice retreat, a lower outlet for the lake was exposed at the 240 m a.s.l.northwest through Kakisa Lake (Fig. 3.13), although there is little evidence of a channel in this region. A more detailed analysis to the west of the study area would be needed to address this question. The interpretation of this drainage route is based on the constraint that ice was blocking the natural northeastward drainage in the area. Furthermore there are glaciolacustrine sediments at this elevation throughout the study area and it appears to have been maintained for a long period of time (see further reconstructions).

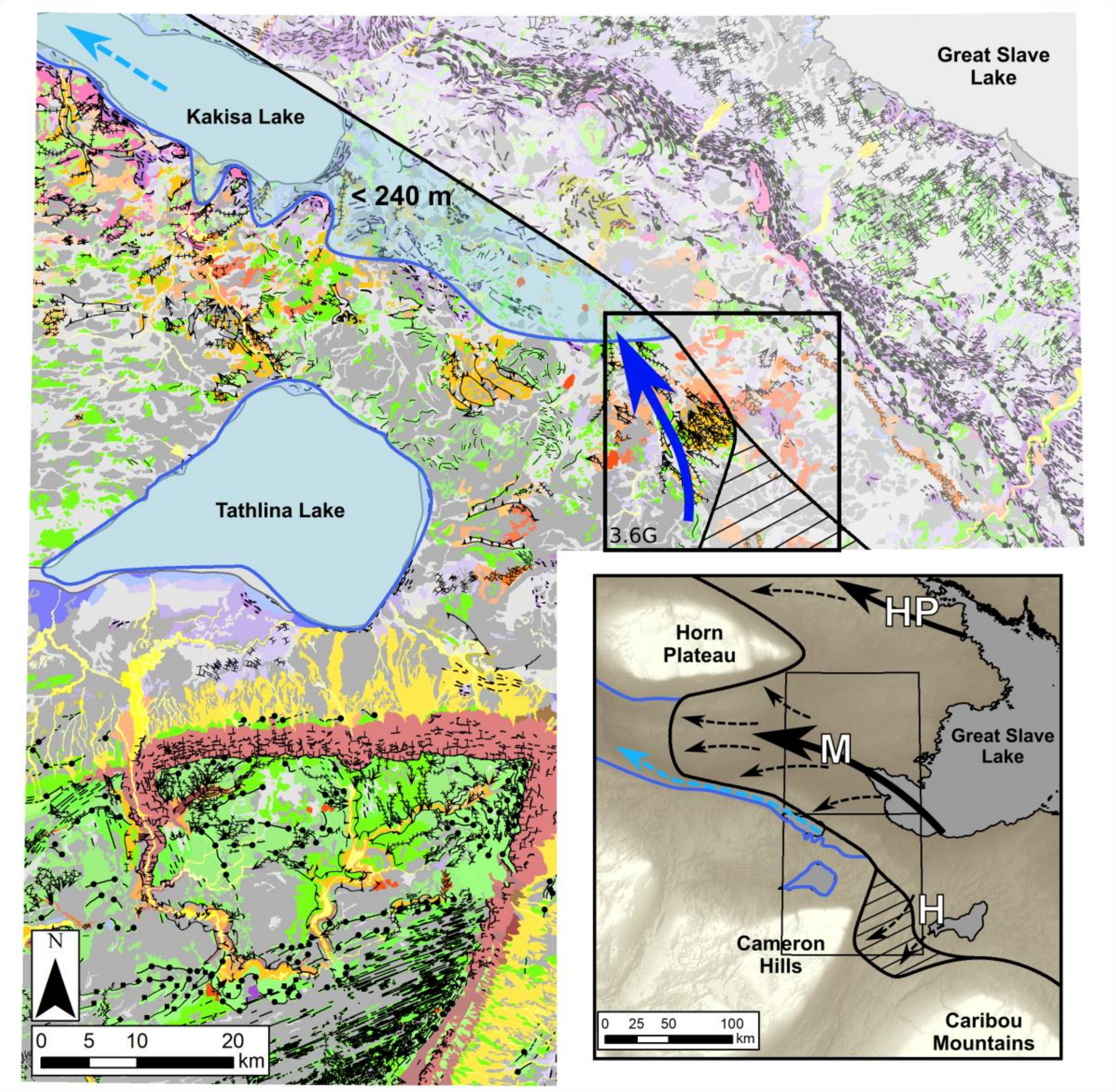

Figure 3.13: Margin 4 extents. Legend same as Fig. 3.6, locations of relevant sediment landform associations from Fig. 3.6 indicated. Key features – Ice retreat to between the escarpments, loss of the Hay River lobe (hash marked) and retreat of other lobes, proglacial lake at 240 m a.s.l., inputs from meltwater channels within the ice embayment and release of meltwater by retreat of the Hay lobe, outlet northwest through Kakisa Lake.

3.5.5 Margin 5

After Margin 4, the ice margin continued its eastward retreat through the study area and a stillstand created the Snake Creek Moraine along the eastern escarpment (Lemmen et al., 1994; Bednarski, 2008; Fig. 3.6A; 3.14). This moraine follows the escarpment throughout the study area and extends northward towards the Horn Plateau. To the south, the Snake Creek Moraine is harder to follow. From Margin 4 to Margin 5 the ice margin had also retreated further east in the Horn Plateau lobe and had retreated significantly south of the study area ~ 100 km away from the Caribou Mountains (Mathews 1980, Lemmen et al. 1994, Huntley et al. 2017, Utting and Atkinson 2019). Overall, Margin 5 was less lobate because of diminishing topographic influence from upland regions (Fig. 3.14).

The escarpment was a significant factor for the ice margin stillstand as ice could no longer flow over top of the escarpment (Krabbendam and Glasser 2011, Barchyn et al. 2016). Northwestward ice flow was continuing in the Mackenzie lobe. To the southeast of the study area, ice flow was more southward feeding the remainder of the Peace lobe wrapping around the Caribou Mountains (Mathews 1980, Utting and Atkinson 2019). Again, erosion due to ice flow was weakened via ice thinning and retreat.

The lake level for Margin 5 remained the same at 240 m a.s.l.as no new outlets had opened although GIA would have changed this lake level over time (Fig. 3.14). Due to the longevity of this lake level phase, prominent strandlines formed at this elevation on the present day landscape and glaciolacustine sediment and winnowing are more abundant below that elevation. Southern areas of the 240 m a.s.l.lake were being progressively exposed due to ice margin retreat and, therefore, were inundated for less time; glaciolacustrine features and sediments are consequently sparse in the southern regions of the lake. Nonetheless, some strandlines and winnowing do occur in the progressively exposed areas, specifically the raised ice-contact glaciofluvial sediments deposited around the meltwater channel complex from Margin 4 (Fig 3.6G). The lake extent has been extrapolated along the 240 m a.s.l.contour to ice free areas east and west of the study area, as GIA was not accounted for (Fig. 3.14). The lake had a limited extent to the east and did not extend beyond the eastern side of the Caribou Mountains because ice was still present in that area at that time.

The 240 m a.s.l.proglacial lake outflow was still to the northwest into the Mackenzie River Valley through the Kakisa Lake basin (Fig. 3.14). Evidence of a shallow lake is similar to that defining Margin 4 with low relief above the escarpment and no iceberg scours in the region. The shallow depth of the lake is further supported by the Snake Creek Moraine's depositional history. The moraine has portions where kettle lakes occur between moraine ridges, a characteristic typical of terrestrial margins (Benn and Evans, 2010; Brown et al., 2011; Menzies et al., 2018; Fig. 3.6A). These kettle lakes are more common to the south of the moraine complex where elevations are slightly higher, which together form evidence for a shallower lake in that area. The moraine was still deposited along the grounding line of the margin into a proglacial lake as evidenced by subaquatic fans at the distal ends of eskers that protrude through the moraine ridges, and the symmetrical morphology of the moraines (King et al., 1991; King, 1993; Menzies, 2001; Fig. 3.6A).

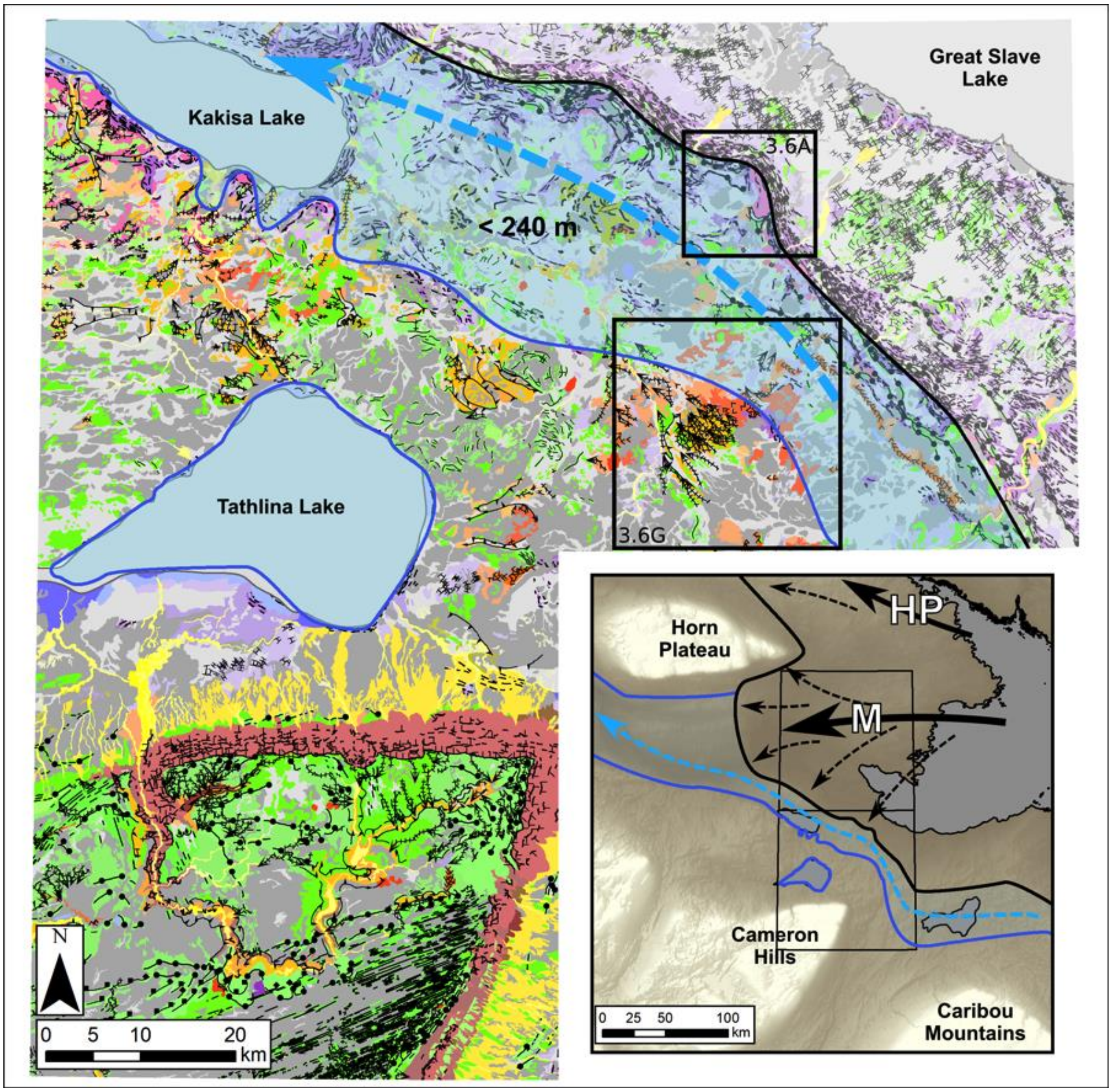

Figure 3.14: Margin 5 extents. Legend same as Fig. 3.6, locations of relevant sediment landform associations from Fig. 3.6 indicated. Key features – Ice retreat back to eastern escarpment creating the Snake Creek Moraine, limited Mackenzie lobe, lake still at 240 m a.s.l., meltwater inputs from ice margin, drainage outlet northwest through Kakisa Lake basin.

3.5.6 Margin 6

The ice at Margin 6 follows a topographic elevation (160 m a.s.l.) that is defined by a small moraine in the northeast corner of the mapped study area (Fig. 3.6B; 3.15). The Mackenzie lobe was still extending slightly down the Mackenzie River Valley. Significant ice retreat had occurred in the south to the present shore of Great Slave Lake (Fig. 3.15). Additionally, ice north of the Horn Plateau had retreated to be parallel with the north arm of Great Slave Lake.

Ice-flow at this stage had completed a rotation from west to northwestward and ice was only flowing through the northern portion of the study area into the last stages of the Mackenzie lobe (Fig. 3.15). To the north, ice-flow was to the north-northwest towards the retreating margin along the north arm of Great Slave Lake and lobes to the south of the study area were likely greatly diminished or gone (Mathews 1980, Lemmen et al. 1994, Utting and Atkinson 2019).

During the retreat of the ice from Margin 5 to Margin 6, a southwestward ice readvance out of the Great Slave Lake basin occurred below the escarpment. This readvance is characterized by streamlined drumlins composed of till with a southwestward direction that terminate in till cored ice-thrust blocks transverse to ice-flow (Figs. 3.6B; 3.15). The record of this final southwestward readvance is found only below the escarpment and therefore ice was not thick enough to overtop the eastern escarpment. Evidence of the escarpments influence on the surge can be observed to the southeast where the escarpment ends as the ice deflected around it (Smith et al., 2021).

It is important to note that before the readvance, the ice margin had been retreating down slope, which means that the proglacial lake was deepening with further retreat. This is a situation that has been linked to ice margin instability, which can lead to rapid calving and retreat, but sometimes also rapid readvances or surges into proglacial water bodies (Rignot and Kanagaratnam 2006, Schoof 2007, Nick et al. 2010, Favier et al. 2014, Quiquet et al. 2021). Intense calving within the lake following the rapid readvance is evidenced by the presence of numerous iceberg scours below the escarpment. The increased water depths below the escarpment allowed icebergs to float and were pushed by wind and lake currents to the northwest. More glaciolacustrine sedimentation also occurred in the deeper lake below the escarpment and was scoured during/after deposition as recorded by the keel marks (Fig. 3.6B; 3.15). Calving and subglacial/englacial drainage from the ice margin were large inputs into the lake, maintaining the water level at 240 m a.s.l.

The lake level at the time of Margin 6 was the same as for Margins 4 and 5, at 240 m a.s.l., although the extent of the lake was much larger due to deglaciation exposing lower topography. Again, GIA was not accounted for but this elevation likely changed over the retreat and uplift from Margins 4 and 5. The extent of the lake was again drawn by extrapolating the 240 m a.s.l.elevation to the surrounding ice-free regions. At that stage, the 240 m a.s.l.lake was connected to the basin that lies north of the Horn Plateau through a small gap between the ice sheet and the tip of the Horn Plateau (Fig. 3.15). The lake also extended to the south as the ice retreat northeastward increased the basin size in this region. To the southeast, the lake was still separated by ice to a basin in the Peace River Valley as is indicated by Mathews, (1980).

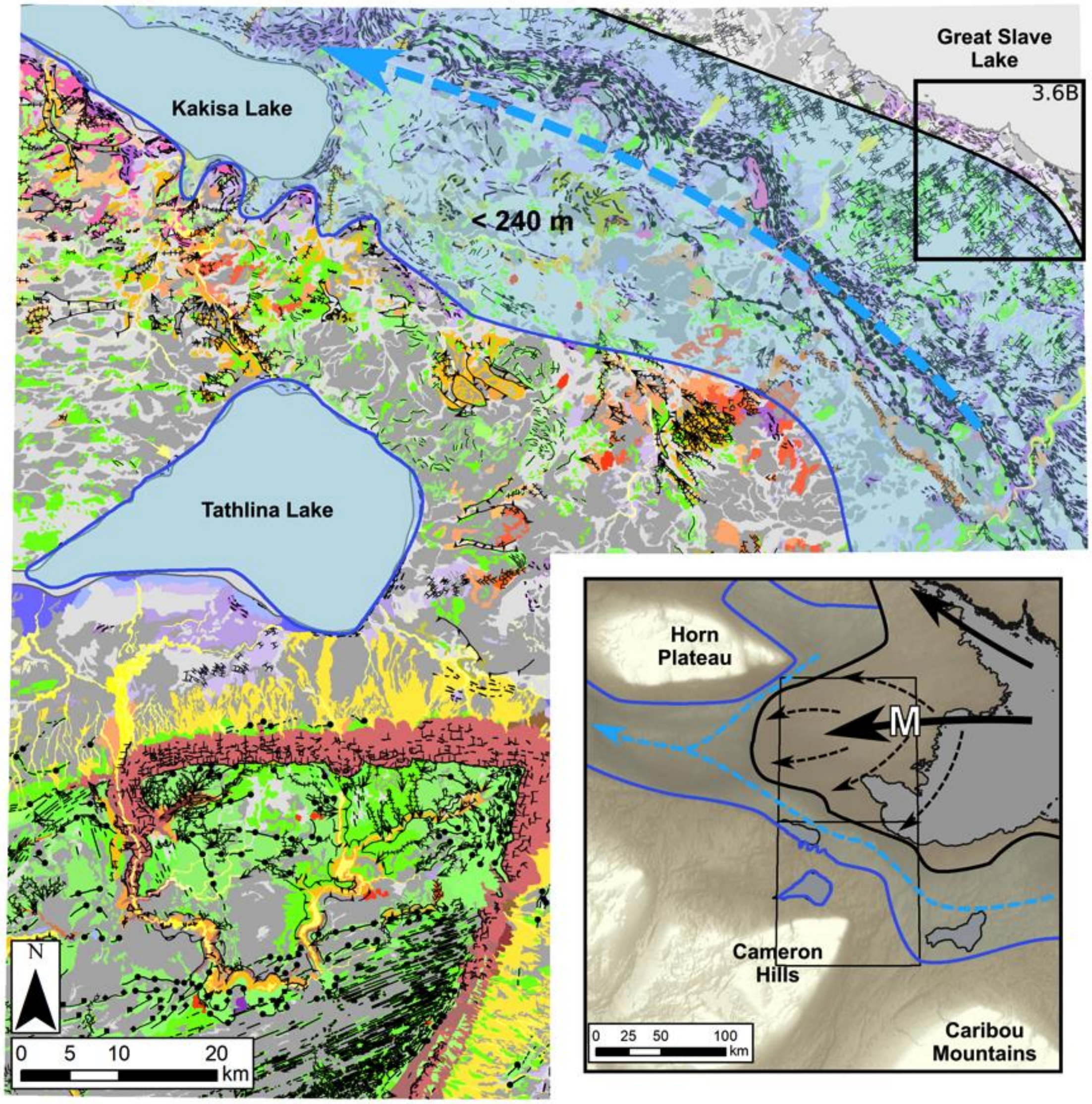

Figure 3.15: Margin 6 extents. Legend same as Fig. 3.6, locations of relevant sediment landform associations from Fig. 3.6 indicated. Key features – Ice margin below the second escarpment, Mackenzie lobe still present, Lake at 240 m a.s.l.but larger extent north and east, drainage northwest toward Mackenzie River.

The outlet for this lake was down the Mackenzie River although drainage through the northwestern Kakisa Lake basin outlet was likely still present, but diminishing as lower elevations became available due to ice retreat. Northwestward drainage of the lake at this stage down the Mackenzie River Valley is consistent with the northwest- southeast orientation of the iceberg scours. Icebergs in this case would have flowed in the direction of lake currents. It is possible that prevailing wind-currents also moved the icebergs in this direction as some westward paleowind morphologies of dunes were observed (Appendix G). Here, a combination of these factors pushing icebergs to the northwest is suggested. Following Margin 6, the ice margin retreated out of the study area and likely sat along the Paleozoic - Canadian Shield boundary due to changing subglacial conditions influenced by underlying bedrock geology. At that time, the lake in the study area was still along the 240 m a.s.l.contour, but had become part of glacial Lake McConnell (McConnell, 1890; Craig, 1965; Mathews, 1980; Lemmen et al., 1994; Smith, 1994). This is further discussed below in Sect. 3.6.1 about the broader regional context.

3.5.7 Shoreline Features 223 m a.s.l.

The following two reconstructed lake levels are presented due to their significance to the optical ages obtained in this study. These are meant to highlight the shape and drainage of the GLM during the formation of the deposits where the optically dated sands were collected. Overall, with the ice margin to the east of the study area, meltwater inputs into GLM began to decline due to isostatic adjustment and incision of outlets down the Mackenzie River. During this phase of GLM, stepwise sub-parallel beach ridges were created below the maximum 240 m elevation (Fig. 3.16). These ridges are typically composed of local limestone rubble as bedrock is close to surface in many locations just above the eastern escarpment.

The lake at 223 m a.s.l.had reduced in size (Lemmen et al. 1994). The 223 m a.s.l.lake was parallel to the southern shores of Great Slave Lake and extended west to include Kakisa Lake. The water level had lowered out of the basin north of the Horn plateau and was also following the northern shores of Great Slave Lake (Fig. 3.16). Down the Mackenzie River, the lake became narrower constrained by the western escarpment and the southern flank of the Horn Plateau. Within the study area, some moraine ridges were reworked by shoreline processes resulting in shoreline sediments being deposited along and within the moraine ridges (Fig. 3.6A; 3.16).

The 223 m a.s.l.lake level is presented because at this elevation the beach ridge with and age of 12.0 ± 0.7 ka BP was formed (Fig. 3.7). This age is the oldest collected during this research and is therefore a limiting age; all the margins described above happened before 12.0 ± 0.7 ka BP as shoreline creation necessitates an ice-free landscape and a proglacial lake at this elevation.

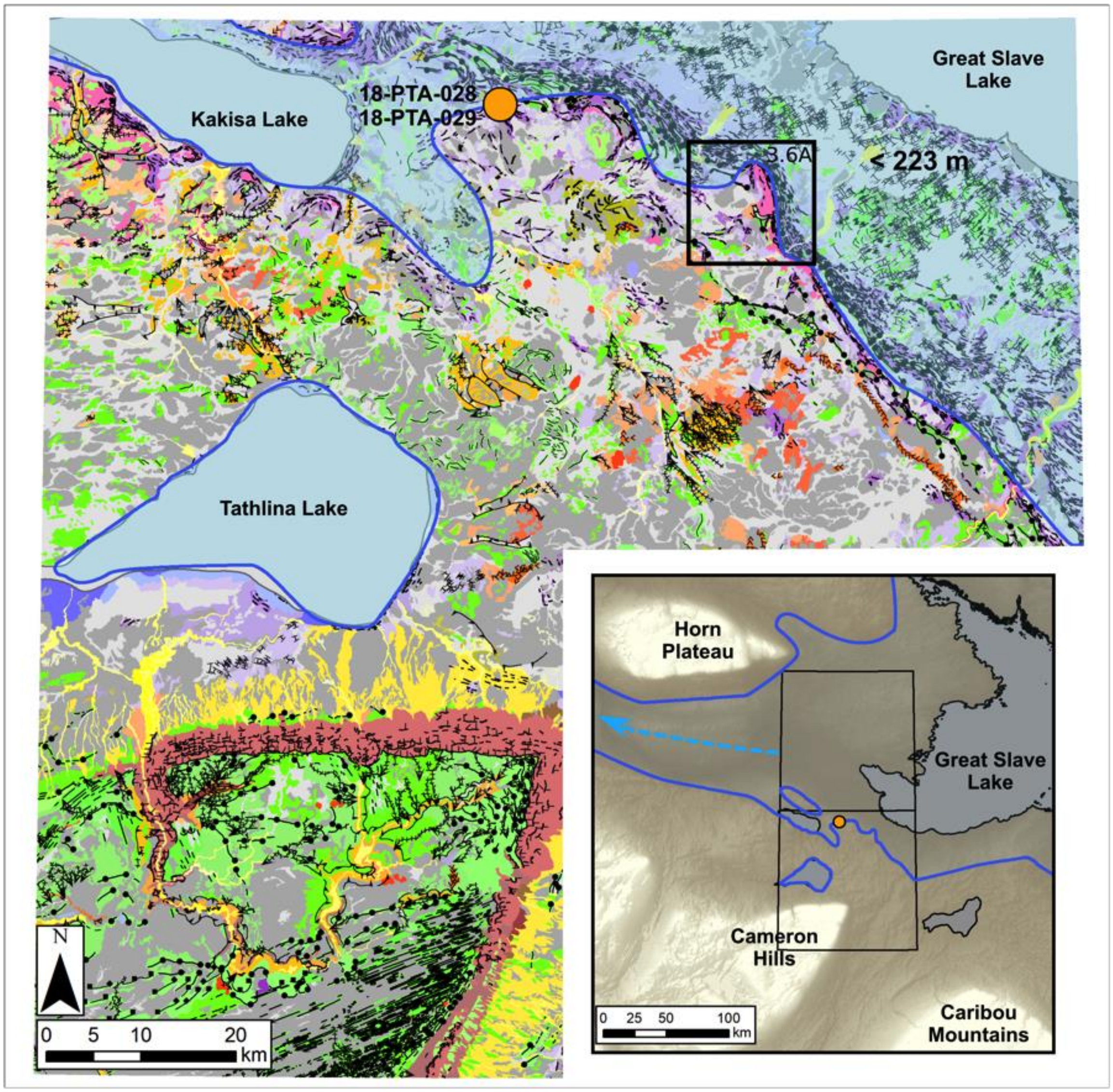

Figure 3.16: Water Level 223 m a.s.l. Legend same as Fig. 3.6, locations of relevant sediment landform associations from Fig. 3.6 indicated, optical ages highlighted as orange points. Key features – Optical date collected along beach ridge, lake is lower and along the moraine, drainage down the Mackenzie River.

3.5.8 Shoreline Features 200 m a.s.l.

The 200 m a.s.l.water level is constrained by the first peak of eolian ages obtained within the study area, which requires land above 200 m a.s.l.to be subaerial. The lake could be at a lower level during the formation of these dunes but that is in turn constrained by the second peak of ages. Ultimately, a definite configuration of the lake during the formation of these dunes would be difficult to determine. Furthermore, this lake level shows the extensive reworking of the Snake Creek Moraine and helps characterize the configuration of GLM as it drained.

The 200 m a.s.l.lake was getting closer to the extent of the modern GSL in the south and was becoming narrower in the Mackenzie River Valley (Fig. 3.17). Within the study area, the shoreline followed the escarpment and reworking of the lower moraine ridges (Fig. 3.6A; 3.17). The lake level was low enough that Kakisa Lake was separated from the GLM using its current outlet to the northeast via the Kakisa River. The 200 m a.s.l.lake was disconnected from the Great Bear Lake basin to the north and Athabasca lake Basin to the south as the elevation for separation between these basins is 214 and 213 m a.s.l.respectively (Lemmen et al. 1994).

Dunes formed in small field throughout the mapped area in close proximity to both the glaciofluvial and glaciolacustrine sediments (Fig. 3.18). Their parabolic and transverse morphologies indicate shifts in wind patterns with westward and eastward paleo-wind directions (Hagedorn et al., 2021a; Hagedorn et al., 2021b; Hagedorn et al., 2022c; Fig. 3.5; See Appendix G for full description of dunes). Optical ages exposed by, at most, the 200 m a.s.l.lake level form a cluster of ages around 10.4 ± 0.3 ka BP (Fig. 3.7). Again, these optical ages are minimum ages for deglaciation in the area, but they also constrain lake phases. They indeed suggest that the Great Bear, Great Slave, and Athabasca basins had separated, and the lakes were closer to modern day extents by at least 10.4 ± 0.3 ka BP.

The second peak observed on Figure 3.6 is related to samples below the 200 m a.s.l.water level. The double peak in the probability density function can be explained by continual lowering of GSL, which exposed lower elevations to eolian dune formation processes. These lower eolian dunes were formed at 8.2 ± 0.4 ka BP.

3.5.9 Post Glacial Lake McConnell

The radiocarbon samples collected along a cut bank of the upper reaches of the Mackenzie River yielded a radiocarbon age ranging from 2.7 – 2.15 cal. ka BP with the highest likelihood at 2.35 cal. ka BP (Table 3.4, Fig 3.8). Only one of the six subsamples collected being was outside this range. The 2.35 cal. ka BP age records the beginning of organic formation atop the till at this site, which corresponds to the Holocene transition of proto Great Slave Lake down to modern day levels.

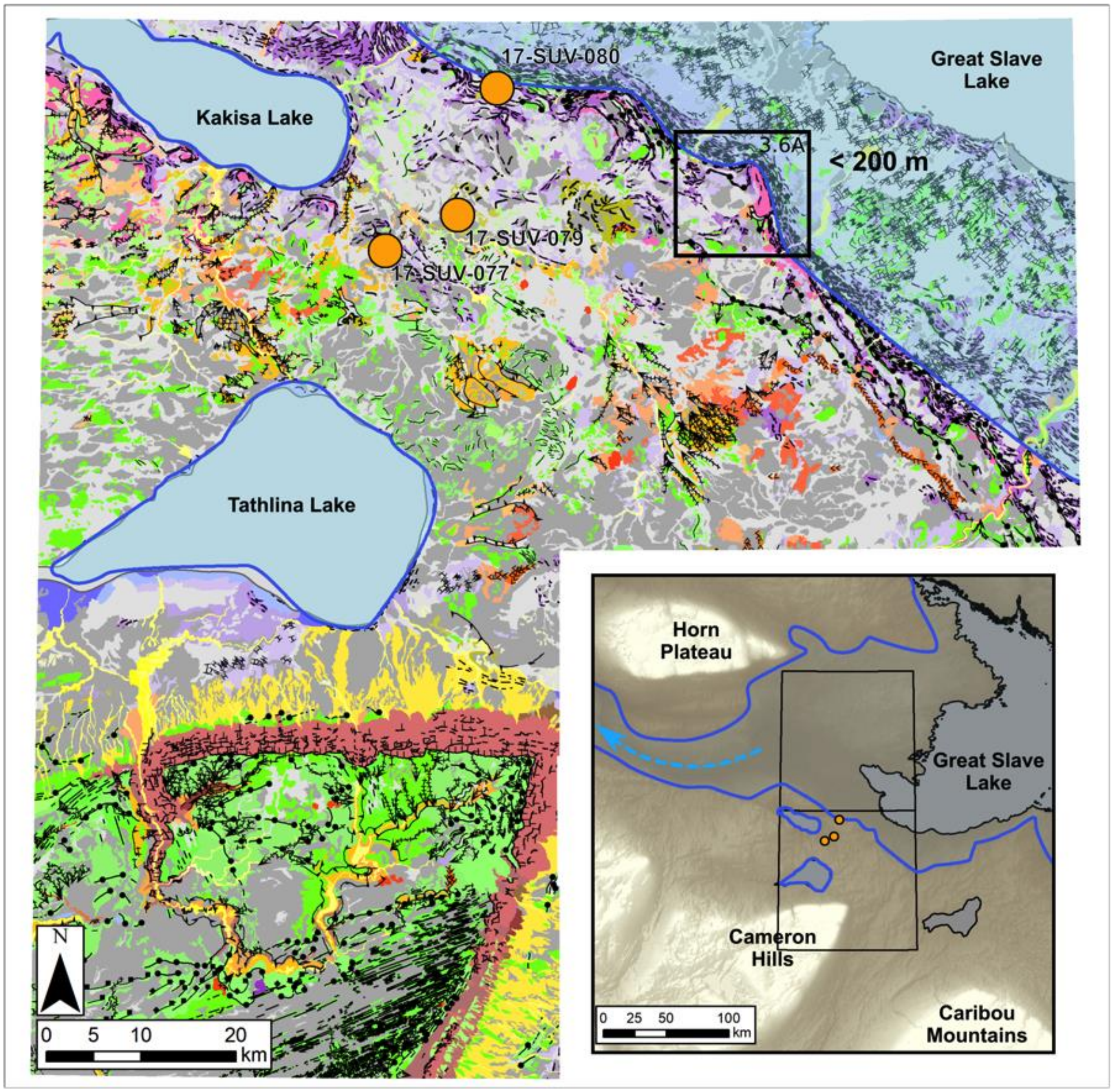

Figure 3.17: Water Level 200 m a.s.l.extent. Legend same as Fig. 3.6, locations of relevant sediment landform associations from Fig. 3.6 indicated, optical ages highlighted as orange points. Key features – Optical ages from dunes above 200 m a.s.l.; water level reduced and along the escarpment in the study area; drainage down the Mackenzie River.

3.6 Discussion

3.6.1 Regional Context

Margin 1 is correlated to the beginning of the Hare Indian Phase of GLM, its smallest extent, when it only occupies the Great Bear Lake Basin north of the study area (Fig. 3.18b). This phase of GLM is estimated to have occurred around 13.0-12.8 cal. ka BP by Lemmen et al. (1994) or 13.7 – 13.3 cal. ka BP by Smith (1994). The correlation is based on an estimation of when the study area was first deglaciated by Lemmen et al., (1994) and Smith, (1994), however, Margin 1 as reconstructed herein show a less extensive ice sheet for that time than in Lemmen et al., (1994; cf. their Fig. 1.5). At Margin 1, glacial Lake Mackenzie was in the northern reaches of the Mackenzie River Valley in contact with the Mackenzie lobe (Lemmen et al., 1994; Couch and Eyles, 2008; Huntley et al., 2017). To the south, the ice sheet is similar to Utting and Atkinson (2019; their Figure 13 A) correlated based on the configuration of the ice margin. Glacial Lake Hay was small and to the southwest of the Cameron Hills draining northwestward down the Fort Nelson River into the Liard River. Glacial Lake Peace was at its Rainbow Stage where it was several kilometers south of the Caribou Mountains and used the Rainbow Lake Outlet flowing north (Mathews, 1980; Utting and Atkinson, 2019).

Margin 2 is also correlated to the Hare Indian Phase, although there has been further ice retreat, with a more similar ice extent to that shown in Lemmen et al., 1994 (Fig 3.18c). Due to the continued ice retreat, GLM to the north was likely larger but still limited to the Great Bear Basin due to ice retreat (Lemmen et al., 1994; Smith, 1994). To the northwest, glacial Lake Mackenzie was increasing in size as it followed the ice margin retreat up the Mackenzie River valley (Lemmen et al., 1994; Couch and Eyles, 2008; Huntley et al., 2017). To the south, Margin 2 is correlated to Utting and Atckinson’s (2019; their Figure 13 B) again based on similar ice sheet configuration. The Hay lobe and the Peace lobe were still connected northeast of Mount Watt causing glacial Lake Hay and glacial Lake Peace to be separated. Glacial Lake Hay was at its Zama stage using the Ekwan outlet to the west while the glacial Lake Peace was at its Keg River stage, using the Chinchaga outlet flowing north into glacial Lake Hay (Mathews, 1980).

Margin 3 had a similar configuration to the north as Margin 2, akin to the limited ice margin retreat in the study between these Margins (Fig. 3.18d). Margin 3 is still correlated to the Hare Indian phase of GLM to the north although it is again closer to the transition into the Great Bear Phase (Lemmen et al., 1994; Smith, 1994). At that stage, Glacial Lake Mackenzie was larger as it followed the retreating Mackenzie Lobe up the Mackenzie River Valley (Lemmen et al., 1994; Couch and Eyles, 2008; Huntley et al., 2017). The arrangement of the ice sheet south of the study area was correlated via the progression of retreat within the study area. Due to retreat of the Hay and Peace ice lobes they separated which reconfigured the proglacial drainage system in the region. Glacial Lake Hay was at its Slavey stage (its largest), in contact with the now separated Hay lobe draining to the southwest. Glacial Lake Peace was in contact with the Peace Lobe and had increased in size to the Chinchaga stage and still drained northward but now via the

Chinchaga outlet, into glacial Lake Hay. A portion of the Peace lobe was still north of Mount Watt separating the Hay and Peace systems (Mathews, 1980; Utting and Atkinson, 2019).

Margin 4 was correlated to the start of the Great Bear Phase of GLM and begins to use the Great Bear River as a northwestward outlet (Lemmen et al., 1994; Smith, 1994; Fig 3.18e). This correlation is based on the configuration of the ice margin in the study area compared to that of the Lemmen et al.'s reconstruction. The 240 m a.s.l.lake observed in the study area during Margin 4 is now connected to glacial Lake Mackenzie. To the south, Margin 4 occurred at the time of Figure 13D of Utting and Atkinson (2019). Glacial Lake Hay had drained northward and a little portion of the Hay River Lobe remained and then retreated back into the larger ice mass. Glacial Lake Peace was at its La Crete Stage where it extended along the southern flank of the Caribou Mountains and in contact with the Peace Lobe. The retreat of the ice opened northward drainage for glacial Lake Peace into the Hay River Valley along the Meander River Spillway. It is possible that the meltwater corridor that crosscuts the braided river channels west of the Snake Creek Moraine is related to either the draining of glacial Lake Hay or the drainage of glacial Lake Peace down the Meander River Spillway (Mathews, 1980; Utting and Atkinson, 2019).

Margin 5 marks the Great Bear phase of GLM to the north at 12.5 – 12.4 cal. ka BP by Lemmen et al., (1994) or 13.3 – 12.8 cal. ka BP by Smith (1994). This correlation is based on the deposition of the Snake Creek Moraine. GLM at this stage used the Great Bear River as the drainage outlet northwest and filled the majority of the Great Bear Lake basin (Fig 3.18f). The 240 m a.s.l.lake in the study area is still connected to glacial Lake Mackenzie (Lemmen et al., 1994; Bednarski, 2008; Couch and Eyles, 2008; Huntley et al., 2017). To the south of the study area, Margin 5 is correlated to later stages of Figure 13 D in Utting an Atkinson, (2019), where glacial Lake Hay had already drained and glacial Lake Peace was at its John D'Or stage. At this stage, glacial Lake Peace still drained northward into the Hay River system (Mathews, 1980). It is possible that the drainage events discussed in Margin 4 happened sometime during this stage as there are no age constraints, but there is no significant fan deposit along the Hay River into a lake at 240 m that might suggest this drainage event.

Margin 6 is at the end of the Great Bear Stage, as ice along the northern arm of Great Slave Lake still separates the Great Bear and Great Slave basins (Lemmen et al., 1994; Smith, 1994; Fig 3.18g). The lake in Margin 6 represents an eastern extension of glacial Lake Mackenzie through the study area and further east, as well as to the north around the Horn Plateau. To the south, the lake is still unconnected to the Peace River and Slave River by ice (Mathews, 1980).

Following Margin 6, the Mackenzie phase of GLM (the maximum) began at 11.6 cal. ka BP in the Lemmen et al., (1994) reconstruction or at 12.6 cal. ka BP in the Smith (1994) reconstruction (Fig 3.18h). The Mackenzie Phase of GLM likely used a similar lake level to the 240 m a.s.l.as glaciolacustrine features are well developed at this elevation and little glaciolacustrine material is found above 240 m a.s.l.although GIA would have influenced this elevation. As such, when compared to the optical age of the shoreline at 223 m a.s.l.(17 m below the estimate maximum of GLM) of 12.0 ± 0.7 ka BP, it indicates that the Lemmen and Smith reconstructions for the Mackenzie Phase of GLM are too young, a similar observation suggested by other work in the region (Munyikwa et al., 2017; Kelley et al., 2020).

The eolian optical ages obtained in this study are similar to those of the surrounding region as the ice sheet and GLM retreated eastward. The eolian dune ages collected in this thesis are younger than those to the south, which range from 13 – 11 ka BP (Munyikwa et al., 2017), as northern Alberta was deglaciated before the study area (Fig 3.19h). They are in the same range as the sample collected to the east with an age of 10.5 ka BP (Wolfe et al., 2004) and those just to the east collected by Oviatt and Paulen (2013). The optical ages collected as part of this thesis are older than those to the north, the oldest of which is 7.13 ka BP (O'Neill et al., 2019). This is because the landscape to the north was exposed after that of the study area, with the O'Neill et al., (2019) sample being from only 14.5 m above the current GSL water levels.

Radiocarbon results are younger than those in the surrounding region, especially the ones to the north collected by O'Neill et al. 2019 (a bulk peat age of 3.85 – 3.7 cal. ka BP). O'Neill et al., (2019) suggest a similar formation process for the peat they sampled; specifically, peat formed when proto Great Slave Lake was retreating exposing the landscape for organics to develop. The younger age of this research is explained by the lower elevation (within the Mackenzie River Valley) than the sample by O'Neill et al., (2019), where organic deposition would have been delayed relative to the more elevated site to the north.

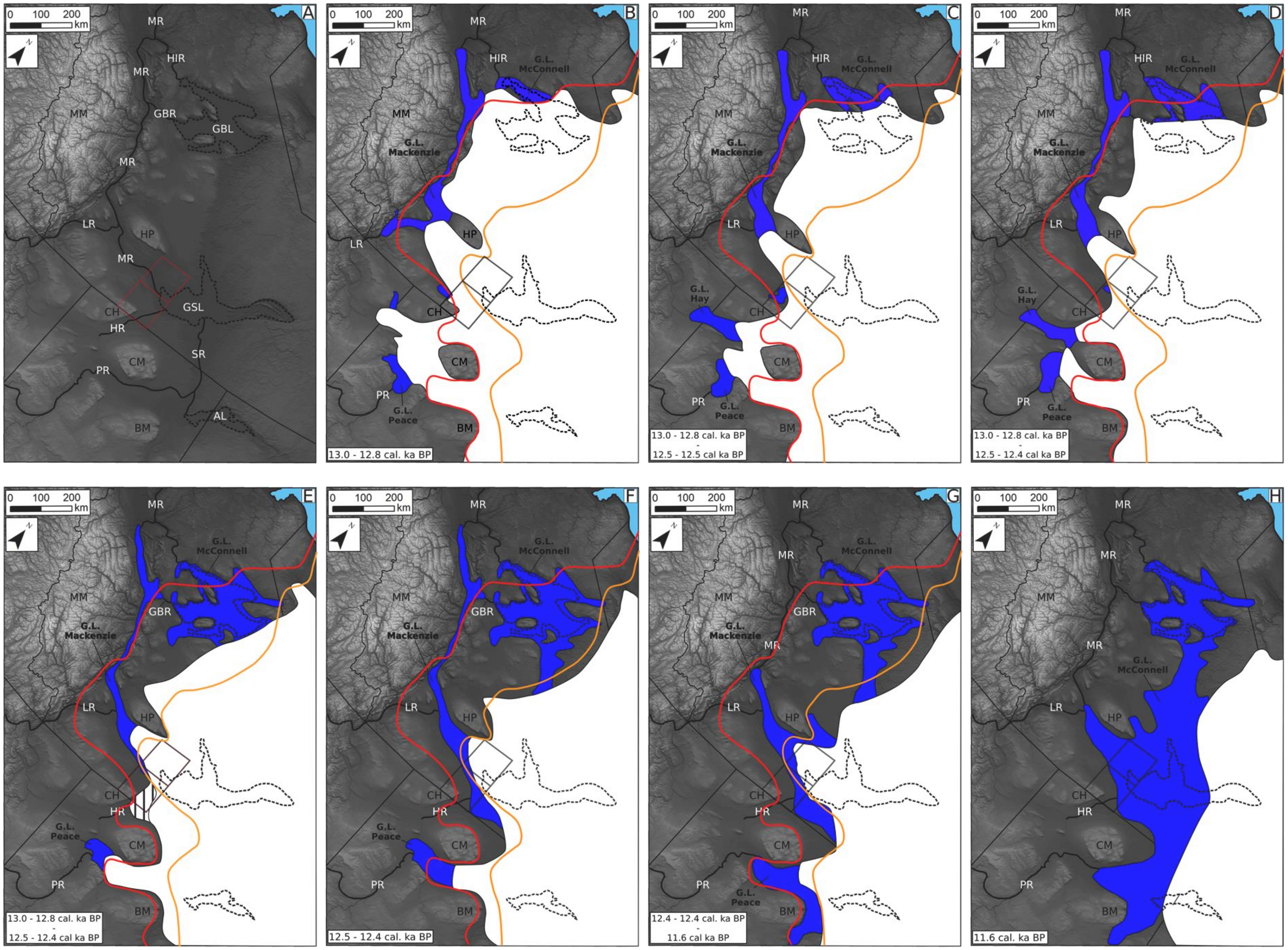

Figure 3.18: Western LIS Margin 1 reconstruction (study area indicated); Ice sheet is white, proglacial lakes are blue. Red line is 12.8 ka BP margin from Dalton et al., 2020. Orange line is 12.1 ka BP margin from Dalton et al., 2020. Geographic locations relevant to reconstructions: MM=Mackenzie Mountains, MR = Mackenzie River, HIR=Hare Indian River, GBR=Great Bear River, LR=Liard River, HP=Horn Plateau, CH=Cameron Hills, HR=Hay River, CM=Caribou Mountains, PR=Peace River, BM=Birch Mountains, SR=Slave River, GBL=Great Bear Lake, GSL=Great Slave Lake, AL=Athabasca Lake. A) Basemap with geographic locations B) Western LIS configuration at Margin 1. C) Western LIS configuration at Margin 2. D) Western LIS configuration at Margin 3. E) Western LIS configuration at Margin 4. F) Western LIS configuration at Margin 5. G) Western LIS configuration at Margin 6. H) Western LIS configuration at max GLM extent.

3.6.2 Ice Margins

As expected with updated fieldwork and mapping, the ice margins of the large-scale reconstructions within the area have been refined. The most notable issues are around the Cameron Hills. This research shows an ice free Cameron Hills while the larger scale reconstructions seem to downplay the influence of the topographic features having ice overtop of the northern extent of the Hills (Dyke, 2004; Dalton et al., 2020; Fig. 3.2, 3.9). Furthermore, this research suggests that while the ice margin was between the two escarpments, glacial Lake Mackenzie extended into the study area (Lemmen et al. 1994, Bednarski 2008). The updated margins presented here are not significantly different with respects to ice extent although it does appear that ice was thin, similar to the conclusions of Gowan et al., (2016).

The research also provides more insight into the Snake Creek Moraine, and the arrangement of the ice margin and glacial lakes during moraine deposition. The moraine was difficult to map due to its extensive reworking from GLM, but appears to be a large continuous feature on the landscape after close examination. Although the moraine was not dated directly, it must have formed before 12.0 ± 0.7 ka BP. This means that the estimates by Lemmen et al., (1994) of 12.5 – 12.4 for its deposition could be too young. The Lemmen et al., (1994) estimate would require the ice to retreat back from the moraine, form the Mackenzie phase of GLM, and then drain 17 m to 223 m a.s.l.all within 500 years. This seems unlikely even with the expected fast retreat of the ice margin due the aqueous margin (Stokes and Clark 2004, Carrivick and Tweed 2013, Favier et al. 2014). This research agrees with previous authors that the Snake Creek Moraine was deposited along an aqueous margin although the proglacial lake at the time of formation likely had different extents than previously thought being shallower and not as laterally extensive (Lemmen et al. 1994, Bednarski 2008).

The moraine also represents a significant stillstand of ice that could possibly be correlated to other regions of the western LIS. For example, a comparison to the Cree Lake Moraine would be an interesting avenue forward with its northern extents often questioned and has recently been dated around 13 ka BP (Norris, 2020; Norris et al., 2021). Dating of the Snake Creek moraine could be a possible area of future work to more precisely delineate the timing and position of the ice margin in relation to other features of the LIS.

3.6.3 Glacial Lakes

The lake sequence over the study area has also been updated although not accounting for GIA. A glacial lake north of the Cameron Hills has been identified and follows the ice sheet as it retreated eastward. Additionally, this research shows that the study area was connected to glacial Lake Mackenzie more than previously thought (Lemmen et al. 1994, Couch and Eyles 2008, Huntley et al. 2017). This could represent a pathway for earlier northwestern drainage through glacial Lake Mackenzie to the Arctic Ocean, influencing the global climate (Tarasov and Peltier, 2006; Murton et al., 2010; Tarasov et al., 2012; Gowan et al., 2016)..

This research also shows that GLM had a lower maximum elevation than previous reconstructions, around 240 m a.s.l.(Craig 1965, Mathews 1980, Lemmen et al. 1994, Smith 1994, Huntley et al. 2017). The differences in maximum elevation of GLM could be related to the quality of elevation data, as the ArcticDEM used in this thesis is the most up-to-date (2019) and has a 2 m resolution and also differential GIA. Detailed field work and mapping could also play a role in the updated lake extent as some glaciolacustrine features are present on the landscape above 240 m a.s.l., but relate to the proglacial lake north of the Cameron Hills rather than to GLM. The updated lake extent reduces the total volume of GLM influencing the amount of meltwater draining northwestward through the Mackenzie River to the Arctic Ocean, which in turn affects the global climate models (Tarasov and Peltier, 2006; Murton et al., 2010; Tarasov et al., 2012; Gowan et al., 2016).

The lakes in this reconstruction also do not show significant drainage from the south, other than drainage related the glacial lake impounded on the southern extent of the Hay Lobe. A southern input from glacial Lake Agassiz is suggested by some and is thought to be a possible source for the large meltwater drainage impulse down the Mackenzie River (Fisher and Smith, 1994; Smith, 1994; Norris et al., 2019). It is possible that glacial Lake Agassiz drainage is what kept GLM at a similar elevation despite the eastward retreat of the LIS and glacioisostatic adjustment. It is also possible that the drainage occurred at a lower stage of GLM so the increase in water level would not be discernable from the previous retreat and formation of strandlines. Nonetheless, there is no geomorphic or sedimetological evidence for a large amount of drainage from the south within the study area (i.e. meltwater channels, fans, lags).

The ages in this thesis provide important new constraints to be incorporated into the larger database of ages along the western margin of the LIS (Dyke 2004, Brown et al. 2011, Gowan et al.

2016, Norris et al. 2019). The optical ages represent limiting timings for the creation of 223 m a.s.l.beach ridges and eolian dunes created above 200 m a.s.l. Overall the impact of these ages suggests that ice sheet reconstructions using the sparse radiocarbon dataset likely underestimate deglaciation and that the area was ice-free and GLM began drainage down the Mackenzie earlier than previously thought. These results are consistent with optical ages obtained to the south, which indicate earlier deglaciation (Munyikwa et al. 2017) compared to radiocarbon-based reconstructions (e.g. Dalton et al. 2020).

The radiocarbon age collected as part of this thesis further adds to the age constraints in the region. This age is useful for Holocene research and has implications for the drainage and evolution of proto-Great Slave Lake.

3.7 Conclusion

Evidence for previously unidentified lakes are documented and lake extents reconstructed north of the Cameron Hills at present day elevations of 290, 265 and 245 m a.s.l. The largest lake phase in the study area was at 240 m a.s.l. The 240 m a.s.l.lake phase corresponds to the southern reaches of glacial Lake Mackenzie and drained into the Mackenzie River Valley (Mathews 1980, Lemmen et al. 1994, Couch and Eyles 2008, Huntley et al. 2017). The Snake Creek Moraine was deposited while the ice margin was in contact with this lake at 240 m a.s.l. The 240 m a.s.l.lake was likely also the maximum filling extent in the study area for GLM.

Ages obtained in this research further inform the retreat of the ice margin in the study area. The beach ridge sample at 223 m a.s.l.indicates that GLM was past its maximum phase by 12.0 ± 0.7 ka BP. This brings the timing of deposition of the Snake Creek Moraine (~12.5 cal. ka BP), and thereby the Mackenzie phase of GLM, to an older time than current reconstructions (Lemmen et al. 1994, Smith 1994, Dyke 2004, Gowan et al. 2016, Dalton et al. 2020). Optical ages collected from dunes yielded two ages of deposition at 10.4 ± 0.3 and 8.2 ± 0.4 ka BP. These ages conform with those from the surrounding area showing successively younger ages as the ice moved to the east and GLM drained exposing more land for eolian dune development (Wolfe et al. 2004, 2007, Munyikwa et al. 2011, 2017). The single radiocarbon age indicates that Holocene lake levels occurred ~ 2.35 cal. ka BP in the upper reaches of the Mackenzie River.

Ultimately, a new ice margin retreat sequence of the western LIS southwest of Great Slave Lake is proposed. It shows a stepwise eastward retreat of the ice margin broadly consistent with previous reconstructions, but brings several new geomorphological and geochronological constraints that previous regional reconstructions did not indicate. The reconstruction shows that the geometry of the ice margin, its retreat style, and the location of stillstands were largely influenced by topography.

Ice margins and proglacial lakes are important factors for meltwater drainage and influence ice sheet dynamics (Stokes and Clark 2004, Carrivick and Tweed 2013, Favier et al. 2014). Integrating the regional ice margins and glacial lakes presented in this thesis can help larger scale ice sheet reconstructions be more accurate, which is important to better understand the connections between ice sheet evolution and global climate (Calov et al. 2002, Balco and Rovey II 2010, Shakun and Carlson 2010, Stokes and Tarasov 2010, Tarasov et al. 2012, Stokes et al. 2015). This improved understanding can also bring useful insights into modern day ice retreat (Evans et al. 1999, 2009, Rignot et al. 2011, Shepherd et al. 2018).

Chapter 4

Conclusion

4.1 Research Contributions

The research investigated the glacial landscape and sedimentary record of the last glaciation in a large region of south-central Northwest Territories, west of Great Slave Lake. This is an area that was covered by the Laurentide Ice Sheet during the last glaciation (Dyke, 2004; Dalton et al., 2020), and where late glacial and deglacial phases were characterized by complex shifts in ice-flow linked to the development of topographically controlled ice lobes, multiple phases of ice-contact lakes, and other proglacial environments (Lemmen, 1990; Lemmen et al., 1994; Dyke, 2004; Stokes et al., 2015; Gowan et al., 2016; Dalton et al., 2020). While this general knowledge of the Late Pleistocene history has been established, several important uncertainties and knowledge gaps were also recognized prior to the start of this research.

One such uncertainty included conflicting ice-flow histories of either a complex sequence of westward ice-flows (Lemmen et al. 1994, Brown et al. 2011, Rice et al. 2013, McClenaghan et al. 2018) or simple westward flow (Sharpe et al. 2017). The research area has had limited field studies to constrain ice-flow observations (i.e. striations and till fabrics) and only large-scale remote mapping campaigns to identify landforms (Prest et al. 1968, Fulton 1995, Brown 2012, Margold et al. 2018).

The limited fieldwork and mapping also lead to uncertainties with respects to till composition and stratigraphy in the region. This is particularly important as the region is highly prospective for Mississippi-Valley Type mineralization (Hannigan 2006b) and where outcrops are limited and thick drift blankets the bedrock. Mineralization is primarily found by drift prospecting is these terrains. Again, there were conflicting reports on patterns within the till composition within the study area. Craig (1965) interpreted that till composition was linked to landforms, while Lemmen (1990) interpreted that till composition reflected the lithology of the underlying bedrock geology. These conflicting observation in combination with the four stacked till units described at Pine Point (Rice et al. 2013, 2019a) meant that a regional understanding of till composition and stratigraphy was needed for the region.

A knowledge gap was also identified with the deglaciation of the study area. The current chronology was based on sparse radiocarbon ages (Fisher and Smith 1994, Lemmen et al. 1994).

These radiocarbon ages have uncertainties with their stratigraphic context and transport history of the carbon samples (i.e. fossilized wood in a delta). These two reconstructions were the first regional compilation attempted over the region and Dyke, 2004 and Dalton et al., 2020 did little to these margins. The limited work over this region meant that it was a suitable target for more detailed fieldwork and mapping to constrain deglaciation (ice margin and glacial lake positions) but also to collect more ages in an attempted to further constrain timing of ice retreat.

4.1.1 Objective 1: Ice-flow History

Based on the knowledge gaps in the region, the first objective was to determine past ice-flow directions and establish their relative age relationships. This objective was completed using multiple records of ice-flow (landform identification, striations, till clast fabrics, till clast lithology counts, till matrix geochemistry); a complex ice-flow history was defined in the study area. They record a clockwise shift; the oldest flow was to the southwest (250°) followed by a westward (280°) and then northwestward flow (305°). A final southwest (250°) surge of ice was found only between the eastern escarpment and the current shore of GSL.

These ice-flows appear have been significantly impacted by ice thickness and the local topography of the area. A thicker ice sheet that was less influenced by topography and flowed southwestward, which indicates that at some time the Plains Ice Divide was north of the study area. As the ice sheet thinned, the Cameron Hills and uplands began to funnel ice to the west/northwest down the Mackenzie River valley. The topographic influence of the ice flows in the region also influenced the late southwestward surge of ice out of the GSL basin, as evidence of this late flow is not found above the escarpment.

4.1.2 Objective 2: Stratigraphy

The second objective was to investigate the regional glacial stratigraphy to establish relationships between the sediments characteristics and the ice-flow phases identified in Objective 1. The second objective was completed by analyzing till matrix geochemistry from till samples collected at surface and at stratigraphic sections. Using this data, four till geochemical groups were identified from the till matrix major oxide PCA. The four geochemical groups were separated primarily based on Canadian Shield/Shale (SiO_2-Al_2O_3-Fe_2O_3-K_2O-TiO_2-Cr_2O_3) vs. Carbonate (CaO-MgO) content. These groups were supported by the clast lithology counts primarily based on Canadian Shield vs.

Carbonate (Paleozoic) percentage. It is noted that some bedrock lithologies have little preservation potential in the coarse fraction of the till due to their competency, specifically the Mesozoic shale in the region. This could influence the compositional data of these tills underestimated the local inputs in the till units. There was also a differentiation between geochemical groups based on proximity to hyper saline beds within the Paleozoic strata, which caused an increase in Na for surface till samples in the north.

The three ice-flows and four till geochemical groups were related. An increased Canadian Shield/shale content till was deposited first by the southwest flow, which was possibly faster resulting in longer transport distances. The increased Canadian shield content till was then subsequently mixed with more local material as the ice sheet thinned and retreated, specifically in the lower lying areas of the study area impacted by the westward and northwestward flows. As a result, the Cameron Hills has the highest Canadian Shield content, and the lower lying areas have increased local carbonate content. Till samples closest to the escarpment contain almost exclusively local material related to plucking as ice flowed transverse over the eastern escarpment. The pattern of till composition generally reflects the ice-flow progression and landforms in the study area although some low-lying areas have older tills preserved at surface.

4.1.3 Objective 3: Deglaciation

The third objective was to reconstruct ice margin retreat and glacial lake positions with surficial geology maps and optical ages and then contrast it to other reconstructions. This final objective was completed using mapped surficial geology and the 2m resolution Arctic DEM (Porter et al. 2018). Sediment landform assemblages composed of meltwater systems, ice-contact sediments, streamlined and ridged till and moraine ridges were used to outline a northeastward ice margin retreat sequence. Again, topography significantly impacted ice margin retreat. The Cameron Hills caused a lobate ice margin down the Mackenzie and Hay River Valley’s and the bedrock escarpments acted as a natural grounding line for the retreating ice margin.

Glacial lake positions were also outlined which helped accurately delineate the ice margin as it blocked natural drainage to the northeast. Due to the northeastward sloping landscape as the margin retreat successive lower outlets were opened changing the arrangement of the proglacial lakes. Lake positions were developed by filling the 2m resolution DEM, not account for GIA, and observing low-lying areas that were related to the surficial geology (i.e. beach ridges, meltwater channels, glaciolacustrine sediments, iceberg scours, fans). The proglacial lakes identified include a previously unreported proglacial lake north of the Cameron Hills, an eastward extension of glacial Lake Mackenzie along the ice margin into the study area, and revised glacial Lake McConnell extents in the study area.

In an effort to fill in the paucity of deglacial ages over this region of the LIS (Lemmen et al. 1994, Smith 1994, Dyke 2004, Wolfe et al. 2007, Gowan et al. 2016, Munyikwa et al. 2017, Dalton et al. 2020) a series of optical ages were collected from a beach ridge and eolian dunes. Two optical ages collected from the same beach ridge indicated that GLM had retreated to present day 223 m a.s.l.by at least 12.0 ± 0.7 ka BP. Five eolian dune dates suggest two peak times of formation, the first at 10.4 ± 0.3 ka BP and the second at 8.2 ± 0.4 ka BP. The two peaks are related to the elevation of the dune as they were progressively exposed by GLM water level recession. The OSL samples recorded here are limiting ages, necessitating that the area be at least ice-free (beach ridge) or ice and lake free (eolian dunes) by at least the age reported. Altogether both the beach and dune optical ages show that the timing of deglaciation presented in previous reconstructions of the study area are too young.

A single radiocarbon age was collected at a location where till was in direct contact with peat in the upper reaches of the Mackenzie River. Five of the six subsamples of the peat indicate that organic formation around 2.3 cal. ka BP providing another date to be used in Holocene reconstruction of proto-Great Slave Lake.

4.2 Implications

The ice flow history presented in this thesis changes the overall configuration of the western LIS. It details evidence that the Plains Ice Divide was likely north of the study area causing the oldest southwestward ice flow across the study area. This is an important improvement over previous ice-flow reconstructions which put the Plains Ice Divide south of the study area with an oldest northwestward flow (Tarasov and Peltier 2005, Brown 2012, Gowan et al. 2016, Margold et al. 2018). This shifts the overall arrangement of ice flow dispersal from the Keewatin to the western LIS, has implication for isostatic rebound rates (due to ice thickness), and the total land ice mass during the last glaciation. The configuration of the western LIS presented here should be reviewed and incorporated into future large-scale ice sheet reconstructions.

The study area lacked regional scale till compositional data. This research identified four different till sheets at surface related to variability in the erosion and deposition, subglacial transport distances, and available material for incorporation (i.e. scavenging from already deposited till or local bedrock). Consequently, when drift prospecting in the region extreme care is needed, specifically when collecting surface till samples as a variety of ice-flow directions and transport distances are preserved. For example, a sample atop the Cameron Hills would be more indicative of a distal bedrock source than a local one, being related to oldest southwestward flow with an increased Canadian Shield content. Complexity arises when this increased Canadian Shield content till is found at surface in the low-lying areas or at the bottom of stratigraphic sections. Ultimately, if drift prospecting in this region, a detailed understanding of the till sampled and its ice-flow history are required for successful vectoring back to its source.

The fieldwork and mapping completed as part of this research indicate further updates to the ice margin are needed when compared to the current reconstructions being used (Lemmen et al. 1994, Dyke 2004, Dalton et al. 2020). The largest change to the ice-margin during the deglaciation is around the Cameron Hills. The current reconstructions have the ice margin moving up the slopes of the Hills and covering just the northern tip. This thesis shows that the whole upland was deglaciated and surrounded by ice lobes; overall, a thinner ice sheet during deglaciation

The reconstruction presented in this thesis also indicates a different arrangement of glacial lakes than current reconstructions being used for the study area (Lemmen et al. 1994, Smith 1994). These include a lake north of the Cameron Hills, but more importantly, an eastward extension of glacial Lake Mackenzie that connects drainage from the study area to the Arctic Ocean (Couch and Eyles 2008). The northward drainage of study area has been indicated as a possible source causing the onset of the Younger Dryas (YD, ~12.9 cal. ka BP); an event observed in various proxy records which is thought to have caused a weakening of the Atlantic Overturning Circulation (AMOC), which in turn influenced global climate (Tarasov and Peltier 2005, Gowan et al. 2016). Glacioisostatic adjustment needs to be considered for the larger scale interpretation of the dataset.

This lake arrangement is also important when taken with the optical ages in the study area. They show at least 500 ka BP earlier age of deglaciation than the current reconstructions being used. This is an observation supported by other researchers, which indicate that using exclusively radiocarbon ages to limit the chronology gives an older deglacial age. The ages presented in this thesis combined with the identified eastward extension of glacial lake Mackenzie indicate that meltwater in the region could be draining into the Arctic Ocean much earlier than previously thought.

The Snake Creek Moraine has only been mentioned in two other reconstructions (Lemmen et al. 1994, Bednarski 2008). This thesis determined that the Snake Creek Moraine was deposited in a shallow eastward extension of glacial Lake Mackenzie while the ice margin was along the eastern escarpment. The sediment-landform assemblages used include esker fan complexes, kettle lakes between ridges and the symmetrical morphology of the ridges. The Moraine is composed of heavily glaciolacustrine-reworked tills, and as such can be difficult to differentiate from superimposed shorelines.

The research also has implications for local stakeholders, allowing them to make more informed decision about their landscape. The knowledge of ice-flows and different till compositions can help mineral exploration target deposits more accurately and efficiently. Furthermore, mapping completed during this thesis has identified areas more suitable for infrastructure development and areas of possible granular aggregate resources to aid northern construction efforts. One such location is in close proximity to the town of Enterprise, where an ice marginal braided river channel was deposited. The mapping also identified areas of organics and permafrost terrain. These can be useful in monitoring landscape evolution as climate change continues to disproportionately impact northern communities.

4.3 Future Work

There are several areas of future work to build on the findings of this thesis. More constraining ages for the ice margins and glacial lake levels would be ideal to help correlate the ice-flows and ice margins in the study area to the surrounding region. This could be completed via further optical dating on dunes or other sandy beach ridges (although these beach ridges are rare). Cosmogenic dating as has been done to the north of the study area could also provide further insight into the Quaternary history although dating material is likely limited (Margold et al. 2017, Kelley et al. 2020, Stoker et al. 2020).

The Snake Creek Moraine represents another area of future work to help understand and correlate its deposition to other features in the surrounding area. The Moraine would be a great target for the above-mentioned cosmogenic dating. Dating the moraine would help with correlation to the surrounding features (Norris et al. 2019). The Snake Creek Moraine could also further help describe the subglacial conditions in the region and be used to study continental ice sheet grounding line moraines in proglacial lakes.

During the course of the larger GEM-2 Southern Mackenzie Surficial program, till matrix trace element geochemistry was also analyzed. This dataset could be used to further differentiated till units helping identify their provenance. This would be particularly useful for till samples within Cluster 4 to determine if the source of the SiO_2-Al_2O_3-Fe_2O_3-K_2O-TiO_2-Cr_2O_3 is from the Canadian Shield or the local Mesozoic shale's.

Further integration of the geoscience data collected during this research with that of the surrounding region would also be beneficial. Streamlined landforms continue north of the study area, and investigating the impact of the Horn Plateau on ice flows would also help create a detailed understanding of the western LIS. Additionally, map sheets to the west could be targeted to further constrain the ice retreat drawn as part of this thesis and identify the proposed drainage pathways and proglacial lake extents.

Finally, this research provides further field data on the mid-Wisconsin extent of the Laurentide Ice Sheet. Pine Point, 50 km the east, is thought to have been ice covered during the mid-Wisconsin (Rice et al. 2013). Therefore, the study area provides and interesting region to test where the retreat of the Mid-Wisconsin ice sheet may have stopped, and how the continental ice sheet began to readvance across the landscape in its transition to the LGM.

References

Atkinson, N., Utting, D.J., and Pawley, S.M. 2014. Landform signature of the Laurentide and Cordilleran ice sheets across Alberta during the last glaciation. Canadian Journal of Earth Sciences, **51**: 1067–1083. doi:10.1139/cjes-2014-0112.

Balco, G., Briner, J.P., Finkel, R.C., Rayburn, J.A., Ridge, J.C., and Schaefer, J.M. 2009. Regional beryllium-10 production rate calibration for late-glacial northeastern North America. Quaternary Geochronology, **4**: 93–107. Elsevier Ltd. doi:10.1016/j.quageo.2008.09.001.

Balco, G., and Rovey II, C.W. 2010. Absolute chronology for major Pleistocene advances of the laurentide ice Sheet. Geology, **38**: 795–798. doi:10.1130/G30946.1.

Barchyn, T.E., Dowling, T.P.F., Stokes, C.R., and Hugenholtz, C.H. 2016. Subglacial bed form morphology controlled by ice speed and sediment thickness. Geophysical Research Letters, **43**: 7572–7580. doi:10.1002/2016GL069558.

Batterson, M.J., and Liverman, D.G.E. 2000. Contrasting styles of glacial dispersal in Newfoundland and Labrador: Methods and case studies. Newfoundland Department of Mines and Energy Current Research, **185**: 1–31. doi:10.1144/GSL.SP.2001.185.01.12.

Bauer, I.E., Gignac, L.D., and Vitt, D.H. 2003. Development of a peatland complex in boreal western Canada: Lateral site expansion and local variability in vegetation succession and long-term peat accumulation. Canadian Journal of Botany, **81**: 833–847. doi:10.1139/b03-076.

Bednarski, J.M. 2008. Landform assemblages produced by the Laurentide Ice Sheet in northeastern British Columbia and adjacent Northwest Territories - Constraints on glacial lakes and patterns of ice retreat. Canadian Journal of Earth Sciences, **45**: 593–610. doi:10.1139/E07-053.

Benediktsson, Í.Ö., Jónsson, S.A., Schomacker, A., Johnson, M.D., Ingólfsson, Ó., Zoet, L., Iverson, N.R., and Stötter, J. 2016. Progressive formation of modern drumlins at Múlajökull, Iceland: stratigraphical and morphological evidence. Boreas, **45**: 567–583. doi:10.1111/bor.12195.

Benn, D.I. 2004. Macrofabric. *In* A Practical Guide to the Study of Glacial Sediments. *Edited by* D.J. Evans and D.I. Benn. Hodder Education, London, Eng.

Benn, D.I., and Evans, D.J.A. 2010. Glaciers and Glaciation. *In* 2nd edition. Hodder Education, London, Eng.

Bentley, C.R., Clough, J.W., Jezek, K.C., and Shabtabie, S. 1979. Ice-Thickness Patterns and the Dynamics of the Ross Ice Shelf, Antarctica. Journal of Glaciology,.

Bøtter-Jensen, L., Thomsen, K.J., and Jain, M. 2010. Review of optically stimulated luminescence (OSL) instrumental developments for retrospective dosimetry. Radiation Measurements, **45**: 253–257. Elsevier Ltd. doi:10.1016/j.radmeas.2009.11.030.

Boulton, G.S. 1978. Boulder shapes and grain- size distributions of debris as indicators of transport paths through a glacier and till genesis. Sedimentology, **25**: 773–799. doi:10.1111/j.1365-3091.1978.tb00329.x.

Boulton, G.S. 1982. Processes and patterns of glacial erosion. *In* Glacial Geomorphology. Springer. pp. 41–87.

Boulton, G.S. 1996. Theory of glacial erosion, transport and deposition as a consequence of subglacial sediment deformation. Journal of Glaciology, **42**: 43–62. doi:10.1017/S0022143000030525.

Boulton, G.S., and Hagdorn, M. 2006. Glaciology of the British Isles Ice Sheet during the last glacial cycle: form, flow, streams and lobes. Quaternary Science Reviews, **25**: 3359–3390. doi:10.1016/j.quascirev.2006.10.013.

Boulton, G.S., Smith, G.D., Jones, A.S., and Newsome, J. 1985. Glacial geology and glaciology of the last mid-latitude ice sheets. Geological Society of London, **142**: 447–474. doi:10.1144/gsjgs.142.3.0447.

Brennand, T.A. 2000. Deglacial meltwater drainage and glaciodynamics: Inferences from Laurentide eskers, Canada. Geomorphology, **32**: 263–293. doi:10.1016/S0169-555X(99)00100-2.

Broecker, W.S., Kennettt, J.P., Flower, B.P., Teller, J.T., Trumbore, S., Bonani, G., and Wolfli, W. 1989. Routing of meltwater from the Laurentide Ice. Nature, **341**: 318–321.

Bronk Ramsey, C. 2008. Radiocarbon dating: Revolutions in understanding. Archaeometry, **50**: 249–275. doi:10.1111/j.1475-4754.2008.00394.x.

Bronk Ramsey, C. 2009. Bayesian Analysis of Radiocarbon Dates. Radiocarbon, **51**: 337–360.

Bronk Ramsey, C. 2020. OxCal.

Brown, V.H. 2012. Ice stream dynamics and pro-glacial lake evolution along the north-western margin of the Laurentide Ice Sheet. Durham Univeristy thesis,. doi:10.1017/CBO9781107415324.004.

Brown, V.H., Stokes, C.R., and O'Cofaigh, C. 2011. The glacial geomorphology of the North-West sector of the Laurentide Ice Sheet. Journal of Maps, **7**: 409–428. doi:10.4113/jom.2011.1224.

Burn, C.R., and Smith, M.W. 1990. Development of thermokarst lakes during the holocene at sites near Mayo, Yukon territory. Permafrost and Periglacial Processes, **1**: 161–175. doi:10.1002/ppp.3430010207.

Calov, R., Ganopolski, A., Petoukhov, V., Claussen, M., and Greve, R. 2002. Large-scale instabilities of the Laurentide ice sheet simulated in a fully coupled climate-system model. Geophysical Research Letters, **29**: 1–4. doi:10.1029/2002gl016078.

Cameron, E.M. 1969. Regional geochemical study of the Slave Point carbonates, Western Canada. Canadian Journal of Earth Sciences, **6**: 247–268. doi:10.1139/e69-023.

Carrivick, J.L., and Tweed, F.S. 2013. Proglacial Lakes: Character, behaviour and geological importance. Quaternary Science Reviews, **78**: 34–52. Elsevier Ltd. doi:10.1016/j.quascirev.2013.07.028.

Chandler, B.M., Lovell, H., Boston, C.M., Lukas, S., Barr, I.D., Benediktsson, Í.Ö., Benn, D.I., Clark, C.D., Darvill, C.M., Evans, D.J.A., Ewertowski, M.W., Loibl, D., Margold, M., Otto, J., Roberts, D.H., Stokes, C.R., Storrar, R.D., and Stroeven, A.P. 2018. Glacial geomorphological mapping: A review of approaches and frameworks for best practice. Earth-Science Reviews, **185**: 806–846. Elsevier. doi:10.1016/j.earscirev.2018.07.015.

Clark, C.D. 1993. Mega-scale lineations and cross-cutting ice-flow landforms. Earth Surface Processes and Landforms, **18**: 1–29.

Clark, P.U. 1987. Subglacial Sediment Dispersal and till Composition. The Journal of Geology, **95**: 527–541.

Clark, P.U. 1991. Striated clast pavements: products of deforming subglacial sediment? Geology, **19**: 530–533. doi:10.1130/0091-7613(1991)019<0530:SCPPOD>2.3.CO;2.

Clarke, G.K.C. 2005. Subglacial processes. Annual Review of Earth and Planetary Sciences, **33**: 247–

276. doi:10.1146/annurev.earth.33.092203.122621.

Cohen, D., Hooyer, T.S., Iverson, N.R., Thomason, J.F., and Jackson, M. 2006. Role of transient water pressure in quarrying: A subglacial experiment using acoustic emissions. Journal of Geophysical Research: Earth Surface, **111**: 1–13. doi:10.1029/2005JF000439.

Condron, A., and Winsor, P. 2012. Meltwater routing and the Younger Dryas. Proceedings of the National Academy of Sciences of the United States of America, **109**: 19928–19933. doi:10.1073/pnas.1207381109.

Couch, A.G., and Eyles, N. 2008. Sedimentary record of glacial Lake Mackenzie, Northwest Territories, Canada: Implications for Arctic freshwater forcing. Palaeogeography, Palaeoclimatology, Palaeoecology, **268**: 26–38. doi:10.1016/j.palaeo.2008.06.011.

Couture, R., Smith, S., Robinson, S.D., Burgess, M.M., and Solomon, S. 2003. On the hazards to inrstructure in the Canadian North associated with thawing of permafrost. *In* Proceedings of the 3rd Canadian Conference on Geohazards.

Craig, B.G. 1965. Glacial Lake McConnell, and the Surficial Geology of Parts of Slave River and Redstone River Map-Areas, District of Mackenzie. Geological Survey of Canada Bulletin 122,: 44. doi:10.1007/978-3-642-41714-6_70729.

Crann, C.A., Murseli, S., St-Jean, G., Zhao, X., Clark, I.D., and Kieser, W.E. 2017. First Status Report on Radiocarbon Sample Preparation Techniques at the A.E. Lalonde AMS Laboratory (Ottawa, Canada). Radiocarbon, **59**: 695–704. doi:10.1017/RDC.2016.55.

Dalton, A.S., Margold, M., Stokes, C.R., Tarasov, L., Dyke, A.S., Adams, R.S., Allard, S., Arends, H.E., Atkinson, N., Attig, J.W., Barnett, P.J., Barnett, R.L., Batterson, M., Bernatchez, P., Borns, H.W., Breckenridge, A., Briner, J.P., Brouard, E., Campbell, J.E., Carlson, A.E., Clague, J.J., Curry, B.B., Daigneault, R.A., Dubé-Loubert, H., Easterbrook, D.J., Franzi, D.A., Friedrich, H.G., Funder, S., Gauthier, M.S., Gowan, A.S., Harris, K.L., Hétu, B., Hooyer, T.S., Jennings, C.E., Johnson, M.D., Kehew, A.E., Kelley, S.E., Kerr, D.E., King, E.L., Kjeldsen, K.K., Knaeble, A.R., Lajeunesse, P., Lakeman, T.R., Lamothe, M., Larson, P., Lavoie, M., Loope, H.M., Lowell, T. V., Lusardi, B.A., Manz, L., McMartin, I., Nixon, F.C., Occhietti, S., Parkhill, M.A., Piper, D.J.W., Pronk, A.G., Richard, P.J.H., Ridge, J.C., Ross, M., Roy, M., Seaman, A.A., Shaw, J., Stea, R.R., Teller, J.T., Thompson, W.B., Thorleifson, L.H., Utting, D.J., Veillette, J.J., Ward, B.C., Weddle, T.K., and Wright, H.E. 2020. An updated radiocarbon-based ice margin chronology for the last deglaciation of the North American Ice Sheet Complex. Quaternary Science Reviews, **234**: 1–27. doi:10.1016/j.quascirev.2020.106223.

Day, S.J.A., Paulen, R.C., Smith, I.R., and King, R.D. 2018. Heavy-mineral and indicator-mineral data from stream sediments of southwest Northwest Territories: new potential for undiscovered mineralization. Geological Survey of Canada Open File 8362,: 20.

Deblonde, C., Plouffe, A., Buller, G., Davenport, P., Everett, D., Huntley, D., Inglis, E., Kerr, D.E., Moore, A., Paradis, S.J., Parent, M., Smith, I.R., and Weatherston, A. 2012. Science Language for an Integrated Geological Survey of Canada Data Model for Surficial Geology Maps, Version 1.2. doi:10.4095/290144.

Dove, D., Evans, D.J.A., Lee, J.R., Roberts, D.H., Tappin, D.R., Mellett, C.L., Long, D., and Callard, S.L. 2017. Phased occupation and retreat of the last British–Irish Ice Sheet in the southern North Sea; geomorphic and seismostratigraphic evidence of a dynamic ice lobe. Quaternary Science Reviews, **163**: 114–134. Elsevier Ltd. doi:10.1016/j.quascirev.2017.03.006.

Dredge, L.A., Kerr, D.E., and Wolfe, S.A. 1999. Surficial materials and related ground ice conditions, Slave Province, N.W.T., Canada. Canadian Journal of Earth Sciences, **36**: 1227–1238. doi:10.1139/cjes-36-7-1227.

Dreimanis, A., and Vagners, U.J. 1974. Bimodal Distribution of Rock and Mineral Fragments in Basal Till. *In* Till: A Symposium. *Edited by* J.T. Andrews and R.P. Goldthwait. p. 100. doi:10.2307/1550375.

Drzyzga, S.A., Shortridge, A.M., and Schaetzl, R.J. 2012. Mapping the phases of Glacial Lake Algonquin in the upper Great Lakes region, Canada and USA, using a geostatistical isostatic rebound model. Journal of Paleolimnology, **47**: 357–371. doi:10.1007/s10933-011-9550-9.

Dyke, A.S. 2004. An outline of North American deglaciation with emphasis on central and northern Canada. *In* Developments in Quaternary Sciences. Elsevier. doi:10.1016/S1571-0866(04)80209-4.

Dyke, A.S., Andrews, J.T., Clark, P.U., England, J.H., Miller, G.H., Shaw, J., and Veillette, J.J. 2002. The Laurentide and Innuitian ice sheets during the Last Glacial Maximum. Quaternary Science Reviews, **21**: 9–31. doi:10.1016/S0277-3791(01)00095-6.

Dyke, A.S., and Prest, V.K. 1987. Late Wisconsinan and Holocene history of the Laurentide Ice Sheet. Geographie Physique et Quaternaire, **41**: 237–263. doi:10.7202/032681ar.

Ely, J.C., Clark, C.D., Spagnolo, M., Stokes, C.R., Greenwood, S.L., Hughes, A.L., Dunlop, P., and Hess, D. 2016. Do subglacial bedforms comprise a size and shape continuum? Geomorphology, **257**: 108–119. Elsevier B.V. doi:10.1016/j.geomorph.2016.01.001.

Evans, D.J.A., and Benn, D.I. 2004. Facies description and the logging of sedimentary exposures. *In* A Practical Guide to the Study of Glacial Sediments. *Edited by* D.J.A. Evans and D.I. Benn. Hodder Education, London, Eng. pp. 11–52.

Evans, D.J.A., Clark, C.D., and Rea, B.R. 2008. Landform and Sediment imprints of fast glacier flow in the southwest Laurentide Ice Sheet. Journal of Quaternary Science, **23**: 249–272. doi:10.1002/jqs.

Evans, D.J.A., Lemmen, D.S., and Rea, B.R. 1999. Glacial landsystems of the southwest Laurentide ice sheet: Modern Icelandic analogues. Journal of Quaternary Science, **14**: 673–691. doi:10.1002/(sici)1099-1417(199912)14:7<673::aid-jqs467>3.0.co;2-%23.

Evans, D.J.A., Phillips, E.R., Hiemstra, J.F., and Auton, C.A. 2006. Subglacial till: Formation, sedimentary characteristics and classification. Earth-Science Reviews, **78**: 115–176. doi:10.1016/j.earscirev.2006.04.001.

Evans, D.J.A., and Rea, B.R. 1999. Geomorphology and sedimentology of surging glaciers: A land-systems approach. Annals of Glaciology, **28**: 75–82. doi:10.3189/172756499781821823.

Evans, D.J.A., Twigg, D.R., Rea, B.R., and Orton, C. 2009. Surging glacier landsystem of tungnaárjökull, iceland. Journal of Maps, **5**: 134–151. doi:10.4113/jom.2009.1064.

Evans, I.S. 2012. Geomorphometry and landform mapping: What is a landform? Geomorphology, **137**: 94–106. Elsevier B.V. doi:10.1016/j.geomorph.2010.09.029.

Favier, L., Durand, G., Cornford, S.L., Gudmundsson, G.H., Gagliardini, O., Gillet-Chaulet, F., Zwinger, T., Payne, A.J., and Le Brocq, A.M. 2014. Retreat of Pine Island Glacier controlled by marine ice-sheet instability. Nature Climate Change, **4**: 117–121. Nature Publishing Group. doi:10.1038/nclimate2094.

Fisher, T.G., and Smith, D.G. 1994. Glacial Lake Agassiz: Its northwest maximum extent and outlet in Saskatchewan (Emerson Phase). Quaternary Science Reviews, **13**: 845–858. doi:10.1016/0277-3791(94)90005-1.

Fulton, R.J. 1995. Surficial Map of Canada; Geological Survey of Canada, “A” Series Map 1880A.

Galbraith, R.F., Roberts, R.G., Laslett, G.M., Yoshida, H., and Olley, J.M. 1999. Optical dating of single and multiple grains of quartz from jinmium rock shelter, northern australia: part i, experimental design and statistical models. Archaeometry, **2**: 339–364.

Gauthier, M.S., Hodder, T.J., Ross, M., Kelley, S.E., Rochester, A., and McCausland, P. 2019. The subglacial mosaic of the Laurentide Ice Sheet; a study of the interior region of southwestern Hudson Bay. Quaternary Science Reviews, **214**: 1–27. Elsevier Ltd. doi:10.1016/j.quascirev.2019.04.015.

Geolgocial Survey of Canada. 2019. Reconassance Surficial Geology, Mills Lake Northwest Territories, NTS 85-E, Canadian Geoscience Map 373.

Girard, I., Klassen, R.A., and Laframboise, R.R. 2004. Sedimentology Laboratory Manual, Terrain Sciences Division. Geological Survey of Canada Open File 4823,: 137.

Gowan, E.J., Tregoning, P., Purcell, A., Montillet, J., and McClusky, S. 2016. A model of the western Laurentide Ice Sheet, using observations of glacial isostatic adjustment. Quaternary Science Reviews, **139**: 1–16. Elsevier Ltd. doi:10.1016/j.quascirev.2016.03.003.

Grünfeld, K. 2007. The separation of multi-element spatial patterns in till geochemistry of southeastern Sweden combining GIS, principal component analysis and high-dimensional visualization. Geochemistry: Exploration, Environment, Analysis, **7**: 303–318. doi:10.1144/1467-7873/06-117.

Grunsky, E.C. 2010. The interpretation of geochemical survey data. Geochemistry: Exploration, Environment, Analysis, **10**: 27–74. doi:10.1144/1467-7873/09-210.

Hagedorn, G.W., Paulen, R.C., Smith, I.R., Ross, M., Neudorf, C.M., Gingerish, T., and Lian, O.B. (n.d.). Optical Dates Near the Southwestern Shore of Great Slave Lake.

Hall, A.M., Krabbendam, M., van Boeckel, M., Goodfellow, B.W., Hättestrand, C., Heyman, J., Palamakumbura, R.N., Stroeven, A.P., and Näslund, J.O. 2020. Glacial ripping: geomorphological evidence from Sweden for a new process of glacial erosion. Geografiska

Annaler, Series A: Physical Geography,. doi:10.1080/04353676.2020.1774244.

Hannigan, P.K. 2006a. Introduction. Bulletin of the Geological Survey of Canada 591,: 9–39.

Hannigan, P.K. 2006b. Synthesis of Mississippi valley-type lead-zinc deposit potential in northern Alberta and southern Northwest Territories. Bulletin of the Geological Survey of Canada,: 305–347.

Head, M.J., Pillans, B., and Zalasiewicz, J.A. 2021. Formal ratification of subseries for the Pleistocene Series of the Quaternary System. Episodes, **44**: 241–247. doi:10.18814/epiiugs/2020/020084.

Heginbottom, J., Dubreuil, M., and Harker, P. 1995. Permafrost. *In* The National Atlas of Canada. Edition 5. National Atlas Information Service, Geomatics Canada and Geological Survey of Canada, Ottawa, ON.

Hickin, A.S., Lian, O.B., Levson, V.M., and Cui, Y. 2015. Pattern and chronology of glacial Lake Peace shorelines and implications for isostacy and ice-sheet configuration in northeastern British Columbia, Canada. Boreas, **44**: 288–304. doi:10.1111/bor.12110.

Hicock, S.R. 1987. Genesis of carbonate till in the lee sides of Precambrian Shield uplands, Hemlo area, Ontario. Canadian Journal of Earth Sciences, **24**: 2004–2015. doi:10.1139/e87-191.

Hicock, S.R., and Dreimanis, A. 1989. Sunnybrook drift indicates a grounded early Wisconsin glacier in the Lake Ontario basin. Geology, **17**: 169–172. doi:10.1130/0091-7613(1989)017<0169:SDIAGE>2.3.CO;2.

Hicock, S.R., Goff, J.R., Lian, O.B., and Little, E.C. 1996. On the Interpretation of Subglacial Till Fabric. Journal of Sedimentary Research, **66**: 928–934.

Hodder, T.J., Ross, M., and Menzies, J. 2016. Sedimentary record of ice divide migration and ice streams in the Keewatin core region of the Laurentide Ice Sheet. Sedimentary Geology, **338**: 97–114. Elsevier B.V. doi:10.1016/j.sedgeo.2016.01.001.

Hoffman, P.F. 1987. Continental transform tectonics: Great Slave Lake shear zone (ca. 1.9 Ga), northwest Canada. Geology, **15**: 785–788. doi:10.1130/0091-7613(1987)15<785:CTTGSL>2.0.CO;2.

Huntley, D.H., Hickin, A.S., and Lian, O.B. 2017. The pattern and style of deglaciation at the Late

Wisconsinan Laurentide and Cordilleran ice sheet limits in northeastern British Columbia. Canadian Journal of Earth Sciences, **54**: 52–75. doi:10.1139/cjes-2016-0066.

Huntley, D.J., and Lamothe, M. 2001. Ubiquity of anomalous fading in K-feldspars and the measurement and correction for it in optical dating. Canadian Journal of Earth Sciences, **38**: 1093–1106. doi:10.1139/e01-013.

Iverson, N.R. 1991a. Potential effects of subglacial water-pressure fluctuations on quarrying. Journal of Glaciology, **37**: 27–36. doi:10.3189/s0022143000042763.

Iverson, N.R. 1991b. Morphology of glacial striae: implications for abrasion of glacier beds and fault surfaces. Geological Society of America Bulletin, **103**: 1308–1316. doi:10.1130/0016-7606(1991)103<1308:MOGSIF>2.3.CO;2.

Iverson, N.R. 1993. Regelation of ice through debris at glacier beds: implication for sediment transport. Geology, **21**: 559–562. doi:10.1029/94JC00571.

Iverson, N.R., Hooyer, T.S., and Baker, R.W. 1998. Ring-shear studies of till deformation: Coulomb-plastic behaviour and distributed strain in glacier beds. Journal of Glaciology, **44**: 634–642.

Iverson, N.R., and Souchez, R. 1996. Isotopic signature of debris-rich ice formed by regelation into a subglacial sediment bed. Geophysical Research Letters, **23**: 1151–1154. doi:10.1029/96GL01073.

Ivy-Ochs, S., and Kober, F. 2008. Surface exposure dating with cosmogenic nuclides. Quaternary Science Journal, **57**: 179–209. doi:10.3285/eg.57.1-2.7.

Jull, A.J.T. 2007. Dating Techniques. *In* Encyclopedia of Quaternary Science. pp. 2911–2918.

Jull, A.J.T., Burr, G.S., and Hodgins, G.W.L. 2013. Radiocarbon dating, reservoir effects, and calibration. Quaternary International, **299**: 64–71. doi:10.1016/j.quaint.2012.10.028.

Kelley, S.E., Ward, B.C., Briner, J.P., Ross, M., Normandeau, P.X., and Elliott, B. 2020. The recession of the Laurentide Ice Sheet in southeast Northwest Territories during the Pleistocene-Holocene transition.

King, L.H. 1993. Till in the Marine Environment. Journal of Quaternary Science, **8**: 347–358.

King, L.H., Rokoengen, K., Fader, G.B.J., and Gunleiksrud, T. 1991. Till-tongue stratigraphy. Geological Society of America Bulletin, **103**: 637–659.

Klassen, R.A., and Thompson, F.J. 1993. Glacial history, drift composition, and mineral exploration, central Labrador. *In* Geological Survey of Canada Bulletin 435. doi:10.4095/183906.

Krabbendam, M., and Glasser, N.F. 2011. Glacial erosion and bedrock properties in NW Scotland: Abrasion and plucking, hardness and joint spacing. Geomorphology, **130**: 374–383. British Geological Survey. doi:10.1016/j.geomorph.2011.04.022.

Layberry, R.L., and Bamber, J.L. 2001. Between Dynamics and Basal Topography. Journal of Geophysical Research, **106**: 33781–33788.

Lemmen, D.S. 1990. Surficial materials associated with glacial Lake McConnell, southern District of Mackenzie. Geological Survey of Canada, Paper 90-1D,: 79–83.

Lemmen, D.S., Duk-Rodkin, A., and Bednarski, J.M. 1994. Late glacial drainage systems along the northwestern margin of the Laurentide Ice Sheet. Quaternary Science Reviews, **13**: 805–828. doi:10.1016/0277-3791(94)90003-5.

Li, T., Wu, P., Wang, H., Steffen, H., Khan, N.S., Engelhart, S.E., Vacchi, M., Shaw, T.A., Peltier, W.R., and Horton, B.P. 2020. Uncertainties of Glacial Isostatic Adjustment Model Predictions in North America Associated With 3D Structure. Geophysical Research Letters, **47**: 1–10. doi:10.1029/2020GL087944.

Lian, O.B., and Roberts, R.G. 2006. Dating the Quaternary: progress in luminescence dating of sediments. Quaternary Science Reviews, **25**: 2449–2468. doi:10.1016/j.quascirev.2005.11.013.

Majorowicz, J.A., and Hannigan, P.K. 2006. New thermal evidence related to carbonate-hosted metal ores in the Northwest Territories. Geological Survey of Canada Bulletin 591,: 105–116. doi:10.4095/222923.

Margold, M., Froese, D.G., Gosse, J.C., Yang, G., Mckenna, J., and Hidy, A.J. 2017. Early and abrupt retreat of the Laurentide Ice Sheet margin from the Mackenzie River valley , southern Northwest Territories.

Margold, M., Gosse, J.C., Hidy, A.J., Woywitka, R.J., Young, J.M., and Froese, D.G. 2019. Beryllium-10 dating of the Foothills Erratics Train in Alberta, Canada, indicates detachment of the Laurentide Ice Sheet from the Rocky Mountains at ~15 ka. Quaternary Research, **92**: 469–482. doi:10.1017/qua.2019.10.

Margold, M., Stokes, C.R., and Clark, C.D. 2018. Reconciling records of ice streaming and ice margin retreat to produce a palaeogeographic reconstruction of the deglaciation of the Laurentide Ice Sheet. Quaternary Science Reviews, **189**: 1–30. Elsevier Ltd. doi:10.1016/j.quascirev.2018.03.013.

Margold, M., Stokes, C.R., Clark, C.D., and Kleman, J. 2015. Ice streams in the Laurentide Ice Sheet: a new mapping inventory. Journal of Maps, **11**: 380–395. Taylor & Francis. doi:10.1080/17445647.2014.912036.

Mark, D.M. 1973. Analysis of axial orientation data, including till fabrics. Geological Society of America Bulletin, **84**: 1369–1374. doi:10.1130/0016-7606(1973)84<1369:AOAODI>2.0.CO;2.

Marshall, S.J., Clarke, G.K.C., Dyke, A.S., and Fisher, D.A. 1996. Geologic and topogrpahic controls on fast flow in the Laurentide and Cordilleran Ice Sheets. Journal of Geophysical Research, **101**.

Mathews, W.H. 1980. Retreat of the Last Ice Sheets in Northeastern British Columbia and Adjacent Alberta. Geological Survey of Canada - Bulletin 331,: 22.

McClenaghan, M.B., Parkhill, M.A., Averill, S.A., Pronk, A.G., Seaman, A.A., Boldon, R., McCurdy, M.W., and Rice, J.M. 2013a. Indicator mineral abundance data for bedrock , till , and stream sediment samples from the Sisson W-Mo deposit , New Brunswick. Geological Survey of Canada Open File 7431,: 29. doi:10.4095/292670.

McClenaghan, M.B., and Paulen, R.C. 2018. Application of Till Mineralogy and Geochemistry to Mineral Exploration. *In* Past Glacial Environments: Second Edition. doi:10.1016/B978-0-08-100524-8.00022-1.

McClenaghan, M.B., Paulen, R.C., and Oviatt, N.M. 2018. Geometry of indicator mineral and till geochemistry dispersal fans from the Pine Point Mississippi Valley-type Pb-Zn district, Northwest Territories, Canada. Journal of Geochemical Exploration, **190**: 69–86. Elsevier. doi:10.1016/j.gexplo.2018.02.004.

McClenaghan, M.B., Plouffe, A., McMartin, I., Campbell, J.E., Spirito, W.A., Paulen, R.C., Garrett, R.G., and Hall, G.E.M. 2013b. Till sampling and geochemical analytical protocols used by the Geological Survey of Canada. Geochemistry: Exploration, Environment, Analysis, **13**: 285–301. doi:10.1144/geochem2011-083.

McConnell, R.G. 1890. Report on an exploration in the Yukon and Mackenzie Basins N.W.T.

Geological and Natural History Survey of Canada,: 163.

McCurdy, M.W., Smith, I.R., Plouffe, A., Bednarski, J.M., Day, S.J.A., Friske, P.W.B., McNeil, R.J., Kjarsgaard, I.M., Ferbey, T., Levson, V.M., Hickin, A.S., Trommelen, M.S., and Demchuk, T.E. 2007. Indicator Mineral Content and Geochemistry of Stream and Glacial Sediments from the Etsho Plateau Region (NTS 094I , P) as an Aid to Kimberlite and Base Metal Exploration , Northeast British Comumbia. Geoscience BC, Report 2007-1, **1**: 361–372.

McLennan, S.M. 2001. Relationships between the trace element composition of sedimentary rocks and the upper continental crust. Geochemistry, Geophysics, Geosystems, **249**. doi:10.1038/scientificamerican0983-130.

McMartin, I., Dredge, L.A., Grunsky, E.C., and Pehrsson, S. 2016. Till geochemistry in West-Central Manitoba: Interpretation of provenance and mineralization based on glacial history and multivariate data analysis. Economic Geology, **111**: 1001–1020. doi:10.2113/econgeo.111.4.1001.

McMartin, I., and Henderson, P.J. 2004. Evidence From Kewatin (Central Nunavut) for Paleo-Ice Divide Migration. Géographie physique et Quaternaire, **58**: 163–186. doi:10.7202/013137ar.

McMartin, I., and Paulen, R.C. 2009. Ice-flow indicators and the importance of ice-flow mapping for drift prospecting. *In* Application of Till and Stream Sediment Heavy Mineral and Geochemical Methods to Mineral Exploration in Western and Northern Canada. *Edited by* R.C. Paulen and I. McMartin. Geolocial Association of Canada, GAC Short Course Notes. pp. 15–34.

Menzies, J. 2001. Subaqueous Grounding-Line Moraines in the Central Niagara Peninsula , Southern Ontario. Geographie Physique Et Quaternaire, **55**: 75–86.

Menzies, J., van der Meer, J.J.M., and Shilts, W.W. 2018. Subglacial Processes and Sediments. *In* Past Glacial Environments: Second Edition. doi:10.1016/B978-0-08-100524-8.00004-X.

Menzies, J., Paulen, R.C., Rice, J.M., McClenaghan, M.B., Oviatt, N.M., and Dhillon, N. 2019. Deformation ‘boundary front’ movements in subglacial tills—A microsedimentological perspective from till sequences near Pine Point, NWT, Canada. The Depositional Record, **5**: 230–246. doi:10.1002/dep2.73.

Millard, A.R. 2014. Conventions for Reporting Radiocarbon Determinations. Radiocarbon, **56**: 555–559. doi:10.2458/56.17455.

Mook, W.G., and van der Plicht, J. 1999. Reporting 14C Activities and Concentrations. Radiocarbon, **41**: 227–239.

Munyikwa, K., Feathers, J.K., Rittenour, T.M., and Shrimpton, H.K. 2011. Constraining the Late Wisconsinan retreat of the Laurentide ice sheet from western Canada using luminescence ages from postglacial aeolian dunes. Quaternary Geochronology, **6**: 407–422. Elsevier B.V. doi:10.1016/j.quageo.2011.03.010.

Munyikwa, K., Rittenour, T.M., and Feathers, J.K. 2017. Temporal constraints for the Late Wisconsinan deglaciation of western Canada using eolian dune luminescence chronologies from Alberta. Palaeogeography, Palaeoclimatology, Palaeoecology, **470**: 147–165. Elsevier B.V. doi:10.1016/j.palaeo.2016.12.034.

Murseli, S., Middlestead, P., St-Jean, G., Zhao, X., Jean, C., Crann, C.A., Kieser, W.E., and Clark, I.D. 2019. The Preparation of Water (DIC, DOC) and Gas (CO 2 , CH 4) Samples for Radiocarbon Analysis at AEL-AMS, Ottawa, Canada. Radiocarbon, **61**: 1563–1571. doi:10.1017/rdc.2019.14.

Murton, J.B., Bateman, M.D., Dallimore, S.R., Teller, J.T., and Yang, Z. 2010. Identification of Younger Dryas outburst flood path from Lake Agassiz to the Arctic Ocean. Nature, **464**: 740–743. doi:10.1038/nature08954.

Neudorf, C.M., Lian, O.B., Walker, I.J., Shugar, D.H., Eamer, J.B.R., and Griffin, L.C.M. 2015. Toward a luminescence chronology for coastal dune and beach deposits on Calvert Island, British Columbia central coast, Canada. Quaternary Geochronology, **30**: 275–281. doi:10.1016/j.quageo.2014.12.004.

Nick, F.M., Van Der Veen, C.J., Vieli, A., and Benn, D.I. 2010. A physically based calving model applied to marine outlet glaciers and implications for the glacier dynamics. Journal of Glaciology, **56**: 781–794. doi:10.3189/002214310794457344.

Normandeau, P.X., Elliott, B., and Kerr, D.E. 2015. Revisiting Lac De Gras Till Geochemisty in Preparation for the Slave Province Surficial Materials Study, Northwest Territories, Canada. International Applied Geochemistry Symposium,: 7.

Norris, S., Tarasov, L., Gosse, J., Hidy, A.J., Margold, M., and Froese, D. 2021. Rapid Retreat of the Southwestern Laurentide Ice Sheet Driven By Bølling-Allerød Warming. **XX**: 1–5.

doi:10.1130/abs/2020am-358989.

Norris, S.L. 2020. Dynamic response of the southwestern Laurentide Ice Sheet during the last glaciation. Department of Earth and Atmospheric Sciences Thesis, **1**: 105–112.

Norris, S.L., Margold, M., Utting, D.J., and Froese, D.G. 2019. Geomorphic, sedimentary and hydraulic reconstruction of a glacial lake outburst flood in northern Alberta, Canada. Boreas, **48**: 1006–1018. doi:10.1111/bor.12403.

O'Neill, H.B., Wolfe, S.A., and Kerr, D.E. 2019. Surficial geology and Holocene shoreline evolution near Whitebeach Point , Great Slave Lake , Northwest Territories. Geological Survey of Canada Current Research 2019-3,: 15. doi:10.4095/314638.

Okulitch, A. V. 2006. Phanerozoic bedrock geology, Slave River, District of Mackenzie, Northwest Territories: Geological Survey of Canada, Open File 5282.

Oviatt, N.M., Gleeson, S.A., Paulen, R.C., McClenaghan, M.B., and Paradis, S.J. 2015. Characterization and dispersal of indicator minerals associated with the pine point mississippi valley-type (MVT) district, northwest territories, Canada. Canadian Journal of Earth Sciences, **52**: 776–794. doi:10.1139/cjes-2014-0108.

Oviatt, N.M., McClenaghan, M.B., Paulen, R.C., and Gleeson, S.A. 2013a. Till geochemical signatures of the Pine Point Pb-Zn Mississippi Valley-type district, Northwest Territories. Geological Survey of Canada Open File 7320,: 59. doi:10.4095/292906.

Oviatt, N.M., McClenaghan, M.B., Paulen, R.C., Gleeson, S.A., Averill, S.A., and Paradis, S.J. 2013b. Indicator minerals in till and bedrock samples from the Pine Point Mississippi Valley-Type (MVT) district, Northwest Territories. Geological Survey of Canada Open File 7423,: 87. doi:10.4095/293031.

Oviatt, N.M., and Paulen, R.C. 2013. Surficial geology, Breynat Point NTS 85-B/15, Northwest Territories, Geological Survey of Canada, Canadian Geoscience Map 114, 1 sheet. Scale 1:50 000.

Oviatt, N.M., Paulen, R.C., and Rufiange, E.C. 2014. Surficial geology field observations and photographs for the Breynat Point map area (NTS 85-B/15). Geological Survey of Canada Open File 7568,: 15. doi:10.4095/293452.

Parent, M., and Occhietti, S. 1999. Late Wisconsinan deglaciation and glacial lake development in the appalachians of southeastern Quebec. Geographie Physique et Quaternaire, **53**: 117–135. doi:10.7202/004859ar.

Parent, M., Paradis, S.J., and Doiron, A. 1996. Palimpsest glacial dispersal trains and their significance for drift prospecting. Journal of Geochemical Exploration, **56**: 123–140.

Paulen, R.C., Day, S.J.A., King, R.D., Piercey, S.J., and Smith, I.R. 2018. New base metals mineral potential in southern Northwest Territories, Canada. EXPLORE,.

Paulen, R.C., and McClenaghan, M.B. 2014. Late wisconsin ice-flow history in the buffalo head hills kimberlite field, north-central alberta. Canadian Journal of Earth Sciences, **52**: 51–67. doi:10.1139/cjes-2014-0109.

Paulen, R.C., Paradis, S.J., Plouffe, A., and Smith, I.R. 2011. Pb and S isotopic composition of indicator minerals in glacial sediments from NW Alberta, Canada: Implications for Zn-Pb base metal exploration. Geochemistry: Exploration, Environment, Analysis, **11**: 309–320. doi:10.1144/1467-7873/10-IM-032.

Paulen, R.C., Prior, G., Plouffe, A., Smith, I.R., McCurdy, M.W., and Friske, P.W.B. 2007. Cretaceous shale of northern Alberta: A new frontier for base metal exploration. Exploration in the New Millennium, Proceedings of the Fifth Decennial International Conference on Mineral Exploration,: 1207–1213. Available from papers://32862730-33e4-4f24-9997-a2585c9ed6b6/Paper/p1146.

Paulen, R.C., Smith, I.R., Day, S.J.A., Hagedorn, G.W., King, R.D., and Pyne, M.D. 2017. GEM2 Southern Mackenzie Surficial Activity 2017 report : surficial geology and heavy mineral studies in southern Northwest Territories. Geological Survey of Canada Open File 8322,: 31.

Paulen, R.C., Smith, I.R., Day, S.J.A., Hagedorn, G.W., King, R.D., and Pyne, M.D. 2019a. GEM2 Southern Mackenzie Surficial Activity 2018 report : surficial geology and heavy mineral studies in southern Northwest Territories. Geological Survey of Canada Open File 8477,: 73.

Paulen, R.C., Smith, I.R., Ross, M., Hagedorn, G.W., and Rice, J.M. 2019b. Ice-flow History of the Laurentide Ice Shet in Southwest Northwest Territories: A Shield to Cordillera Transect. Geological Survey of Canada Scientific Poster 0105,: 315274.

Pedersen, V.K., Huismans, R.S., Herman, F., and Egholm, D.L. 2014. Controls of initial topography on temporal and spatial patterns of glacial erosion. Geomorphology, **223**: 96–116. Elsevier B.V. doi:10.1016/j.geomorph.2014.06.028.

Peltier, W.R., Argus, D.F., and Drummond, R. 2016. Space geodesy constraints ice age terminal deglaciation: the global ICE-6G_C (VM5A) model. Journal of Geophysical Research: Solid Earth,: 3782–3803. doi:10.1002/2015JB012608.Received.

Piercey, S.J. 2014. A Review of Quality Assurance and Quality Control (QA/QC) Procedures for Lithogeochemical Data. Geoscience Canada, **41**: 75–88.

Piotrowski, J.A., Larsen, N.K., and Junge, F.W. 2004. Reflections on soft subglacial beds as a mosaic of deforming and stable spots. Quaternary Science Reviews, **23**: 993–1000. doi:10.1016/j.quascirev.2004.01.006.

Plakholm, J.A., Paulen, R.C., and Paré, D. 2020. Clast-lithology data for selected surficial samples from the Trout Lake and Kakisa Lake protected area strategy surveys , southwest Northwest Territories. Geological Survey of Canada Open File 8437,.

van der Plicht, J. 2007. Radiocarbon Dating | Variations in Atmospheric 14C. *In* Encyclopedia of Quaternary Science. pp. 2923–2931.

Plouffe, A., McClenaghan, M.B., Paulen, R.C., McMartin, I., Campbell, J.E., and Spirito, W.A. 2013. Processing of glacial sediments for the recovery of indicator minerals: Protocols used at the Geological Survey of Canada. Geochemistry: Exploration, Environment, Analysis, **13**: 303–316. doi:10.1144/geochem2011-109.

Plouffe, A., Paulen, R.C., and Smith, I.R. 2006. Indicator mineral content and geochemistry of glacial sediments from northwest Alberta (NTS 84L, M): new opportunities in mineral exploration. Geological Survey of Canada Open File 5121,: 29.

Plouffe, A., Paulen, R.C., Smith, I.R., and Kjarsgaard, I.M. 2008. Sphalerite and kimberlite indicator minerals in till from the Zama Lake region, northwest Alberta (NTS 84L and 84M). Geological Survey of Canada Open File 5692,: 32.

Porter, C., Morin, P., Howat, I., Noh, M., Bates, B., Peterman, K., Keesey, S., Schlenk, M., Gardiner, J., Tomko, K., Willis, M., Kelleher, C., Cloutier, M., Husby, E., Foga, S., Nakamura, H., Platson, M., Wethington, M., Williamson, C., Bauer, G., Enos, J., Arnold, G., Kramer, W., Becker, P., Doshi, A., D’Souza, C., Cummens, P., Laurier, F., and Bojesen, M. 2018.

ArcticDEM. Harvard Dataverse, V1.

Prest, V.K., Grant, D.R., and Rampton, V.N. 1968. Glacial map of Canada. Geological Survey of Canada: Map 1253A,: Scale 1 : 5 000 000.

Prowse, T.D., Furgal, C., Chouinard, R., Melling, H., Milburn, D., and Smith, S.L. 2009. Implications of climate change for economic development in Northern Canada: Energy, resource, and transportation sectors. Ambio, **38**: 272–281. doi:10.1579/0044-7447-38.5.272.

Punkari, M. 1997. Glacial and glaciofluvial deposits in the interlobate areas of the Scandinavian Ice Sheet. Quaternary Science Reviews, **16**: 741–753. doi:10.1016/S0277-3791(97)00020-6.

Qing, H., and Mountjoy, E.W. 1994. Rare earth element geochemistry of dolomites in the Middle Devonian Presqu'ile barrier, Western Canada Sedimentary Basin: implications for fluid- rock ratios during dolomitization. Sedimentology, **41**: 787–804. doi:10.1111/j.1365-3091.1994.tb01424.x.

Quiquet, A., Dumas, C., Paillard, D., Ramstein, G., Ritz, C., and Roche, D.M. 2021. Deglacial Ice Sheet Instabilities Induced by Proglacial Lakes. Geophysical Research Letters, **48**. doi:10.1029/2020GL092141.

Rea, B.R., Evans, D.J.A., Dixon, T.S., and Whalley, W.B. 2000. Contemporaneous, localized, basal ice-flow variations: Implications for bedrock erosion and the origin of P-forms. Journal of Glaciology, **46**: 470–476. doi:10.3189/172756500781833197.

Refsnider, K.A., and Miller, G.H. 2010. Reorganization of ice sheet flow patterns in Arctic Canada and the mid-Pleistocene transition. Geophysical Research Letters, **37**: 1–5. doi:10.1029/2010GL043478.

Refsnider, K.A., and Miller, G.H. 2013. Ice-sheet erosion and the stripping of Tertiary regolith from Baffin Island, eastern Canadian Arctic. Quaternary Science Reviews, **67**: 176–189. Elsevier Ltd. doi:10.1016/j.quascirev.2013.01.010.

Remier, P.J., Bard, E., Bayliss, A., Beck, J.W., Blackwell, P.G., Bronk Ramsey, C., Buck, C.E., Cheng, H., Lawrence Edwards, R., Friedrich, M., Grootes, P.M., Guilderson, T.P., Haflidason, H., Hajda, I., Hatté, C., Heaton, T.J., Hoffmann, D.L., Hogg, A.G., Hughen, K.A., Kaiser, K.F., Kromer, B., Manning, S.W., Niu, M., Remier, R.W., Richards, D.A., Scott, E.M., Southon, J.R., Staff, R.A., Turney, C.S.M., and van der Plicht, J. 2013. Intcal13 and Marine13 Radiocarbon Age Calibration Curves 0–50,000 Years Cal Bp. Radiocarbon, **55**: 1869–1887. doi:10.1017/S0033822200048864.

Remier, P.J., and Remier, R.W. 2007. Radiocarbon Dating | Calibration. *In* Encyclopedia of Quaternary Science. pp. 2941–2950.

Rhodes, D., Lantos, E.A., Lantos, J.A., Webb, R.J., and Owens, D.C. 1984. Pine Point orebodies and their relationship to the stratigraphy, structure, dolomitization, and karstification of the Middle Devonian barrier complex. Economic Geology, **79**: 991–1055. doi:10.2113/gsecongeo.79.5.991.

Rice, J.M., Menzies, J., Paulen, R.C., and McClenaghan, M.B. 2019a. Microsedimentological evidence of vertical fluctuations in subglacial stress from the northwest sector of the Laurentide Ice Sheet, Northwest Territories, Canada. Canadian Journal of Earth Sciences, **56**: 363–379. doi:10.1139/cjes-2018-0201.

Rice, J.M., Paulen, R.C., Menzies, J., and McClenaghan, M.B. 2013. Glacial stratigraphy of the Pine Point Pb-Zn mine site , Northwest Territories. Geological Survey of Canada Current Research 2013-5,: 17.

Rice, J.M., Ross, M., Paulen, R.C., Kelley, S.E., Briner, J.P., Neudorf, C.M., and Lian, O.B. 2019b. Refining the ice flow chronology and subglacial dynamics across the migrating Labrador Divide of the Laurentide Ice Sheet with age constraints on deglaciation. Journal of Quaternary Science, **34**: 519–535. John Wiley & Sons, Ltd. doi:10.1002/jqs.3138.

Rignot, E., and Kanagaratnam, P. 2006. Changes in the Velocity Structure of the Greenland Ice Sheet. Science, **311**: 986–990.

Rignot, E., Mouginot, J., and Scheuchl, B. 2011. Ice flow of the Antarctic Ice Sheet. Science, **33**: 1427–1430. doi:10.1017/CBO9781107415324.004.

Ross, M., Lajeunesse, P., and Kosar, K.G.A. 2011. The subglacial record of northern Hudson Bay: Insights into the Hudson Strait Ice Stream catchment. Boreas, **40**: 73–91. doi:10.1111/j.1502-3885.2010.00176.x.

Roy, K., and Peltier, W.R. 2017. Space-geodetic and water level gauge constraints on continental uplift and tilting over North America: Regional convergence of the ICE-6G C (VM5a/VM6) models. Geophysical Journal International, **210**: 1115–1142. doi:10.1093/gji/ggx156.

Sannel, A.B.K., and Kuhry, P. 2011. Warming-induced destabilization of peat plateau/thermokarst lake complexes. Journal of Geophysical Research: Biogeosciences, **116**. doi:10.1029/2010JG001635.

Schoof, C. 2007. Ice sheet grounding line dynamics: Steady states, stability, and hysteresis. Journal of Geophysical Research: Earth Surface, **112**: 1–19. doi:10.1029/2006JF000664.

Schuur, E.A.G., McGuire, A.D., Schädel, C., Grosse, G., Harden, J.W., Hayes, D.J., Hugelius, G., Koven, C.D., Kuhry, P., Lawrence, D.M., Natali, S.M., Olefeldt, D., Romanovsky, V.E., Schaefer, K., Turetsky, M.R., Treat, C.C., and Vonk, J.E. 2015. Climate change and the permafrost carbon feedback. Nature, **520**: 171–179. doi:10.1038/nature14338.

Sella, G.F., Stein, S., Dixon, T.H., Craymer, M., James, T.S., Mazzotti, S., and Dokka, R.K. 2007. Observation of glacial isostatic adjustment in “stable” North America with GPS. Geophysical Research Letters, **34**: 1–6. doi:10.1029/2006GL027081.

Shakun, J.D., and Carlson, A.E. 2010. A global perspective on Last Glacial Maximum to Holocene climate change. Quaternary Science Reviews, **29**: 1801–1816. doi:10.1016/j.quascirev.2010.03.016.

Sharpe, D.R., Kjarsgaard, B.A., Knight, R.D., Russell, H.A.J., and Kerr, D.E. 2017. Glacial dispersal and flow history, East Arm area of Great Slave Lake, NWT, Canada. Quaternary Science Reviews, **165**: 49–72. Elsevier Ltd. doi:10.1016/j.quascirev.2017.04.011.

Shepherd, A., Ivins, E., Rignot, E., Smith, B., van den Broeke, M., Velicogna, I., Whitehouse, P., Briggs, K., Joughin, I., Krinner, G., Nowicki, S., Payne, T., Scambos, T., Schlegel, N., Guero, A., Agosta, C., Ahlstrøm, A., Babonis, G., Barletta, V., Blazquez, A., Bonin, J., Csatho, B., Cullather, R., Felikson, D., Fettweis, X., Forsberg, R., Gallee, H., Gardner, A., Gilbert, L., Groh, A., Gunter, B., Hanna, E., Harig, C., Helm, V., Horvath, A., Horwath, M., Khan, S., Kjeldsen, K.K., Konrad, H., Langen, P., Lecavalier, B., Loomis, B., Luthcke, S., McMillan, M., Melini, D., Mernild, S., Mohajerani, Y., Moore, P., Mouginot, J., Moyano, G., Muir, A., Nagler, T., Nield, G., Nilsson, J., Noel, B., Otosaka, I., Pattle, M.E., Peltier, W.R., Pie, N., Rietbroek, R., Rott, H., Sandberg-Sørensen, L., Sasgen, I., Save, H., Scheuchl, B., Schrama, E., Schröder, L., Seo, K., Simonsen, S., Slater, T., Spada, G., Sutterley, T., Talpe, M., Tarasov, L., van de Berg, W., van der Wal, W., van Wessem, M., Vishwakarma, B.D., Wiese, D., and Wouters, B. 2018.

Mass balance of the Antarctic Ice Sheet from 1992 to 2017. Nature, **558**: 219–222. doi:10.1038/s41586-018-0179-y.

Shilts, W.W. 1984. Till geochemistry in Finland and Canada. Journal of Geochemical Exploration, **21**: 95–117. doi:10.1016/0375-6742(84)90037-2.

Smith, D.G. 1994. Glacial lake McConnell: Paleogeography, age, duration, and associated river deltas, mackenzie river basin, western Canada. Quaternary Science Reviews, **13**: 829–843. doi:10.1016/0277-3791(94)90004-3.

Smith, I.R., and Lesk-Winfield, K. 2010. Seismic Shothole Drillers' Log-derived Thematic GIS, Northwest Territories and Northern Yukon: Bedrock Outcrop and Subcrop, Geohazards, and Muskeg Thickness: Geological Survey of Canada Open File 6410.

Spirito, W.A., McClenaghan, M.B., Plouffe, A., Mcmartin, I., Campbell, J.E., Paulen, R.C., Garrett, R.G., and Hall, G.E.M. 2011. Till Sampling and Analytical Protocols for GEM Projects : from field to archive. Geological Survey of Canada Open File 6850,: 73.

St-Jean, G., Kieser, W.E., Crann, C.A., and Murseli, S. 2017. Semi-Automated Equipment for CO2 Purification and Graphitization at the A.E. Lalonde AMS Laboratory (Ottawa, Canada). Radiocarbon, **59**: 941–956. doi:10.1017/RDC.2016.57.

Stea, R.R., and Finck, P.W. 2001. An evolutionary model of glacial dispersal and till genesis in Maritime Canada. Geological Society Special Publication, **185**: 237–265. doi:10.1144/GSL.SP.2001.185.01.11.

Stoker, B.J., Margold, M., Froese, D.G., and Gosse, J.C. 2020. The deglaciaion of the northwestern Laurentide Ice Sheet in the Mackenzie Mountains. 22nd AGU General Assembly,.

Stokes, C.R., and Clark, C.D. 2004. Evolution of late glacial ice-marginal lakes on the northwestern Canadian Shield and their influence on the location of the Dubawnt Lake palaeo-ice stream. Palaeogeography, Palaeoclimatology, Palaeoecology, **215**: 155–171. doi:10.1016/j.palaeo.2004.09.006.

Stokes, C.R., Clark, C.D., and Storrar, R.D. 2009. Major changes in ice stream dynamics during deglaciation of the north-western margin of the Laurentide Ice Sheet. Quaternary Science Reviews, **28**: 721–738. Elsevier Ltd. doi:10.1016/j.quascirev.2008.07.019.

Stokes, C.R., and Tarasov, L. 2010. Ice streaming in the Laurentide Ice Sheet: A first comparison between data-calibrated numerical model output and geological evidence. Geophysical Research Letters, **37**: 1–5. doi:10.1029/2009GL040990.

Stokes, C.R., Tarasov, L., Blomdin, R., Cronin, T.M., Fisher, T.G., Gyllencreutz, R., Hättestrand, C., Heyman, J., Hindmarsh, R.C.A., Hughes, A.L., Jakobsson, M., Kirchner, N., Livingstone, S.J., Margold, M., Murton, J.B., Noormets, R., Peltier, W.R., Peteet, D.M., Piper, D.J.W., Preusser, F., Renssen, H., Roberts, D.H., Roche, D.M., Saint-Ange, F., Stroeven, A.P., and Teller, J.T. 2015. On the reconstruction of palaeo-ice sheets: Recent advances and future challenges. Quaternary Science Reviews, **125**: 15–49. doi:10.1016/j.quascirev.2015.07.016.

Stouffer, R.J., Yin, J., Gregory, J.M., Dixon, K.W., Spelman, M.J., Hurlin, W., Weaver, A.J., Eby, M., Flato, G.M., Hasumi, H., Hu, A., Jungclaus, J.H., Kamenkovich, I. V., Levermann, A., Montoya, M., Murakami, S., Nawrath, S., Oka, A., Peltier, W.R., Robitaille, D.Y., Sokolov, A., Vettoretti, G., and Weber, S.L. 2006. Investigating the cause of the response of the thermohaline circulation to past and future climage changes. Journal of Climate, **19**: 1365–1387. doi:10.1175/JCLI3689.1.

Strobel, M.L., and Faure, G. 1987. Transport of Indicator Clasts by Ice Sheets and the Transport Half-Distance : A Contribution to Prospecting for ORE Deposits. The Journal of Geology, **95**: 687–697.

Stuiver, M., and Polach, H.A. 1977. Discussion: Reporting of 14C data. Radiocarbon, **19**: 355–363.

Tarasov, L., Dyke, A.S., Neal, R.M., and Peltier, W.R. 2012. A data-calibrated distribution of deglacial chronologies for the North American ice complex from glaciological modeling. Earth and Planetary Science Letters, **315**–**316**: 30–40. doi:10.1016/j.epsl.2011.09.010.

Tarasov, L., and Peltier, W.R. 2005. Arctic freshwater forcing of the Younger Dryas cold reversal. Nature, **435**: 662–665. doi:10.1038/nature03617.

Tarasov, L., and Peltier, W.R. 2006. A calibrated deglacial drainage chronology for the North American continent: evidence of an Arctic trigger for the Younger Dryas. Quaternary Science Reviews, **25**: 659–688. doi:10.1016/j.quascirev.2005.12.006.

Trommelen, M.S., Ross, M., and Campbell, J.E. 2012. Glacial terrain zone analysis of a fragmented paleoglaciologic record, southeast Keewatin sector of the Laurentide Ice Sheet. Quaternary

Science Reviews, **40**: 1–20. Elsevier Ltd. doi:10.1016/j.quascirev.2012.02.015.

Trommelen, M.S., Ross, M., and Campbell, J.E. 2013. Inherited clast dispersal patterns: Implications for palaeoglaciology of the SE Keewatin Sector of the Laurentide Ice Sheet. Boreas, **42**: 693–713. doi:10.1111/j.1502-3885.2012.00308.x.

Ugelvig, S. V., Egholm, D.L., and Iverson, N.R. 2016. Glacial lanndscape evolution by subglacial quarrying : A multiscale computational approach. Journal of Geophysical Research: Earth Surface,: 1–27. doi:10.1002/2016JF003960.Abstract.

Ullman, D.J., Carlson, A.E., Anslow, F.S., Legrande, A.N., and Licciardi, J.M. 2015. Laurentide ice-sheet instability during the last deglaciation. Nature Geoscience, **8**: 534–537. doi:10.1038/ngeo2463.

Utting, D.J., and Atkinson, N. 2019. Proglacial lakes and the retreat pattern of the southwest Laurentide Ice Sheet across Alberta, Canada. Quaternary Science Reviews, **225**. doi:10.1016/j.quascirev.2019.106034.

Väliranta, M., Salojärvi, N., Vuorsalo, A., Juutinen, S., Korhola, A., Luoto, M., and Tuittila, E. 2017. Holocene fen–bog transitions, current status in Finland and future perspectives. Holocene, **27**: 752–764. doi:10.1177/0959683616670471.

Wang, Y. 2018. Statistical analysis of till geochemistry in the Nelson River area, northeastern Manitoba; implications for Quaternary glacial stratigraphy. University of Waterloo Thesis,.

Wolfe, S.A., Huntley, D.J., and Ollerhead, J. 2004. Relict late Wisconsinan dune fields of the northern Great Plains, Canada. Geographie Physique et Quaternaire, **58**: 323–336. doi:10.7202/013146ar.

Wolfe, S.A., Morse, P.D., Kokelj, S. V., and Gaanderse, A.J. 2017. Great Slave Lowland: The Legacy of Glacial Lake McConnell. *In* Landscapes and Landforms of Western Canada. pp. 381–393. doi:10.1007/978-3-319-44595-3.

Wolfe, S.A., Morse, P.D., Neudorf, C.M., Kokelj, S. V., Lian, O.B., and O'Neill, H.B. 2018. Contemporary sand wedge development in seasonally frozen ground and paleoenvironmental implications. Geomorphology, **308**: 215–229. Elsevier B.V. doi:10.1016/j.geomorph.2018.02.015.

Wolfe, S.A., Paulen, R.C., Smith, I.R., and Lamothe, M. 2007. Age and paleoenvironmental significance of Late Wisconsinan dune fields in the Mount Watt and Fontas River map areas, northern Alberta and British Columbia. Geological Survey of Canada Current Research 2007-B4,: 10.

Wu, X., Heflin, M.B., Schotman, H., Vermeersen, B.L.A., Dong, D., Gross, R.S., Ivins, E.R., Moore, A.W., and Owen, S.E. 2010. Simultaneous estimation of global present-day water transport and glacial isostatic adjustment. Nature Geoscience, **3**: 642–646. Nature Publishing Group. doi:10.1038/ngeo938.

Zoltai, S., 1993. Cyclic development of permafrost in the peatlands of northwestern Alberta, Canada; Arctic and Alpine Research, v. 25, n. 3, p. 240-246.

Appendix A

Thesis Publications

Hagedorn, G.W., Paulen, R.C., Smith, I.R., and Ross, M., 2021a. Surficial geology, Kakisa and Tathlina lakes, Northwest Territories, NTS 85-C/11, 12, 13, and 14; Geological Survey of Canada, Canadian Geoscience Map 432, scale 1:100 000.

Hagedorn, G.W., Paulen, R.C., Smith, I.R., and Ross, M., 2021b. Surficial geology, Enterprise, Northwest Territories, NTS 85-C/9, 10, 15 and 16; Geological Survey of Canada, Canadian Geoscience Map 438, scale 1:100 000.

Smith, I.R., Paulen, R.C., and **Hagedorn, G.W.**, 2021. Surficial geology, Northeastern Cameron Hills, Northwest Territories, NTS 85-C/3, 4, 5, and 6; Geological Survey of Canada, Canadian Geoscience Map 431, scale 1:100 000.

Hagedorn G.W., Ross, M., Paulen, R.C., and Smith, I.R. in Geological Association of Canada-Mineralogical Association of Canada, Joint Annual Meeting, Abstract Volume 44, 2021, p. 122

Hagedorn, G.W., Ross, M., Paulen, R.C., Smith, I.R., Neudorf, C.M., Gingerich, T., and Lian, O.B. in 47th Annual Yellowknife Geoscience Forum, abstracts; Gervais, S. D., Irwin, D., Terlaky, V., Northwest Territories Geological Survey, Yellowknife Geoscience Forum Abstract and Summary Volume 2019, 2019 p. 107-108

Hagedorn, G.W., Ross, M., Paulen, R.C., Smith, I.R., Neudorf, C.M., Gingerich, T., and Lian, O.B., 2019. Ice-flow and deglacial history of the Laurentide Ice Sheet in the southwestern Great Slave Lake area, Northwest Territories; Geological Survey of Canada, Scientific Presentation 106, 1 poster. doi:10.4095/315361

Hagedorn, G.W., Paulen, R.C., Smith, I.R., Ross, M., Neudorf, C.M., and Lian, O.B., 2019. Surficial geology constraints on Laurentide Ice Sheet reconstruction in the southern Northwest Territories; *in* GEM-2 Southern Mackenzie Surficial Activity 2018 report: Surficial Geology and Heavy Mineral Studies in Southern Northwest Territories, (eds.) R.C. Paulen, I.R. Smith and S.J.A. Day; Geological Survey of Canada, Open File 8477, p. 17-26. doi:10.4095/313422

Smith, I.R., Paulen, R.C., Deblonde, C., **Hagedorn, G.W.**, King, R.D., and Pyne, M.D., 2019. Surficial geology and drift isopach mapping; *in* GEM-2 Southern Mackenzie Surficial Activity 2018 report: Surficial Geology and Heavy Mineral Studies in Southern Northwest Territories, (eds.) R.C. Paulen, I.R. Smith and S.J.A. Day; Geological Survey of Canada, Open File 8477, p. 7-16. doi:10.4095/313421

Plakholm, J.A., Paulen, R.C., Sapera, J.R., and **Hagedorn, G.W.**, 2019. Pebble lithology counts from till samples collected in the southern Northwest Territories (2010-2017); *in* GEM-2 Southern Mackenzie Surficial Activity 2018 report: Surficial Geology and Heavy Mineral Studies in Southern Northwest Territories, (eds.) R.C. Paulen, I.R. Smith and S.J.A. Day; Geological Survey of Canada, Open File 8477, p. 43-51. doi:10.4095/313426

Paulen, R.C., Smith, I.R., Day, S.J.A., **Hagedorn, G.W.**, King, R.D. and Pyne, M.D. 2017. GEM2 Southern Mackenzie Surficial Activity 2017 report: surficial geology and heavy mineral studies in southern Northwest Territories; Geological Survey of Canada, Open File 8322, 27 p. doi:10.4095/306090

Appendix B

Striations

Striation Number	Easting	Northing	Elevation	Set 1 (oldest)	Set 2	Set 3	Comments	Feature
10-MPB-001	536561	6702705	278	332				water forms
11-PTA-101	418802	6648552	246	254	290	233	Fossfiliferous limestone	striae
11-PTA-103	652556	6697240	287	292			limestone	polished surface
11-PTA-104	652145	6697955	286	320			flat outcrop	polish
11-PTA-111	539945	6719156	266	225			flat fossiliferous limestone	grooves + striae
11-PTA-112	534139	6724913	260	241			flat area of outcrop	striae
11-PTA-113	528372	6732185	247	251			flat outcrop	grooves
11-PTA-114	525776	6736391	230	330	315	212	flat area of outcrop, subglacial modification of outcrop?	grooves + striae
11-PTA-115	523825	6737714	248	335			outcrop by road	grooves
11-PTA-116	523468	6737884	236	245			sculpted bedrock	grooves
11-PTA-117	521077	6745559	253	302				fine polished striae
11-PTA-118	508236	6753895	222	200	5		old pit	grooves, polish
11-PTA-119	483011	6765207	275	335			no order of directions	grooves, polish
11-PTA-122	354889	6787012	164	272				small polish
17-SUV-008	521111	6745402		313			in crinoid limestone	striation
17-SUV-009	520931	6742401		241				p form
17-SUV-012	522430	6739015		317-137			bedrock outcrop by road	striations, Rod's notes say direction unknown
17-SUV-013	523513	6737826		240-60	288, 295-155		major deformed bedrock,	1=grooves, 2=striations
17-SUV-015	525230	6736966	213	254	264		silicic cover on bedrock	cross cutting striations
17-SUV-018	543581	6719604	137	252			highly weathered face in quarry	striations
17-SUV-	536550	6702511		331			old quarry, calcium	striations +

Striation Number	Easting	Northing	Elevation	Set 1 (oldest)	Set 2	Set 3	Comments	Feature
033							buildup on rocks	furrows
17-SUV-052	523838	6723410		216-36			low certainly off bedrock	striations, direction unknown
17-SUV-057	376385	6780992		239			found in gravel pit	striations
GAC1	537203	6702112		330			outcrop just below till	possible sculpting, uncertain
GAC3	643259	6751149		255			3rd pit of field trip	stirae
GAC4	535004	6723927		315	255, 210-030		polished limestone outcrop, lots of bull dover influence	grooves + striae
GAC5	531177	6727885		265	295		fresh outcrop	Striations
GAC6	521513	6741833		270			flat Outcrop easily eroded	striations
GAC7	520884	6742506		255	300	335	roadside outcrop	grooves, shaping, striations
17-PTA-046	502028	6653466	451	228	248			striations
17-PTA-067	660596	6788631	282	262			roadside outcrop with polished surface	striations
17-PTA-068	344049	6783639	242	253			small outcrop	striations
17-PTA-069	363252	6782004	258	263	294		large flat outcrop, cross cutting relationship	striations
17-PTA-070	390859	6780163	225	302			small area of outcrop explored at SE corner of gravel pit, outcrop eroded by meltwater	striations
17-PTA-071	398521	6776563	257	241			flat outcrop, preservation of striations	striations
17-PTA-072	400047	6775897	241	243			fossilized limestone outcrop	striations
17-PTA-073	407800	6774417	232	244			rock quarry edges	striations
18-PTA-038	467080	6799161		285			2 boulders in different units	boulder striations
18-PTA-039	465171	6801039		285				boulder striations
18-PTA-041	463241	6803400		287, 255			2 boulders in different units	boulder striations
18-PTA-042	467296	6798717		335, 340			off two different boulders same unit	boulder striations

Appendix C

Major Oxide Geochemistry Data

Sample	Easting (UTM 11N)	Northing (UTM 11N)	Cluster	Geographic Class	Bedrock Class	SiO_2 (wt%)	Al_2O_3 (wt%)	Fe_2O_3 (wt%)	MgO (wt%)	CaO (wt%)	Na_2O (wt%)	K_2O (wt%)	TiO_2 (wt%)	P_2O_5 (wt%)	MnO (wt%)	Cr_2O_3 (wt%)
						MDL 0.01	0.01	0.04	0.01	0.01	0.01	0.01	0.01	0.01	0.01	0.002
17-PTA-036	548322	6701513	Cluster 4	Middle (flatlying)	Lime_Shale	36.21	5.63	2.5	5.39	21.08	0.45	1.34	0.36	0.14	0.05	0.005
17-PTA-039	550872	6721181	Cluster 3	Middle (flatlying)	Shale	36.12	9.12	3.29	2.39	23.17	0.1	2.8	0.49	0.16	0.07	0.008
17-PTA-059	521494	6741844	Cluster 3	Escarpment	Lime_Shale	40.31	10.51	3.86	2.14	18.83	0.2	2.26	0.51	0.13	0.05	0.011
17-PTA-060	512421	6750061	Cluster 3	Escarpment	Lime_Shale	22.07	6.87	2.98	3.42	30.98	0.07	2.01	0.35	0.04	0.05	0.006
17-PTA-061	486460	6761242	Cluster 1	Escarpment	Lime_Shale	42.36	11.79	4.41	3.67	15.51	0.33	2.79	0.54	0.11	0.07	0.01
17-SUV-010	545765	6717707	Cluster 3	Escarpment	Shale	31.76	7.62	6.19	2.79	23.44	0.14	2.8	0.42	0.08	0.12	0.008
17-SUV-016	535188	6724081	Cluster 4	Escarpment	Lime_Shale	40.55	6.27	3.88	3.21	19.78	0.49	1.39	0.39	0.17	0.05	0.009
17-SUV-017	535018	6724009	Cluster 1	Escarpment	Lime_Shale	45.58	9.51	3.75	4.48	14.22	0.45	2.23	0.48	0.14	0.05	0.011
17-SUV-019	546023	6715471	Cluster 3	Escarpment	Shale	24	3.51	1.76	2.6	32.95	0.18	1.1	0.22	0.1	0.03	0.004
17-SUV-020	501692	6800332	Cluster 1	Middle (flatlying)	Lime_Shale	44.16	11.27	4.07	2.91	15.1	0.54	2.41	0.49	0.12	0.05	0.011
17-SUV-021	506446	6814482	Cluster 4	North (SW landforms)	Lime_Shale	37.76	8.55	3.15	3.21	21.38	0.67	1.88	0.39	0.1	0.05	0.01
17-SUV-022	452843	6830781	Cluster 4	North (SW landforms)	Lime_Shale	43.66	9.34	3.24	3.9	16.91	1.02	2.29	0.43	0.12	0.05	0.009
17-SUV-024	529574	6872062	Cluster 4	North (SW landforms)	Lime	38.35	8.15	2.98	3.65	20.07	0.93	2.03	0.37	0.12	0.04	0.009
17-SUV-025	519815	6857832	Cluster 4	North (SW landforms)	Lime	38.58	8.42	3.2	3.12	20.96	0.78	1.91	0.38	0.1	0.04	0.009
17-SUV-027	498629	6838311	Cluster 4	North (SW landforms)	Lime_Shale	41.81	8.95	3.14	3.79	18.08	0.93	2.05	0.41	0.12	0.04	0.008
17-SUV-028	492487	6830329	Cluster 4	North (SW landforms)	Lime_Shale	42.68	8.09	3.23	3.57	18.84	1.2	1.73	0.39	0.12	0.05	0.009
17-SUV-031	473394	6803995	Cluster 4	Middle (flatlying)	Lime_Shale	38.36	9.28	3.62	3.39	20.25	0.6	2.1	0.44	0.1	0.06	0.01
17-SUV-033A	526550	6702511	Cluster 3	Middle (flatlying)	Lime	36.87	7.49	2.91	1.94	23.01	0.33	1.68	0.4	0.11	0.04	0.009

Sample	Easting (UTM 11N)	Northing (UTM 11N)	Cluster	Geographic Class	Bedrock Class	SiO_2 (wt%)	Al_2O_3 (wt%)	Fe_2O_3 (wt%)	MgO (wt%)	CaO (wt%)	Na_2O (wt%)	K_2O (wt%)	TiO_2 (wt%)	P_2O_5 (wt%)	MnO (wt%)	Cr_2O_3 (wt%)
17-SUV-033B	526550	6702511	Cluster 1	Middle (flatlying)	Lime	45.83	8.85	3.22	2.17	15.51	0.43	1.52	0.46	0.16	0.03	0.009
17-SUV-034	529658	6689516	Cluster 1	Middle (flatlying)	Lime	41.21	9.5	3.85	3.76	17.49	0.37	2.4	0.48	0.12	0.07	0.009
17-SUV-035	512989	6661657	Cluster 1	Middle (flatlying)	Cret	46.69	10.84	4.05	3.95	12.94	0.46	2.73	0.52	0.14	0.05	0.009
17-SUV-036	512989	6661657	Cluster 1	Middle (flatlying)	Cret	45.33	11.35	4.18	4.16	13.16	0.46	2.9	0.55	0.13	0.06	0.01
17-SUV-037	519249	6674652	Cluster 1	Middle (flatlying)	Shale	44.75	10.77	3.89	3.8	13.93	0.46	2.56	0.5	0.12	0.05	0.01
17-SUV-041	472687	6778180	Cluster 3	Middle (flatlying)	Lime_Shale	36.18	9.5	3.67	2.35	21.94	0.33	1.99	0.47	0.11	0.06	0.009
17-SUV-043	461673	6777553	Cluster 1	Escarpment	Lime_Shale	47.01	11.29	4.42	1.92	14.43	0.4	2.47	0.56	0.14	0.06	0.011
17-SUV-045	534751	6751248	Cluster 2	Middle (flatlying)	Shale	58.25	16.43	6.48	2.43	1.38	1.13	2.67	0.69	0.2	0.07	0.014
17-SUV-046	506625	6739770	Cluster 1	Middle (flatlying)	Lime	43.79	11.08	4.19	2.91	15.45	0.31	2.58	0.54	0.13	0.05	0.011
17-SUV-047	510009	6731181	Cluster 1	Middle (flatlying)	Lime	50.41	12.55	4.9	2.59	9.98	0.3	3	0.62	0.15	0.07	0.012
17-SUV-048	514666	6712309	Cluster 1	Middle (flatlying)	Lime	40.7	10.28	3.99	3.42	17.46	0.32	2.42	0.49	0.11	0.06	0.01
17-SUV-050	517215	6697369	Cluster 3	Middle (flatlying)	Shale	36.08	8.47	3.54	2.89	22.22	0.26	2.03	0.43	0.11	0.06	0.008
17-SUV-051	530686	6712803	Cluster 2	Middle (flatlying)	Lime	65.75	11.26	4.15	1.34	2.84	0.65	2.07	0.74	0.04	0.03	0.011
17-SUV-052	523838	6723410	Cluster 1	Middle (flatlying)	Lime	45.31	10.72	4.1	2.84	14.14	0.32	2.14	0.54	0.13	0.06	0.01
17-SUV-053	498019	6753894	Cluster 3	Escarpment	Lime_Shale	31.1	5.85	3.9	2.91	26.44	0.32	1.5	0.37	0.11	0.05	0.006
17-SUV-054	493730	6731767	Cluster 1	Middle (flatlying)	Shale	43.97	8.94	3.51	2.66	17.37	0.41	1.85	0.48	0.13	0.04	0.009
17-SUV-055	499198	6716310	Cluster 1	Middle (flatlying)	Shale	46.25	9.95	3.88	2.75	15.16	0.4	2.17	0.5	0.13	0.04	0.009
17-SUV-056	463501	6682498	Cluster 2	Cameron Hills	Cret	61.64	13.55	4.96	2.15	3.23	0.55	2.61	0.67	0.16	0.05	0.011
17-SUV-062	455998	6680852	Cluster 2	Cameron Hills	Cret	69.17	11.82	4.81	1.39	1.4	0.77	2.35	0.7	0.2	0.05	0.012
17-SUV-063	478731	6653700	Cluster 2	Cameron Hills	Cret	61.18	11.61	5.02	2.91	4.15	0.69	2.1	0.6	0.16	0.05	0.011
17-SUV-064	512166	6680852	Cluster 1	Middle (flatlying)	Shale	43.97	10.85	4.03	2.86	13.64	0.34	2.06	0.5	0.12	0.06	0.01
17-SUV-066	497609	6697068	Cluster 1	Middle (flatlying)	Lime	42.68	9.94	3.7	3.28	16.84	0.38	2.23	0.48	0.11	0.04	0.009
17-SUV-068	482859	6700705	Cluster 2	Middle (flatlying)	Lime	54.9	12.75	9.73	2.87	3.05	0.58	2.64	0.64	0.24	0.06	0.014
17-SUV-069	484167	6720967	Cluster 1	Middle (flatlying)	Lime	42.03	8.81	3.33	2.6	18.74	0.36	2.13	0.45	0.12	0.04	0.008
17-SUV-072	447995	6748214	Cluster 3	Middle (flatlying)	Lime	38.13	7.45	2.91	2.73	22.69	0.29	1.86	0.42	0.11	0.04	0.008

Sample	Easting (UTM 11N)	Northing (UTM 11N)	Cluster	Geographic Class	Bedrock Class	SiO_2 (wt%)	Al_2O_3 (wt%)	Fe_2O_3 (wt%)	MgO (wt%)	CaO (wt%)	Na_2O (wt%)	K_2O (wt%)	TiO_2 (wt%)	P_2O_5 (wt%)	MnO (wt%)	Cr_2O_3 (wt%)
17-SUV-073	463625	6739877	Cluster 1	Middle (flatlying)	Lime	48.01	10.6	3.86	2.63	13.49	0.42	2.19	0.51	0.14	0.04	0.01
17-SUV-074	483699	6752978	Cluster 1	Middle (flatlying)	Lime	45.18	10.85	4.19	3.17	14.87	0.58	2.44	0.51	0.12	0.05	0.009
17-SUV-075	476557	6759822	Cluster 1	Middle (flatlying)	Lime	46.04	9.07	3.92	2.4	15.96	0.4	1.93	0.49	0.13	0.04	0.009
17-SUV-076	477243	6743928	Cluster 1	Middle (flatlying)	Shale	51.24	13.14	4.5	3.1	9.04	0.5	2.77	0.58	0.14	0.04	0.012
17-SUV-078	476783	6734209	Cluster 1	Middle (flatlying)	Shale	46.62	9.05	4.14	2.5	15.31	0.39	1.93	0.51	0.13	0.05	0.01
17-SUV-081	447393	6696059	Cluster 1	Middle (flatlying)	Cret	47.86	12.16	5.01	2.11	11.78	0.32	1.99	0.53	0.14	0.03	0.01
17-SUV-090	493897	6739136	Cluster 1	Middle (flatlying)	Shale	46.66	10.57	4.11	3.13	14.26	0.39	2.57	0.53	0.12	0.06	0.01
17-SUV-091	467479	6731040	Cluster 3	Middle (flatlying)	Lime	36.61	6.86	2.86	3.23	23.52	0.34	1.9	0.37	0.1	0.05	0.007
17-SUV-092	453875	6739127	Cluster 1	Middle (flatlying)	Lime	47.26	12.61	4.32	2.69	11.22	0.4	2.55	0.57	0.14	0.05	0.011
17-SUV-093	464024	6764276	Cluster 1	Middle (flatlying)	Shale	40.87	9.26	3.75	2.4	19.49	0.36	1.98	0.48	0.1	0.06	0.009
17-SUV-094	448932	6772359	Cluster 1	Middle (flatlying)	Shale	43.2	9.76	3.71	2.63	17.42	0.43	2.02	0.49	0.09	0.04	0.009
17-SUV-095	450638	6791304	Cluster 1	Middle (flatlying)	Lime_Shale	38.53	8.77	3.64	2.51	20.52	0.38	1.81	0.45	0.1	0.06	0.008
17-SUV-096	490691	6768844	Cluster 1	Middle (flatlying)	Shale	58.06	11.85	5.05	2.46	6.55	0.54	2.43	0.61	0.15	0.07	0.011
17-SUV-097	490691	6768844	Cluster 2	Middle (flatlying)	Shale	61.83	12.43	4.96	2.18	4.4	0.58	2.43	0.65	0.18	0.05	0.011
17-SUV-099	551471	6660360	Cluster 1	Middle (flatlying)	Lime	45.15	11.06	3.92	4.77	12.27	0.44	2.39	0.52	0.11	0.04	0.01
17-SUV-108	525140	6863662	Cluster 4	North (SW landforms)	Lime	47.65	12.09	4.4	4.86	10.17	1.25	2.98	0.52	0.12	0.06	0.012
17-SUV-109	509192	6846424	Cluster 4	North (SW landforms)	Shale	45.27	8.8	3.12	3.78	16.73	1.08	2	0.41	0.1	0.05	0.007
17-SUV-110	485717	6818527	Cluster 4	North (SW landforms)	Lime_Shale	42.45	9.16	3.58	4.02	17.64	0.91	2.14	0.44	0.1	0.06	0.008
17-SUV-111	480586	6812550	Cluster 4	North (SW landforms)	Lime_Shale	37.53	9.67	3.54	3.49	20.46	0.61	2.13	0.43	0.08	0.06	0.009
18-PTA-004	523452	6769865	Cluster 1	Middle (flatlying)	Shale	46.14	12.01	4.44	3.8	12.46	0.51	2.88	0.53	0.13	0.06	0.011
18-PTA-005	456285	6799419	Cluster 1	Middle (flatlying)	Lime_Shale	48.85	10.83	4.34	3.1	12.89	0.54	2.33	0.55	0.13	0.06	0.011
18-PTA-006	446632	6800306	Cluster 1	Middle (flatlying)	Lime_Shale	47.72	10.32	4.28	3.26	13.83	0.52	2.24	0.53	0.12	0.07	0.01
18-PTA-008	537485	6862865	Cluster 4	North (SW landforms)	Lime	35.81	8.13	2.9	3.69	22.1	0.81	1.91	0.36	0.1	0.04	0.009

Sample	Easting (UTM 11N)	Northing (UTM 11N)	Cluster	Geographic Class	Bedrock Class	SiO_2 (wt%)	Al_2O_3 (wt%)	Fe_2O_3 (wt%)	MgO (wt%)	CaO (wt%)	Na_2O (wt%)	K_2O (wt%)	TiO_2 (wt%)	P_2O_5 (wt%)	MnO (wt%)	Cr_2O_3 (wt%)
18-PTA-019	547189	6686133	Cluster 4	Middle (flatlying)	Lime_Shale	35.43	6.58	5.08	4.14	20.58	0.5	1.48	0.42	0.17	0.08	0.008
18-PTA-020	496684	6682877	Cluster 2	Cameron Hills	Cret	67.21	11.76	5	1.6	1.7	0.67	2.25	0.66	0.18	0.05	0.012
18-PTA-021	490282	6665174	Cluster 2	Cameron Hills	Cret	63.75	14.27	5.96	1.59	1.21	0.59	2.41	0.7	0.19	0.04	0.014
18-PTA-035	454213	6808750	Cluster 1	North (SW landforms)	Lime_Shale	48.77	10.1	4.08	3.12	13.59	0.58	2.16	0.55	0.13	0.07	0.011
18-PTA-036	467286	6798713	Cluster 1	Middle (flatlying)	Lime_Shale	45.08	10.58	4.65	2.95	15.32	0.41	2.41	0.53	0.12	0.08	0.011
18-PTA-037	467286	6798713	Cluster 1	Middle (flatlying)	Lime_Shale	45.67	10.84	4.67	3.02	14.94	0.41	2.43	0.53	0.12	0.08	0.01
18-PTA-041-E	462535	6803552	Cluster 1	Middle (flatlying)	Lime_Shale	50.17	11.95	4.33	2.89	11.39	0.57	2.42	0.56	0.14	0.08	0.011
18-PTA-041-F	462535	6803552	Cluster 1	Middle (flatlying)	Lime_Shale	49.32	10.53	4.5	3.19	12.89	0.54	2.24	0.55	0.13	0.08	0.01
18-PTA-042	467296	6798717	Cluster 2	Middle (flatlying)	Lime_Shale	59.96	14.81	4.66	2.55	5.12	2.45	2.95	0.51	0.15	0.06	0.014
18-SUV-002	481112	6799106	Cluster 1	Middle (flatlying)	Lime_Shale	42.6	10.59	3.95	3.11	16.82	0.53	2.32	0.49	0.11	0.06	0.01
18-SUV-003	490788	6787820	Cluster 1	Middle (flatlying)	Lime_Shale	49.36	12.17	4.32	3.68	10.97	0.79	2.91	0.56	0.13	0.06	0.011
18-SUV-004	509106	6789740	Cluster 1	Middle (flatlying)	Lime_Shale	49.75	12.36	4.53	3.2	11.1	0.73	2.75	0.55	0.12	0.06	0.011
18-SUV-006	533489	6799623	Cluster 4	Middle (flatlying)	Lime_Shale	41.68	10.11	3.72	3.32	17.61	0.6	2.15	0.45	0.11	0.05	0.009
18-SUV-007	534131	6814263	Cluster 1	North (SW landforms)	Shale	45.89	11.79	4.23	3.32	13.75	0.78	2.83	0.5	0.11	0.06	0.011
18-SUV-008	478159	6836922	Cluster 4	North (SW landforms)	Lime_Shale	46.41	9.37	3.38	3.93	15.26	1.14	2.15	0.43	0.12	0.05	0.009
18-SUV-014	539415	6835816	Cluster 4	North (SW landforms)	Shale	42.46	7.31	3.06	4.38	18.46	0.96	1.84	0.36	0.12	0.04	0.007
18-SUV-015	513831	6867883	Cluster 4	North (SW landforms)	Lime	48.56	13.32	4.99	5.2	8.77	1.52	3.3	0.56	0.15	0.06	0.015
18-SUV-016	484710	6864077	Cluster 4	North (SW landforms)	Shale	34.94	8.13	3.01	3.02	21.69	0.74	1.79	0.37	0.12	0.04	0.009
18-SUV-017	496019	6850654	Cluster 4	North (SW landforms)	Lime_Shale	42.77	9.59	3.46	3.71	16.89	0.95	2.13	0.43	0.11	0.05	0.010
18-SUV-018	467492	6847572	Cluster 4	North (SW landforms)	Lime_Shale	49.73	11.95	4.53	4.86	9.56	1.3	3.58	0.56	0.16	0.05	0.013
18-SUV-019	506248	6859680	Cluster 4	North (SW landforms)	Shale	39.3	9.03	3.2	3.29	19.65	0.86	2.05	0.39	0.11	0.04	0.01
18-SUV-020	511253	6830650	Cluster 4	North (SW landforms)	Lime_Shale	38.62	8.88	3.06	3.31	20.06	0.72	1.9	0.4	0.12	0.04	0.009

Sample	Easting (UTM 11N)	Northing (UTM 11N)	Cluster	Geographic Class	Bedrock Class	SiO_2 (wt%)	Al_2O_3 (wt%)	Fe_2O_3 (wt%)	MgO (wt%)	CaO (wt%)	Na_2O (wt%)	K_2O (wt%)	TiO_2 (wt%)	P_2O_5 (wt%)	MnO (wt%)	Cr_2O_3 (wt%)
18-SUV-021	528230	6848548	Cluster 4	North (SW landforms)	Lime	33.43	7.48	2.6	3.09	23.84	0.6	1.56	0.34	0.11	0.04	0.008
18-SUV-025	515976	6809547	Cluster 4	North (SW landforms)	Lime_Shale	41.38	9.97	3.77	3.4	17.67	0.66	2.26	0.45	0.11	0.05	0.01
18-SUV-026	492910	6810680	Cluster 4	North (SW landforms)	Lime_Shale	39.84	10.39	3.74	3.46	18.24	0.63	2.31	0.45	0.11	0.05	0.01
18-SUV-027	517168	6821411	Cluster 4	North (SW landforms)	Lime_Shale	41.89	9.84	3.52	3.68	17.34	0.84	2.27	0.44	0.12	0.05	0.01
18-SUV-030	481291	6684029	Cluster 2	Cameron Hills	Cret	68.52	13.47	4.99	1.26	0.54	0.69	2.39	0.73	0.13	0.04	0.013
18-SUV-031	484193	6664767	Cluster 2	Cameron Hills	Cret	60.16	12.54	5.41	2.76	4.2	0.7	2.18	0.66	0.2	0.06	0.013
18-SUV-032	472085	6655479	Cluster 2	Cameron Hills	Cret	66.58	13.6	5.32	1.31	0.89	0.67	2.35	0.69	0.15	0.04	0.013
18-SUV-033	472085	6655479	Cluster 2	Cameron Hills	Cret	67.01	13.4	5.29	1.29	0.9	0.67	2.32	0.67	0.16	0.04	0.014
18-SUV-034	468166	6666397	Cluster 2	Cameron Hills	Cret	60.63	12.4	5.1	2.08	5.03	0.68	2.17	0.64	0.18	0.06	0.012

Appendix D

Quality Assurance and Quality Control

Duplicate bi-plots for the major oxide geochemistry data from 2017 samples

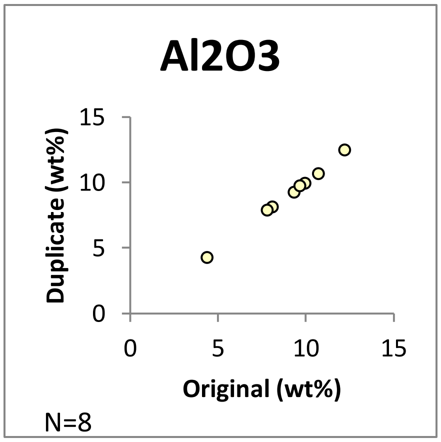

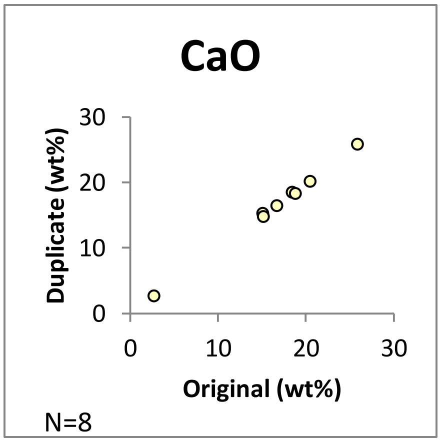

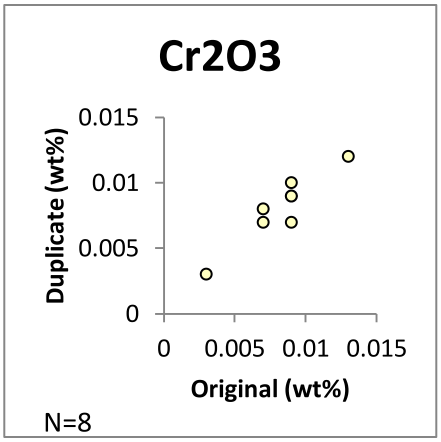

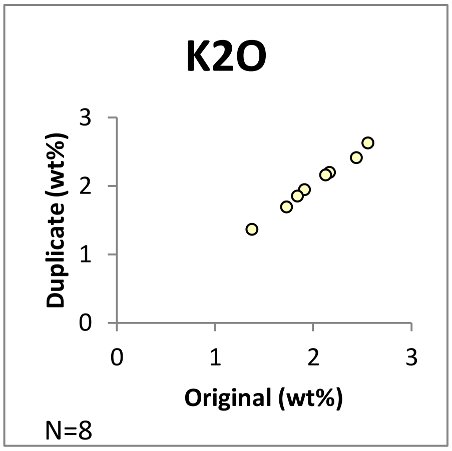

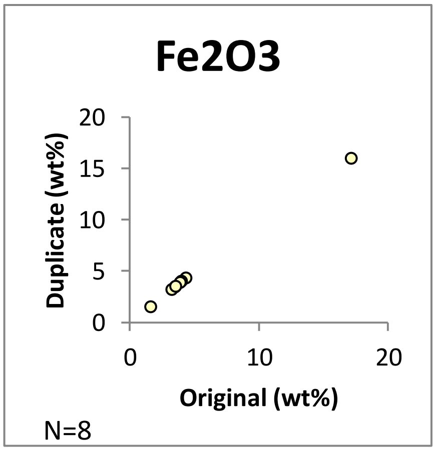

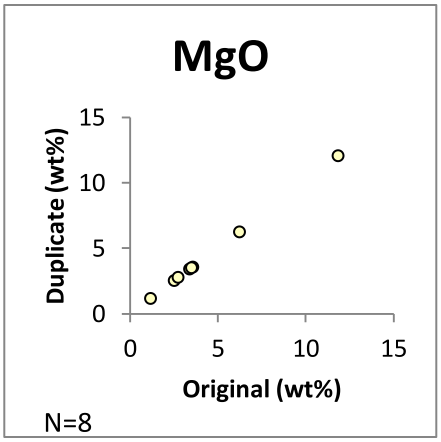

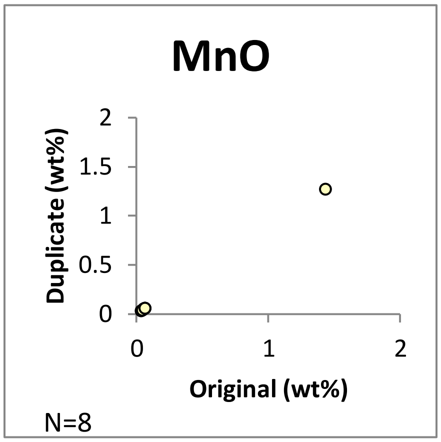
MnO
Duplicate (wt%)
2
1.5
1
0.5
0
0
1
2
Original (wt%)
N=8

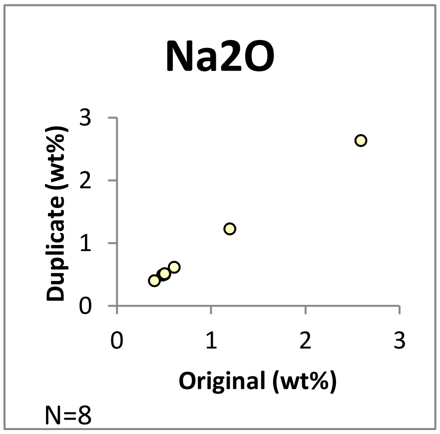
Na2O
Duplicate (wt%)
3
2
1
0
0
1
2
3
Original (wt%)
N=8

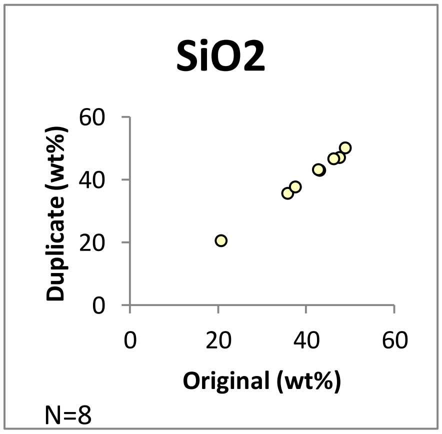
SiO2
Duplicate (wt%)
60
40
20
0
0
20
40
60
Original (wt%)
N=8

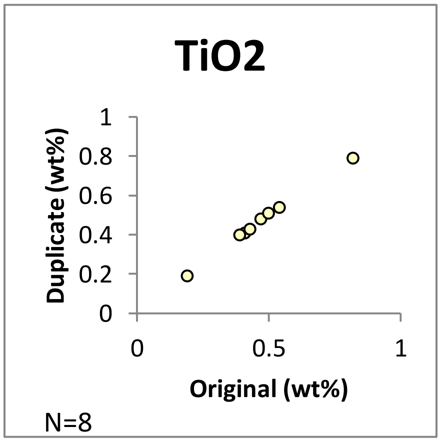
TiO2
Duplicate (wt%)
1
0.8
0.6
0.4
0.2
0
0
0.5
1
Original (wt%)
N=8

Thompson-Howarth plots for the major oxide geochemistry data from 2017 samples.

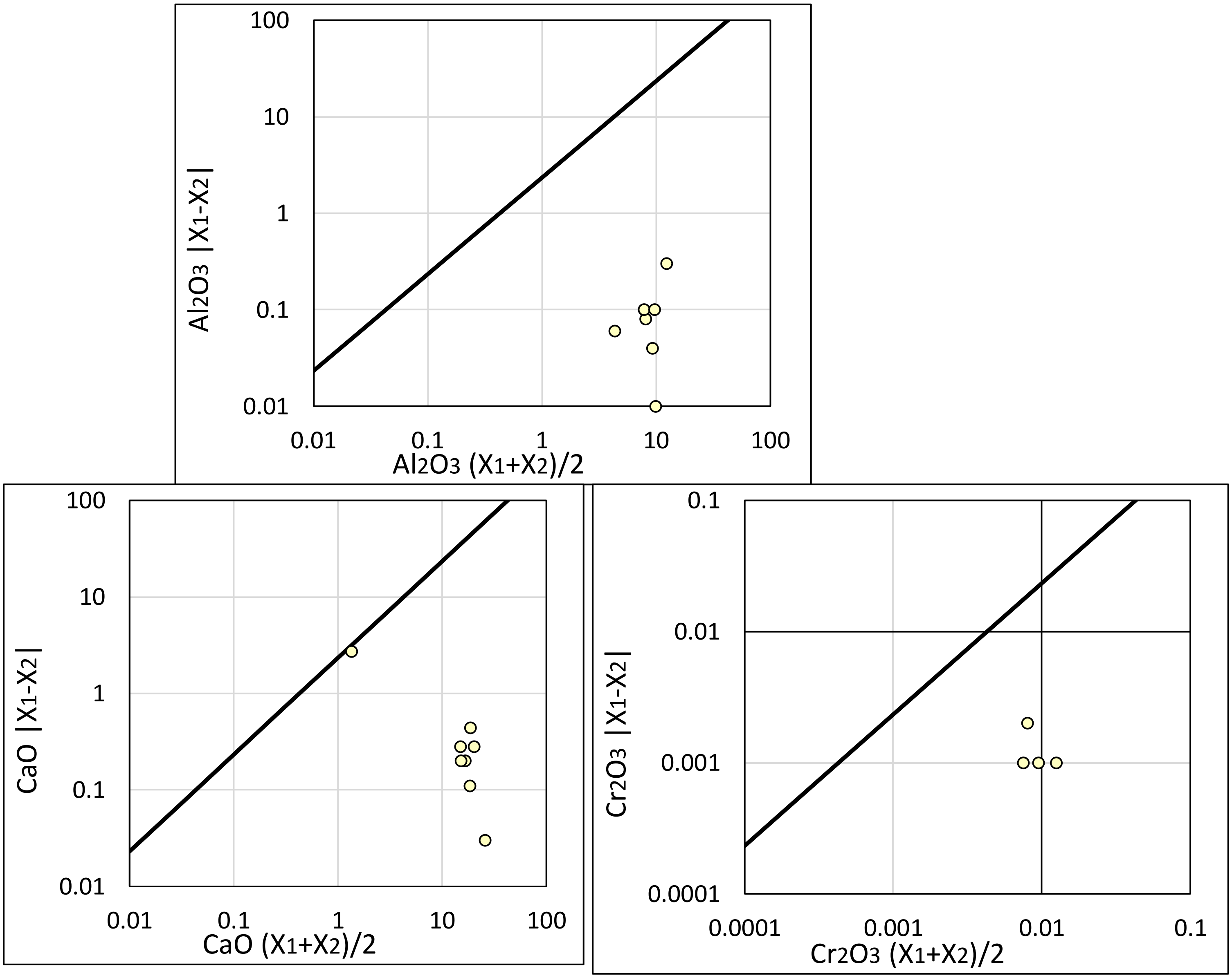

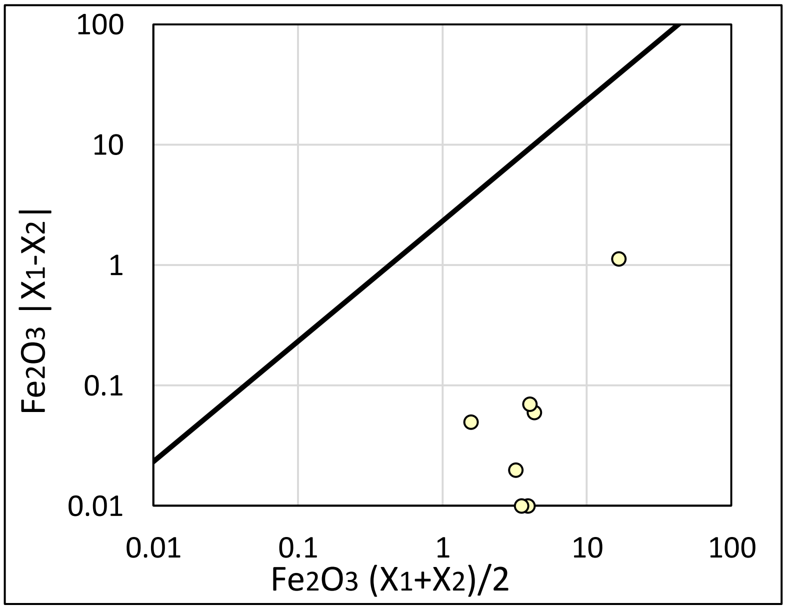
100
10
1
0.1
0.01
0.01
0.1
1
10
100
Fe2O3 |X1-X2|
Fe2O3 (X1+X2)/2

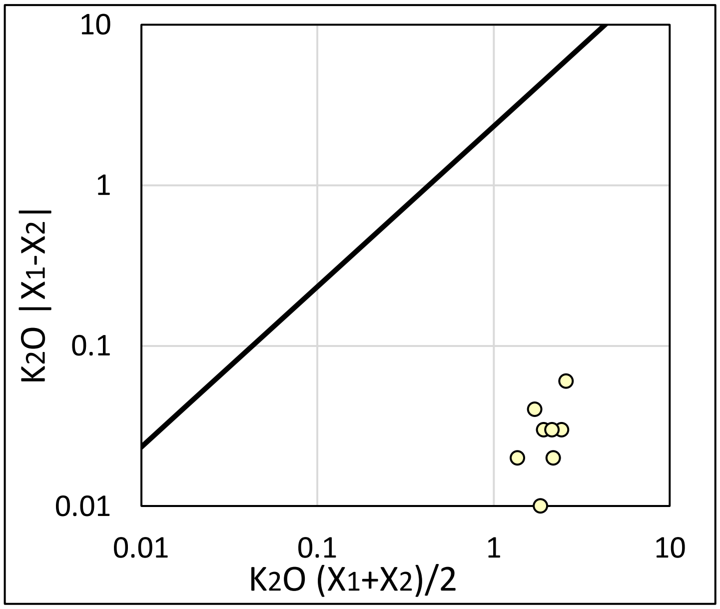
10
1
0.1
0.01
0.01
0.1
1
10
K2O |X1-X2|
K2O (X1+X2)/2

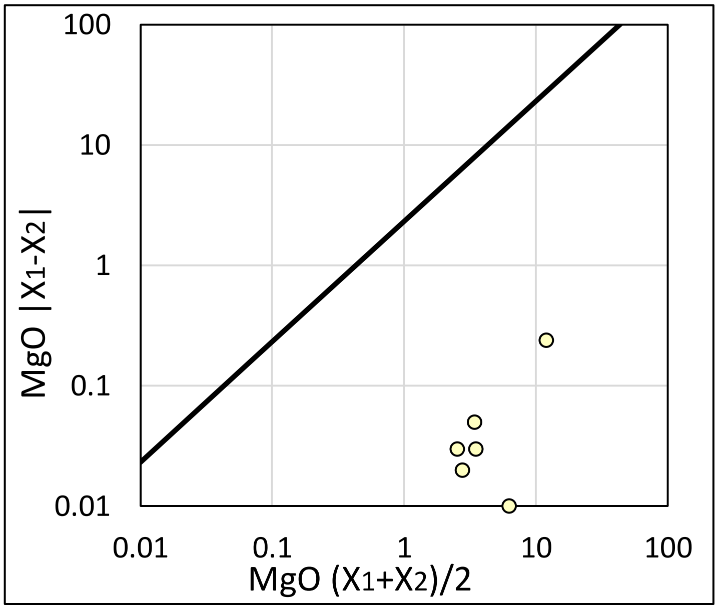
100
10
1
0.1
0.01
MgO |X1-X2|
0.01
0.1
1
10
100
MgO (X1+X2)/2

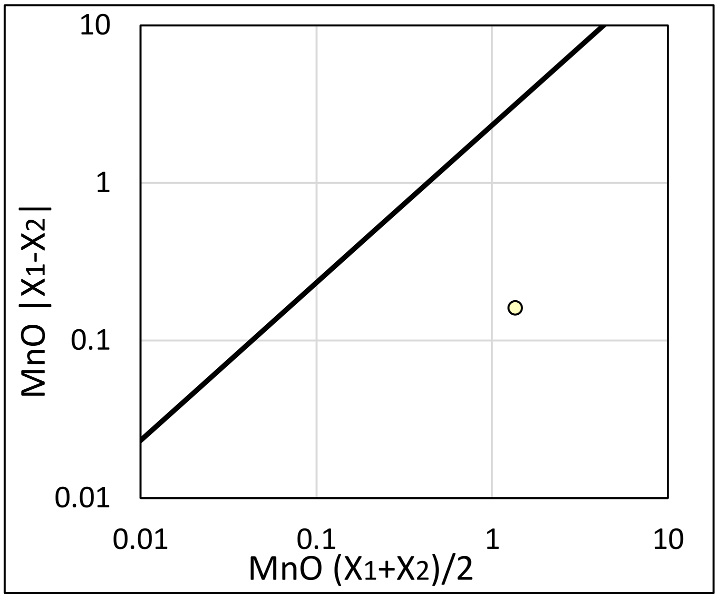
10
1
0.1
0.01
MnO |X1-X2|
0.01
0.1
1
10
MnO (X1+X2)/2

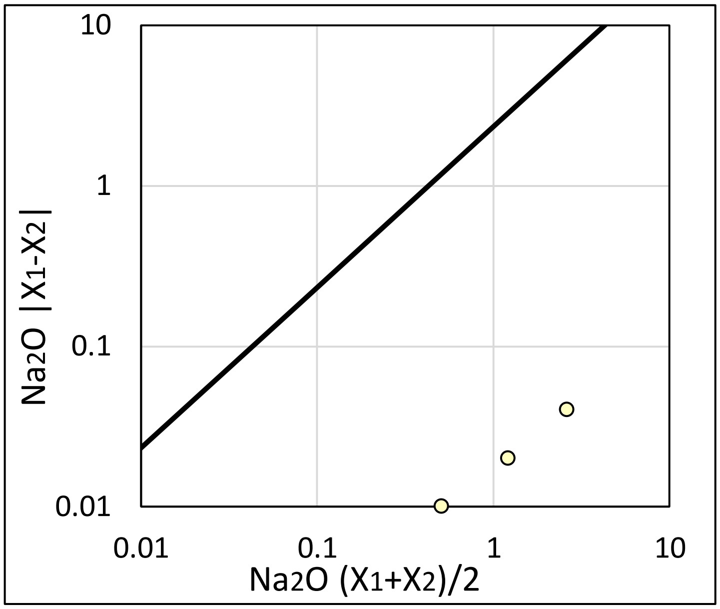
10
1
0.1
0.01
Na2O |X1-X2|
0.01
0.1
1
10
Na2O (X1+X2)/2

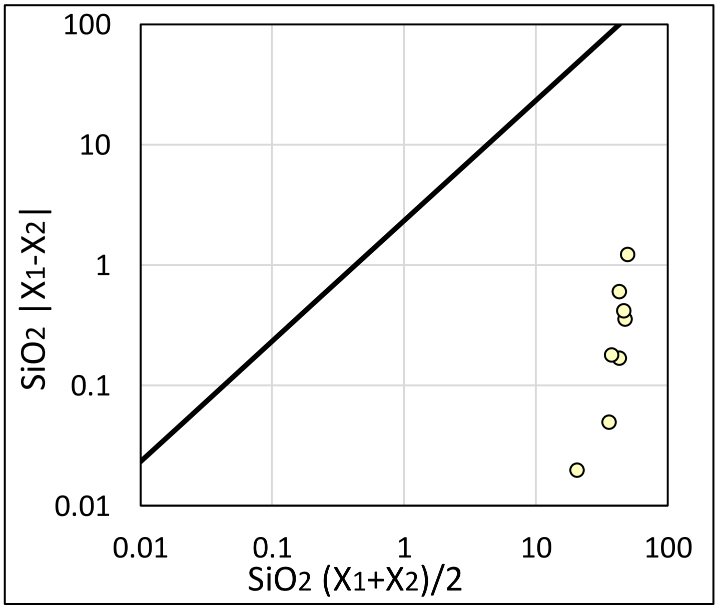
100
10
1
0.1
0.01
SiO2 |X1-X2|
0.01
0.1
1
10
100
SiO2 (X1+X2)/2

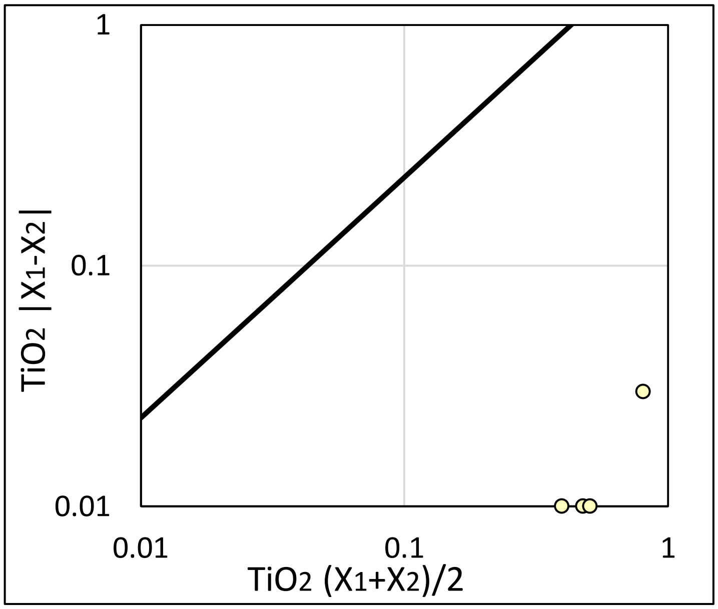
1
0.1
0.01
TiO2 |X1-X2|
0.01
0.1
1
TiO2 (X1+X2)/2

Summary table for 2017 major oxide data.

Element	**Mean (N=8)**	**Range**	**%RSD**
Al2O3	9.04	4.31 - 12.51	0.96
CaO	16.60	2.67 - 25.9	1.00
Cr2O3	0.008	0.003 - 0.013	8.079
Fe2O3	5.07	1.54 - 17.11	5.60
K2O	2.02	1.36 - 2.62	1.16
MgO	4.39	1.17 - 12.07	1.42
MnO	0.21	0.03 - 1.43	18.82
Na2O	0.85	0.4 - 2.63	1.34
SiO2	40.38	20.55 - 50.09	0.93
TiO2	0.47	0.19 - 0.82	1.85

Duplicate bi-plots for the major oxide geochemistry data from 2018 samples.

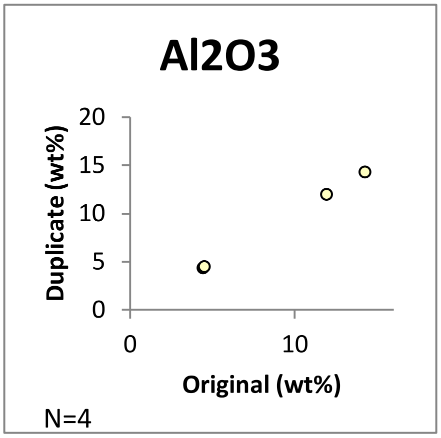

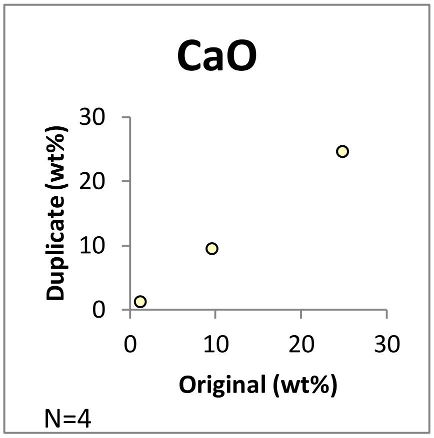

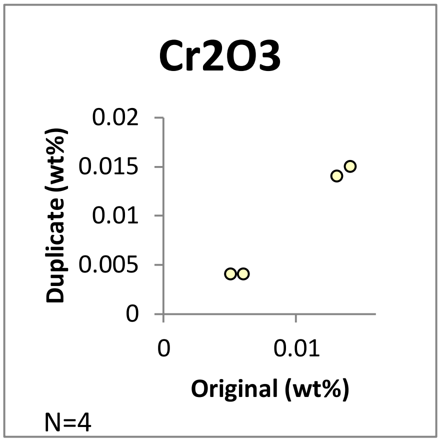

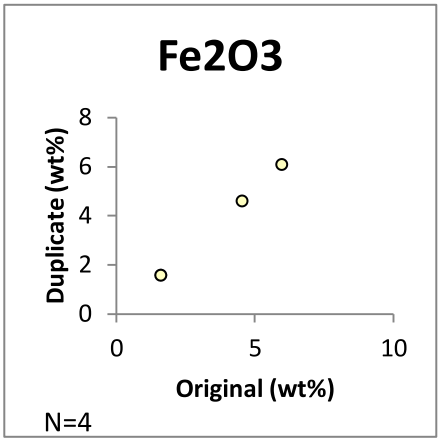

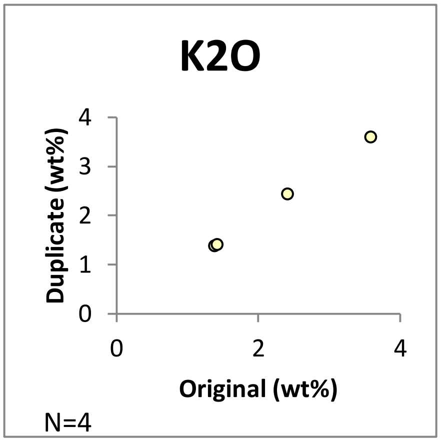

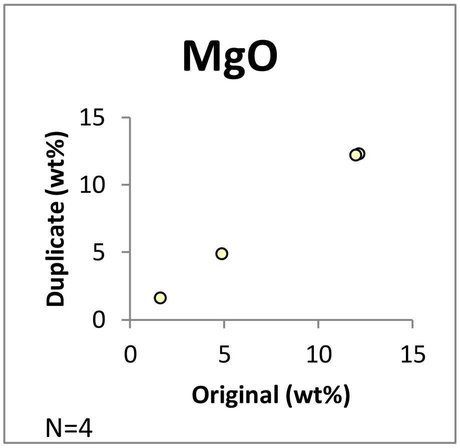

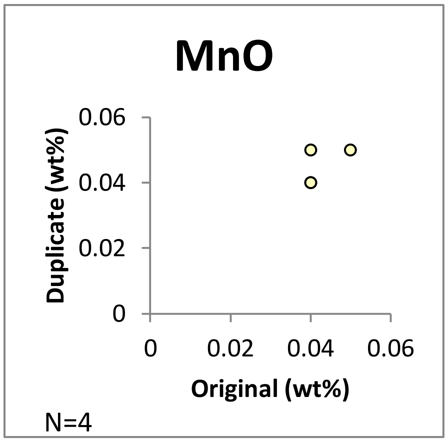
MnO
Duplicate (wt%)
0.06
0.04
0.02
0
0
0.02
0.04
0.06
Original (wt%)
N=4

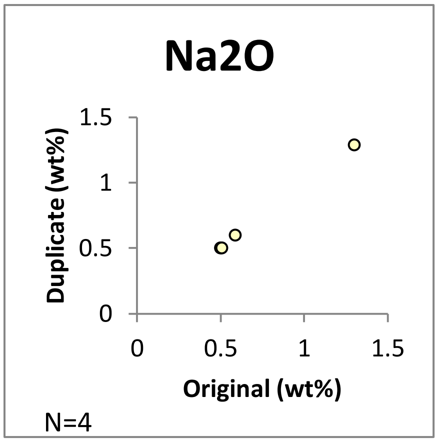
Na2O
Duplicate (wt%)
1.5
1
0.5
0
0
0.5
1
1.5
Original (wt%)
N=4

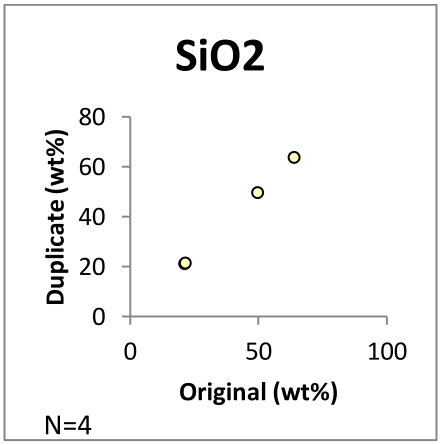
SiO2
Duplicate (wt%)
80
60
40
20
0
0
50
100
Original (wt%)
N=4

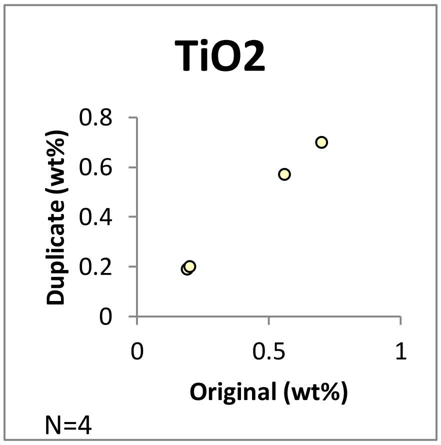
TiO2
Duplicate (wt%)
0.8
0.6
0.4
0.2
0
0
0.5
1
Original (wt%)
N=4

Thompson-Howarth plots for the major oxide geochemistry data from 2018 samples.

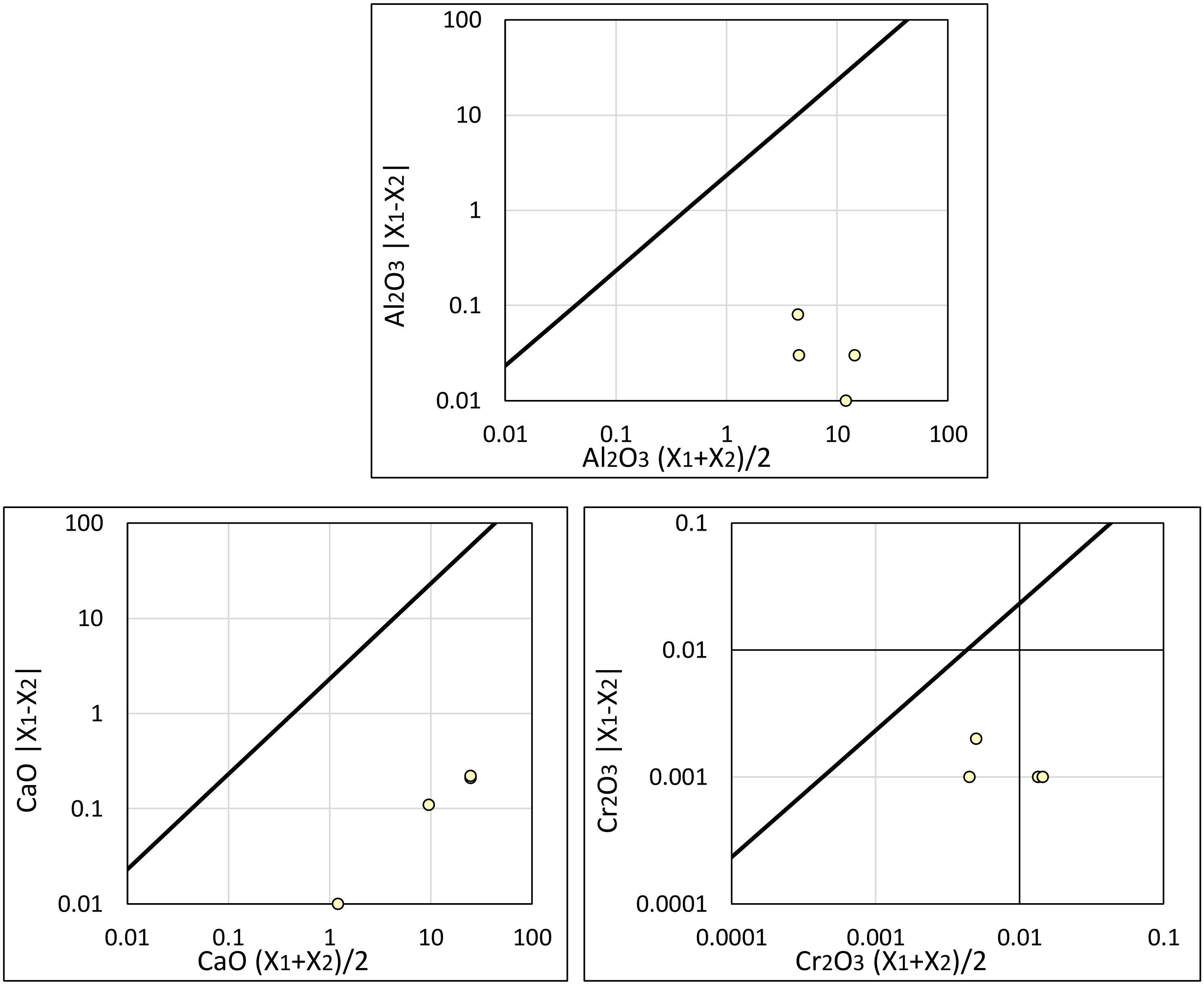

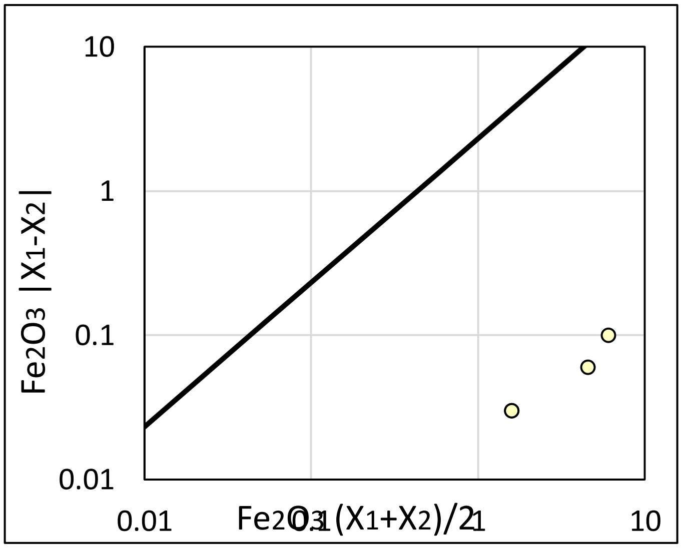
10
1
0.1
0.01
Fe2O3 |X1-X2|
0.01
0.1
1
10
Fe2O3 (X1+X2)/2

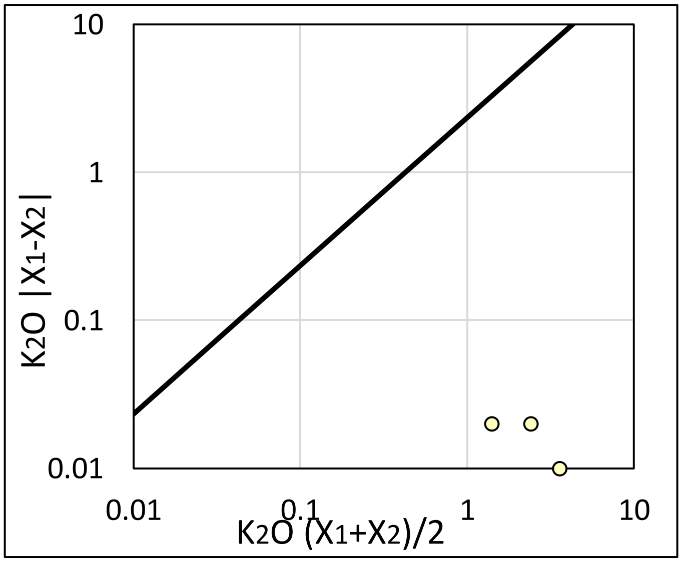
10
1
0.1
0.01
K2O |X1-X2|
0.01
0.1
1
10
K2O (X1+X2)/2

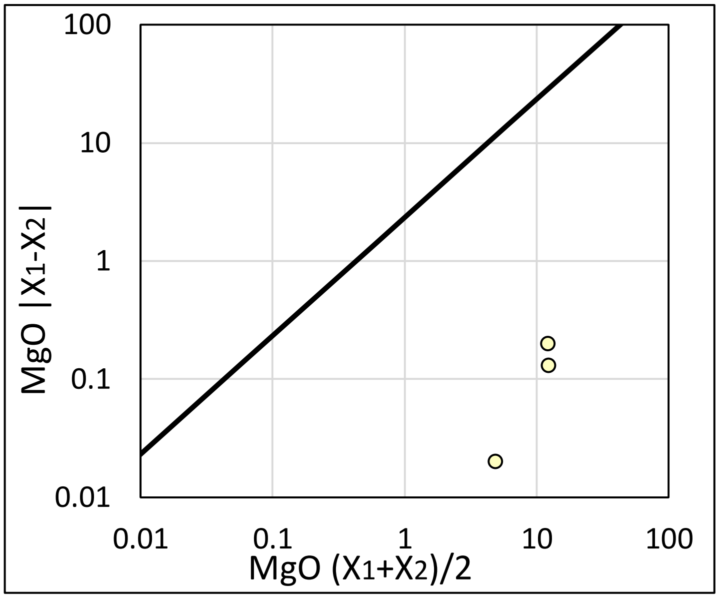
100
10
1
0.1
0.01
MgO |X1-X2|
0.01
0.1
1
10
100
MgO (X1+X2)/2

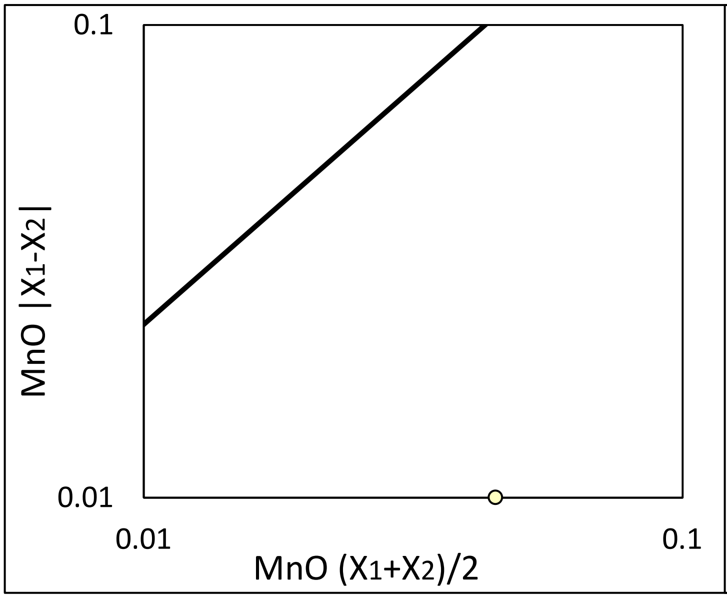
0.1
0.01
MnO |X1-X2|
0.01
0.1
MnO (X1+X2)/2

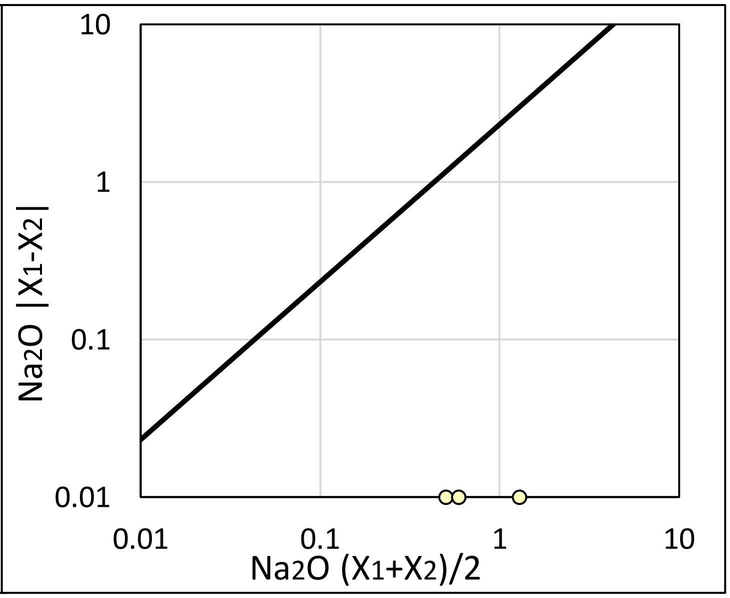
10
1
0.1
0.01
Na2O |X1-X2|
0.01
0.1
1
10
Na2O (X1+X2)/2

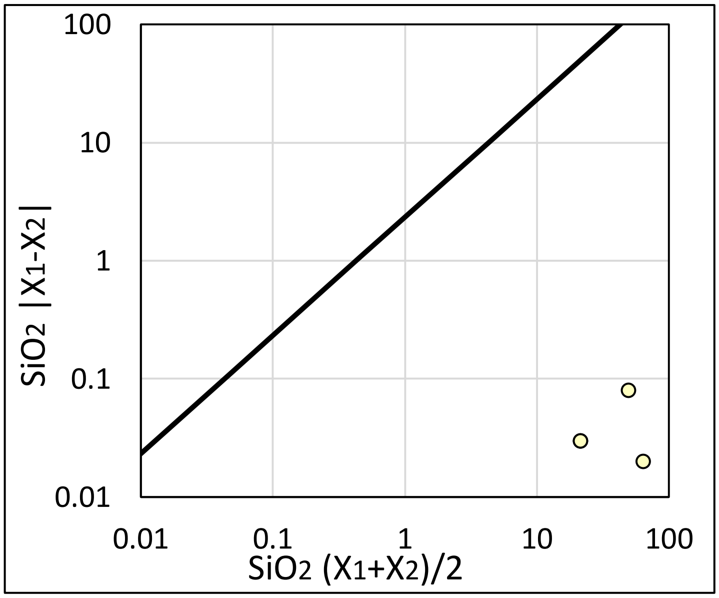
100
10
1
0.1
0.01
SiO2 |X1-X2|
0.01
0.1
1
10
100
SiO2 (X1+X2)/2

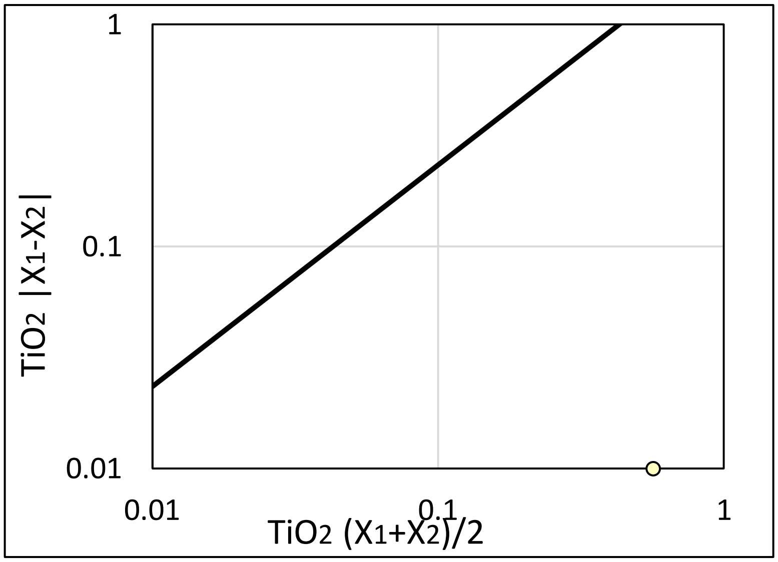
1
0.1
0.01
TiO2 |X1-X2|
0.01
0.1
1
TiO2 (X1+X2)/2

Summary Table for 2018 field data

Element	Mean (N=8)	Range	%RSD
Al2O3	8.78	4.36 - 14.3	0.37
CaO	15.04	1.2 - 24.84	0.76
Cr2O3	0.009	0.004 - 0.015	9.978
Fe2O3	3.44	1.57 - 6.06	1.28
K2O	2.20	1.38 - 3.59	0.48
MgO	7.69	1.59 - 12.27	1.10
MnO	0.04	0.04 - 0.05	8.08
Na2O	0.72	0.5 - 1.3	0.85
SiO2	39.08	21.31 - 63.75	0.08
TiO2	0.41	0.19 - 0.7	0.85

Appendix E

Clast Lithology Counts

Sample Number	Felsic	Mafic	Meta_Vol	Meta_Sed	Shield_Qtzite	Shield_TOT	Shield_PER
17-PTA-036	59	5	0	3	8	75	16.38
17-PTA-039	23	5	0	0	5	33	18.64
17-PTA-059	22	1	3	3	7	36	12.33
17-PTA-060	3	1	0	0	3	7	1.68
17-PTA-061	20	3	0	5	13	41	11.11
17-SUV-010	22	0	1	8	6	37	11.49
17-SUV-016	65	17	0	1	22	105	21.13
17-SUV-017	58	9	1	6	21	95	22.51
17-SUV-019	43	2	0	1	9	55	16.18
17-SUV-020	9	6	0	3	9	27	26.73
17-SUV-021	38	15	1	9	12	75	26.88
17-SUV-022							
17-SUV-024	59	18	8	4	22	111	43.70
17-SUV-025	67	9	1	10	20	107	31.47
17-SUV-027	61	12	2	6	20	101	31.27
17-SUV-028	67	20	2	5	10	104	34.32
17-SUV-031	37	11	3	4	19	74	21.45
17-SUV-033A	46	2	0	5	6	59	15.69
17-SUV-033B	16	1	0	0	7	24	20.69
17-SUV-034	43	2	0	5	12	62	20.53
17-SUV-035	89	7	0	7	3	106	30.11
17-SUV-036	43	10	0	4	1	58	35.58
17-SUV-037	68	10	0	6	9	93	35.63
17-SUV-041	27	5	0	7	16	55	31.07
17-SUV-043	36	3	0	7	9	55	15.94
17-SUV-045	18	2	0	1	6	27	81.82
17-SUV-046	61	6	0	10	24	101	24.94
17-SUV-047	53	10	1	12	18	94	32.19
17-SUV-048	59	9	0	4	8	80	26.76
17-SUV-050	71	9	0	3	27	110	34.59
17-SUV-051	117	14	1	10	22	164	72.57
17-SUV-052	68	3	0	4	16	91	30.64
17-SUV-053	22	6	0	2	14	44	11.34

Sample Number	Felsic	Mafic	Meta_Vol	Meta_Sed	Shield_Qtzite	Shield_TOT	Shield_PER
17-SUV-054	46	1	0	1	21	69	24.30
17-SUV-055	62	6	2	6	21	97	23.10
17-SUV-056	93	8	2	15	49	167	48.41
17-SUV-062	185	6	0	16	10	217	69.33
17-SUV-063	151	4	0	8	21	184	51.54
17-SUV-064	96	8	2	3	24	133	33.33
17-SUV-066	45	7	0	9	16	77	27.60
17-SUV-068	130	6	0	7	23	166	54.79
17-SUV-069	50	4	3	6	15	78	30.12
17-SUV-072	20	7	0	2	9	38	6.20
17-SUV-073	54	6	2	1	28	91	29.74
17-SUV-074	74	10	0	15	21	120	43.64
17-SUV-075	33	4	1	5	11	54	13.33
17-SUV-076	3	0	0	1	2	6	50.00
17-SUV-078	45	5	1	3	3	57	14.54
17-SUV-081	25	1	0	6	13	45	11.42
17-SUV-090	46	7	2	4	12	71	16.90
17-SUV-091	20	4	0	0	1	25	7.89
17-SUV-092	7	0	0	1	3	11	32.35
17-SUV-093	42	4	0	8	1	55	13.35
17-SUV-094	41	4	1	9	15	70	21.08
17-SUV-095	37	7	4	8	16	72	19.41
17-SUV-096	58	8	0	2	17	85	29.11
17-SUV-097	61	6	0	2	18	87	38.67
17-SUV-099	135	9	0	3	14	161	44.23
17-SUV-108	12	4	1	1	3	21	48.84
17-SUV-109	48	12	0	5	12	77	27.80
17-SUV-110	34	13	0	5	9	61	18.15
17-SUV-111	33	10	3	5	13	64	17.02
18-PTA-004	43	4	2	9	22	80	25.89
18-PTA-005	50	12	2	5	26	95	28.27
18-PTA-006	55	6	0	12	9	82	28.18
18-PTA-008	71	10	2	0	11	94	30.23
18-PTA-019	148	18	1	0	24	191	30.13
18-PTA-020	147	10	1	20	24	202	61.40
18-PTA-021	111	8	3	11	20	153	71.50
18-PTA-035	65	8	3	5	12	93	24.16

Sample Number	Felsic	Mafic	Meta_Vol	Meta_Sed	Shield_Qtzite	Shield_TOT	Shield_PER
18-PTA-036	48	7	4	7	18	84	26.92
18-PTA-037	57	5	2	6	6	76	22.42
18-PTA-041E	36	7	4	4	6	57	21.76
18-PTA-041F	41	13	1	5	16	76	25.59
18-PTA-042	156	64	18	63	10	311	75.49
18-SUV-002	29	3	2	6	13	53	17.91
18-SUV-003	18	8	4	11	26	67	38.95
18-SUV-004	18	9	2	12	42	83	47.98
18-SUV-006	45	6	3	7	19	80	21.22
18-SUV-007	44	10	3	17	9	83	26.10
18-SUV-008	85	16	6	11	16	134	28.15
18-SUV-014	11	2	0	1	4	18	32.14
18-SUV-015	7	1	0	0	2	10	33.33
18-SUV-016	77	12	2	15	17	123	39.30
18-SUV-017	83	12	6	6	16	123	41.14
18-SUV-018	116	23	3	94	25	261	73.11
18-SUV-019							
18-SUV-020	56	14	2	19	23	114	33.43
18-SUV-021	54	10	0	12	3	79	20.63
18-SUV-025	43	4	1	12	13	73	24.01
18-SUV-026	46	7	3	8	11	75	23.36
18-SUV-027	40	8	0	11	11	70	22.44
18-SUV-030	162	4	4	16	22	208	72.73
18-SUV-031	141	5	1	16	25	188	57.85
18-SUV-032	175	7	0	10	16	208	74.82
18-SUV-033	157	5	5	11	18	196	77.47
18-SUV-034	138	6	0	16	30	190	46.68

Lime_Dolo	**Mirage**	**Paleo_Seds**	**Sandstone**	**Paleo_TOT**	**Paleo_PER**
351	0	14	9	374	81.66
134	0	4	4	142	80.23
227	0	17	5	249	85.27
408	0	0	1	409	98.32
273	0	33	12	318	86.18
274	0	5	4	283	87.89
363	0	2	11	376	75.65
291	0	23	9	323	76.54
260	0	8	9	277	81.47
56	0	5	5	66	65.35
168	0	23	10	201	72.04
115	0	19	2	136	53.54
173	0	43	4	220	64.71
184	0	22	12	218	67.49
170	0	18	7	195	64.36
219	0	28	9	256	74.20
292	0	3	11	306	81.38
67	0	8	5	80	68.97
188	0	31	11	230	76.16
220	0	19	5	244	69.32
95	0	5	1	101	61.96
150	0	8	6	164	62.84
76	0	31	12	119	67.23
254	0	18	11	283	82.03
0	0	0	4	4	12.12
246	0	26	18	290	71.60
153	0	22	13	188	64.38
183	0	17	14	214	71.57
176	0	13	12	201	63.21
25	0	12	18	55	24.34
170	0	21	6	197	66.33
300	0	26	1	327	84.28
194	0	12	2	208	73.24
297	0	11	6	314	74.76

Lime_Dolo	**Mirage**	**Paleo_Seds**	**Sandstone**	**Paleo_TOT**	**Paleo_PER**
60	0	69	28	157	45.51
14	0	27	30	71	22.68
117	0	15	16	148	41.46
221	0	16	19	256	64.16
165	0	21	14	200	71.68
95	0	8	23	126	41.58
159	0	8	9	176	67.95
557	0	12	3	572	93.31
170	0	9	16	195	63.73
103	0	19	26	148	53.82
322	0	5	18	345	85.19
3	0	0	3	6	50.00
291	0	11	11	313	79.85
312	0	29	6	347	88.07
307	0	17	13	337	80.24
250	0	21	9	280	88.33
19	0	0	1	20	58.82
322	0	18	12	352	85.44
233	0	17	3	253	76.20
256	0	15	9	280	75.47
161	0	16	26	203	69.52
103	0	8	12	123	54.67
172	0	3	9	184	50.55
16	0	6	0	22	51.16
143	0	37	14	194	70.04
220	0	39	10	269	80.06
261	0	33	5	299	79.52
156	0	45	22	223	72.17
175	0	32	23	230	68.45
169	0	17	5	191	65.64
185	0	23	7	215	69.13
389	0	29	12	430	67.82
63	0	25	19	107	32.52
14	0	12	12	38	17.76
230	0	31	16	277	71.95
177	0	25	15	217	69.55
222	0	20	14	256	75.52

Lime_Dolo	**Mirage**	**Paleo_Seds**	**Sandstone**	**Paleo_TOT**	**Paleo_PER**
156	0	18	11	185	70.61
167	0	26	8	201	67.68
49	0	33	6	88	21.36
180	0	38	11	229	77.36
64	0	22	10	96	55.81
42	0	25	12	79	45.66
233	0	37	16	286	75.86
185	0	28	6	219	68.87
260	0	47	9	316	66.39
24	0	10	0	34	60.71
8	0	2	4	14	46.67
151	0	21	4	176	56.23
133	0	29	5	167	55.85
71	19	0	1	91	25.49
181	0	37	2	220	64.52
247	0	43	7	297	77.55
158	0	33	15	206	67.76
193	0	37	6	236	73.52
190	0	33	17	240	76.92
0	0	15	20	35	12.24
78	0	21	11	110	33.85
0	0	23	10	33	11.87
0	0	7	20	27	10.67
138	0	38	18	194	47.67

Cord_Qtzite	Cord_Chert	Cord_TOT	Cord_PER	Cret_Sand	Cret_Black_Shale	Coal	Ironstone	Cret_TOT	Cret_PER
0	3	3	0.66	0	0	0	4	4	0.87
0	1	1	0.56	0	0	0	0	0	0.00
1	0	1	0.34	0	2	4	0	6	2.05
0	0	0	0.00	0	0	0	0	0	0.00
0	1	1	0.27	3	5	0	1	9	2.44
0	1	1	0.31	0	0	0	0	0	0.00
0	12	12	2.41	2	0	0	1	3	0.60
1	1	2	0.47	0	1	0	1	2	0.47
3	0	3	0.88	3	0	0	0	3	0.88
0	1	1	0.99	0	3	1	0	4	3.96
0	1	1	0.36	0	1	0	0	1	0.36
0	2	2	0.79	0	3	0	0	3	1.18
0	3	3	0.88	0	8	0	0	8	2.35
0	1	1	0.31	0	3	0	0	3	0.93
1	2	3	0.99	0	1	0	0	1	0.33
1	2	3	0.87	0	8	0	2	10	2.90
1	1	2	0.53	0	0	0	8	8	2.13
2	0	2	1.72	0	0	0	10	10	8.62
0	5	5	1.66	0	0	0	1	1	0.33
1	0	1	0.28	0	0	0	1	1	0.28
1	0	1	0.61	2	0	0	1	3	1.84
0	0	0	0.00	0	0	0	1	1	0.38
0	2	2	1.13	0	0	0	1	1	0.56
0	4	4	1.16	0	0	0	2	2	0.58
0	1	1	3.03	1	0	0	0	1	3.03
3	2	5	1.23	0	2	0	6	8	1.98
3	2	5	1.71	0	2	0	0	2	0.68
0	1	1	0.33	0	2	0	0	2	0.67
0	1	1	0.31	3	0	0	0	3	0.94
2	1	3	1.33	0	1	0	2	3	1.33
1	2	3	1.01	0	0	0	6	6	2.02

Cord_Qtzite	Cord_Chert	Cord_TOT	Cord_PER	Cret_Sand	Cret_Black_Shale	Coal	Ironstone	Cret_TOT	Cret_PER
0	1	1	0.26	0	0	0	14	14	3.61
0	2	2	0.70	3	1	0	1	5	1.76
1	2	3	0.71	3	1	0	2	6	1.43
2	2	4	1.16	4	0	0	11	15	4.35
8	2	10	3.19	0	0	0	7	7	2.24
3	5	8	2.24	2	0	0	15	17	4.76
1	2	3	0.75	0	6	0	1	7	1.75
0	0	0	0.00	0	0	0	1	1	0.36
2	3	5	1.65	0	1	1	1	3	0.99
1	2	3	1.16	0	0	0	2	2	0.77
0	1	1	0.16	0	0	0	2	2	0.33
1	7	8	2.61	10	1	0	1	12	3.92
0	4	4	1.45	1	0	0	1	2	0.73
2	2	4	0.99	0	0	0	1	1	0.25
0	0	0	0.00	0	0	0	0	0	0.00
0	2	2	0.51	15	0	0	4	19	4.85
0	1	1	0.25	1	0	0	0	1	0.25
2	4	6	1.43	0	3	0	3	6	1.43
1	0	1	0.32	8	2	0	0	10	3.15
0	0	0	0.00	3	0	0	0	3	8.82
2	0	2	0.49	0	0	0	1	1	0.24
2	2	4	1.20	3	0	0	2	5	1.51
2	3	5	1.35	4	4	0	6	14	3.77
0	1	1	0.34	0	0	0	3	3	1.03
1	1	2	0.89	2	3	0	6	11	4.89
0	2	2	0.55	5	0	0	11	16	4.40
0	0	0	0.00	0	0	0	0	0	0.00
0	0	0	0.00	1	5	0	0	6	2.17
0	1	1	0.30	0	4	0	1	5	1.49
0	3	3	0.80	0	8	0	1	9	2.39
2	2	4	1.29	0	0	0	0	0	0.00
4	1	5	1.49	1	1	0	3	5	1.49
2	3	5	1.72	0	10	0	1	11	3.78
0	0	0	0.00	0	1	0	0	1	0.32
3	5	8	1.26	0	0	0	3	3	0.47
6	4	10	3.04	0	1	0	5	6	1.82
5	4	9	4.21	2	5	0	4	11	5.14

Cord_Qtzite	Cord_Chert	Cord_TOT	Cord_PER	Cret_Sand	Cret_Black_Shale	Coal	Ironstone	Cret_TOT	Cret_PER
0	3	3	0.78	4	6	0	2	12	3.12
2	4	6	1.92	0	4	0	0	4	1.28
0	2	2	0.59	1	1	0	2	4	1.18
5	7	12	4.58	0	6	0	1	7	2.67
2	4	6	2.02	3	8	0	2	13	4.38
0	3	3	0.73	1	6	0	0	7	1.70
1	6	7	2.36	2	4	0	0	6	2.03
1	4	5	2.91	3	0	0	0	3	1.74
0	5	5	2.89	1	0	0	1	2	1.16
1	3	4	1.06	0	7	0	0	7	1.86
0	1	1	0.31	5	7	0	2	14	4.40
4	9	13	2.73	0	9	0	0	9	1.89
0	0	0	0.00	0	4	0	0	4	7.14
0	1	1	3.33	2	3	0	0	5	16.67
6	3	9	2.88	1	1	0	0	2	0.64
0	1	1	0.33	0	8	0	0	8	2.68
1	1	2	0.56	0	0	0	0	0	0.00
1	2	3	0.88	0	2	0	1	3	0.88
1	1	2	0.52	0	3	0	1	4	1.04
0	2	2	0.66	0	21	0	1	22	7.24
2	3	5	1.56	1	0	0	1	2	0.62
1	1	2	0.64	0	0	0	0	0	0.00
4	4	8	2.80	0	5	0	24	29	10.14
6	5	11	3.38	0	2	0	11	13	4.00
1	2	3	1.08	0	2	0	30	32	11.51
2	1	3	1.19	1	1	0	24	26	10.28
3	6	9	2.21	0	6	0	8	14	3.44

Other	Overall_TOT	Comments
2	458	2 - qtz vein.
1	177	1 - lime looking with "petroleum"
0	292	
0	416	
0	369	
1	322	1 - fine grained, red, crack/breaking up.
1	497	1 - green, soft fine-graned.
0	422	
2	340	2 - banded, hard, porous, buff.
3	101	1 - pale, vuggy. 2 - brown-maroon, powdery, angular.
1	279	1 - qtz vein.
2	254	2 - qtz vein.
2	340	2 - qtz vein.
0	323	
0	303	
2	345	2 - red, angular, no reaction, soft
1	376	1 - calcareous accretion.
0	116	
4	302	2 - Qtz vein. 2 - soft, angular, effervesce, porous.
0	352	
0	163	
3	261	1 - quartz vein. 1 - black with bright red specs. 1 - possible chert?
0	177	
1	345	1 - qtz vein.
0	33	Counted all.
1	405	1 - qtz vein.
3	292	3 - qtz vein.
2	299	1 - red, angular, granular. 1 - large buff, very soft, vuggy buff doesn't effervesce
3	318	1 - banded sandstone, red, buff. 1 - hard red fine grained calcite attached. 1 - white calcite in grey fine grained matrix soft.
1	226	1 - purple buff, can see crystals, soft, porous, sandstone??
0	297	
2	388	1 - qtz vein. 1 - orange - buff, soft, conglomerate.
0	284	
0	420	
2	345	1 - Qtz vein. 1 - black with white grains, spikey
8	313	5 - quartz vein. 1 -iron outside layered with metased. 1 - pink very scratched, mottled. 1 - angular

Other	Overall_TOT	Comments
		maroon, iron stained, may be sst.
0	357	
0	399	
1	279	1 - qtz vein.
3	303	2 - hard red veins, felsic. 1 - vuggy, dolo?? Beige.
0	259	brown limestone
0	613	
0	306	
1	275	1 - yellow - orange, hard, angular, mildly foliated?
1	405	1 - buff porous rounded soft, Lime??
0	12	counted all.
1	392	1 - qtz vein.
0	394	
0	420	
1	317	1 - soft, angular, green with red veins.
0	34	Counted all.
2	412	black with white fossiliferous remnants. Grey veins with black crystals soft, doesn’t effervesce.
0	332	
0	371	
0	292	
2	225	2 - rounded flat, grey with white spots, soft, no reaction.
1	364	3 - qtz vein. 1 - planar, black/brown, mica-rich, very hard.
0	43	Counted all.
0	277	
0	336	
1	376	1 - qtz vein
2	309	1 - qtz vein. 1 - dark grey vuggy with oxidation, mica-rich.
1	336	1 - large, angular, maroon, hard, small white grains.
2	291	2 - red buff, mega crysts, soft mainly black
1	311	counted all. 1 - qtz vein.
2	634	1 - red small platy vuggy.
4	329	3 - qtz vein. 1 - light, pink beige, volcanic??
3	214	1 - qtz vein. 2 - red vuggy coarse grained, sandstone.
0	385	2 - red coarse grained.
1	312	1 - qtz vein.
1	339	1 - pink with white crystals rounded, soft
1	262	1 - green matrix, white megacrysts, soft, volcanic??

Other	Overall_TOT	Comments
1	297	1 - grey, vuggy, not effervesce, 3 limestones with pyrite.
3	412	3 - qtz vein.
1	296	1 - brown, hard, globular, sandstone.
1	172	1 - qtz vein.
4	173	1 - qtz. Vein. 2 - buff rough texture. 1 - mafic with vein.
0	377	
1	318	1 - contact white
4	476	2 - conglomerate with calcite. 1 - buff contact. 1 - flat concoidal chert, beige.
0	56	Counted all
0	30	
3	313	1 - qtz vein. 2 - hard fine grained pink mottled buff.
0	299	
3	357	1 - qtz vein. 1 - thin red ironstained, fine grained. 1 - red porous soft.
1	341	1 - iron-stained, hard, finegrained, porous
1	383	1 - fine grained, buff, medium soft, subrounded.
1	304	1 - weird shape, pink buff, angular
3	321	1 - qtz vein. 1 - green qtzite. 1 - pale hard, cherty?
0	312	
6	286	Counted all. 3 - vuggy light, pink beige, volcanic. 2 - qtz vein. 1 - green with macrocryst, soft.
3	325	1 - qtz vein. 1 - soft yellow flat. 1 - green with white dots, hard.
2	278	1 - weird qtzite?? With holes, beige, hard, porous. 1 - weird texture, black beige.
1	253	1 - red matrix white crystals, hard, angular.
0	407	

Appendix F

Clast Fabric Data

See Appendix C for sample locations.

17-PTA-041 - Above Boulder Lag		
Clast #	**Azimuth**	**Dip**
1	240	3
2	168	5
3	183	9
4	27	12
5	245	21
6	284	3
7	198	1
8	283	5
9	287	5
10	58	12
11	276	5
12	355	4
13	223	3
14	2	4
15	324	9
16	276	9
17	10	15
18	9	23
19	350	13
20	272	7
21	176	17
22	23	15
23	334	4
24	287	8
25	54	15
26	334	11
27	316	2
28	343	30
29	139	31
30	4	3
31	283	3
32	38	26

33	27	15
34	90	11
35	17	1
36	26	5
37	34	16
38	218	7
39	46	9
40	315	4
41	331	10
42	28	41
43	26	11
44	25	14
45	262	3
46	50	17
47	225	24
48	25	12
49	24	4
50	8	4
51	6	3
52	293	3
53	72	8

17-PTA-041 - Lower Grey Till		
Clast #	**Azimuth**	**Dip**
1	6	13
2	215	9
3	236	22
4	119	10
5	117	16
6	22	21
7	108	7
8	97	12
9	141	18
10	70	32
11	131	10
12	138	18
13	62	34

14	350	21
15	311	20
16	274	8
17	112	8
18	318	25
19	40	17
20	73	9
21	265	20
22	51	21
23	116	32
24	162	11
25	162	18
26	310	6
27	348	31
28	316	22
29	53	21
30	57	282
31	10	23
32	28	6
33	36	11
34	31	7
35	352	5
36	46	25
37	312	16
38	345	16
39	1	15
40	321	5
41	306	22
42	42	37
43	28	21
44	16	44
45	84	17
46	63	16
47	247	10
48	348	35
49	82	20
50	160	70
51	330	15

17-PTA-041 - Upper Beige Till		
Clast #	**Azimuth**	**Dip**
1	104	12
2	135	26
3	152	34
4	304	9
5	193	8
6	190	11
7	183	10
8	150	4
9	186	15
10	147	27
11	323	9
12	212	50
13	210	36
14	155	24
15	144	20
16	333	15
17	290	25
18	82	4
19	318	3
20	118	46
21	134	22
22	187	31
23	271	6
24	352	1
25	124	17
26	166	6
27	347	6
28	172	28
29	184	3
30	144	42
31	63	4
32	353	40
33	304	1
34	210	47

35	351	5
36	308	2
37	157	10
38	343	14
39	188	12
40	94	18
41	91	48
42	314	30
43	61	5
44	322	16
45	84	37
46	168	44
47	5	11
48	94	37
49	193	8
50	167	13
51	326	4
52	212	43
53	19	4
54	264	55

18-PTA-035		
Clast #	**Azimuth**	**Dip**
1	20	9
2	68	6
3	41	2
4	36	8
5	43	2
6	42	13
7	344	10
8	46	11
9	101	14
10	51	20
11	53	16
12	51	19
13	21	4
14	161	24

15	75	7
16	116	29
17	68	9
18	44	6
19	28	2
20	25	6
21	33	9
22	47	6
23	333	7
24	9	15
25	22	9
26	28	9
27	337	14
28	70	10
29	50	12
30	46	7
31	55	15
32	30	5
33	85	13
34	66	4
35	59	6
36	32	3
37	120	6
38	55	44
39	75	15
40	95	49
41	60	20
42	26	2
43	91	19
44	97	19
45	131	24
46	141	33
47	46	3
48	144	28
49	89	13
50	72	8
51	35	19
52	46	23

53	195	14
54	194	15

17-SUV-035		
Clast #	**Azimuth**	**Dip**
1	205	10
2	179	24
3	284	3
4	68	46
5	246	5
6	45	36
7	278	8
8	349	9
9	52	27
10	75	10
11	257	4
12	333	20
13	64	18
14	66	30
15	310	13
16	73	16
17	279	3
18	276	4
19	59	34
20	267	12
21	44	20
22	83	11
23	269	7
24	50	30
25	55	7
26	55	26
27	322	4
28	87	18
29	296	42
30	102	35
31	269	4
32	310	36

33	279	15
34	21	9
35	245	24
36	42	8
37	329	4
38	19	24
39	74	12
40	250	5
41	58	2
42	261	29
43	205	12
44	294	20
45	290	32
46	68	28
47	50	17
48	291	24
49	91	15
50	86	18

Appendix G

Beach Ridges

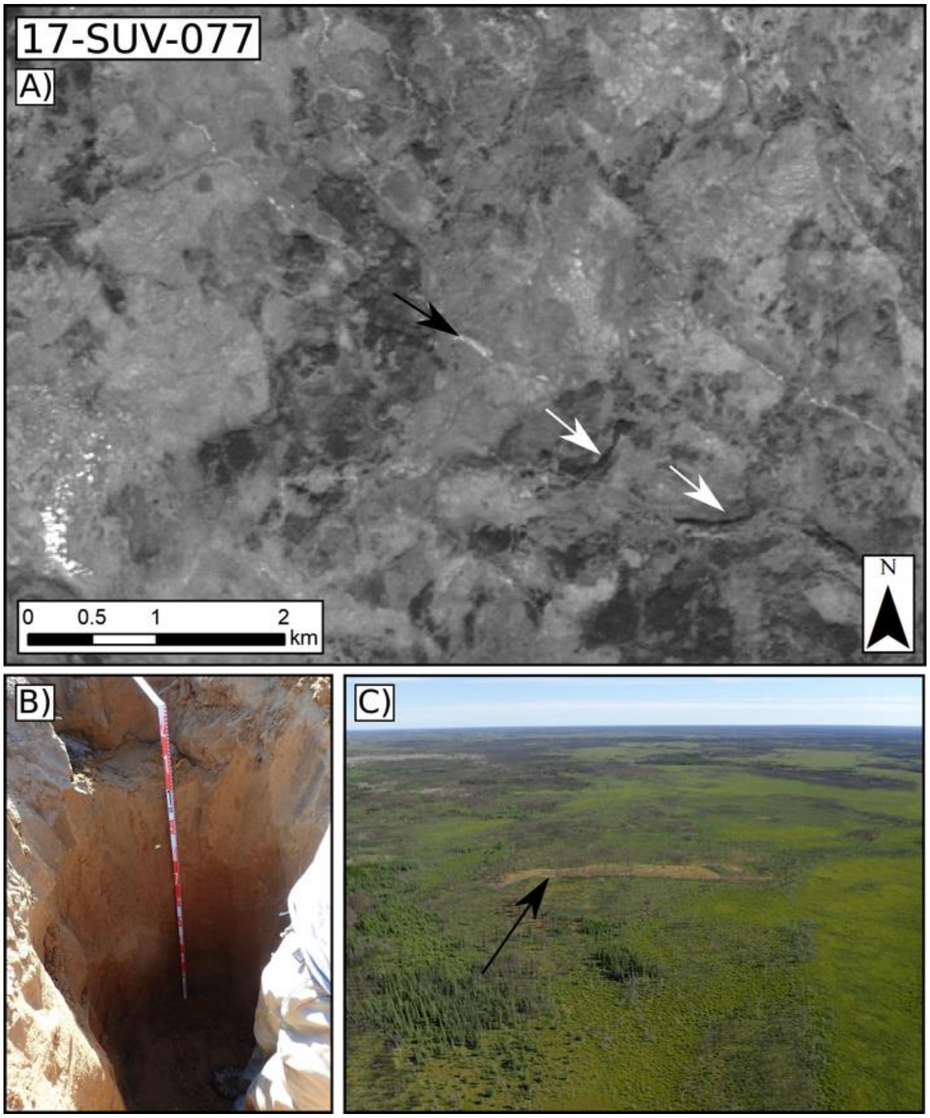

A) Landsat 8 Band 8 image of the parabolic dune where 17-SUV-077 was collected (black arrow points to sample location and direction of paleo-wind flow). Notice vegetated parabolic dune forms below and to the right (white arrow) recording a southeast paleo-wind flow direction. B) Photograph of the exposed face in the 1.45 m dug pit. C) Dune ridge as seen from helicopter looking northeast. Sample collected from highest point of parabolic ridge form (black arrow).

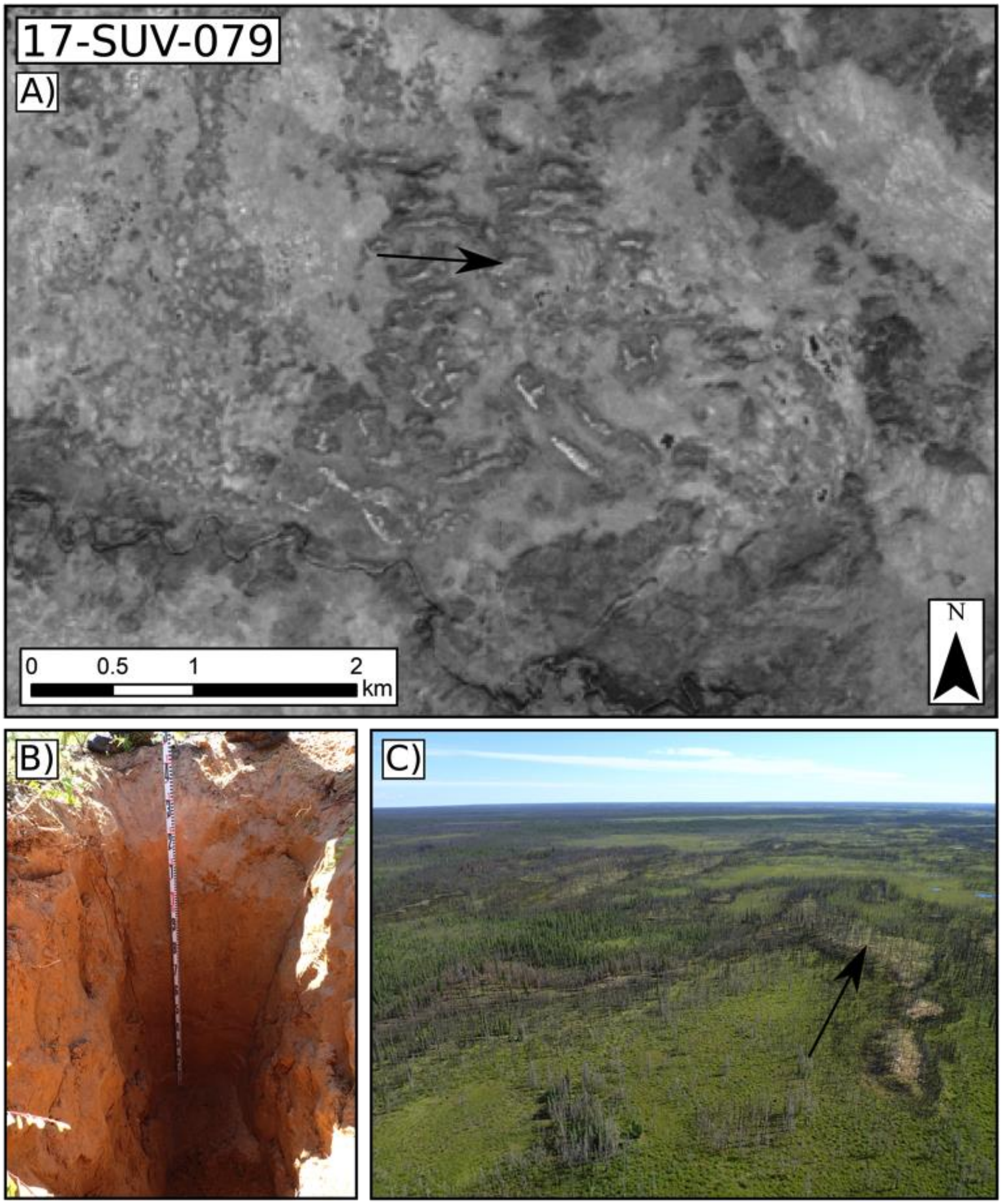

A) Landsat 8 Band 8 image of the parabolic and linear dune field where sample 17-SUV-079 was collected (black arrow points to sample location and direction of paleo-wind flow). B) Photograph of the exposed face in the 1.50 m deep dug pit. C) Dune ridge as seen from helicopter looking east; sample collection site indicated by black arrow.

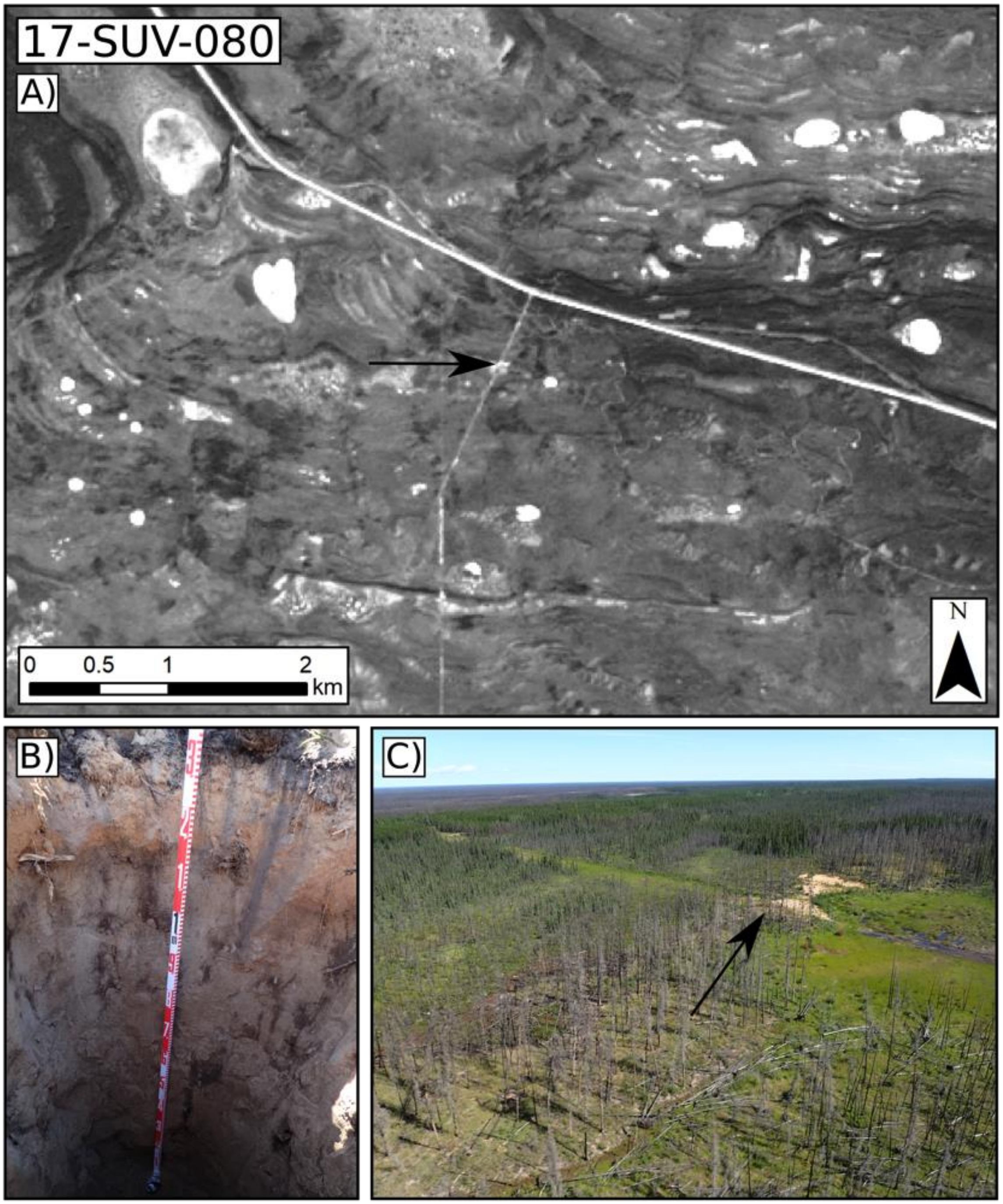

A) Landsat 8 Band 8 image of a large, broad longitudinal dune where 17-SUV-080 was collected (black arrow points to sample location and direction of paleo-wind flow). B) Photograph of the exposed face of the 1.5 m deep dug pit. C) Dune ridge as seen from helicopter looking northeast; sample collection site indicated by black arrow.

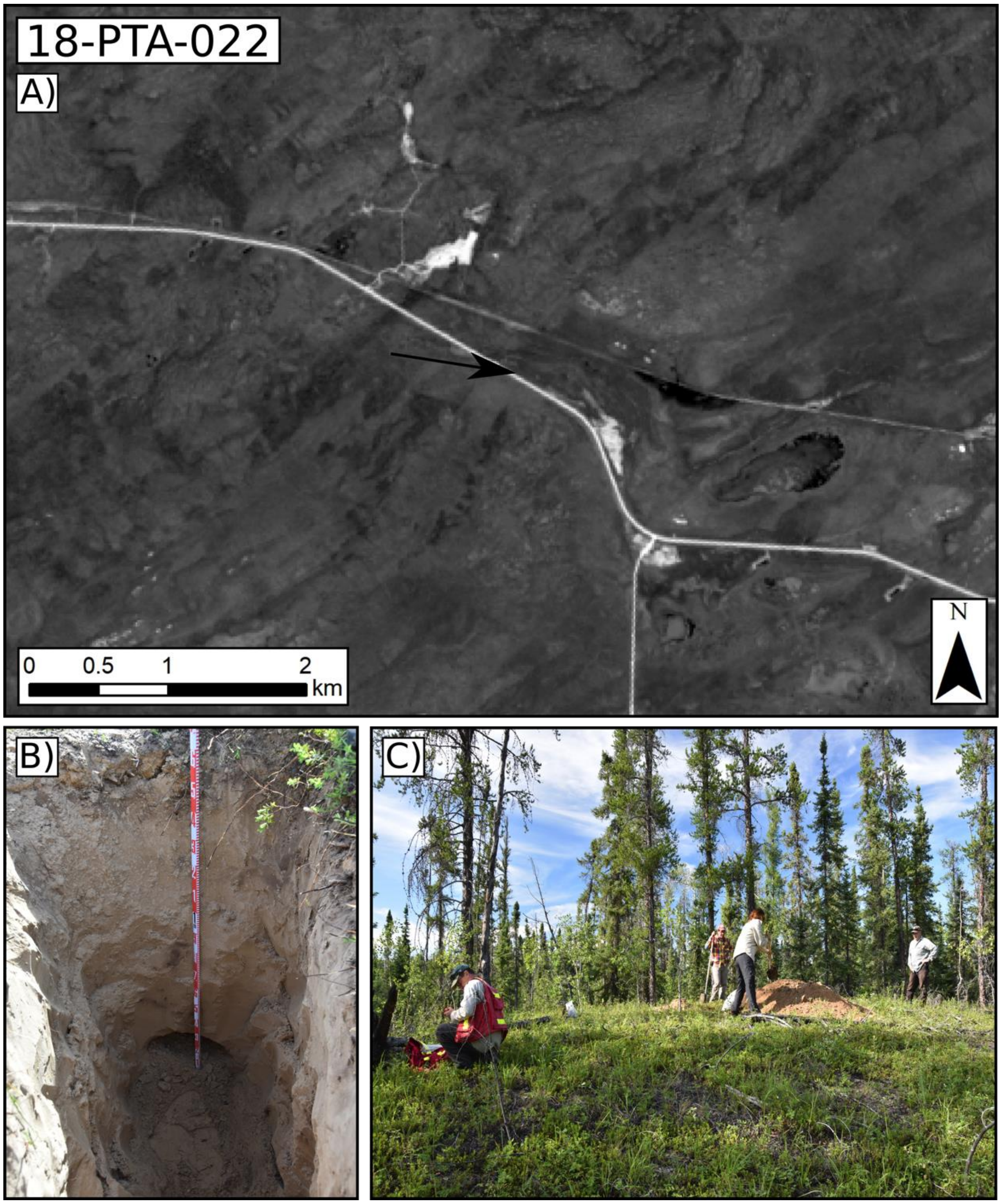

A) Landsat 8 Band 8 image of a parabolic dune where 18-PTA-022 was collected (black arrow points to sample location and direction of paleo-wind flow). B) Photograph of exposed face of the 1.6 m deep dug pit. C) Landscape of dune surface looking northwest; sample collection site to the right of image.

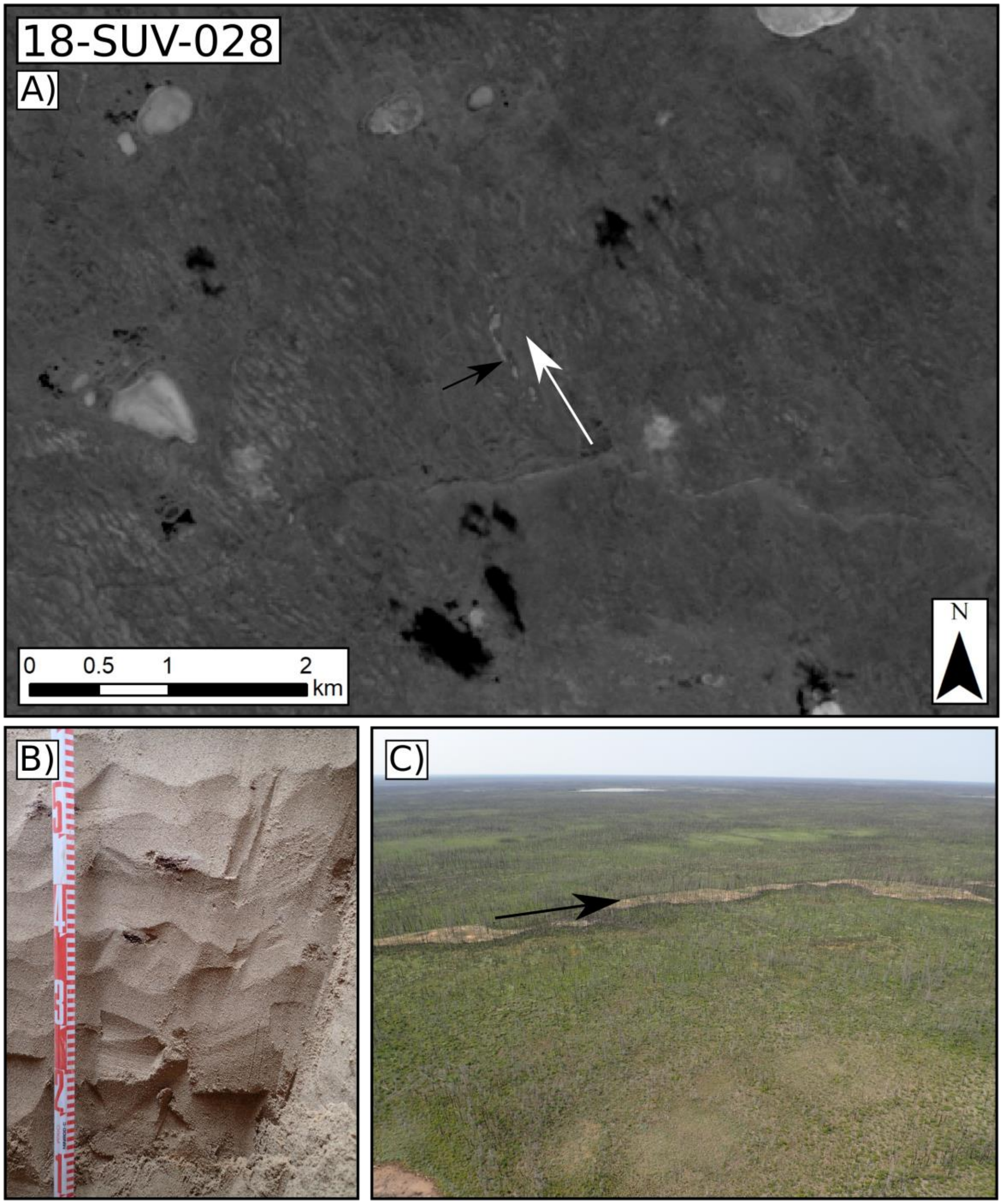

A) Landsat 8 Band 8 image of an elongate parabolic dune where 18-SUV-028 was collected (black arrow points to sample location and white arrow indicated direction of paleo-wind flow). B) Photograph of exposed face of 1.5 deep dug pit. C) Dune ridge as seen from helicopter looking southwest; sample collection site indicated by black arrow.

Appendix H

Optical Stimulated Luminesce

May 28, 2018

Optical ages, sample preparation and measurement procedures for SUV samples

Christina M. Neudorf & Olav B. Lian, Luminescence Dating Laboratory, University of the Fraser Valley

Optical dating sample sediments were extracted from the tubes under dim orange light conditions. The outermost (light-exposed) scrapings of each tube sample was retained for dosimetry and water content measurements. The concentrations of radioisotopes K^{40}, Th, U and Rb were determined from the dosimetry samples using neutron activation analysis at a commercial laboratory. A component of the sand size fraction (180–250 µm) was treated with HCl acid (10%) and H_2O_2 solution (10%) to remove any traces of carbonates and organic material, respectively. Quartz and potassium-rich (K) feldspar was concentrated using heavy liquid separation. The optical signal from quartz (sample 17-SUV-077) was measured and found to be unsuitable for optical dating because it contains a weak "fast" component. Thus, optical ages were determined from K-feldspar. Concentrated K-feldspar grains were subjected to standard HF treatments to remove the outermost part of the grains that would have been exposed to α radiation, rinsed in dilute HCl acid to remove fluoride precipitation, and then rinsed with deionized water, and then finally methanol. Dry grains were mounted on aluminum discs using silicone oil. All measurements were made using a Risø TL/OSL DA-20 reader equipped with a calibrated $^{90}Sr/^{90}Y$ β source that delivered β particles to the sample at a rate of ~5–6 Gy/min (Bøtter-Jensen et al., 2010). The optical signal was measured at 50°C while stimulated with infrared (IR) (880 nm) light; the blue-violet (~400 nm) emissions were detected using an Electron Tubes Ltd. 9235QA photomultiplier tube (PMT) fitted with Schott BG-39 and Corning 7-59 optical filters.

The equivalent dose (D_e) of each sample was measured using the single-aliquot regenerative-dose (SAR) protocol shown in Table 1. The relatively low (160°C) preheat temperature and 180°C hotwash in this protocol have been applied successfully to K-rich feldspar on the coast of British Columbia (Neudorf et al., 2015), in the Northwest Territories (Wolfe et al., 2018) and in Quebec (Rice et al., in prep). The D_e of all samples was measured using aliquots prepared using a 2 mm mask (~100 grains per aliquot). Aliquots were rejected from analysis if their recuperation value was greater than 5% of the natural signal and if their recycling ratio deviated from unity by more than 10% (Wintle and Murray, 2006). The suitability of the SAR protocol was tested using a dose recovery experiment. This entailed bleaching K-feldspar grains from 17-SUV-077 with direct natural sunlight for ~3 h, then administering a ~20 Gy laboratory dose and attempting to recover this dose using the protocol (Fig. 1). The measured/give dose ratio was 1.01 ± 0.01 suggesting that our SAR protocol was appropriate for these samples.

Typical IR stimulated luminescence (IRSL) signals, dose response curves, recycling ratios and recuperation values (all aliquots), and D_e distributions of accepted aliquots (i.e., those that passed all quality-control tests) are shown in Figure 2. The rate of fading of the IRSL signal (Fig. 3) was measured from 12 aliquots of each sample using the SAR protocol of Auclair et al. (2003) using the same preheat and stimulation temperatures and durations shown in Table 1. All samples were corrected for fading using the model of Huntley and Lamothe (2001).

Ages were calculated using weighted mean equivalent dose (D_e) values found using the Central Age Model (CAM) (Galbraith et al., 1999) (Table 2) and the environmental dose rate (Table 3). Overdispersion (OD) values for all samples are less than 18% suggesting that the grains were adequately bleached prior to deposition.

Table 1. SAR protocol used for the SUV samples.

1. Natural / Regenerative Dose
2. Preheat (160°C, 10 s)
3. IR diodes (50°C, 200 s @ 90% power) → L_n, L_x[1]
4. Test dose (4.2 Gy)
5. Preheat (160°C, 10 s)
6. IR diodes (50°C, 200 s @ 90% power)….→ T_n, T_x[1]
7. Hotwash (180°C, 40 s)
8. Return to step 1.

[1] Ln = natural signal, Lx = regenerative dose signal, Tn = natural test dose signal, Tx = regenerative test dose signal. A "zero dose" point was measured before the second highest regenerative dose to measure recuperation and build-up of background signal, and a repeat dose point was measured after the highest regenerative dose for the recycling ratio.

Table 2. Sample D_e values and optical ages (uncertainties are reported as ±1σ).

Sample	Grain size fraction (µm)	Total dose rate (Gy/ka)	Number of aliquots measured	Number of aliquots accepted	D_e (CAM) (Gy)	OD (%)	Fading rate[1] (%/decade)	Uncorrected age (ka)	Fading-corrected CAM age[2] (ka)
17-SUV-077	180-250	2.49 ± 0.14	24	24	20.7 ± 0.4	8	2.59 ± 0.05	8.3 ± 0.5	10.5 ± 0.6
17-SUV-079	180-250	2.49 ± 0.14	24	24	19.1 ± 0.6	14	2.85 ± 0.06	7.7 ± 0.5	9.9 ± 0.6
17-SUV-080	180-250	2.14 ± 0.12	24	24	16.7 ± 0.6	18	3.42 ± 0.09	7.8 ± 0.5	10.8 ± 0.7

[1] Fading rates were measured using the SAR method of Auclair et al. (2003) and are reported as the weighted mean *g*-value of 12 aliquots.

[2] Fading corrections were applied using the method of Huntley and Lamothe (2001).

Table 3. Dosimetry information (uncertainties are reported as ±1σ).

Sample	Total dose rate (Gy/ka)	Sample depth (cm)	Water content[1] (Δ^w)	Rb (ppm)	Th (ppm)	U (ppm)	K (%)
17-SUV-077	2.49 ± 0.14	135	0.048 ± 0.005	33 ± 2	3.7 ± 0.2	1.1 ± 0.1	1.0 ± 0.1
17-SUV-079	2.49 ± 0.14	140	0.028 ± 0.003	31 ± 2	3.0 ± 0.2	1.5 ± 0.1	0.9 ± 0.1
17-SUV-080	2.14 ± 0.12	140	0.027 ± 0.003	26 ± 2	2.8 ± 0.1	0.8 ± 0.1	0.7 ± 0.1

[1] Water contents are "as collected" values and are defined as (mass water)/(mass dry minerals).

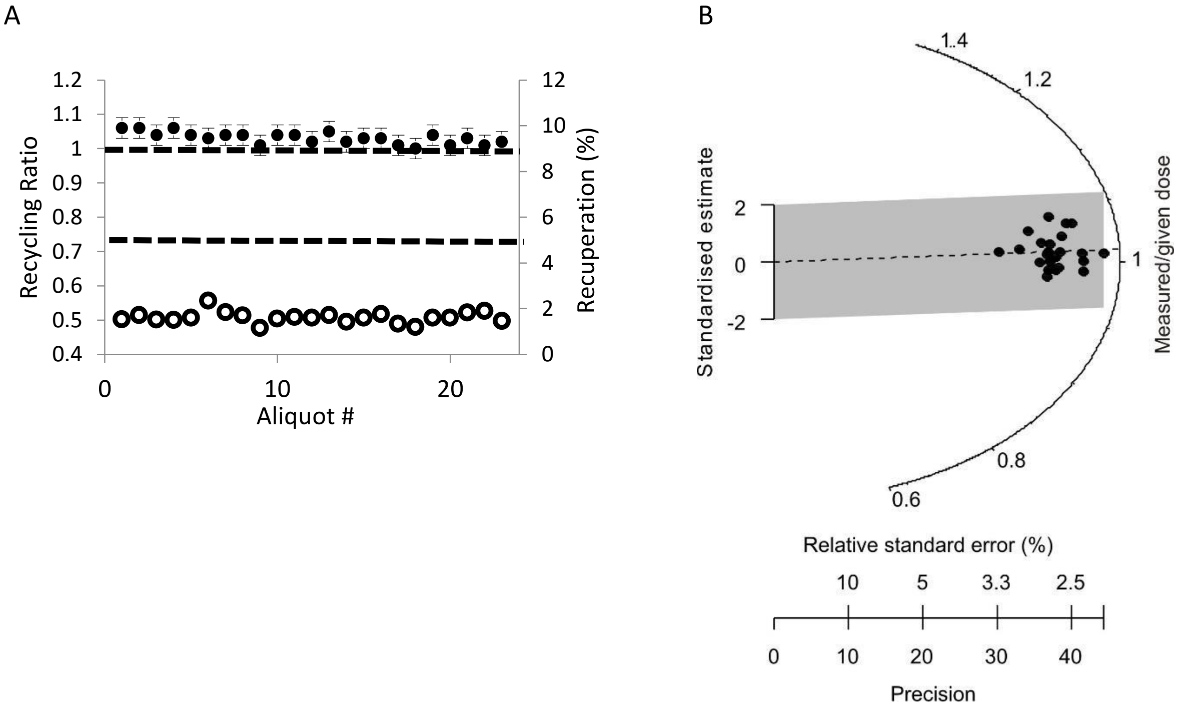

Figure 1. Dose recovery test results for sample 17-SUV-077. A) Recuperation values (open symbols) and recycling ratios (closed symbols) of all measured aliquots. B) The measured/given dose distribution. The shaded region is ± 2σ of the CAM weighted mean measured/given dose value (1.01 ± 0.01), which is indicated by the solid line.

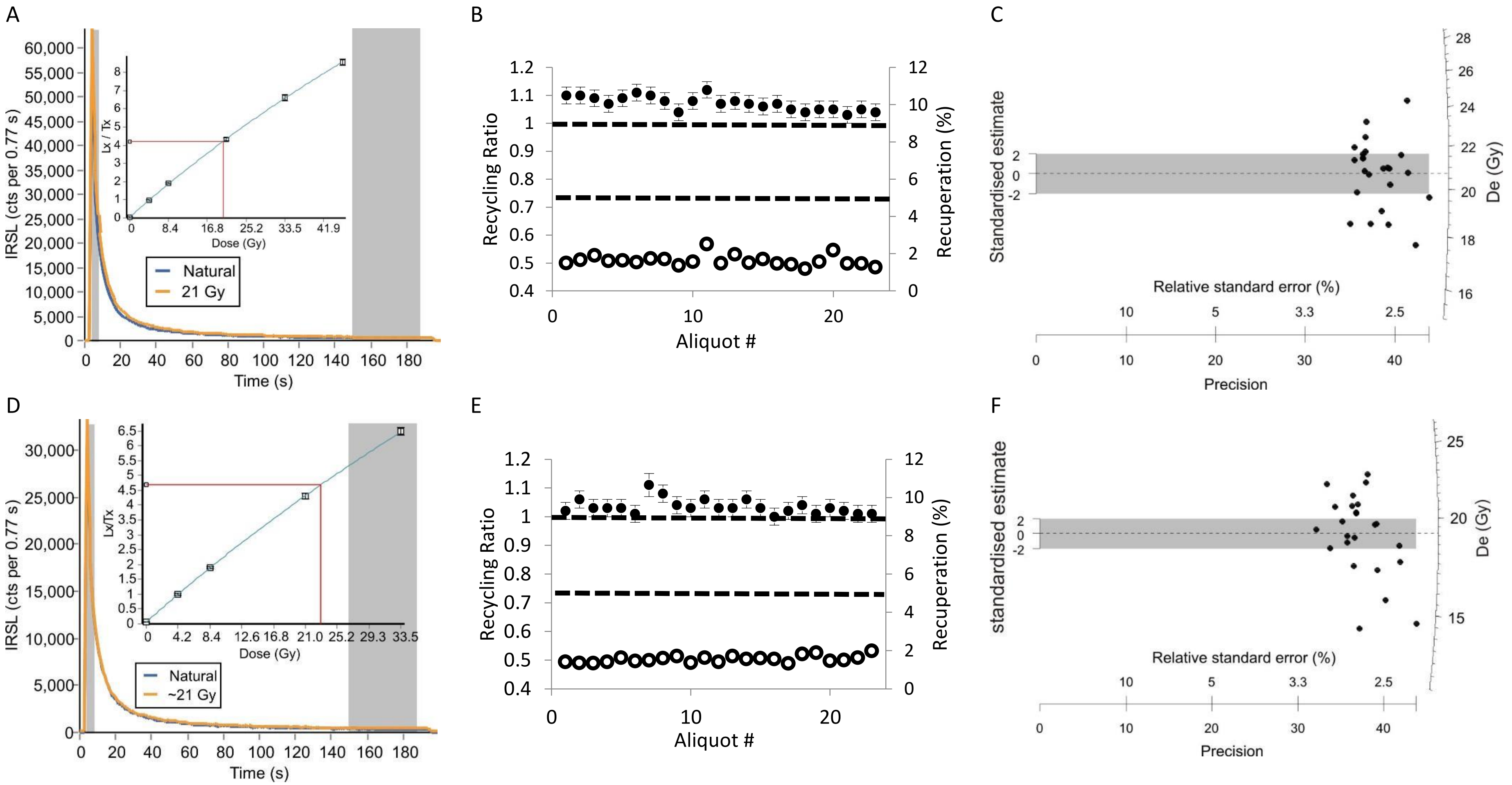

Figure 2. Optical decay curves, dose response curves (inset), recycling ratios and recuperation values (all aliquots) and D_e distributions (accepted aliquots) for samples 17-SUV-077 (A, B, C), 17-SUV-079 (D, E, F) and 17-SUV-080 (G, H, I). The shaded region of the radial plots is ± 2σ of the CAM weighted mean D_e value.

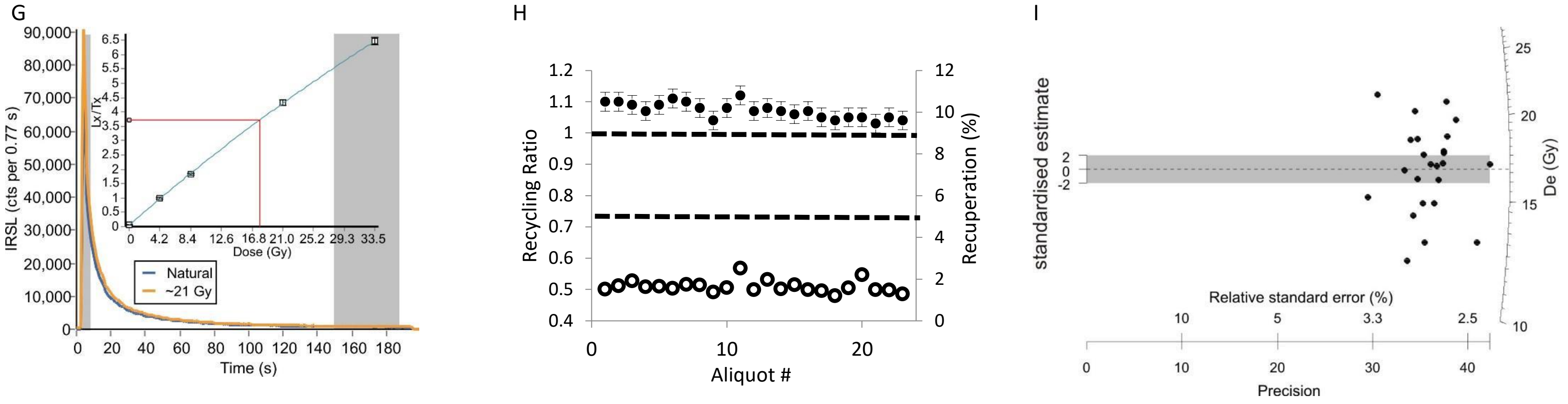

Figure 2. Continued.

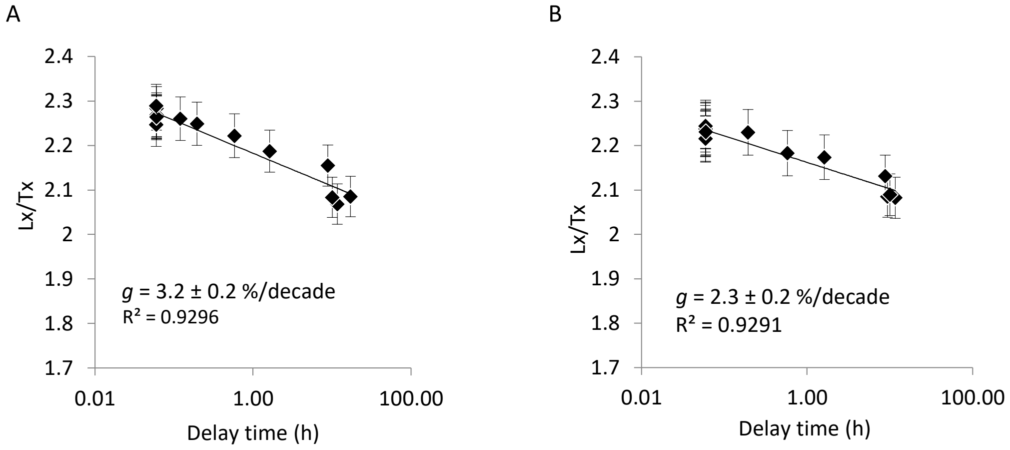

Figure 3. Typical fading plots for one aliquot of samples 17-SUV-077 (A) and 17-SUV-079 (B).

References

Auclair, M., Lamothe, M., Huot, S., 2003. Measurement of anomalous fading for feldspar IRSL using SAR. Radiation Measurements 37, 487–492.

Bøtter-Jensen, L., Thomsen, K.J., Jain, M., 2010. Review of optically stimulated luminescence (OSL) instrumental developments for retrospective dosimetry. Radiation Measurements 45, 253–257.

Galbraith, R.F., Roberts, R.G., Laslett, G.M., Yoshida, H., Olley, J.M., 1999. Optical dating of single and multiple grains of quartz from Jinmium rock shelter, northern Australia: Part I, experimental design and statistical models. Archaeometry 41, 339–364.

Huntley, D.J., Lamothe, M., 2001. Ubiquity of anomalous fading in K-feldspars and the measurement and correction for it in optical dating. Canadian Journal of Earth Sciences 38, 1093–1106.

Neudorf, C.M., Lian, O.B., Walker, I.J., Shugar, D.H., Eamer, J.B.R., Griffin, L.C.M., 2015. Toward a luminescence chronology for coastal dune and beach deposits on Calvert Island, British Columbia central coast, Canada. Quaternary Geochronology 30, 275–281.

Wolfe, S.A., Morse, P.D., Neudorf , C.M., Kokelj, S.V., Lian, O.B., O'Neill, H.B., 2018. Contemporary sand wedge development in seasonally-frozen ground and paleoenvironmental implications. Geomorphology 308, 215–229.

Wintle, A.G., Murray, A.S., 2006. A review of quartz optically stimulated luminescence characteristics and their relevance in single-aliquot regeneration dating protocols. Radiation Measurements 41, 369–391.

Table 1. Dosimetry information

Sample	Depth (cm)[1]	Δ^{w}[2]	Rb (ppm)	Th (ppm)	U (ppm)	K (%)
17-SUV-077	135	0.0481	33.1 ± 2.0	3.68 ± 0.19	1.07 ± 0.07	0.956 ± 0.100
17-SUV-079	140	0.0276	30.7 ± 1.8	2.97 ± 0.15	1.52 ± 0.09	0.868 ± 0.090
17-SUV-080	140	0.0267	26.4 ± 1.6	2.79 ± 0.14	0.830 ± 0.057	0.653 ± 0.070
18-SUV-028	145	0.0468	51.0 ± 3.1	4.20 ± 0.21	1.30 ± 0.09	1.48 ± 0.12
18-PTA-022	160	0.0683	38.0 ± 2.4	3.20 ± 0.16	1.00 ± 0.08	1.20 ± 0.10
18-PTA-028	70	0.0524	36.0 ± 2.3	3.50 ± 0.18	1.20 ± 0.09	1.13 ± 0.09
18-PTA-029	65	0.0738	23.0 ± 1.7	2.70 ± 0.14	0.900 ± 0.007	0.840 ± 0.077

[1] Sample depth beneath the ground surface

[2] Water contents (Δ^{w}) are "as collected" values and are defined as (mass water)/(mass dry minerals). Uncertainties of ±10 % were included in the dose rate calculations.

Note: Rb, Th, U, and K concentrations were determined using neutron activation analysis; uncertainties are reported as ±1σ.

Table 2. Sample dose rates, equivalent dose (D_e) values, fading rates (*g*), and optical ages (uncertainties are reported as ±1σ).

Sample	Cosmic-ray dose rate (Gy/ka)	Total dose rate (Gy/ka)[1]	D_e (CAM)[2] (Gy)	OD (%)[3]	Fading rate[4] (%/decade)	Uncorrected age (ka)	Fading-corrected CAM age (ka)[4]
17-SUV-077	0.166 ± 0.008	2.49 ± 0.14	20.7 ± 0.4	8.40 ± 1.3	2.59 ± 0.05	8.33 ± 0.48	10.5 ± 0.6
17-SUV-079	0.165 ± 0.008	2.49 ± 0.14	19.1 ± 0.6	13.9 ± 2.1	2.85 ± 0.06	7.66 ± 0.48	9.9 ± 0.6
17-SUV-080	0.165 ± 0.008	2.14 ± 0.12	16.7 ± 0.6	18	3.42 ± 0.09	7.8 ± 0.5	10.8 ± 0.7
18-SUV-028	0.163 ± 0.008	3.06 ± 0.19	18.6 ± 0.4	10.3 ± 1.6	2.87 ± 0.16	6.07 ± 0.40	7.85 ± 0.54
18-PTA-022	0.159 ± 0.008	2.61 ± 0.16	17.3 ± 0.3	8.04 ± 1.27	2.83 ± 0.16	6.60 ± 0.42	8.52 ± 0.56
18-PTA-028	0.186 ± 0.009	2.67 ± 0.16	22.8 ± 1.8[5]	36.5 ± 5.3	3.21 ± 0.16	8.53 ± 0.82[5]	11.5 ± 1.1[5]
18-PTA-029	0.187 ± 0.009	2.23 ± 0.13	19.8 ± 0.9	22.5 ± 3.3	3.22 ± 0.17	8.87 ± 0.67	12.0 ± 0.9

[1] Dose rates due to α, β, and γ radiation were calculated from radioisotope concentrations using the absorption and attenuation coefficients of Guérin et al. (2012), the conversion factors of Guérin et al. (2011), and as-collected water contents. An internal α dose rate of 0.09 Gy/ka was used based on Ollerhead et al. (1994).

[2] CAM = central age model (Galbraith et al. 1999).

[3] OD = overdispersion.

[4] Fading rates (*g*-values) were measured using the SAR method of Auclair et al. (2003) and are reported as the weighted mean *g*-value of those determined from 12 aliquots.

[5] Fading corrections were applied using the method of Huntley and Lamothe (2001).

[5] If the minimum age model (MAM) (Galbraith et al. 1999) is applied to sample 18-PTA-028, the D_e, uncorrected age, and fading-corrected age for this sample become 16.6 ± 1.5 Gy, 6.22 ± 0.68 ka, and 8.28 ± 0.91 ka, respectively.

Note: all D_e determinations were based on 24 aliquots. All aliquots contained K-feldspar concentrates in the 180–250 µm size range

Appendix I

Radiocarbon Data

Sample Processing

Sample pretreatment techniques, processing and definitions of media codes can be found in Crann et al. (2017) and Murseli et al. (2019). For more information about the equipment used for sample preparation, please see St-Jean et al. (2017). All manuscripts can be found at www.ams.uottawa.ca/Research.html

Reporting of Data

In this analysis report, we have followed the conventions recommended by Millard (2014).

Radiocarbon Analysis

Radiocarbon analyses are performed on a 3MV tandem accelerator mass spectrometer built by High Voltage Engineering (HVE). $^{12,13,14}C^{+3}$ ions are measured at 2.5 MV terminal voltage with Ar stripping. The fraction modern carbon, $F^{14}C$, is calculated according to Reimer et al. (2004) as the ratio of the sample $^{14}C/^{12}C$ ratio to the standard $^{14}C/^{12}C$ ratio (in our case Ox-II) measured in the same data block. Both $^{14}C/^{12}C$ ratios are background-corrected and the result is corrected for spectrometer and preparation fractionation using the AMS measured $^{13}C/^{12}C$ ratio and is normalized to $\delta^{13}C$ (PDB). Radiocarbon ages are calculated as $-8033\ln(F^{14}C)$ and reported in ^{14}C yr BP (BP=AD 1950) as described by Stuiver and Polach (1977). The errors on 14C ages (1σ) are based on counting statistics and $^{14}C/^{12}C$ and $^{13}C/^{12}C$ variation between data blocks. We do not report $\delta^{13}C$ as it is measured on the AMS and contains machine fractionation.

Calibration

Calibration was performed using OxCal v4.3 (Bronk Ramsey, 2009). Calibrated results are given as a range (or ranges) with an associated probability as point estimates (mean, median) cannot represent the uncertainties involved (Millard, 2014). We acknowledge that point estimates are often desired and are thus included on the calibration plots in the Appendix, but we recommend that data tables used in publication maintain calibrated age ranges.

Where the $F^{14}C$ is less than 1, the IntCal13 calibration curve was used for Northern Hemisphere samples and ShCal13 for Southern Hemisphere samples (Reimer et al., 2013).

For samples with an $F^{14}C$ greater than 1, the post-bomb atmospheric curve was used (Hua et al., 2013). Post-bomb samples have two age ranges due to calibration on both sides of the bomb pulse. There are methods for deciding which side of the bomb pulse to select as the more appropriate date so feel free to contact us for further information.

Samples that calibrate between the 1700's and early 1950's will always result in a calibrated age range covering the majority of this period. This is due to the "Seuss Effect", which is a flat portion of the calibration curve caused by the burning of fossil fuels.

Rounding

Calibrated ages and ranges are rounded to the nearest year which may be too precise in many instances. Users are advised to round results to the nearest 10 yr for samples with standard deviation in the radiocarbon age greater than 50 yr, but rounding should only be done at the final reporting stage as intermediate rounding may introduce errors (Millard, 2014).

References

Bronk Ramsey C. 2009. Bayesian analysis of radiocarbon dates. *Radiocarbon* 51: 337–360.

Crann CA, Murseli S, St-Jean G, Zhao X, Clark ID, Kieser WE. 2017. First status report on radiocarbon sample preparation at the A.E. Lalonde AMS Laboratory (Ottawa, Canada). Radiocarbon 59(3): 695–704. http://doi.org/10.1017/RDC.2016.55

Hua Q, Barbetti M, Rakowski AZ. 2013. Atmospheric radiocarbon for the period 1950-2010. *Radiocarbon* 55(4): 2059–2072.

Millard A. 2014. Conventions for reporting radiocarbon determinations. *Radiocarbon* 56(2): 555–559.

Murseli S, Middlestead P, St-Jean G, Zhao X, Jean C, Crann CA, Kieser, WE, Clark ID. 2019 The preparation of water (DIC, DOC) and gas (CO2, CH4) samples for radiocarbon analysis at AEL-AMS, Ottawa, Canada. Radiocarbon. http://doi.org/10.1017/RDC.2019.14

Reimer PJ, Bard E, Bayliss A, Beck JW, Blackwell PG, Bronk Ramsey C, Buck CE, Cheng H, Edwards RL, Friedrich M, Grootes PM, Guilderson TP, Haflidason H, Hajdas I, Hatté C, Heaton TJ, Hogg AG, Hughen KA, Kaiser KF, Kromer B, Manning SW, Niu M, Reimer RW, Richards DA, Scott EM, Southon JR, Turney CSM, van der Plicht J. 2013. IntCal13 and MARINE13 radiocarbon age calibration curves 0-50000 years calBP. Radiocarbon 55(4): 1869–1887.

St-Jean G, Kieser WE, Crann CA, Murseli S. 2017. Semi-automated equipment for CO2 purification and graphitization at the A.E. Lalonde AMS Laboratory (Canada). Radiocarbon 59(3): 941–956. https://doi.org/10.1017/RDC.2016.57

Stuiver M, Polach HA. 1977. Discussion: reporting of 14C data. Radiocarbon 19(3):355–63.

Table 1. Radiocarbon results. Calibration was performed using OxCal v4.3 (Bronk Ramsey, 2009) and the IntCal13 calibration curve (Reimer et al., 2013). Material codes are described in Crann et al. (2017).

Lab ID	Submitter ID	Material	Mat. Code	^{14}C yr BP	±	F^{14}C	±	cal BP
UOC-12476	18PTA004_wood	wood	AAA	2451	22	0.73701	0.00206	2701 – 2631 (30.8%) 2618 – 2585 (11.8%) 2575 – 2563 (1.8%) 2542 – 2363 (51.0%)
UOC-12477	18PTA004	Peat	AAA	2917	26	0.69550	0.00225	3158 – 2970 (95.4%)

Appendix 1: Sampling Photos 18PTA004_wood

Appendix 2: Calibration Plots

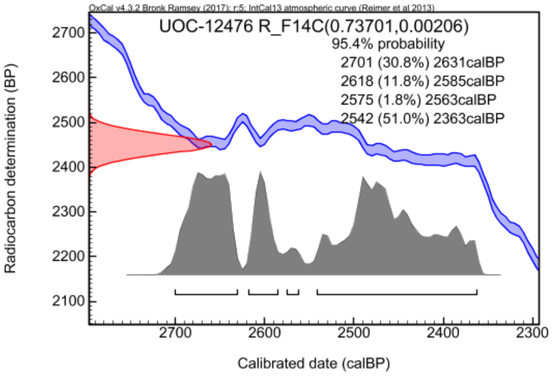

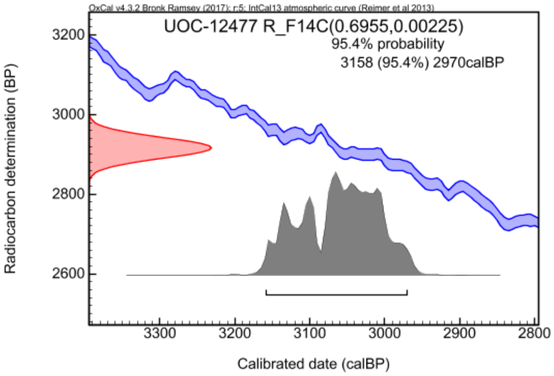

Sample Processing

Sample pretreatment techniques, processing and definitions of media codes can be found in Crann et al. (2017) and Murseli et al. (2019). For more information about the equipment used for sample preparation, please see St-Jean et al. (2017). All manuscripts can be found at www.ams.uottawa.ca/Research.html

Reporting of Data

In this analysis report, we have followed the conventions recommended by Millard (2014).

Radiocarbon Analysis

Radiocarbon analyses are performed on a 3MV tandem accelerator mass spectrometer built by High Voltage Engineering (HVE). $^{12,13,14}C^{+3}$ ions are measured at 2.5 MV terminal voltage with Ar stripping. The fraction modern carbon, $F^{14}C$, is calculated according to Reimer et al. (2004) as the ratio of the sample $^{14}C/^{12}C$ ratio to the standard $^{14}C/^{12}C$ ratio (in our case Ox-II) measured in the same data block. Both $^{14}C/^{12}C$ ratios are background-corrected and the result is corrected for spectrometer and preparation fractionation using the AMS measured $^{13}C/^{12}C$ ratio and is normalized to $\delta^{13}C$ (PDB). Radiocarbon ages are calculated as $-8033\ln(F^{14}C)$ and reported in ^{14}C yr BP (BP=AD 1950) as described by Stuiver and Polach (1977). The errors on 14C ages (1σ) are based on counting statistics and $^{14}C/^{12}C$ and $^{13}C/^{12}C$ variation between data blocks. We do not report $\delta^{13}C$ as it is measured on the AMS and contains machine fractionation.

Calibration

Calibration was performed using OxCal v4.3 (Bronk Ramsey, 2009). Calibrated results are given as a range (or ranges) with an associated probability as point estimates (mean, median) cannot represent the uncertainties involved (Millard, 2014). We acknowledge that point estimates are often desired and are thus included on the calibration plots in the Appendix, but we recommend that data tables used in publication maintain calibrated age ranges.

Where the $F^{14}C$ is less than 1, the IntCal13 calibration curve was used for Northern Hemisphere samples and ShCal13 for Southern Hemisphere samples (Reimer et al., 2013).

For samples with an $F^{14}C$ greater than 1, the post-bomb atmospheric curve was used (Hua et al., 2013). Post-bomb samples have two age ranges due to calibration on both sides of the bomb pulse. There are methods for deciding which side of the bomb pulse to select as the more appropriate date so feel free to contact us for further information.

Samples that calibrate between the 1700's and early 1950's will always result in a calibrated age range covering the majority of this period. This is due to the "Seuss Effect", which is a flat portion of the calibration curve caused by the burning of fossil fuels.

Rounding

Calibrated ages and ranges are rounded to the nearest year which may be too precise in many instances. Users are advised to round results to the nearest 10 yr for samples with standard deviation in the radiocarbon age greater than 50 yr, but rounding should only be done at the final reporting stage as intermediate rounding may introduce errors (Millard, 2014).

References

Bronk Ramsey C. 2009. Bayesian analysis of radiocarbon dates. *Radiocarbon* 51: 337–360.

Crann CA, Murseli S, St-Jean G, Zhao X, Clark ID, Kieser WE. 2017. First status report on radiocarbon sample preparation at the A.E. Lalonde AMS Laboratory (Ottawa, Canada). Radiocarbon 59(3): 695–704. http://doi.org/10.1017/RDC.2016.55

Hua Q, Barbetti M, Rakowski AZ. 2013. Atmospheric radiocarbon for the period 1950-2010. *Radiocarbon* 55(4): 2059–2072.

Millard A. 2014. Conventions for reporting radiocarbon determinations. *Radiocarbon* 56(2): 555–559.

Murseli S, Middlestead P, St-Jean G, Zhao X, Jean C, Crann CA, Kieser, WE, Clark ID. 2019 The preparation of water (DIC, DOC) and gas (CO2, CH4) samples for radiocarbon analysis at AEL-AMS, Ottawa, Canada. Radiocarbon. http://doi.org/10.1017/RDC.2019.14

Reimer PJ, Bard E, Bayliss A, Beck JW, Blackwell PG, Bronk Ramsey C, Buck CE, Cheng H, Edwards RL, Friedrich M, Grootes PM, Guilderson TP, Haflidason H, Hajdas I, Hatté C, Heaton TJ, Hogg AG, Hughen KA, Kaiser KF, Kromer B, Manning SW, Niu M, Reimer RW, Richards DA, Scott EM, Southon JR, Turney CSM, van der Plicht J. 2013. IntCal13 and MARINE13 radiocarbon age calibration curves 0-50000 years calBP. Radiocarbon 55(4): 1869–1887.

St-Jean G, Kieser WE, Crann CA, Murseli S. 2017. Semi-automated equipment for CO2 purification and graphitization at the A.E. Lalonde AMS Laboratory (Canada). Radiocarbon 59(3): 941–956. https://doi.org/10.1017/RDC.2016.57

Stuiver M, Polach HA. 1977. Discussion: reporting of 14C data. Radiocarbon 19(3):355–63.

Table 1. Radiocarbon results. Calibration was performed using OxCal v4.3 (Bronk Ramsey, 2009) and the IntCal13 calibration curve (Reimer et al., 2013). Material codes are described in Crann et al. (2017).

Lab ID	Submitter ID	Material	Mat. Code	^{14}C yr BP	±	F^{14}C	±	cal BP
UOC-12678	18PTA004_5-12	wood	AAA	2373	26	0.7443	0.0024	2484 – 2477 (1.2%) 2470 – 2341 (94.2%)
UOC-12679	18PTA004_5-12	Peat	AAA	2247	30	0.7560	0.0028	2343 – 2295 (29.2%) 2270 – 2155 (66.2%)
UOC-12680	18PTA004_>5	wood	AAA	2421	25	0.7398	0.0023	2685 – 2637 (12.7%) 2612 – 2596 (3.2%) 2497 – 2353 (79.5%)
UOC-12681	18PTA004_>5	Peat	AAA	2351	29	0.7463	0.0027	2461 – 2327 (95.4%)

Appendix: Calibration Plots